UNIVERSITÀ
DEGLI STUDI
DI PADOVA

Sede Amministrativa: Università degli Studi di Padova
Dipartimento di Ingegneria Civile, Edile e Ambientale (ICEA)

SCUOLA DI DOTTORATO DI RICERCA IN:
SCIENZE DELL'INGEGNERIA CIVILE ED AMBIENTALE
XXVII CICLO

MULTIPHASE MATERIAL MODELLING IN FINITE DEFORMATIONS: THEORETICAL ASPECTS, NUMERICAL IMPLEMENTATION AND APPLICATIONS

Direttore della Scuola: Ch.mo Prof. Stefano Lanzoni

Supervisori: Ch.mo Prof. C. Majorana

Dott.ssa Valentina Salomoni

Dottorando: Nicolò Spiezia

This doctoral thesis has been approved as follows:

Prof. Lanzoni .....
Director of the PhD program

Prof. Majorana .....
Thesis Supervisor

Dr. Salomoni .....
Thesis Supervisor

Nicolò Spiezia .....
PhD Candidate

Abstract

Multiphase materials are of primary relevance in many disciplines in engineering and science. They consist of a porous solid skeleton, whose pores are filled by one or more fluid phases, such as water, air, gas, oil etc. The relevant number of applications involving multiphase material motivated the development of several theoretical models and numerical procedures to describe the coupled behavior between the different phases. Most of these models, based on the formulation of the balance laws for the coexisting phases, rely upon the assumption of small strains, which is a simplifying but restrictive hypothesis for several applications. The aim of this thesis is to investigate the theoretical aspects and the numerical solutions of a multiphase material undergoing large elastoplastic strains, taking into account the fully coupling between the solid and the fluid phases. The essential idea of the model consists in imposing the balance laws for the two (or more) phases in the current deformed configuration, and to solve it numerically with a finite element method. To deal with elastoplasticity at finite strains, the formulation adopts the multiplicative decomposition of the deformation gradient. The developed numerical model has been applied, in particular, to assess the stability of a horizontal wellbore drilled through a high porous rock formation, quantifying the stress and strain distribution, the evolution of the plastic deformations and the propagation of band of intense deformation. To capture both the shear-enhanced compaction and the shear-induced dilation characteristic of porous rock, an innovative elastoplastic constitutive model has been derived, endowed with a linear and elliptical yield surface that intersect smoothly. The results of the simulations show the capability of the finite deformations coupled approach to simulate the whole process.

Sommario

I materiali multifase sono di primaria importanza in molte discipline dell'ingegneria e della scienza. Essi sono costituiti da uno scheletro solido poroso, i cui pori sono riempiti da una o più fluidi, ad esempio acqua, aria, gas, petrolio, etc. Il vasto campo di applicazione dei materiali multifase ha motivato lo sviluppo di diversi modelli teorici e procedure numeriche per descrivere il comportamento accoppiato fra le diverse fasi. La maggior parte di questi modelli, basati sulla formulazione delle leggi di bilancio per le differenti fasi coesistenti, si basano sul presupposto di piccole deformazioni, ipotesi che comporta una semplificazione dei modelli ma allo stesso tempo risulta essere restrittiva per diverse applicazioni.

Lo scopo di questa tesi è indagare gli aspetti teorici e le soluzioni numeriche di un materiale multifase che subisce grandi deformazioni elastoplasticche, tenendo conto del completo accoppiamento tra la fase solida e la fase fluida. L'idea essenziale del modello consiste nell'imporre le leggi di bilancio per le due (o più) fasi nella configurazione corrente deformata, e poi risolvere tali equazioni numericamente con un metodo agli elementi finiti. Per quanto concerne l'elastoplasticità a deformazioni finite, la formulazione adotta la decomposizione moltiplicativa del gradiente di deformazione. Il modello numerico sviluppato è stato applicato, in particolare, per valutare la stabilità di un pozzo perforato orizzontalmente attraverso una formazione rocciosa altamente porosa, per quantificare la distribuzione delle tensioni e delle deformazioni, per descrivere l'evoluzione delle deformazioni plastiche e la propagazione di bande di deformazione. Per cogliere tanto il fenomeno di compattazione e di dilatazione plastica, caratteristico di rocce ad alta porosità, è stato sviluppato un innovativo modello costitutivo elastoplastico, dotato di una superficie lineare e di una superficie ellittica che si intersecano mantenendo la derivabilità in ogni punto. I risultati delle simulazioni mostrano la capacità dell'approccio a grandi deformazioni per simulare l'intero processo accoppiato.

Acknowledgments

This work would not have been possible without the encouragement and help of so many people that may be difficult to count all of them in these acknowledgments.

I would like to express my deep gratitude to Prof. Majorana and Dr. Salomoni, my research supervisors, for their patient guidance during the PhD, fundamental support and useful critiques of this research work.

I would like to express my very great gratitude to Prof. Borja for his valuable and constructive suggestions during the nine months at Stanford University. His constant enthusiasm, his support in every situation and the willingness to give his time so generously has been very much appreciated. I would like also to thank Prof. Regueiro and Prof. Linder, for the constructive discussions we had about the topic of this work.

I would like to thank the italian colleagues at Department ICEA: Dr. Mazzucco, for his humble and extremely precious advices, Dr. Xotta, Dr. Pomaro and Dr. Fincato, for the great time we spent together, and Dr. Muraro, for being the best office mate ever. My gratitude also goes to Dr. Sanavia, for the inspiring discussions and his kindness.

My grateful thanks are also extended to the colleagues at Stanford University, in particular to Dr. Song, Dr. Choo, Dr. Tjioe, Dr. Bennett and Dr. Semnani for their help end friendship, and all the mates at Moreno Avenue.

Finally, I wish to thank my parents and friends for their support and encouragement throughout my study.

This project would have been impossible without the support of the Gini Foundation, which provided financial support during the research period at Stanford University.

Contents

List of Figures

List of Tables

Chapter 1

Introduction

1.1 Motivation and scope

Multiphase materials consist of a solid phase, usually referred to as matrix or skeleton, as well as closed and open pores which are filled with fluid phases, as water, air, oil, gas, etc. Examples of multiphase materials - also referred to as porous materials - are soils, rocks, biological tissues, human bones and porous aluminum foam, to name a few. The mechanics of porous media is of utmost relevance in many disciplines in engineering and science, such as geotechnical engineering, biomechanics, physical chemistry, agricultural engineering and material science. The great importance of this type of material and the broad field of applications motivated the development of various multiphase and poromechanics models and numerical procedures to asses the mechanical behavior of this type of material (5; 6; 7; 8; 9; 10; 11).

Capturing the fully coupled physical process involving the solid and the fluid phases is, nevertheless, not a trivial task. Realistic physical simulations require either an iterative sequential scheme or a monolithic scheme, to handle the multiple-field governing equations. The corner stone of the coupled formulation is to write the linear momentum and mass balance equations in terms of the solid displacement and fluid pore pressure, and then solve them simultaneously with a monolithic solver via a two-field (or more) mixed formulation. This approach is fairly well developed and adequately documented (12; 13; 10). Usually this formulation assumes infinitesimal strains, which simplifies the linear momentum balance equation since the equilibrium is imposed in the initial undeformed configuration which is considered coincident with the deformed one. Furthermore, the infinitesimal strain assumption also simplifies the mass conservation equation since the volume change of the mixture becomes a linear function of the nodal solid displacements.

Even though the small strain theory is suitable to describe the mechanical behavior of several applications, in some contexts it is fundamental to take into account the large deformations experienced

by the solid skeleton. There are many applications where the geometric non linear effects could critically influence the outcome of a numerical analysis. As far as the geotechnical field, large deformations and displacements are in general observed in every situation where the limit state condition is reached. One example is the large movement of slopes, the consolidation over a significant load, the tilting of a tower due to the $P-\delta$ effect, the stability of a tunnel or a borehole. In particular, the impact of finite deformation is most evident in soft clays, loose sands and high porous rocks, where movements develop with time due to so-called hydrodynamic lag, a phenomenon which involves transient interaction between the solid and fluid phases. Furthermore, in certain circumstances involving dynamic effects, finite strain assumption plays a major role in the prediction of the local site response, where the buildup of fluid pressure induced for example by seismic shaking could lead to a rapid loss of strength of the saturated soil deposit, a phenomenon commonly referred to in the literature as liquefaction. As far as the biomechanical field, finite strain assumption is essential to model hard and soft tissue growth and remodeling as cyclic stresses applied to the tissue solid/fluid mixture generate solid deformation, resulting in fluid flow and mass transport through the tissue solid matrix. Multiphase finite assumption also plays a significant role during head impacts as skull and brain tissues contact and deform with concomitant fluid flow in and out the tissues. Although deformation of bone is relatively small (0.4% strain), a geometrically nonlinear theory is needed in order to account properly for large rotations and translations experienced during dynamic loading such as head impact and knee bending. The finite deformation theory is also necessary for modeling contact of hard tissue with soft tissue (e.g., skull with brain, bone with cartilage, etc.) and resulting fluid flow. With regard to multiphase continuum formulations in biomechanics, two- and three-field formulations (and more fields when chemical and electrical effects are included) have been used for simulating deformation of soft, hydrated biological tissues, such as cartilage and heart muscle, for small strains and finite strains (14; 15; 16).

The aim of this thesis it to investigate the theoretical aspects and the numerical solutions of a multiphase material undergoing large elastoplastic strains, taking into account the coupling effects between the solid and the fluid phases. This topic has been studied by several authors in the last decades, but still remains of particular interest and critical for a lot of applications, especially in the geotechnical field. This work is mainly based on the pioneer research done by Borja et al. (17; 1; 18; 19; 20; 21; 22; 23) and by Armero et al. (24; 25; 26; 27) on the topic of finite strains fully coupled formulation of porous media.

This thesis want to focus on three fundamental aspects, namely, theoretical formulation, numerical implementation and real applications, considering these as three inseparable elements. As far as the theoretical formulation, the essential idea is to write the balance laws for the two (or more) phases in the current deformed configuration, and then combine the equations considering the material as the overlap of different continua. Then, the idea is to *pull back* all the equations and solve it in

the initial configuration, since the initial undeformed domain is fixed throughout the entire solution process. The developed model assumes that the porous material is fully saturated by a unique fluid, hence only two phases are considered. However, the model can be extended to deal with more material phases. An interesting point arises in the formulation of elastoplasticity at finite strain, since the additive decomposition into the elastic and plastic part of the infinitesimal deformation tensor looses of significance. The formulation adopted in this work is based on the multiplicative decomposition of the deformation gradient (28; 29). This method completely circumvents the "rate issue" in finite deformation analysis, and allows for the development of large elastic strains. In particular, the fundamental work of Simo (30) indicates that the multiplicative decomposition technique can be exploited to such an extent that the resulting algorithm may inherit all the features of the classical models of infinitesimal plasticity. The local multiplicative decomposition of the deformation gradient provides a means for describing mathematically the relationships between the reference configuration, the current configuration, and the unloaded, stress-free intermediate configuration of a solid skeleton subjected to finite deformation in the macroscopic sense.

As far as the numerical implementation, this work presents the main feature of a new finite element toolbox, especially coded to solve coupled elastoplastic problem undergoing finite strains, based on the theoretical model derived in the thesis (*www.geofem973.it*). As far as the application part, particular interest is devoted to the analysis of plasticity and strain localization around a horizontal wellbore, drilled through a porous rock formation. Predicting plastic deformation and localization band is a challenging task that could have immense implications for the prediction of instability and sand production. The developed numerical model can therefore accurately simulate the drilling process, taking into account the interaction between the solid and the fluid phases and the elasto-plastic finite deformations that can experience the porous rock surrounding the wellbore. A key aspect to quantify the stress and strain field is the constitutive model used to describe the mechanical behavior of the solid phase. Several experiments conducted on high porous rock in the last two decades show that compaction failure can take place under certain stress conditions, in contrast with the more common dilatant failure (31; 32; 33). Compactant failure typically occurs in porous rocks under relatively high confining pressure, with a failure mode conventionally described as homogeneous cataclastic flow. Since the compactant plastic mechanism can have an important role in the analysis of wellbore, an appropriate constitutive elastoplastic model is necessary. This model must capture both the dilatant and compactant behavior, and the transition between these two failure criteria (2). This thesis presents a new constitutive model developed to capture shear-enhanced compaction and shear-induced dilation, characterized by a linear yield surface for the dilatant side and an elliptical yield surface for the compactant side. An innovative characteristic of this model is a simple but efficient method to ensure the smooth continuity between the two plastic mechanisms, as regards both the yield surface and the plastic flow rule. This new developed constitutive model has been

implemented into the coupled multiplicative framework, in order to quantify the elastoplastic finite strains around the wellbore.
Summing up, the innovative contributions of this research reside especially in the investigation of finite strains coupled elastoplasticity and the subsequent numerical implementation of a new finite element toolbox, the formulation of a new constitutive model for porous rock and the utilization of the aforementioned model to asses the stability of a horizontal wellbore.

1.2 Outline of the thesis

The thesis is organized as follow. Chapter 2 deals with the theoretical formulation of porous media at finite strains. The kinematics of multiphase continuum body is recalled, and the balance laws are presented for the solid and fluid phases and for the multiphase body.
Chapter 3 deals with the constitutive laws for both the solid and the fluid phase. Particular interest is devoted to the general formulation of elastoplasticity at finite strain, based on the multiplicative decomposition of the deformation gradient. While for the fluid phase only the generalized Darcy's law is presented, three different models are discussed for the solid phase, namely, an hyperelastic model, the Modified Cam Clay Model and the new developed Continuous Cap model for porous rock.
Chapter 4 covers the numerical implementation of the model, presenting the main aspects of the spatial and temporal discretization of the linearized equations, and introducing the main structure of the new finite element toolbox called GEOFEM 973 (*www.geofem973.it*) developed by the author to solve the boundary-value problems.
Chapter 5 discusses some numerical results obtained with the aforementioned model and code. Two real situations are investigated: a consolidation process under a uniformed distributed load on soft clays and a drilling process of a horizontal wellbore through a porous rock formation. The first example was mainly carried on to asses the validity of the code, comparing the results with available benchmarks. The second example aims to determine the stress and strain distributions around a horizontal wellbore. The parameters of the innovative constitutive model were calibrated using experimental data available from a deep water reservoir, located offshore Brazil (4). In the numerical analysis, particular interest is devoted to predict the conditions for the formation of localized bands of intense deformation, discussing the factors that either enhance or prevent these formations.
Chapter 6 draws the conclusions of the work and gives some hints for future developments in this field.

1.3 Notations and symbols

Notations and symbols used in this thesis are as follows: bold-face letters denote matrices and vectors; the symbol '$\cdot$' denotes an inner product of two vectors (e.g. $\boldsymbol{a}\cdot\boldsymbol{b} = a_i b_i$), or a single contraction of adjacent indices of two tensor (e.g. $\boldsymbol{c}\cdot\boldsymbol{d} = c_{ij}d_{jk}$); the symbol ':' denotes an inner product of two second-order tensor (e.g. $\boldsymbol{c} : \boldsymbol{d} = c_{ij}d_{ij}$), or a double contraction of adjacent indices of tensor of rank two and higher (e.g. $\boldsymbol{C} : \boldsymbol{\epsilon}^e = C_{ijkl}\epsilon^e_{kl}$); the symbol '$\otimes$' denotes a juxtaposition, e.g. $(\boldsymbol{a}\otimes\boldsymbol{b})_{ij} = a_i b_j$. For any symmetric second-order tensor $\boldsymbol{\alpha}$ and $\boldsymbol{\beta}$ we have $(\boldsymbol{\alpha}\otimes\boldsymbol{\beta})_{ijkl} = \alpha_{ij}\beta_{kl}$; $(\boldsymbol{\alpha}\oplus\boldsymbol{\beta})_{ijkl} = \alpha_{jl}\beta_{ik}$; and $(\boldsymbol{\alpha}\ominus\boldsymbol{\beta})_{ijkl} = \alpha_{il}\beta_{jk}$.

Chapter 2

Theoretical formulation of porous media at finite strains

2.1 Fundamentals of continuum mechanics

In the real world all physical objects are composed of molecules which are formed by atomic and subatomic particles. Microscopic studies are effective at the atomic level and very important in the exploration of a variety of physical phenomena. The atomistic point of view, however, is not a useful and adequate approach for common engineering applications (34).

The fundamental approach used in this work, and corner stone of most of the engineering applications, is the method of *continuum mechanics*, to explain various physical phenomena successfully without detailed knowledge of the complexity of their internal (micros)structures. For example, soil, water, rock, oil are made of billions of molecules: a good approximation is to treat these materials as a continuous medium characterized by certain field quantities which are associated with the internal structure, such as density, velocity, temperature, etc. (35; 36; 37; 38).

From the physical point of view this is an approximation in which the very large numbers of particles are replaced by few quantities, end only the macroscopic system is considered. Of course the predictions based on macroscopic studies are not exact but good enough for the engineering design. The study of continuum mechanics roughly comprises the following basic aspects: the study of motion and deformation (kinematic), the study of stress and the mathematical description of the fundamental laws of physics governing the motion of a continuum (balance principles). In particular, the classical balance principles, i.e. conservation of mass, the momentum balance principles and balance of energy, are the fundamentals laws that govern the mechanic of the continuum body. They are applicable to any particular material and they must be satisfied for all times.

The basic idea behind this chapter, essential to understand all the aspects of the research, is to

consider the porous media as a mixture of two or more continuum bodies, overlapping and interacting together. Therefore we will consider the kinematic and the balance laws separately for the two phases, and then we will use the mixture theory to combine the field equations.

2.2 Kinematics of multiphase continuum

The starting point in the formulation of the multiphase continuum mechanic consists in defining the kinematic of the body, introducing all the relevant quantities needed to describe the different configurations of the body.

Consider a porous solid material point, whose initial position in the reference solid configuration $\mathscr{B}$ is given by the position vector $\boldsymbol{X}_s$. Since the special role played by the solid matrix in leading the motion of the coupled body, we should drop the subscript " s " and take the notation $\boldsymbol{X} \equiv \boldsymbol{X}_s$.

Let $\boldsymbol{\varphi} : \mathscr{B} \to R^{n_{sd}}$ (with $n_{sd} = 2, 3$ the number of dimension) be the motion, or set of configuration, of a fluid-saturated simple body. The velocity of the material point $\boldsymbol{X}$ is defined as

$$\boldsymbol{V}(\boldsymbol{X}, t) = \frac{\partial \boldsymbol{\varphi}(\boldsymbol{X}, t)}{\partial t}, \tag{2.1}$$

assuming that the map is a differentiable function. If $\boldsymbol{V}$ is also differentiable, the acceleration of the solid matrix is defined as

$$\boldsymbol{A}(\boldsymbol{X}, t) = \frac{\partial \boldsymbol{V}(\boldsymbol{X}, t)}{\partial t} = \frac{\partial^2 \boldsymbol{\varphi}(\boldsymbol{X}, t)}{\partial t^2}. \tag{2.2}$$

The two quantities above are obtained deriving with respect of time the material point in the initial undeformed configuration, and are usually called *Lagrangian* or *material* description of the motion.

Alternatively, let $\boldsymbol{x}$ denote the current position of the solid point identified by $\boldsymbol{X}$, defined as

$$\boldsymbol{x} = \boldsymbol{\varphi}(\boldsymbol{X}, t), \tag{2.3}$$

assuming that there is unique mapping between $\boldsymbol{x}$ and $\boldsymbol{X}$ such that $\boldsymbol{X} = \boldsymbol{\varphi}^{-1}(\boldsymbol{x}, t)$. Thus, the velocity of the solid can be rewritten as

$$\boldsymbol{V}(\boldsymbol{X}, t) = \frac{\partial \boldsymbol{\varphi}(\boldsymbol{\varphi}^{-1}(\boldsymbol{x}, t), t)}{\partial t} = \boldsymbol{v}(\boldsymbol{x}, t), \tag{2.4}$$

where $\boldsymbol{v}$ is now called *Eulerian* or *spatial* description of the solid motion.

The corresponding solid acceleration can be obtained simply taking the total derivative of Eq. (2.4) with respect of time

$$\boldsymbol{a}(\boldsymbol{x},t) = \frac{\mathrm{d}\boldsymbol{v}(\boldsymbol{x},t)}{\mathrm{d}t} = \frac{\partial \boldsymbol{v}}{\partial \boldsymbol{x}}\frac{\partial \boldsymbol{x}}{\partial t} + \frac{\partial \boldsymbol{v}}{\partial t} = \boldsymbol{v}\cdot\mathrm{grad}(\boldsymbol{v}) + \frac{\partial \boldsymbol{v}}{\partial t}, \tag{2.5}$$

taking into account that the position of the spatial point $\boldsymbol{x}$ varies with time.

In hypothesis of fully saturated medium, the voids are filled with fluid. Therefore the solid matrix at point $\boldsymbol{x}$ also contains a fluid element that is moving instantaneously with velocity $\boldsymbol{v}_f$. Hence, let's define $\boldsymbol{\varphi}_f : \mathscr{B}^f \to R^{n_{sd}}$ the motion of the fluid, which could be distinct from $\boldsymbol{\varphi}$ if seepage takes place in the saturated region $\mathscr{B} \subset \mathscr{B}^f$.

Again, we can write the velocity of the fluid at point $\boldsymbol{x}$ as

$$\boldsymbol{V}_f(\boldsymbol{X}_f,t) = \frac{\partial \boldsymbol{\varphi}_f(\boldsymbol{\varphi}_f^{-1}(\boldsymbol{x},t),t)}{\partial t} = \boldsymbol{v}_f(\boldsymbol{x},t). \tag{2.6}$$

The fluid acceleration at point $\boldsymbol{x}$ then takes the form

$$\boldsymbol{a}_f(\boldsymbol{x},t) = \boldsymbol{v}_f\cdot\mathrm{grad}(\boldsymbol{v}_f) + \frac{\partial \boldsymbol{v}_f}{\partial t}. \tag{2.7}$$

Conceptually, the fluid point in the initial position $\boldsymbol{X}_f$ belongs to the fluid domain $\mathscr{B}^f$ in the reference configuration, but in general it would be very difficult to reconstruct such initial configuration for every fluid element in the pores of the solid matrix at point $\boldsymbol{x}$. Therefore, only the Eulerian description is used for the fluid phase motion.

Once the kinematic aspects of the multiphase continuum body has been defined, we can proceed introducing the tensorial measures of finite deformation. These measures follow straightforward as an extension of the classical measures used in one-phase continua, taking into account the fact that now the body is the result of two overlapping phases.

The deformation gradients for the solid matrix and fluid are defined as

$$\boldsymbol{F} = \frac{\partial \boldsymbol{\varphi}}{\partial \boldsymbol{X}} = \mathrm{GRAD}\boldsymbol{\varphi}, \qquad\qquad \boldsymbol{F}_f = \frac{\partial \boldsymbol{\varphi}_f}{\partial \boldsymbol{X}_f} = \mathrm{GRAD}_f\boldsymbol{\varphi}_f. \tag{2.8}$$

Hence, the right and left Cauchy-Green deformation tensors are for the solid phase

$$\boldsymbol{C} = \boldsymbol{F}^T\cdot\boldsymbol{F}, \qquad\qquad \boldsymbol{b} = \boldsymbol{F}\cdot\boldsymbol{F}^T, \tag{2.9}$$

and for the fluid phase

$$\boldsymbol{C}_f = \boldsymbol{F}_f^T\cdot\boldsymbol{F}_f, \qquad\qquad \boldsymbol{b}_f = \boldsymbol{F}_f\cdot\boldsymbol{F}_f^T. \tag{2.10}$$

Therefore, let's introduce the velocity gradients for the solid and fluid phase as

$$\boldsymbol{l} = \text{grad}(\boldsymbol{v}), \qquad \boldsymbol{l}_f = \text{grad}(\boldsymbol{v}_f), \tag{2.11}$$

and the relative deformation tensors

$$\boldsymbol{d} = \frac{1}{2}(\boldsymbol{l} + \boldsymbol{l}^T), \qquad \boldsymbol{d}_f = \frac{1}{2}(\boldsymbol{l}_f + \boldsymbol{l}_f^T), \tag{2.12}$$

defined as the symmetric parts of the corresponding velocity gradients. On the other hand, let define the vorticity tensors as the skew-symmetric parts of the velocity gradients

$$\boldsymbol{\omega} = \frac{1}{2}(\boldsymbol{l} - \boldsymbol{l}^T), \qquad \boldsymbol{\omega}_f = \frac{1}{2}(\boldsymbol{l}_f - \boldsymbol{l}_f^T). \tag{2.13}$$

Finally, the Jacobian of the solid and fluid motions are given as

$$J = \det\boldsymbol{F}, \qquad J_f = \det\boldsymbol{F}_f. \tag{2.14}$$

The Jacobian J and J_f play an important role, since they relate the current differential volume $\mathrm{d}V$ to the corresponding reference differential volume $\mathrm{d}V_0$ and $\mathrm{d}V_0^f$, through the expression

$$\mathrm{d}V = J\mathrm{d}V_0 = J_f\mathrm{d}V_0^f. \tag{2.15}$$

We conclude this section recalling the Piola transformation (36), which will be used in a subsequent part of the work. Let's define $\boldsymbol{y}$ a vector field on $\mathscr{B}$. We define Piola transformation of the vector $\boldsymbol{y}$ the vector field

$$\boldsymbol{Y} = J\boldsymbol{F}^{-1}\boldsymbol{y}(\boldsymbol{\varphi}(\boldsymbol{X})). \tag{2.16}$$

In addition, we can proof that if $\boldsymbol{Y}$ is the Piola transformation of $\boldsymbol{y}$, the following equation holds

$$\int_{\mathscr{B}} \boldsymbol{Y}\mathrm{d}V_0 = \int_{\boldsymbol{\varphi}(\mathscr{B})} \text{div}\boldsymbol{y}\mathrm{d}V \tag{2.17}$$

The demonstration follows from the divergence theorem and the theorem of surface integrals transformation.

2.3 Transport equations

In a two-phases material a general Eulerian transport variable $\psi(\boldsymbol{x}, t)$ can move with either the solid matrix or the fluid flow. The key concept of this section is to define the material time derivative following one among the two phases and define the relation between the two different derivatives. Examples of transport variable are the mass of the solid or the the concentration of a component of the fluid flow.

The material time derivative following the solid phase (omitting the superscript " s ") is given by

$$\frac{\mathrm{d}\psi}{\mathrm{d}t} = \frac{\partial\psi}{\partial t} + \mathrm{grad}\psi \cdot \frac{\partial\boldsymbol{\varphi}}{t} = \frac{\partial\psi}{\partial t} + \mathrm{grad}\psi \cdot \boldsymbol{v}, \tag{2.18}$$

where $\partial/\partial t$ is the *local* rate of change of ψ, obtained holding $\boldsymbol{x}$ fixed, and $\boldsymbol{v}$ is the velocity of the solid phase.

Analogously, the material time derivative of a fluid transport variable $\psi(\boldsymbol{x}, t)$ following the trajectory of the fluid is define as

$$\frac{\mathrm{d}^f\psi}{\mathrm{d}t} = \frac{\partial\psi}{\partial t} + \mathrm{grad}\psi \cdot \frac{\partial\boldsymbol{\varphi}_f}{t} = \frac{\partial\psi}{\partial t} + \mathrm{grad}\psi \cdot \boldsymbol{v}_f, \tag{2.19}$$

since now the position of the spatial point $\boldsymbol{x}$ is defined as $\boldsymbol{x} = \boldsymbol{\varphi}_f(\boldsymbol{X}_f, t)$. Note that from the Eulerian form of the above expression that is not necessary to identify the reference configuration of the the point $\boldsymbol{X}_f$, but it is sufficient to know the current fluid velocity.

We want to define now a relation between the two material time derivatives introduced above. Subtracting the two material time derivatives and rearranging the terms, we obtain an expression of the material time derivative following the fluid motion with respect to the one following the solid motion, i.e.

$$\frac{\mathrm{d}^f\psi}{\mathrm{d}t} = \frac{\mathrm{d}\psi}{\mathrm{d}t} + \mathrm{grad}\psi \cdot \tilde{\boldsymbol{v}}, \tag{2.20}$$

where $\tilde{\boldsymbol{v}} = \boldsymbol{v}_f - \boldsymbol{v}$ is the relative velocity of the fluid with respect to the solid.

2.4 Multiphase continuum mechanics

2.4.1 Multiphase continuum body

Porous media consists of a solid phase, usually referred to as *matrix* or *skeleton*, with closed and open pores. The multiphase nature of a macroelement requires an explicit consideration of the relative movement of the constituent materials. Let us consider a macroelement, defined as a control volume geometrically occupied by a solid matrix whose pores are statistically distributed, in order to allow

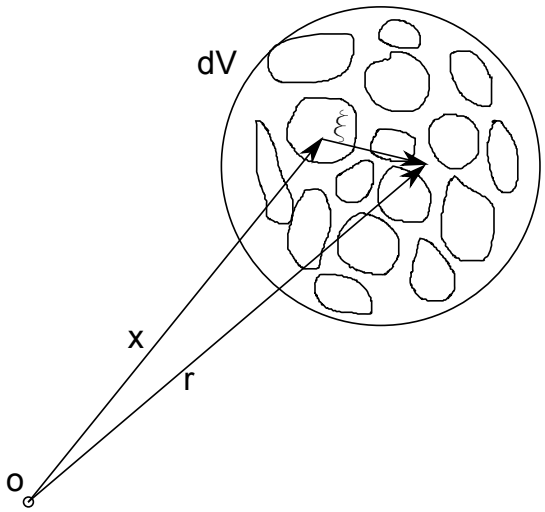

Figure 2-1: Typical averaging volume dV of a porous medium consisting in two phases.

homogenization of the properties and responses. This macroelement is associated to a representative elementary volume, or REV, as depicted in fig. 2-1 for a fully saturated mixture.

The center of this volume is denoted by the position vector $\boldsymbol{x}$, a macroscale measure. Relative to $\boldsymbol{x}$ the position vector of any point inside the control volume is denoted by $\boldsymbol{\xi}$, a microscale measure. Letting $\boldsymbol{r} = \boldsymbol{x} + \boldsymbol{\xi}$, solid and fluid indicator functions (7) may be defined as

$$\chi^{\alpha} = \begin{cases} 1 & \boldsymbol{r} \in dV^{\alpha} \\ 0 & \boldsymbol{r} \notin dV^{\alpha} \end{cases} \tag{2.21}$$

where $\alpha = s, f$ and $\mathrm{d}V^{\alpha}$ is the region in $\mathrm{d}V$ occupied by the phase α. Obviously, $\chi^s + \chi^f = 1$ and

$$\mathrm{d}V^s = \int_{\mathrm{d}V} \chi^s \mathrm{d}v, \qquad\qquad \mathrm{d}V^f = \int_{\mathrm{d}V} \chi^f \mathrm{d}v. \tag{2.22}$$

For a fully saturated mixture the volume fractions are defined as

$$\phi^s = \frac{\mathrm{d}V^s}{\mathrm{d}V}, \qquad\qquad \phi^f = \frac{\mathrm{d}V^f}{\mathrm{d}V}, \tag{2.23}$$

subjected again to the closure condition $\phi^s + \phi^f = 1$.

The mass of each phase contained in the volume $\mathrm{d}V$ is

$$\mathrm{d}M_\alpha = \int_{\mathrm{d}V} \rho_\alpha \chi^\alpha dv, \qquad \alpha = s, f, \tag{2.24}$$

where ρ_α is the intrinsic (true) mass density of the α phase. The total mass for the two-phase mixture is then

$$\mathrm{d}M = \mathrm{d}M_s + \mathrm{d}M_f. \tag{2.25}$$

Assuming that ρ_s and ρ_f are sufficiently uniform over the volume dV, the total mass density of the mixture is then

$$\rho = \frac{\mathrm{d}M}{\mathrm{d}V} = \rho_s \phi^s + \rho_f \phi^f = \rho^s + \rho^f. \tag{2.26}$$

where $\rho^\alpha = \rho_\alpha \phi^\alpha$ is the partial mass density of the α phase, defined as the mass of the α phase per unit total volume of the mixture. By smearing the total mass of each phase over the entire volume $\mathrm{d}V$, we can interpret this volume as being occupied simultaneously by all of the constituent phases.

2.4.2 Balance laws

This section presents the balance principles that govern the interaction between the solid and the fluid constituents of a two-phase saturated solid-fluid mixture. In the derivation of the balance laws we will consider initially the motion of the solid and the fluid phase separately. Then, we will use the mixture theory (39; 40; 6; 7) to combine the field equations. The intrinsic motion of the solid phase will be the reference motion, to which the motion of the fluid phase is described.

Balance of mass

Let V denote any arbitrary volume in the current configuration. Let the total masses of the solid and fluid be denoted by M_s and M_f, respectively. In terms of densities, these masses are given by the volume integrals

$$M_s = \int_V \rho^s \mathrm{d}V, \qquad M_f = \int_V \rho^f \mathrm{d}V, \tag{2.27}$$

where ρ^s is the partial mass density of the solid phase, ρ^f is the partial mass density of the fluid phase. By the law of conservation of mass the total mass is constant throughout all the process, therefore the material time derivatives of these masses vanish individually. M_s is a solid transport

variable and its material time derivative is given by

$$\frac{\mathrm{d}M_s}{\mathrm{d}t} = \int_V \left\{ \frac{\mathrm{d}\rho^s}{\mathrm{d}t} + \rho^s \mathrm{div}(\boldsymbol{v}) \right\} dV = 0 \tag{2.28}$$

where $\boldsymbol{v}$ is the intrinsic velocity of the solid phase. We assumed that there is no mass production within the mixture. Similarly, for the fluid phase, we have

$$\frac{\mathrm{d}^f M_f}{\mathrm{d}t} = \int_V \left\{ \frac{\mathrm{d}^f \rho^f}{\mathrm{d}t} + \rho^f \mathrm{div}\ (\boldsymbol{v}_f) \right\} dv = 0. \tag{2.29}$$

where $\boldsymbol{v}_f$ is the velocity of the fluid phase.

The above equations hold for any arbitrary volume V, so Eq. (2.28) and (2.29) can be localized as follows

$$\frac{\mathrm{d}\rho^s}{\mathrm{d}t} + \rho^s \mathrm{div}(\boldsymbol{v}) = 0, \qquad \frac{\mathrm{d}^f \rho^f}{\mathrm{d}t} + \rho^f \mathrm{div}(\boldsymbol{v}_f) = 0. \tag{2.30}$$

We introduce now the hypothesis of barotropic flows for the solid and fluid phases, which state the existence of a functional relation between the pressure and the density. The presence of a functional relations allows to write the following equations between the intrinsic pressure and the density

$$\frac{\mathrm{d}p_s}{\mathrm{d}t} = K_s \left(\frac{1}{\rho_s} \frac{\mathrm{d}\rho_s}{\mathrm{d}t} \right), \qquad \frac{\mathrm{d}^\mathrm{f} p_f}{\mathrm{d}t} = K_f \left(\frac{1}{\rho_f} \frac{\mathrm{d}^\mathrm{f} \rho_f}{\mathrm{d}t} \right), \tag{2.31}$$

where K_s and K_f are the intrinsic bulk moduli of the solid and fluid constituents, respectively. Again, ignoring any mass exchange between the solid and the fluid, balance of mass can be written as

$$\frac{\mathrm{d}\phi^s}{\mathrm{d}t} + \frac{\phi^s}{K_s} \frac{\mathrm{d}p_s}{\mathrm{d}t} + \phi^s \mathrm{div}(\boldsymbol{v}) = 0, \qquad \frac{\mathrm{d}^\mathrm{f} \phi^f}{\mathrm{d}t} + \frac{\phi^f}{K_f} \frac{\mathrm{d}^\mathrm{f} p_f}{\mathrm{d}t} + \phi^f \mathrm{div}(\boldsymbol{v_f}) = 0. \tag{2.32}$$

In addition to the intrinsic constitutive properties of the solid and fluid, we also consider the compressibility of the solid matrix. The compressibility of the solid matrix differs from that of the solid in that the former reflects the effect of pore expansion/compaction through changes in the volume fraction ϕ^s, whereas the latter does not. Now, it is easy to verify that

$$\frac{1}{\rho^s} \frac{\mathrm{d}\rho^s}{\mathrm{d}t} = \frac{\mathrm{d}}{\mathrm{d}t} \left[\ln \left(\frac{\rho^s}{\rho_0^s} \right) \right] = \frac{\mathrm{d}}{\mathrm{d}t} \left(\ln J^{-1} \right) = -\mathrm{div}\boldsymbol{v}, \tag{2.33}$$

where $\rho_0^s = J\rho^s$ is the pull-back solid partial mass density.

Therefore, assuming again the existence of a functional relation between p^s and ρ^s the following equation, similar to eq. (2.31) holds

$$\frac{\mathrm{d}p_s}{\mathrm{d}t} = \frac{\bar{K}}{\phi^s}\left(\frac{1}{\rho^s}\frac{\mathrm{d}\rho^s}{\mathrm{d}t}\right) = -\frac{\bar{K}}{\phi^s}\mathrm{div}\boldsymbol{v}, \tag{2.34}$$

where $\bar{K}$ is the bulk modulus of the solid matrix. The bulk modulus $\bar{K}$ represents the volumetric stiffness of the solid matrix and must not be confused with the bulk modulus K_s representing the volumetric stiffness of the solid itself.

Inserting Eq. (2.34) into Eq. (2.32) we obtain the two equation of the conservation of mass for the solid and fluid phase, taking into account the compressibility of the the phases and of the solid skeleton

$$\frac{\mathrm{d}\phi^s}{\mathrm{d}t} - \frac{\bar{K}}{K_s}\mathrm{div}(\boldsymbol{v}) + \phi^s\mathrm{div}(\boldsymbol{v}) = 0, \qquad \frac{\mathrm{d}^\mathrm{f}\phi^f}{\mathrm{d}t} + \frac{\phi^f}{K_f}\frac{\mathrm{d}^\mathrm{f}p_f}{\mathrm{d}t} + \phi^f\mathrm{div}(\boldsymbol{v_f}) = 0. \tag{2.35}$$

In order to combine the two above equations, we need to write all material time derivatives with respect to the motion of the solid matrix alone, which is assumed as the leading phase of the motion of the mixture. Noting that

$$\frac{\mathrm{d}^\mathrm{f}\rho^\mathrm{f}}{\mathrm{dt}} = \frac{\mathrm{d}\rho^\mathrm{f}}{\mathrm{dt}} + \mathrm{grad}\rho^f \cdot \tilde{\boldsymbol{v}} \tag{2.36}$$

and $\boldsymbol{v}_f = \boldsymbol{v} + \tilde{\boldsymbol{v}}_f$, we get the complete balance of mass for a mixture of compressible solid-fluid

$$B\mathrm{div}(\boldsymbol{v}) + \mathrm{div}(\bar{\boldsymbol{v}}) + \frac{\phi^f}{K_f}\frac{\mathrm{d}p_f}{\mathrm{d}t} + \frac{\bar{\boldsymbol{v}}}{K_f}\cdot\mathrm{grad}(p_f) = 0, \tag{2.37}$$

where

$$\bar{\boldsymbol{v}} = \rho^f\tilde{\boldsymbol{v}} = \rho^f(\boldsymbol{v}_f - \boldsymbol{v}), \tag{2.38}$$

is the so called Darcy velocity and

$$B = 1 - \frac{\bar{K}}{K_s}, \tag{2.39}$$

is the so called Biot Coefficient. The parameter B is very close to unity when the bulk modulus of the solid matrix is much smaller than that of the solid constituent, which is true in granular soils. However, in rocks, typical values of B are on the order of 0.5 to 0.6, suggesting that $\bar{K}$ and K_s are of comparable values.

Eq. (2.37) can be simplified under certain conditions of incompressible flow. If the solid is incompressible, then $K_s \to \infty$ and $B = 1$, and the balance of mass for the mixture reduces to

$$\mathrm{div}(\boldsymbol{v}) + \mathrm{div}(\overline{\boldsymbol{v}}) + \frac{\phi^f}{K_f}\frac{\mathrm{d}p_f}{\mathrm{d}t} + \frac{\overline{\boldsymbol{v}}}{K_f} \cdot \mathrm{grad}(p_f) = 0. \tag{2.40}$$

If the fluid is incompressible, then $K_f \to \infty$ and the balance of mass for the mixture reduces to

$$B\mathrm{div}(\boldsymbol{v}) + \mathrm{div}(\overline{\boldsymbol{v}}) = 0. \tag{2.41}$$

In the end, if both the solid and fluid are incompressible, we obtain

$$\mathrm{div}(\boldsymbol{v}) + \mathrm{div}(\overline{\boldsymbol{v}}) = 0. \tag{2.42}$$

Balance of linear and angular momentum

Consider a macroscopic area $\mathrm{d}A$ intersecting portions of the solid matrix and fluid in the void space. Let $\boldsymbol{t}_s$ and $\boldsymbol{t}_f$ denote the intrinsic traction vectors, defined as the resultant forces acting on the solid and fluid per unit area of the solid and fluid. On the area $\mathrm{d}A$ the total forces acting on the solid and fluid are, respectively,

$$\mathrm{d}\boldsymbol{f}_s = \int_{\mathrm{d}A} \boldsymbol{t}_s \chi^s \mathrm{d}a \qquad\qquad \mathrm{d}\boldsymbol{f}_f = \int_{\mathrm{d}A} \boldsymbol{t}_f \chi^f \mathrm{d}a \tag{2.43}$$

where $\mathrm{d}a \ll \mathrm{d}A$ as before. If $\boldsymbol{t}_s$ and $\boldsymbol{t}_f$ are sufficiently uniform over $\mathrm{d}A$, then it is possible to write

$$\mathrm{d}\boldsymbol{f}_s = \boldsymbol{t}_s \int_{\mathrm{d}A} \chi^s \mathrm{d}a = \boldsymbol{t}_s \phi^s \mathrm{d}A = \boldsymbol{t}^s \mathrm{d}A \qquad \mathrm{d}\boldsymbol{f}_f = \boldsymbol{t}_f \int_{\mathrm{d}A} \chi^f \mathrm{d}a = \boldsymbol{t}_f \phi^s \mathrm{d}A = \boldsymbol{t}^f \mathrm{d}A \tag{2.44}$$

where ϕ^α is the volume fraction (assumed equal to the area fraction by virtue of the REV assumption), and $\boldsymbol{t}^\alpha = \phi^\alpha \boldsymbol{t}_\alpha$ is the partial traction vector, defined as the resultant force developed in each phase per unit total area of mixture.
Let's now introduce the Cauchy theorem to obtain the Cauchy stress tensor

$$\boldsymbol{t}^s = \boldsymbol{n} \cdot \boldsymbol{\sigma}^s \qquad\qquad \boldsymbol{t}^f = \boldsymbol{n} \cdot \boldsymbol{\sigma}^f \tag{2.45}$$

where $\boldsymbol{n}$ is the unit normal vector to $\mathrm{d}A$ and $\boldsymbol{\sigma}^\alpha$ is the Cauchy partial stress tensor on the solid and fluid phase. The total traction vector is given by summing up the the contributions of the two phases

$$\boldsymbol{t} = \boldsymbol{t}^s + \boldsymbol{t}^f = \boldsymbol{n} \cdot \boldsymbol{\sigma}, \tag{2.46}$$

where

$$\boldsymbol{\sigma} = \boldsymbol{\sigma}^s + \boldsymbol{\sigma}^f \tag{2.47}$$

is the total Cauchy stress tensor for the mixture.

Let's consider now an arbitrary volume V bounded by a surface A. The sum of forces acting on the solid phase must be equal to the material time derivative of the linear momentum

$$\int_A \boldsymbol{t}^s \mathrm{d}A + \int_V \rho^s \boldsymbol{g} \mathrm{d}V + \int_V \boldsymbol{h}^s \mathrm{d}V = \frac{\mathrm{d}}{\mathrm{d}t} \int_V \rho^s \boldsymbol{v} \mathrm{d}V, \tag{2.48}$$

where $\boldsymbol{g}$ is the gravity acceleration vector, $\boldsymbol{h}^s$ is the force per unit total volume exerted by the fluid on the solid matrix. The body force $\boldsymbol{h}^s$ can be interpreted as a frictional drag induced by the fluid on the solid. Using the Cauchy theorem the first integral can be converted into a volume integral, and Eq. (2.48) can be localized to get

$$\mathrm{div}(\boldsymbol{\sigma^s}) + \rho^s \boldsymbol{g} + \boldsymbol{h}^s = \rho^s \boldsymbol{a}, \tag{2.49}$$

where $\boldsymbol{a} = \mathrm{d}\boldsymbol{v}/\mathrm{d}t$ is the material acceleration of the solid. In Eq. (2.49) we assumed there is no mass exchange between the two phases.

Analogously, for the fluid phase we can write

$$\int_A \boldsymbol{t}^f \mathrm{d}A + \int_V \rho^f \boldsymbol{g} \mathrm{d}V + \int_V \boldsymbol{h}^f \mathrm{d}V = \frac{\mathrm{d}^f}{\mathrm{d}t} \int_V \rho^f \boldsymbol{v_f} \mathrm{d}V, \tag{2.50}$$

where now $\boldsymbol{h}^f$ is the force per unit total volume exerted by the solid on the fluid. Again, using the Cauchy theorem the first integral can be converted into a volume integral, and Eq. (2.50) can be localized to get

$$\mathrm{div}(\boldsymbol{\sigma^f}) + \rho^f \boldsymbol{g} + \boldsymbol{h}^f = \rho^f \boldsymbol{a}_f, \tag{2.51}$$

where $\boldsymbol{a}_f = \mathrm{d}^f \boldsymbol{v}_f/\mathrm{d}t$ is the material acceleration of the fluid phase. Since $\boldsymbol{h}^s$ and $\boldsymbol{h}^f$ are internal forces which naturally do not affect the mixture as a whole, their sum must be equal to zero

$$\boldsymbol{h}^s + \boldsymbol{h}^f = \boldsymbol{0}. \tag{2.52}$$

Summing over the solid and fluid phases of the mixture gives the balance of linear momentum for the entire mixture,

$$\mathrm{div}(\boldsymbol{\sigma}) + \rho\boldsymbol{g} = \rho^s\boldsymbol{a} + \rho^f\boldsymbol{a}_f. \tag{2.53}$$

If there is no relative flow between the solid and the fluid phase, then $\boldsymbol{a} \equiv \boldsymbol{a}_f$ and we recover the classical form of linear momentum balance equation for a one-phase material. In this case, the deformation in the mixture is said to be locally undrained.

The balance of angular momentum can be satisfied assuming the symmetry of both solid and fluid Cauchy partial stress tensors in the absence of couple stresses. This follows from classical derivation of the continuum mechanics, and proof is omitted for the sake of brevity.

The linear momentum balance equation can be written in the reference to the initial configuration, thus assuming a fix integration domain.

Let's initially define $\boldsymbol{T}^s$ and $\boldsymbol{T}^f$ the nominal solid and fluid partial traction vectors, as the forces per unit area of the mixture in the reference configuration

$$\mathrm{d}\boldsymbol{f}_s = \boldsymbol{T}^s\mathrm{d}A_0, \qquad\qquad \mathrm{d}\boldsymbol{f}_f = \boldsymbol{T}^f\mathrm{d}A_0, \tag{2.54}$$

where $\mathrm{d}A_0$ is the differential area of the mixture in the solid reference configuration. The relation between $\mathrm{d}A$ and $\mathrm{d}A_0$ is provided by Nanson's formula, which reads

$$\boldsymbol{n}\mathrm{d}A = J\boldsymbol{F}^{-T} \cdot \boldsymbol{N}\mathrm{d}A_0, \tag{2.55}$$

where $\boldsymbol{n}$ and $\boldsymbol{N}$ are unit normal vectors to $\mathrm{d}A$ and $\mathrm{d}A_0$, respectively. Expressed on terms of the Cauchy partial stress tensor, we have for the solid and fluid phase

$$\mathrm{d}\boldsymbol{f}_s = \boldsymbol{\sigma}^s \cdot \boldsymbol{n}\mathrm{d}A = J\boldsymbol{\sigma}^s \cdot \boldsymbol{F}^{-T} \cdot \boldsymbol{N}\mathrm{d}A_0 = \boldsymbol{P}^s \cdot \boldsymbol{N}\mathrm{d}A_0, \tag{2.56}$$

$$\mathrm{d}\boldsymbol{f}_f = \boldsymbol{\sigma}^f \cdot \boldsymbol{n}\mathrm{d}A = J\boldsymbol{\sigma}^f \cdot \boldsymbol{F}^{-T} \cdot \boldsymbol{N}\mathrm{d}A_0 = \boldsymbol{P}^f \cdot \boldsymbol{N}\mathrm{d}A_0. \tag{2.57}$$

In the above equations we introduced the non-symmetric first Piola-Kirchhoff partial stress tensors for the solid and fluid, respectively

$$\boldsymbol{P}^s = J\boldsymbol{\sigma}^s \cdot \boldsymbol{F}^{-T}, \qquad\qquad \boldsymbol{P}^f = J\boldsymbol{\sigma}^f \cdot \boldsymbol{F}^{-T}, \tag{2.58}$$

which allows a formal definition for the nominal traction vectors

$$\boldsymbol{T}^s = \boldsymbol{P}^s \cdot \boldsymbol{N}, \qquad \boldsymbol{T}^f = \boldsymbol{P}^f \cdot \boldsymbol{N}. \tag{2.59}$$

It is important to note that both stress tensors $\boldsymbol{P}^s$ and $\boldsymbol{P}^f$ are defined in terms of the deformation gradient $\boldsymbol{F}$ since the motion is described in reference to the solid matrix.
The total nominal tractions and stresses are then obtained as

$$\boldsymbol{T} = \boldsymbol{T}^s + \boldsymbol{T}^f = \boldsymbol{P} \cdot \boldsymbol{N}, \qquad \boldsymbol{P} = \boldsymbol{P}^s + \boldsymbol{P}^f. \tag{2.60}$$

The linear momentum balance equation in reference to the undeformed configuration for the solid phase gives

$$\int_{A_0} \boldsymbol{T}^s \mathrm{d}A_0 + \int_{V_0} \rho^s \boldsymbol{g} \mathrm{d}V_0 + \int_{V_0} \boldsymbol{H}^s \mathrm{d}V_0 = \frac{\mathrm{d}}{\mathrm{d}t} \int_{V_0} \rho^s \boldsymbol{v} \mathrm{d}V_0, \tag{2.61}$$

where $\boldsymbol{H}^s = J\boldsymbol{h}^s$ is the nominal body force vector acting on the solid resulting from the frictional drag induced by the fluid flow. Again, converting the first integral into a volume integral, we obtain the localiz form of the linear momentum equation for the solid phase

$$\mathrm{DIV}(\boldsymbol{P}^s) + \rho_0^s \boldsymbol{g} + \boldsymbol{H}^s = \rho_0^s \boldsymbol{a}. \tag{2.62}$$

Similarly, for the fluid phase we have

$$\int_{A_0} \boldsymbol{T}^f \mathrm{d}A_0 + \int_{V_0} \rho^f \boldsymbol{g} \mathrm{d}V_0 + \int_{V_0} \boldsymbol{H}^f \mathrm{d}V_0 = \frac{\mathrm{d}}{\mathrm{d}t} \int_{V_0} \rho^f \boldsymbol{v} \mathrm{d}V_0, \tag{2.63}$$

where $\boldsymbol{H}^f = J\boldsymbol{h}^f$. Localizing we get

$$\mathrm{DIV}(\boldsymbol{P}^f) + \rho_0^f \boldsymbol{g} + \boldsymbol{H}^f = \rho_0^f \boldsymbol{a}_f. \tag{2.64}$$

Again, the body forces $\boldsymbol{H}$ are internal to the mixture, anf hence, $\boldsymbol{H}^s + \boldsymbol{H}^f = \boldsymbol{0}$. Summing the momentum balance equation for the two phases we obtain the equilibrium equation for the mixture,

$$\mathrm{DIV}(\boldsymbol{P}) + \rho_0 \boldsymbol{g} = \rho_0^s \boldsymbol{a} + \rho_0^f \boldsymbol{a}_f. \tag{2.65}$$

Note that the above equation could have been obtained from Eq. (2.53) by multiplying both sides of the equation by the Jacobian J and using the Piola identity.

Balance of energy

The concept of solid ($\boldsymbol{\sigma}^s$ or $\boldsymbol{P}^s$) and fluid ($\boldsymbol{\sigma}^f$ or $\boldsymbol{P}^f$) partial stress tensors developed in the former section is useful for addressing the multiphase nature of porous materials. However, the solid partial stress tensor is not an appropriate measure of stress for constitutive modeling of the solid matrix. To identify an appropriate constitutive stress tensor for the solid matrix, we utilize the balance of energy, or first law of thermodynamics. The first law of thermodynamics identifies a stress measure that is energy conjugate to the rate of deformation of the solid matrix. This stress measure is often referred to as the effective stress.

The first law states that the rate of increase of the total energy (internal and kinetic) of any arbitrary volume V of the mixture is equal to the rate of work done on the mixture (from the body forces and surface traction) plus the rate of increase of heat energy. If there are no mass exchanges between the solid and the fluid, the rate of change of internal energy is

$$\dot{E} = \int_V \rho \dot{e} \mathrm{d}V = \frac{\mathrm{d}}{\mathrm{d}t} \int_V \rho^s e_s \mathrm{d}V + \frac{\mathrm{d}^f}{\mathrm{d}t} \int_V \rho^f e_f \mathrm{d}V = \int_v \left(\rho^s \frac{\mathrm{d}e_s}{\mathrm{d}t} + \rho^f \frac{\mathrm{d}^f e_f}{\mathrm{d}t} \right) \mathrm{d}V, \tag{2.66}$$

where e_s and e_f are the internal energies per unit mass of solid and fluid, respectively, and $\dot{e}$ is the rate of increase in total internal energy per unit total mass of the mixture. The rate of change of kinetic energy is

$$\dot{K} = \frac{\mathrm{d}}{\mathrm{d}t} \int_V \rho^s \left(\frac{1}{2} \boldsymbol{v} \cdot \boldsymbol{v} \right) \mathrm{d}V + \frac{\mathrm{d}^f}{\mathrm{d}t} \int_V \rho^f \left(\frac{1}{2} \boldsymbol{v_f} \cdot \boldsymbol{v_f} \right) \mathrm{d}V = \int_V \left(\rho^s \boldsymbol{a} \cdot \boldsymbol{v} + \rho^f \boldsymbol{a}_f \cdot \boldsymbol{v}_f \right) \mathrm{d}V. \tag{2.67}$$

The total power is the sum of the mechanical power and the rate of increase of heat energy,

$$P = \frac{\mathrm{d}}{\mathrm{d}t} \int_V \left(\rho^s \boldsymbol{g} \cdot \boldsymbol{v} + \rho^f \boldsymbol{g} \cdot \boldsymbol{v}_f + \boldsymbol{h}^s \cdot \boldsymbol{v} + \boldsymbol{h}^f \cdot \boldsymbol{v}_f \right) \mathrm{d}V + \int_A \left(\boldsymbol{t}^s \cdot \boldsymbol{v} + \boldsymbol{t}^f \cdot \boldsymbol{v}_f \right) \mathrm{d}A, \tag{2.68}$$

where we we assumed there is no heat source in the mixture and no heat fluxes. In other words we assumed that the mixture is in isothermal equilibrium.

Since $\boldsymbol{t}^s = \boldsymbol{n} \cdot \boldsymbol{\sigma}^s$ and $\boldsymbol{t}^f = \boldsymbol{n} \cdot \boldsymbol{\sigma}^f$ by the Cauchy stress relations, it is possible to convert the area integrals in Eq. (2.68) into volume integrals.

By the first law of thermodynamics

$$\dot{E} = P - \dot{K}, \tag{2.69}$$

noting that V is arbitrary, and using the equilibrium equations (2.49) and (2.51), we obtain the local form of balance of energy for a solid-fluid mixture avoiding thermal effects,

$$\rho\dot{e} = \boldsymbol{\sigma}^s : \boldsymbol{d} + \boldsymbol{\sigma}^f : \boldsymbol{d}_f, \tag{2.70}$$

where $\boldsymbol{d} = \mathrm{sym}(\boldsymbol{l})$ and $\boldsymbol{d}_f = \mathrm{sym}(\boldsymbol{l}_f)$ are the rate of deformation tensors corresponding to the solid and the fluid motions. The mechanical component of the power density is seen as the sum of the mechanical powers generated by the two partial stress tensors.
Let's now consider a more specific isotropic form for the fluid partial stress tensor $\boldsymbol{\sigma}^f$. The diagonal components of this tensor are obtained from the intrinsic fluid pressure p_f multiplied by the fluid volume fraction ϕ^f

$$\boldsymbol{\sigma}^f = -\phi^f p_f \mathbf{1}, \tag{2.71}$$

where $\mathbf{1}$ is the second-order identity tensor. Inserting the above relation into Eq. (2.70) and recalling that $\boldsymbol{\sigma}^s = \boldsymbol{\sigma} - \boldsymbol{\sigma}^f$ we obtain

$$\rho\dot{e} = \boldsymbol{\sigma} : \boldsymbol{d} - \phi^f \mathrm{div}(\tilde{\boldsymbol{v}}_{\boldsymbol{f}}) p_f. \tag{2.72}$$

Therefore we observe that the mechanical power in a solid-fluid mixture is composed of two terms: the first term is the mechanical power of the total stress tensor $\boldsymbol{\sigma}$ deforming the solid matrix and the second term is the the mechanical power of the fluid pressure $_f$ in injecting or extracting fluid into or from the solid matrix. Hence the first law of thermodynamics suggests two conjugate pairs

$$\langle \boldsymbol{\sigma}, \boldsymbol{d} \rangle, \qquad\qquad \left\langle p_f, \phi^f \mathrm{div}(\tilde{\boldsymbol{v}}_{\boldsymbol{f}}) \right\rangle. \tag{2.73}$$

Let's manipulate further the above equations to obtain the desired effective stress. Noting that $\phi^f \mathrm{div}(\tilde{\boldsymbol{v}}_{\boldsymbol{f}}) = \mathrm{div}(\bar{\boldsymbol{v}}) - \tilde{\boldsymbol{v}}_f \cdot \mathrm{grad}(\phi^f)$ we obtain from Eq. (2.37)

$$\phi^f \mathrm{div}(\tilde{\boldsymbol{v}}_f) = -B\mathrm{div}(\boldsymbol{v}) - G \tag{2.74}$$

where G is the Gibb's potential

$$G = \frac{\phi^f}{K_f}\frac{\mathrm{d}p_f}{\mathrm{d}t} + \frac{\bar{\boldsymbol{v}}}{K_f} \cdot \mathrm{grad}(p_f) + \frac{\bar{\boldsymbol{v}}}{\phi_f} \cdot \mathrm{grad}(\phi_f). \tag{2.75}$$

Inserting Eq. (2.74) into Eq. (2.72) we obtain

$$\rho\dot{e} = \bar{\boldsymbol{\sigma}} : \boldsymbol{d} + G p_f, \tag{2.76}$$

where

$$\bar{\boldsymbol{\sigma}} = \boldsymbol{\sigma} + Bp_f\mathbf{1}. \tag{2.77}$$

Therefore, from the above equations we obtain two new conjugate pairs

$$\langle \bar{\boldsymbol{\sigma}}, \boldsymbol{d} \rangle , \qquad\qquad \langle p_f, G \rangle . \tag{2.78}$$

It's important to note that, since there are no other gradients of solid velocity appearing in the expression for Gibb's potential, we conclude that $\bar{\boldsymbol{\sigma}}$ is the complete constitutive stress tensor conjugate to $\boldsymbol{d}$.

As we did for the balance of linear momentum, we want now express the first law of thermodynamics in reference to the undeformed configurations, and define therefore the conjugate quantity in the initial configuration.

We start again from the rate of change of internal energy, which can be written as

$$E = \int_V \rho\dot{e}\mathrm{d}V = \int_{v_0} J\rho\dot{e}\mathrm{d}V_0 = \int_{V_0} \rho_0\dot{e}\mathrm{d}V_0, \tag{2.79}$$

where again $J = \det(\boldsymbol{F})$ is the Jacobian of thee solid motion and $\rho_0 = J\rho$ is the pull-back total mass density in the solid reference configuration. The energy-rate density is now written with respect to a unit reference volume and takes the form

$$\rho_0\dot{e} = \bar{\boldsymbol{\tau}} : \boldsymbol{d} + G\theta_f, \tag{2.80}$$

where

$$\bar{\boldsymbol{\tau}} = J\bar{\boldsymbol{\sigma}} = \boldsymbol{\tau} + B\theta_f\mathbf{1} \tag{2.81}$$

is the symmetric Kirchhoff effective stress tensor, $\boldsymbol{\tau} = J\boldsymbol{\sigma}$ is the Kirchhoff total stress tensor, $\theta_f = Jp_f$ is the Kirchhoff pore water pressure. Therefore we conclude that the effective Kirchhoff stress is work conjugate with the rate of deformation of the solid phase.

Alternatively, the mechanical power produced by the Kirchhoff effective stress tensor take the form

$$\bar{\boldsymbol{\tau}} : \boldsymbol{d} = \bar{\boldsymbol{\tau}} : \boldsymbol{l} = J\bar{\boldsymbol{\sigma}} : (\dot{\boldsymbol{F}} \cdot \boldsymbol{F}^{-\mathbf{1}}) = (J\bar{\boldsymbol{\sigma}} \cdot \boldsymbol{F}^{-T}) : \dot{\boldsymbol{F}} = \bar{\boldsymbol{P}} : \dot{\boldsymbol{F}}, \tag{2.82}$$

where $\bar{\boldsymbol{P}} = J\bar{\boldsymbol{\sigma}} \cdot \boldsymbol{F}^{-T}$ is the non-symmetric first Piola-Kirchhoff constitutive stress tensor. This produces the conjugate pair $\left\langle \bar{\boldsymbol{P}}, \boldsymbol{F} \right\rangle$. Alternatively, introducing the second Piola-Kirchhoff effective stress tensor $\bar{\boldsymbol{S}} = \boldsymbol{F}^{-1} \cdot \bar{\boldsymbol{\tau}} \cdot \boldsymbol{F}^{-T}$ we obtain

$$\bar{\boldsymbol{\tau}} : \boldsymbol{d} = \bar{\boldsymbol{P}} : \dot{\boldsymbol{F}} = (\boldsymbol{F} \cdot \bar{\boldsymbol{S}}) : \dot{\boldsymbol{F}} = \frac{1}{2}\bar{\boldsymbol{S}} : (\dot{\boldsymbol{F}}^{\boldsymbol{T}} \cdot \boldsymbol{F} + \boldsymbol{F}^{T} \cdot \dot{\boldsymbol{F}}) = \frac{1}{2}\bar{\boldsymbol{S}} : \dot{\boldsymbol{S}}, \tag{2.83}$$

where $\boldsymbol{C}$ is the right Cauchy-Green deformation tensor, which is work conjugate with the tensor $\bar{\boldsymbol{S}}$.

The definition of this conjugate stress-stress strain measure will play a central role in formulating the constitutive model, as expressed in the following part of the work.

Chapter 3

Constitutive law for the solid and fluid phases

3.1 Introduction

This chapter presents the constitutive law for both the solid and fluid phases, which are fundamental to complete the formulation of the problem and close the set of balance equations presented in the previous chapter. Obviously, the general framework presented so far is valid for a general porous material, and it's the adoption of the constitutive laws that characterizes the particular material.
As far as the solid phase, we investigated mainly three constitutive models at finite strains. These models are mainly devoted to the numerical simulation of geomaterials, such as soil or rock. These models are based on the concept of multiplicative decomposition of the deformation gradient, which is summarized at the beginning of the chapter.
As far as the fluid phase, we assumed a generalized Darcy's law, considering a laminar flow through the porous of the solid skeleton.
The aim of this chapter is to combine theoretical aspects with implementation procedures. Therefore, both the equations and the main coded functions will be presented together, to compare the two aspects. All the coded functions refer to the 2D implementation, assuming plane strain condition. Developing the 3D case is straightforward, and it follows as an extension of the presented functions.

3.2 Constitutive law for the solid phase

A major problem in applying finite element analysis, especially for geotechincal or reservoir engineering problems, is to provide a realistic representation of the constitutive law, i.e. of the stress-strain characteristics for the porous skeleton, especially for those material subjected to large deformations.

In fact, the choice of an appropriate constitutive relationship has an incredible influence on the numerical results.

A lot of constitutive models abounds in literature, and a complete overview of all the possibilities is behind the scope of this work. Constitutive models can vary from the simplest linear elastic law to the more advanced laws, such as elastoplastic laws, which take into account the irreversible deformations of the solid matrix. The constitutive models can also depend on the temperature, the degree of saturation, the presence of some chemical components, and so on. Furthermore, constitutive laws may be time dependent, i.e. related with the evolution of some parameters with time, to take into account for example the creep process. In this work we will focus on elastoplastic materials, without any further extensions. In particular, attention is focused on materials which do not creep, and the term *time dependance* relates purely to the consolidation process.

A crucial point in determining the choice of a suitable soil or rock constitutive model is the ease with which values can be assigned to the constants defining it. It may be possible to reproduce measured behavior accurately using a model defined by many constants. However, this is of little practical use if the determination of these constants as in itself a research project. An important objective is therefore to minimize the number of constants involved in the choice of a constitutive law.

In this chapter we will introduce three different constitutive model. The first model is an hyperelastic constitutive model, defined as Kirchhoff-De Saint Venant (41), which is an extension at finite strain of the classical linear elastic model in the small strain regime. This model, although not really useful for geotechnical applications, is important as starting point to develop more advanced model. The second model is an extension of the Modified Cam-Clay model for finite strain analysis. It was mainly developed by Borja and Tamagnini (42) and it is one of the most appropriate model for clays. Finally, the third model is a continuous cap model, that is proposed by the author of this thesis, with the mainly scope of simulate the constitutive behavior of porous rock. Both the two elastoplastic models are based on the fundamental concept of multiplicative decomposition of the deformation gradient, which will be recalled in the first part of this chapter.

Since the state of stress in soil and rock can be considered to consist of two components - deviatoric and hydrostatic stress - it is more convenient to work in terms of stress invariants when dealing with isotropic models, which will be introduced through the chapter.

It is fundamental to observe that the constitutive relation for the solid phase is between a strain measure and an *effective* stress measure. Therefore, all the stress measures reported in this chapter are intended to be *effective* measure of stress, and the bar (e.g. $\bar{\boldsymbol{\tau}}$) has been removed for the sake of simplicity.

3.2.1 General framework for elastoplasticity at finite strain

Introduction

This section of the work focuses on the theoretical formulation and algorithmic implementation of a finite deformation theory of elastoplasticity (43). Whereas numerous finite deformation theories abound in the literature, we shall focus mainly on a formulation based on a multiplicative decomposition of the deformation gradient, which gives rise to so-called multiplicative plasticity theory. The initial development of multiplicative plasticity theory is due to Lee (28). Since then, it has become a standard platform of many computer codes for nonlinear analysis of boundary-value problems in the finite deformation range. The theory is based on the notion of reference and current configurations, as well as on the existence of an intermediate stress-free configuration to which a body will return when it is unloaded. In this part of the thesis we will introduce the main aspects related to the multiplicative decomposition theory, with particular interest on the numerical procedures for solving an elastoplastic boundary value problem. These procedures will then be implemented in the numerical code to solve the elastoplastic behavior of the porous media at finite strain. Before discussing the multiplicative plasticity theory, we will recall the fundamental concepts of frame indifference and isotropy, two *a priori* assumptions for the development of the theory.

Frame indifference and isotropy

The concept of frame indifference (or frame invariance, or objectivity) in science means that qualitative and quantitative descriptions of physical phenomena remain unchanged when the phenomena are observed under a variety of conditions (34). For example, physical processes (e.g. material properties) are invariant under changes of observers; that is, it is possible to reconcile observations of the process into a single coherent description of it. Therefore, it's fundamental that every constitutive law satisfies the frame indifference criteria.
Let $\boldsymbol{x} = \boldsymbol{\varphi}(\boldsymbol{X}, t)$ denote a mapping of material point X from the reference position $\boldsymbol{X}$ to a current position $\boldsymbol{x}$. A rigid body motion on the current configuration is defined by uniform translation $\boldsymbol{c}(t)$ and a rotation $\boldsymbol{Q}(t)$

$$\boldsymbol{x}^{+} = \boldsymbol{c}(t) + \boldsymbol{Q}(t) \cdot \boldsymbol{x}. \tag{3.1}$$

The corresponding deformation gradient of this motion is

$$\boldsymbol{F}^{+}(\boldsymbol{X}, t) = \frac{\partial \boldsymbol{x}^{+}}{\partial \boldsymbol{X}} = \boldsymbol{Q}(t) \cdot \boldsymbol{F}(\boldsymbol{X}, t) \tag{3.2}$$

which implies that $J^{+} = \det\boldsymbol{F}^{+} = \det\boldsymbol{F} = J$. Also

$$\boldsymbol{F}^+ = \boldsymbol{Q}\boldsymbol{F} = \boldsymbol{Q}\boldsymbol{R}\boldsymbol{U} = \boldsymbol{R}^+\boldsymbol{U}^+ \quad \rightarrow \boldsymbol{R}^+ = \boldsymbol{Q}\boldsymbol{R} \text{ and } \boldsymbol{U}^+ = \boldsymbol{U}; \tag{3.3a}$$

$$\boldsymbol{F}^+ = \boldsymbol{Q}\boldsymbol{F} = \boldsymbol{Q}\boldsymbol{v}\boldsymbol{R} = \boldsymbol{v}^+\boldsymbol{R}^+ \quad \rightarrow \boldsymbol{v}^+ = \boldsymbol{Q}\boldsymbol{v}\boldsymbol{Q}^t. \tag{3.3b}$$

We conclude the following identities:

- a scalar field J is called frame indifferent if $J^+ = J$;
- a material tensor $\boldsymbol{U}$ is called frame indifferent if $\boldsymbol{U}^+ = \boldsymbol{U}$;
- a spatial tensor $\boldsymbol{v}$ is called frame indifferent if $\boldsymbol{v}^+ = \boldsymbol{Q}\boldsymbol{v}\boldsymbol{Q}^t$;
- a two-point tensor $\boldsymbol{F}$ is called frame indifferent if $\boldsymbol{F}^+ = \boldsymbol{Q}\boldsymbol{F}$.

After these statements, it is easy to demonstrate that as fa as the velocity gradients

$$\boldsymbol{l}^+ = \boldsymbol{Q}\boldsymbol{l}\boldsymbol{Q}^t + \dot{\boldsymbol{Q}}\boldsymbol{Q}^t \quad \text{is not frame indifferent;} \tag{3.4a}$$

$$\boldsymbol{d}^+ = \operatorname{symm}(\boldsymbol{l}^+) = \boldsymbol{Q}\boldsymbol{d}\boldsymbol{Q}^t \quad \text{is frame indifferent;} \tag{3.4b}$$

$$\boldsymbol{w}^+ = \operatorname{skw}(\boldsymbol{l}^+) = \boldsymbol{Q}\boldsymbol{w}\boldsymbol{Q}^t + \dot{\boldsymbol{Q}}\boldsymbol{Q}^t \quad \text{is not frame indifferent,} \tag{3.4c}$$

and the Cauchy stress tensor

$$\boldsymbol{\sigma}^+ = \boldsymbol{Q}\boldsymbol{\sigma}\boldsymbol{Q}^t \quad \text{is frame indifferent;} \tag{3.5a}$$

$$\dot{\boldsymbol{\sigma}}^+ = \boldsymbol{Q}\dot{\boldsymbol{\sigma}}\boldsymbol{Q}^t + (\dot{\boldsymbol{Q}}\boldsymbol{Q})\boldsymbol{\sigma}^+ - \boldsymbol{\sigma}^+(\dot{\boldsymbol{Q}}\boldsymbol{Q}^t) \quad \text{is not frame indifferent.} \tag{3.5b}$$

The lack of objectivity of the rate tensor $\dot{\boldsymbol{\sigma}}$ is a crucial point in developing a constitutive model at finite strains, since we are forced to use a different material time derivative of the stress tensor to ensure the objectivity of the rate-constitutive equations. To preserve objectivity of the stress rate, we will use the Lie derivative of the Kirchhoff stress tensor, also known as the Truesdell stress rate, which takes the form

$$\mathscr{L}_v\boldsymbol{\tau} = \dot{\boldsymbol{\tau}} - \boldsymbol{l}\boldsymbol{\tau} - \boldsymbol{\tau}\boldsymbol{l}^t. \tag{3.6}$$

As mentioned before, the notion of objectivity plays a central role in the formulation of the constitutive equation, since the material response may not depend on the choice of reference frame. A class of material response that automatically satisfies the requirement of objectivity is provided by a hyperelastic material. In a hyperelastic material the stress is obtained from a stored energy

function that depends on the local deformation. Now, consider a stored energy function of the form $\Psi^e(\boldsymbol{X}, \boldsymbol{F})$, and write the first Piola-Kirchhoff stress tensor for any material point

$$\boldsymbol{P}(\boldsymbol{X}, t) = \frac{\partial \Psi^e(\boldsymbol{X}, \boldsymbol{F})}{\partial \boldsymbol{F}}. \tag{3.7}$$

It can be shown that the restriction of frame invariance of the stored energy function is satisfied if it depends on the right Cauchy-Green deformation tensor, i.e.

$$\Psi^e(\boldsymbol{X}, \boldsymbol{F}) = \tilde{\Psi}^e(\boldsymbol{X}, \boldsymbol{C}). \tag{3.8}$$

With frame invariance, the hyperelastic constitutive equations, using different stress tensors, become

$$\boldsymbol{P} = \frac{\partial \tilde{\Psi}^e}{\partial \boldsymbol{C}} \cdot \frac{\partial \boldsymbol{C}}{\partial \boldsymbol{F}} = 2\boldsymbol{F} \cdot \frac{\partial \tilde{\Psi}^e}{\partial \boldsymbol{C}}; \tag{3.9a}$$

$$\boldsymbol{S} = 2\frac{\partial \tilde{\Psi}^e}{\partial \boldsymbol{C}}; \tag{3.9b}$$

$$\boldsymbol{\tau} = 2\boldsymbol{F} \cdot \frac{\partial \tilde{\Psi}^e}{\partial \boldsymbol{C}} \cdot \boldsymbol{F}^t. \tag{3.9c}$$

Let's introduce now a further assumption, namely the hypothesis of isotropy. By isotropy at a point $\boldsymbol{X}$, we mean that the material is insensitive to superposed rigid body motions on the reference configuration. This assumption should not be confused with frame indifference: the former pertains to some particular property of material response, whereas the latter is a fundamental principle of mechanics that must hold for all the possible material, and therefore response functions (44).
Frame invariance along with isotropy allows the replacement

$$\Psi^e(\boldsymbol{X}, \boldsymbol{F}) = \tilde{\Psi}^e(\boldsymbol{X}, \boldsymbol{C}) = \psi^e(\boldsymbol{X}, \boldsymbol{b}) = \hat{\Psi}^e(\boldsymbol{X}, \lambda_1^2, \lambda_2^2, \lambda_3^2), \tag{3.10}$$

where λ_A^2 for $A = 1, 2, 3$ are the eigenvalues of $\boldsymbol{C}$ (or $\boldsymbol{b}$), i.e. the stored energy functions depends solely on the eigenvalues. In this case, the hyperelastic constitutive relations between stress and strain simplifies further, and we get

$$\boldsymbol{P} = \frac{\partial \tilde{\psi}^e}{\partial \boldsymbol{b}} \cdot \frac{\partial \boldsymbol{b}}{\partial \boldsymbol{F}} = 2\frac{\partial \psi^e}{\partial \boldsymbol{b}} \cdot \boldsymbol{F}; \tag{3.11a}$$

$$\boldsymbol{S} = 2\boldsymbol{F}^{-1} \cdot \frac{\partial \psi^e}{\partial \boldsymbol{b}} \cdot \boldsymbol{F}; \tag{3.11b}$$

$$\boldsymbol{\tau} = 2\frac{\partial \psi^e}{\partial \boldsymbol{b}} \cdot \boldsymbol{b} = 2\boldsymbol{b} \cdot \frac{\partial \psi^e}{\partial \boldsymbol{b}}. \tag{3.11c}$$

These relations will constitute the basis to develop the constitutive theories in the following sections of the Chapter.

Multiplicative plasticity theory

Let's consider again simple body $\mathscr{B}$ in the initial undeformed and stress-free configuration, with $\boldsymbol{X}$ the coordinates of the material point. Let $\varphi(\mathscr{B})$ denote the final deformed configuration after following some elastoplastic deformation, and assume a mapping $\boldsymbol{x} = \boldsymbol{\varphi}(\boldsymbol{X})$. We define the intermediate configuration as one that results if each point in the body is unstressed.
Let $\boldsymbol{\chi}$ denote the position vector of the point in the intermediate configuration, and consider the sequential mapping

$$\boldsymbol{\chi} = \boldsymbol{\varphi}^p(\boldsymbol{X}, t) \qquad\qquad \boldsymbol{x} = \boldsymbol{\varphi}^e(\boldsymbol{\chi}, t). \tag{3.12}$$

Then, by the chain rule, we have

$$\boldsymbol{F}(\boldsymbol{X}, t) = \frac{\partial \boldsymbol{\varphi}^e}{\partial \boldsymbol{\chi}} \cdot \frac{\partial \boldsymbol{\varphi}^p}{\partial \boldsymbol{X}} = \boldsymbol{F}^e \cdot \boldsymbol{F}^p. \tag{3.13}$$

We define $\boldsymbol{F}^e$ and $\boldsymbol{F}^p$ as the elastic and plastic components of the deformation gradient, and Eq. (3.13) the multiplicative decomposition of $\boldsymbol{F}$.
From a micromechanical standpoint, $\boldsymbol{F}^p$ is an internal variable related to the amount of slipping, crushing, yielding, and (for plate-like particles) plastic bending of the granules comprising the soil or rock assembly (45). The product decomposition then represents the overall kinematics of deformation of the macroscopic material point X and may be interpreted as the volume average of the responses derived from the aforementioned micromechanical processes.
Along with the multiplicative decomposition (3.13) we define the elastic left Cauchy-Green deformation tensor

$$\boldsymbol{b}^e = \boldsymbol{F}^e \cdot \boldsymbol{F}^{et} \tag{3.14}$$

whereas $\boldsymbol{b}^e$ is a contravariant tensor field defined with respect to the current configuration. The time differentiation of $\boldsymbol{b}^e$ yields the expression

$$\dot{\boldsymbol{b}}^e = \boldsymbol{l}\boldsymbol{b}^e + \boldsymbol{b}^e\boldsymbol{l}^t + \mathscr{L}_v\boldsymbol{b}^e \tag{3.15}$$

where $\mathscr{L}_v\boldsymbol{b}^e$ is the Lie derivative of $\boldsymbol{b}^e$.
We restrict now the theory to isotropic stored energy function. As derived in Eq. (3.10), we write the free energy function in the form

$$\psi = \psi(\boldsymbol{b}^e, \boldsymbol{\xi}), \tag{3.16}$$

where $\boldsymbol{\xi}$ is a vector of strain-like plastic internal variable. Further, we assume that ψ can be decomposed additively into an elastic stored energy function $\psi^e(\boldsymbol{b}^e)$ and a part $\psi^p(\boldsymbol{\xi})$ that depends solely on the plastic internal variable $\boldsymbol{\xi}$. This results in complete uncoupling of the elastic and plastic responses. Let $\mathscr{D}$ denote the local dissipation function per unit reference volume of the solid matrix associated with the material point $\boldsymbol{X} \in \mathscr{B}$. Ignoring non-mechanical power and kinetic energy production, the second law states that

$$\mathscr{D} = \boldsymbol{\tau} : \boldsymbol{d} - \frac{\mathrm{d}\psi}{\mathrm{d}t} = \frac{1}{2}\boldsymbol{S} : \dot{\boldsymbol{C}} - \frac{\mathrm{d}\psi}{\mathrm{d}t} \geq 0, \tag{3.17}$$

where

$$\frac{\mathrm{d}\psi}{\mathrm{d}t} = \frac{\partial \psi}{\partial \boldsymbol{b}^e} : \dot{\boldsymbol{b}}^e + \frac{\partial \psi}{\partial \boldsymbol{\xi}} \cdot \dot{\boldsymbol{\xi}}. \tag{3.18}$$

Inserting the time derivative of $\boldsymbol{b}^e$ derived in Eq. (3.15) yields

$$\mathscr{D} = \left(\boldsymbol{\tau} - 2\frac{\partial \psi}{\partial \boldsymbol{b}^e} \cdot \boldsymbol{b}^e\right) : \boldsymbol{d} + \left(2\frac{\partial \psi}{\partial \boldsymbol{b}^e} \cdot \boldsymbol{b}^e\right) : \left(-\frac{1}{2}\mathscr{L}_v \boldsymbol{b}^e \cdot \boldsymbol{b}^{e-1}\right) - \frac{\partial \psi}{\partial \boldsymbol{\xi}} \cdot \dot{\boldsymbol{\xi}} \geq 0, \tag{3.19}$$

where the skew-symmetric term of $\boldsymbol{l}$ drops out. Since Eq. (3.19) must hold for all admissible processes, a standard argument leads to the following hyperelastic constitutive equation

$$\boldsymbol{\tau} = 2\frac{\partial \psi}{\partial \boldsymbol{b}^e} \cdot \boldsymbol{b}^e \tag{3.20}$$

and the following reduced dissipation inequality

$$\mathscr{D} = \boldsymbol{\tau} : \left(-\frac{1}{2}\mathscr{L}_v \boldsymbol{b}^e \cdot \boldsymbol{b}^{e-1}\right) + \boldsymbol{k} \cdot \dot{\boldsymbol{\xi}} \geq 0, \tag{3.21}$$

where $\boldsymbol{k} = -\partial\psi/\partial\boldsymbol{\xi}$ is a vector of stress-like plastic internal variables conjugate to $\boldsymbol{\xi}$. From Eq. (3.21) we identify the expression inside the parentheses as the plastic flow direction

$$-\frac{1}{2}\mathscr{L}_v \boldsymbol{b}^e \cdot \boldsymbol{b}^{e-1} = \dot{\gamma}\frac{\partial \mathscr{G}}{\partial \boldsymbol{\tau}}, \tag{3.22}$$

where $\mathscr{G}$ is the plastic potential function and $\dot{\gamma}$ is a non-negative plastic multiplier. Maximum plastic dissipation is ensured by assuming an associative flow rule, i.e. $\mathscr{G} \equiv \mathscr{F}$ along with associative hardening $\dot{\boldsymbol{\xi}} = \dot{\gamma}\frac{\partial \mathscr{F}}{\partial \boldsymbol{k}}$. The yield function takes the form now

$$\mathscr{F}(\boldsymbol{\tau}, \boldsymbol{k}) \leq 0. \tag{3.23}$$

i.e. is a function of the Kirchhoff stress tensor. Similar to the infinitesimal formulation, maximum plastic dissipation implies the convexity of the yield function, the associative flow rule and the respect of the Kuhn-Tucker conditions

$$\dot{\gamma} \geq 0; \qquad \mathscr{F}(\boldsymbol{\tau}, \boldsymbol{k}) \leq 0 \qquad \dot{\mathscr{F}}(\boldsymbol{\tau}, \boldsymbol{k}) = 0. \tag{3.24}$$

Stress-update algorithm and algorithmic tangent operator

In this section we will discuss how to solve numerically the equations developed so far for accounting the plasticity at finite strains. The crucial point is integrate numerically the rate form of the constitutive equation, in order to quantify the local stresses and deformations, to enforce the equilibrium condition. The idea is to subdivide the dummy time interval into intervals, and impose the equilibrium conditions at every discrete time instant. Consider for example a time interval (t_n, t_{n+1}) at let's look to a specific arbitrary point $\boldsymbol{X} \in \mathscr{B}$. The task consists in computing, for a given displacement increment, the elastic left Cauchy-Green tensor $\boldsymbol{b}^e_{n+1}$ and the Kirchhoff stress tensor $\boldsymbol{\tau}_{n+1}$, starting form the known solution at time step t_n

$$\begin{cases} \boldsymbol{F}_n \\ \boldsymbol{b}^e_n = \boldsymbol{F}^e_n \boldsymbol{F}^{et}_n \rightarrow \boldsymbol{\tau_n} \\ \boldsymbol{\xi}_n \end{cases} \Longrightarrow \begin{cases} \boldsymbol{F}_{n+1} \\ \boldsymbol{b}^e_{n+1} = ? \rightarrow \boldsymbol{\tau_{n+1}} = ? \\ \boldsymbol{\xi}_{n+1} = ? \end{cases} \tag{3.25}$$

Following the standard deformation-driven format, we then prescribe a local displacement field $\boldsymbol{u}_t$ over the time interval in question. This is equivalent to prescribing the relative deformation gradient over the same time interval (t_n, t_{n+1}),

$$\boldsymbol{f}_t = \boldsymbol{F}_t \cdot \boldsymbol{F}_n^{-1} = \boldsymbol{1} - \frac{\partial \boldsymbol{u}_t}{\partial \boldsymbol{x}_n}. \tag{3.26}$$

Note that the relative deformation gradient $\boldsymbol{f}$ is the analog of the incremental strain tensor $\boldsymbol{\Delta\epsilon}$ in the infinitesimal formulation. In the finite deformation range, we want to determine the statically admissible values of $\boldsymbol{b}^e$ and $\boldsymbol{\xi}$ given the relative deformation gradient $\boldsymbol{f}$.
The essential rate equation that need to be integrated is Eq. (3.15). Note that the first two terms correspond to the predictor value (what would arise if there was no plastic flow) and the last term corresponds to the corrector value, in the presence of plastic flow. The incremental version of the predictor-corrector algorithm in the finite deformation range now takes a multiplicative form (44). The algorithm consists of two steps. First, the incremental counterpart of the predictor step is computed, which is given by

$$\boldsymbol{b}^{e\,Tr}_{n+1} = \boldsymbol{f} \cdot \boldsymbol{b}^{e}_{n} \cdot \boldsymbol{f}^{t}. \tag{3.27}$$

If there is no plastic flow then $\boldsymbol{b}^e = \boldsymbol{b}^{e\,Tr}$. The second step is the incremental plastic corrector in the presence of plastic flow, obtained by the integration of the Lie derivative. This can be done in spectral form

$$\mathscr{L}_v \boldsymbol{b}^e = \sum_{A=1}^{3} \mathscr{L}_v {\lambda^e_A}^2 \boldsymbol{m}^{(A)} = -2\dot{\gamma} \sum_{A=1}^{3} \frac{\partial \mathscr{G}}{\partial \tau_A} {\lambda^e_A}^2 \boldsymbol{m}^{(A)}. \tag{3.28}$$

This fundamental result is obtained taking into account the spectral decomposition of $\boldsymbol{b}^e$ and $\boldsymbol{\tau}$

$$\boldsymbol{b}^e = \sum_{A=1}^{3} (\lambda^e_A)^2 \boldsymbol{m}^{(A)} \qquad\qquad \boldsymbol{\tau} = \sum_{A=1}^{3} (\beta_A)^2 \boldsymbol{m}^{(A)} \tag{3.29}$$

From the coaxiality of the relevant tensors, the principal values of the left and right side of Eq. (3.28) must be equal, and we can work therefore only with the scalar quantities. Integrating both sides using a simple backward integration, and enforcing the limits, we get

$$\log\left(\frac{{\lambda^e_A}^2}{{\lambda^{e\,Tr}_A}^2}\right) = -2\Delta\gamma \frac{\partial \mathscr{G}}{\partial \beta_A}. \tag{3.30}$$

Expanding the left-hand side of the above equation and noting that $\log({\lambda^e_A}^2) = 2\epsilon^e_A$, we obtain the desired incremental update equation in the space of principal elastic logarithmic stretches as follows,

$$\epsilon^e_A = \epsilon^{e\,Tr}_A - \Delta\gamma \frac{\partial \mathscr{G}}{\partial \beta_A}. \tag{3.31}$$

What it is really important to note, is that the above predictor-corrector equation, presented by Simo (30), preserves the additive return-mapping format of the infinitesimal theory.

The plastic multiplier $\Delta\gamma$ can be determined by imposing the discrete condition $\mathscr{F}(\boldsymbol{\tau}, \boldsymbol{\xi}) = 0$. Typically, this computation requires a local iteration due to the nonlinearity introduced by the flow direction.

The plastic internal variable $\boldsymbol{\xi}$ could also change with deformation, and needs to be updated along the stress-update algorithm. In general the update equation for this variable depends on the specific constitutive model used for the material.

The last aspect that needs to be investigated is the consistent elastoplastic tangent operator in the finite deformation range. In doing so, we will invoke the property of isotropy so that we can use all of the nice results developed so far. First, we derive the variation of the Kirchhoff stress tensor from the spectral form as

$$\delta\boldsymbol{\tau} = \sum_{A=1}^{3} \delta\beta_A \boldsymbol{n}^{(A)} \otimes \boldsymbol{n}^{(A)} + \sum_{A=1}^{3}\sum_{B\neq A}^{3} \omega_{AB}(\beta_B - \beta_A)\boldsymbol{n}^{(A)} \otimes \boldsymbol{n}^{(B)}, \tag{3.32}$$

where ω_{AB} are the relevant spins. Similarly, taking advantage of the spectral form, the variation of $\boldsymbol{b}^{e\,Tr}$ takes a similar form,

$$\delta\boldsymbol{b}^{e\,Tr} = \sum_{A=1}^{3} \delta\lambda_A^{e\,Tr\,2} \boldsymbol{n}^{(A)} \otimes \boldsymbol{n}^{(A)} + \sum_{A=1}^{3}\sum_{B\neq A}^{3} \omega_{AB}(\lambda_B^{e\,Tr\,2} - \lambda_A^{e\,Tr\,2})\boldsymbol{n}^{(A)} \otimes \boldsymbol{n}^{(B)}, \tag{3.33}$$

where again the spins of the two tensors are the same.
At the same time, deriving Eq. (3.27) we get

$$\delta\boldsymbol{b}^{e\,Tr} = \delta\boldsymbol{f} \cdot \boldsymbol{b}_n^e \cdot \boldsymbol{f}^t + \boldsymbol{f} \cdot \boldsymbol{b}_n^e \cdot \delta\boldsymbol{f}^t = (\boldsymbol{\Delta}\delta\boldsymbol{u}) \cdot \boldsymbol{b}^{e\,Tr} + \boldsymbol{b}^{e\,Tr} \cdot (\boldsymbol{\Delta}\delta\boldsymbol{u}) \tag{3.34}$$

The tangent constitutive relation arises from

$$\delta\boldsymbol{\tau} = \boldsymbol{\Phi} : \delta\boldsymbol{b}^{e\,Tr} = \boldsymbol{\Phi} : (\boldsymbol{\Delta}\delta\boldsymbol{u}) \cdot \boldsymbol{b}^{e\,Tr} + \boldsymbol{b}^{e\,Tr} \cdot (\boldsymbol{\Delta}\delta\boldsymbol{u}) = \boldsymbol{\alpha} : \boldsymbol{\Delta}\delta\boldsymbol{u}, \tag{3.35}$$

where

$$\begin{aligned}\boldsymbol{\alpha} = &\sum_{A=1}^{3}\sum_{B=1}^{3} a_{AB}\boldsymbol{m}^{(A)} \otimes \boldsymbol{m}^{(B)} + \\ &\sum_{A=1}^{3}\sum_{B\neq A}^{3} \omega_{AB}\left(\frac{(\tau_B - \tau_A)}{(\lambda_B^{e\,Tr\,2} - \lambda_A^{e\,Tr\,2})}\right)(\lambda_B^{e\,Tr\,2}\boldsymbol{m}^{(AB)} \otimes \boldsymbol{m}^{(AB)} + \lambda_A^{e\,Tr\,2}\boldsymbol{m}^{(AB)} \otimes \boldsymbol{m}^{(BA)}).\end{aligned} \tag{3.36}$$

The term $a_{AB} = \partial\tau_A/\partial\lambda_A^{e\,Tr\,2}$ is the algorithmic stress-strain matrix in principal axis. This matrix depends on the specific constitutive elastoplastic law, i.e. the algorithm for detemining τ_A, rather the remaining framework it's general and can be used for all kind of material. The following Box summarizes the implementation of the general stress-update algorithm for elastoplasticity at finite strains.

1. Elastic deformation predictor: $\boldsymbol{b}^{e\,Tr} = \boldsymbol{f}_{n+1} \cdot \boldsymbol{b}^{e}_{n} \cdot \boldsymbol{f}^{t}_{n+1}$.

2. Trial Kirchhoff stress tensor: $\boldsymbol{\tau}^{Tr} = 2\boldsymbol{b}^{e\,Tr} \cdot \partial\psi^{e}/\partial\boldsymbol{b}^{e\,Tr}$

3. Check if yielding: $\mathscr{F}(\boldsymbol{\tau}^{Tr}, \boldsymbol{\xi}_n) \geq 0$?
   No: elastic step. Then $\boldsymbol{b}^{e} = \boldsymbol{b}^{e\,Tr}$, $\boldsymbol{\tau} = \boldsymbol{\tau}^{Tr}$, $\boldsymbol{\xi} = \boldsymbol{\xi}_n$ and exit. Yes: continue.

4. Spectrally decompose: $\boldsymbol{b}^{e\,Tr} = \sum_{A=1}^{3} {\lambda^{e\,Tr}_{A}}^{2} \boldsymbol{m}^{(A)}$

5. Compute $\Delta\gamma$ such that:

$$\begin{cases} \epsilon^{e}_{A} = \epsilon^{e\,Tr}_{A} - \Delta\gamma\partial\mathscr{G}/\partial\beta_A \longrightarrow \boldsymbol{b}^{e} \longrightarrow \boldsymbol{\tau} \\ \mathscr{F}(\boldsymbol{\tau}, \boldsymbol{\xi}) = 0 \end{cases} \tag{3.37}$$

6. Exit with the corrected values of $\boldsymbol{b}^{e}$, $\boldsymbol{\tau}$, $\boldsymbol{\xi}$.

7. Algorithmic stress-strain matrix: $a_{AB} = \partial\beta_A/\partial{\lambda^{e\,Tr}_{A}}^{2}$

8. Algorithmic tangent operator $\boldsymbol{\alpha}$ according to Eq. (3.36).

The box summarizes the stress-update procedure with the computation of the algorithmic tangent operator, which ha been implemented in a finite element code, as described in the next section.

Numerical code

The stress-update procedure described so far is a fundamental part of the complete finite element code to describe the mechanic of the porous media at finite strains. We will report in this section the main function written to fulfill this task.
The full code is quote in the following Box, and represents the stress-update algorithm for every gauss integration point. The code is written for a 2D plain strain/stress analysis.
The fundamental input data for thi subroutine are the set of material parametet `Ge`, the total displacement `ue`, the incremental displacement `due` and the vector that contains the internal state variables (namely, $\boldsymbol{b}^{e}_{n}$, $\boldsymbol{\xi}_n$) `PLne`. Obviously, the set of parameter `Ge` depends on the specific constitutive law.

```
% Loop over every Gauss point ip = 1:nip

% Total deformation gradient
 [F,b] = FbQuad(Xe,r(i),r(j),ue+due);

% Incremental deformation gradient
```

```
Ue = reshape(ue,size(Xe,2),size(Xe,1))';
X1e = (Xe + Ue);

[Fincr,b] = FbQuad(X1e,r(i),r(j),due);

% Control Jacobian
if det(F)<0
warn=1; % Warning for negative determinant of F
end

% Recall variables at time step n : b^e_n and xi_n

Be =  [PLne(1,ip)  PLne(3,ip)  0
       PLne(3,ip)  PLne(2,ip)  0
       0           0           PLne(4,ip)];

xin = xine(5,ip);

% Compute Trial left cauchy-Green
BeTr = Fincr*Be*Fincr';

% Compute principal deformation and direction

[eigve,eigva] = eig(BeTr);

epseTr = [log(sqrt(eigva(1,1)))
                  log(sqrt(eigva(2,2)))
                  log(sqrt(eigva(3,3)))];

dirpr = eigve;

% Compute principal Kirchhoff tension and stress-strain matrix
[tenspr,epse,xi,aep,FLAGe(ip,1)] = tens(Ge,epseTr,xin);

% Compute left Cauchy Green tensor at n+1

stretpr(:,1) = exp(epse(:,1));

Be = zeros(3);

for ii=1:3

    Be(1:3,1:3) = Be(1:3,1:3)+(stretpr(ii))^2*dirpr(:,ii)*dirpr(:,ii)';

end

% Compute Kirchhoff tension tensor

TTe = zeros(3);

for ii=1:3

    TTe(1:3,1:3) = TTe(1:3,1:3)+tenspr(ii)*dirpr(:,ii)*dirpr(:,ii)';

```

```
61  end
62
63  % Allocate Kirchhoff tension tensor
64
65  Te(:,ip) = [TTe(1,1) TTe(2,2) TTe(1,2) TTe(3,3) ]';
66
67  % Compute Cauchy tension
68  Se(:,ip) = Te(:,ip)/det(F);
69
70
71  % Allocate internal state variables at time n+1 for next plastic algorithm
72
73  PLe(:,ip)= [Be(1,1); Be(2,2); Be(1,2); Be(3,3); xi];
74
75  % Compute tangent operator alfa
76
77  stretTr(:,1) = exp(epseTr(:,1));
78  ALFAe(:,ip) = alfa(aep,tenspr,stretTr.^2,dirpr);
```

The function `alfa` computes the algorithmic tangent tensor $\boldsymbol{\alpha}$ according to Eq. (3.36) as reported in the following box.

```
1   function alfavet = alfa(aep,tenspr,lambar,avett)
2   %-------------------------------------------------------
3   % Compute tangent operator and store in vector form.
4   %
5   % Date: 29/10/2013
6   %    Version 1.0
7   %
8   % Created by: Nicolo' Spiezia
9   %-------------------------------------------------------
10
11  toll = 10e-6;
12  pert = 10e-5;
13
14  % Compute the first term:
15
16  alfa1 = zeros(3,3,3,3);
17  alfa2 = zeros(3,3,3,3);
18
19  for A=1:3
20      for B=1:3
21
22      alfa1 = alfa1+aep(A,B)*dyadic(avett(:,A)*avett(:,A)',avett(:,B)*avett(:,B)');
23
24      end
25  end
26
27  % Compute the second term:
28
29          % Check for singularity
30          if abs(lambar(1)-lambar(2)) < toll
```

```
31              lambar(2)=lambar(1)+pert; end
32          if abs(lambar(1)-lambar(3)) < toll
33              lambar(3)=lambar(1)-pert; end
34          if abs(lambar(2)-lambar(3)) < toll
35              lambar(3)=lambar(3)-pert; end
36
37  for A=1:3
38      for B=1:3
39
40      if B ~= A
41      alfa2 = alfa2+((tenspr(B)-tenspr(A))/(lambar(B)-lambar(A)))*...
42             (lambar(B)*dyadic( avett(:,A)*avett(:,B)',avett(:,A)*avett(:,B)')+...
43             lambar(A)*dyadic( avett(:,A)*avett(:,B)',avett(:,B)*avett(:,A)'));
44      end
45
46      end
47  end
48
49
50  % Total alfa tensor
51  alfatens = alfa1+alfa2;
52
53  % Allocate alfa as vector for 2D plain strain (non-symmetric)
54
55  alfamat=[alfatens(1,1,1,1)  alfatens(1,1,2,1)  alfatens(1,1,1,2) alfatens(1,1,2,2)
56           alfatens(2,1,1,1)  alfatens(2,1,2,1)  alfatens(2,1,1,2) alfatens(2,1,2,2)
57           alfatens(1,2,1,1)  alfatens(1,2,2,1)  alfatens(1,2,1,2) alfatens(1,2,2,2)
58           alfatens(2,2,1,1)  alfatens(2,2,2,1)  alfatens(2,2,1,2) alfatens(2,2,2,2)];
59
60  alfavet = reshape(alfamat,16,1);
61
62  end
```

However, the corner stone of the stress-update procedure consists in the function to compute the Kirchhoff stress tensor $\boldsymbol{\tau}$ and the algorithmic stress-strain matrix in principal axes a_{AB}. This is carried out by the function `[tenspr,epse,xi,aep,FLAGe(ip,1)] = tens(Ge,epseTr,xin)`, which depends on the specific constitutive law. In the next section some constitutive laws will be presented, and therefore the function `tens` will be specified properly.

3.2.2 Hyperelastic law

Introduction

Before moving to more complex elastoplastic laws, let's begin from a purely elastic constitutive law, which is simply derived from a free energy function. Deriving an hyperelastic law is important, not even to describe the behavior of elastic material, but also to account for the elastic domain of elastoplastic material.

A material frequently encountered in the literature is defined by a hyperelastic potential in terms of

the logarithmic stretches and two material parameters λ and μ as

$$\hat{\Psi} = \frac{1}{2}\lambda[\epsilon_1^e + \epsilon_2^e + \epsilon_3^e]^2 + \mu[(\epsilon_1^e)^2 + (\epsilon_2^e)^2 + (\epsilon_3^e)^2], \tag{3.38}$$

where $\epsilon_A^e = \ln(\lambda_A^e)$ are the elastic logarithmic principal stretches. The principal kirchhoff stresses can be obtained deriving the elastic potential defined in Eq. (3.38), which reads

$$\tau_A = \frac{2\mu}{J}\epsilon_A + \frac{\lambda}{J}\ln J \tag{3.39}$$

where $\ln J = \epsilon_1^e + \epsilon_2^e + \epsilon_3^e$. Furthermore, the coefficients of the elasticity tensor are

$$a_{AB} = \lambda + 2\mu\delta_{AB} \tag{3.40}$$

The similarities between these equations and linear elasticity can be established if we first recall the standard small strain elastic equations as

$$\sigma_A = \lambda(\varepsilon_1 + \varepsilon_2 + \varepsilon_3) + 2\mu\varepsilon_A \tag{3.41}$$

Recalling that $\ln J = \ln\lambda_1 + \ln\lambda_2 + \ln\lambda_3$, it transpires that Eq. (3.39) and Eq. (3.41) are identical except for the small strains having been replaced by the logarithmic stretches and the Cauchy stress $\boldsymbol{\sigma}$ by the Kirchhoff stress $\boldsymbol{\tau}$.

The stress-update procedure is straightforward and doesn't require particular algorithm, differently from the elastoplastic models that will be implemented later on. The following box contains the main function to compute the stress state.

```
1  function [tens] = tensHY(Ge,F,b)
2  %-------------------------------------------------------
3  % File: tensHY.m
4  %   Compute the kirchhoff tensor of tension with hyperelastic
5  %   Saint Venant Kirchhoff material.
6  %
7  % Input:
8  %    F    : Deformation gradient.
9  %   Ge    : Element property vector.
10 %    b    : Left Cauchy-Green tensor
11 %
12 % Output:
13 %  tens   : Tensor of Kirchhoff tension
14 %
15 % Reference:
16 % Bonet J., Wood R.D., Non linear continuum mechanics for finite element
17 % analysis.
18 %
19 % Date:
```

```
20 %   Version 1.0   24.03.14
21 %
22 % Created by: Nicolo' Spiezia
23 %-------------------------------------------------------
24
25 % Initialize tensor of Kirchhoff tension
26 tens = zeros(2);
27
28 % Set isotropic elasticity parameter
29
30 E  = Ge(2);
31 nu = Ge(3);
32
33 lam = (E*nu)/((1+nu)*(1-2*nu));
34 mu = E/(2*(1+nu));
35
36 %Compute eigenvalues and eigenvector of left Cauchy-Green b
37
38 [avett,aval] = eig(b(1:2,1:2));
39
40 % Compute principal deformation and direction
41
42 defpr = [ sqrt(aval(1,1))
43           sqrt(aval(2,2))];
44
45 dirpr = [avett(:,1) avett(:,2)];
46
47 % Compute principal tension
48
49 tenspr = lam*log(det(F))*[1 1]'+2.0*mu*log(defpr);
50
51 for i=1:2
52
53     tens = tens+tenspr(i)*dirpr(:,i)*dirpr(:,i)';
54
55 end
56
57 end
```

What it's important to observe is that very small changes are needed to implement this model with respect to the infinitesimal linear elastic model. Essentially, it's just necessary to compute the deformation gradient $\boldsymbol{F}$ and the Jacobian $J = \det\boldsymbol{F}$, and modify the equations with these values.

3.2.3 Modified Cam Clay

Introduction

Cam-Clay models of critical state mechanics are widely used in many geotechnical applications involving numerical predictions of stability and deformation behavior of compressible soil materials such as soft clays. The general features of these models include pressure sensitivity, hardening

response with plastic volumetric compaction, softening response with plastic dilation, and coupled volumetric and deviatoric plastic deformations, which are essential to model the prototype granular material behavior realistically.

In this section we will present a Cam-Clay constitutive model, which will be implemented in the coupled non linear finite element code. The classical constitutive model needs to be extended appropriately to be inserted in a finite strains framework. The two main modifications are, first, the introduction of a linear relationship between the logarithm of specific volume and the logarithm of effective mean normal stress to describe the compressibility behavior of the soil in the effective deformation regime. Second, the introduction of a class of two-invariant stored energy function, that takes into account the pressure-dependency of both the bulk and shear moduli, along with the conservation of the energy.

In the next section we will recall the main relation of the adopted constitutive law, while later on we will address the numerical solution and the implementation of the code.

Constitutive relations

In this section we will recall the fundamental equations of the constitutive model. In general, the aspects that need to be defined in an elastoplastic model are:

1. *The free energy function*: several elastic law have been proposed for geomaterials, to capture the correct response given by experimental data (46; 47; 48).

   For this model we employ a hyperelastic model with pressure-dependent bulk and shear moduli. This model was originally proposed by Houlsby (49) and subsequently modified by Borja et al. (42), Callari et al. (50) and Yamakawa et al. (51), to describe the elastic response of mainly clay and sands. Consider the volumetric and deviatoric elastic invariants defined as

$$\epsilon_v^e = \boldsymbol{\epsilon}^{\boldsymbol{e}} \cdot \boldsymbol{\delta}; \qquad \epsilon_s^e = \sqrt{\frac{2}{3}} \left\| \boldsymbol{e}^{\boldsymbol{e}} \right\|; \qquad \boldsymbol{e}^{\boldsymbol{e}} = \boldsymbol{\epsilon}^{\boldsymbol{e}} - \frac{1}{3}\epsilon_v^e \boldsymbol{\delta}, \tag{3.42}$$

   where $\boldsymbol{\epsilon}^{\boldsymbol{e}} = (\epsilon_1^e, \epsilon_2^e, \epsilon_3^e)$ is the vector of the elastic logarithmic principal stretches defined as $\epsilon_A^e = \ln(\lambda_A^e)$, and $\boldsymbol{\delta} = (1, 1, 1)$. Next, consider a class of two-invariant free energy functions of the form

$$\hat{\psi}(\epsilon_v^e, \epsilon_s^e) = \tilde{\psi}(\epsilon_v^e) + \frac{3}{2}\mu^e \epsilon_s^{e2}, \tag{3.43}$$

   where

$$\tilde{\psi}(\epsilon_v^e) = -P_0 k \exp(\Omega); \qquad \Omega = -(\epsilon_v^e - \epsilon_{v0}^e)/k. \tag{3.44}$$

   The term $\tilde{\psi}(\epsilon_v^e)$ represents the stored energy function for isotropic loading. The parameters involved are the elastic compressibility modulus k and the elastic volumetric strain ϵ_{v0}^e at a

mean normal effective stress of P_0. The term

$$\mu^e = \mu_0 + \frac{\alpha}{k}\tilde{\psi} \tag{3.45}$$

represents the elastic shear modulus. It is the sum of a constant term μ_0 and a variable term, that depends on the elastic volumetric strain through the constant coefficient α. If $\alpha = 0$, then the elasticity model is defined by a variable elastic bulk modulus and a constant elastic shear modulus.

Consider now the vector of the principal Kirchhoff tension $\boldsymbol{\beta} = (\beta_1, \beta_2, \beta_3)$ and define P and Q, respectively the mean normal and deviatoric Kirchhoff stress invariants, given by

$$P = \frac{1}{3}\boldsymbol{\beta}\cdot\boldsymbol{\delta}; \qquad Q = \sqrt{\frac{3}{2}}\left\|\boldsymbol{s}\right\|; \qquad \boldsymbol{s} = \boldsymbol{\beta} - P\boldsymbol{\delta}. \tag{3.46}$$

The relation between stress and strain invariants derives directly from the derivation of the stored energy function with respect of the deformation, and reads

$$P = \frac{\partial\hat{\psi}}{\partial\epsilon_v^e} = P_0\exp(\Omega)\left[1 + \frac{3\alpha}{2k}(\epsilon_s^e)^2\right]; \tag{3.47a}$$

$$Q = \frac{\partial\hat{\psi}}{\partial\epsilon_s^e} = 3(\mu_0 - \alpha P_0\exp\Omega)\epsilon_s^e. \tag{3.47b}$$

2. *The yield function*: consider a two-invariant yield function of the form

$$\mathscr{F} = \mathscr{F}(P, Q, P_c) = \frac{Q^2}{M^2} + P(P - P_c) = 0, \tag{3.48}$$

where P and Q are the mean normal and deviatoric Kirchhoff stress invariants as defined in Eq. (3.46). Eq. (5.2) defines the ellipsoid of the modified Cam-Clay model whose size is determined by the Kirchhoff preconsolidation pressure P_c.

3. *The hardening law*: the model assumes that the yield surface can expand and shrink according to the accumulated plastic volumetric strains. In other worlds, the preconsolidation pressure P_c changes according to the accumulated plastic volumetric strain ϵ_v^p. The equation in rate form reads

$$\dot{P}_c = -P_c\Theta\dot{\epsilon}_v^p, \tag{3.49}$$

where $\Theta = 1/(\lambda - k)$. The hardening parameter P_c can be expressed as a known function of the plastic volumetric strain, since Eq. (3.49) can be integrated exactly.

4. *The flow rule*: consider an associative flow rule, which means that the plastic potential is

equivalent to the yield surface. Therefore the model assumes that

$$\mathscr{F} \equiv \mathscr{G}. \tag{3.50}$$

5. *The K-K-T conditions*: the model has to fulfill the classical Karush-Kuhn-Tucker conditions as follows

$$\gamma \geq 0 \qquad \mathscr{F} \leq 0 \qquad \gamma\mathscr{F} = 0. \tag{3.51}$$

6. *The consistency conditions*: in case of plasticity, the following condition has to be satisfied

$$\gamma\dot{\mathscr{F}} = 0 \qquad \text{if} \qquad \mathscr{F} = 0. \tag{3.52}$$

The above realtions constitute the set of equations that need to be solved numerically, in order to account for the elastoplsatic behavior of the solid skeleton.

Return Mapping algorithm and algorithmic tangent operator

The model permits a fully implicit numerical integration utilizing a classical return mapping scheme performed in the strain invariant space (42), leading to a system of non linear equations with three unknowns. As described in the previous section, it is assumed that the updated displacements are given, which implies that the elastic trial strain $\boldsymbol{\epsilon}^{e\,Tr}$ and the solution at time step t_n are known. The task is to compute the updated stress state $\boldsymbol{\beta}$ and the discrete plastic multiplier $\Delta\gamma$ for a given displacement increment. According to (42), consider the following local residual equations generated by the applied strain increment $\Delta\boldsymbol{\epsilon}$

$$\boldsymbol{r} = \boldsymbol{r}(\boldsymbol{x}) = \begin{Bmatrix} \epsilon_v^e - \epsilon_v^{e\,Tr} + \Delta\gamma\partial_P\mathscr{F} \\ \epsilon_s^e - \epsilon_s^{e\,Tr} + \Delta\gamma\partial_Q\mathscr{F} \\ \mathscr{F} \end{Bmatrix}; \qquad \boldsymbol{x} = \begin{Bmatrix} \epsilon_v^e \\ \epsilon_s^e \\ \Delta\gamma \end{Bmatrix}. \tag{3.53}$$

The aim is to dissipate the residual vector $\boldsymbol{r}$ by finding the solution vector $\boldsymbol{x}^*$ using a Newton's method

$$\boldsymbol{x}^{k+1} = \boldsymbol{x}^k + \delta\boldsymbol{x}^k; \qquad -\boldsymbol{A}^k\delta\boldsymbol{x}^k = \boldsymbol{r}^k; \qquad \boldsymbol{A}^k = \frac{\partial\boldsymbol{r}^k}{\partial\boldsymbol{x}^k};\ k \leftarrow k+1, \tag{3.54}$$

where k plays the role of an iteration counter. A closed form expression for the consistent tangent operator $\boldsymbol{A}$ can be derived following standard procedures.

At every iteration the value of P_c needs to be updated, according to (3.49). The current value of

the volumetric plastic strain ϵ_v^e can be easily computed assuming the additive decomposition of the logarithmic strains

$$\epsilon_v = \epsilon_v^e + \epsilon_v^p = \epsilon_v^{e\,Tr} + \epsilon_{v,n}^p, \tag{3.55}$$

where $\epsilon_{v,n}^p$ is the plastic volumetric deformation at time step t_n.

Of great importance is to derive the tangential tensor, required in Eq. (**??**) which is defined in principal direction as

$$\boldsymbol{a}^e = \frac{\partial \boldsymbol{\beta}}{\partial \boldsymbol{\epsilon}^e}. \tag{3.56}$$

Naturally, two distinct tangential tensor has to be computed, depending on the either elastic or elastoplastic status of stress

The tangential elastic tensor $\boldsymbol{a}^e$ can be computed taking advantage of the invariant decomposition. The derivation of the stress invariants with respect of the strain invariants reads

$$\frac{\partial P}{\partial \boldsymbol{\epsilon}^e} = D_{11}^e \boldsymbol{\delta} + \sqrt{\frac{2}{3}} D_{12}^e \hat{\boldsymbol{n}}; \tag{3.57a}$$

$$\frac{\partial Q}{\partial \boldsymbol{\epsilon}^e} = D_{21}^e \boldsymbol{\delta} + \sqrt{\frac{2}{3}} D_{22}^e \hat{\boldsymbol{n}}, \tag{3.57b}$$

where $\hat{\boldsymbol{n}} = \boldsymbol{e}^{\boldsymbol{e}} / \|\boldsymbol{e}^e\|$ and $\boldsymbol{D}^e$ is the symmetric Hessian matrix of $\hat{\psi}$that can be found in Appendix A. Therefore, the consistent tangent operator $\boldsymbol{a}^e$ for the hyperelastic law is computed using Eq. (3.57) and reads (52)

$$a_{AB} = \left(D_{11}^e - \frac{2Q}{9\epsilon_s^e} \right) \delta_A \delta_B + \sqrt{\frac{2}{3}} (D_{12}^e \delta_A \hat{n}_B + D_{21}^e \hat{n}_A \delta_B) + \frac{2Q}{3\epsilon_s^e} (\delta_{AB} - \hat{n}_A \hat{n}_B) + \frac{2}{3} D_{22}^e \hat{n}_A \hat{n}_B. \tag{3.58}$$

Note that, if $\alpha = 0$ the volumetric and deviatoric elastic responses uncouple and the consistent tangent operator in Eq. (3.58) degenerates to the following expression for an isotropic elastic model

$$a_{AB} = K^e \delta_A \delta_B + 2\mu^e \left(\delta_{AB} - \frac{1}{3} \delta_A \delta_B \right). \tag{3.59}$$

where $K^e = -P/k$ is the pressure sensitive elastic bulk modulus. As done for the hyperelastic constitutive law, it is necessary to derive the algorithmic tangent modulus of the model in the principal space for the plastic constitutive law. The operator is obtained taking the derivative of the principal Kirchhoff tension with respect to the trial logarithmic principal strain, which are used to compute the update state of stress in the elastoplastic regime

$$\boldsymbol{a}^{ep} = \frac{\partial \boldsymbol{\beta}}{\partial \boldsymbol{\epsilon}^{eTr}}. \tag{3.60}$$

Consider the following strain derivative

$$\boldsymbol{a}^{ep} := \frac{\partial \boldsymbol{\beta}}{\boldsymbol{\epsilon}^{e\,Tr}} = \boldsymbol{\delta} \otimes \frac{\partial P}{\boldsymbol{\epsilon}^{e\,Tr}} + \sqrt{\frac{2}{3}}\hat{\boldsymbol{n}} \otimes \frac{\partial Q}{\boldsymbol{\epsilon}^{e\,Tr}} + \sqrt{\frac{2}{3}} Q \otimes \frac{\partial \hat{\boldsymbol{n}}}{\boldsymbol{\epsilon}^{e\,Tr}}, \tag{3.61}$$

where

$$\frac{\partial \hat{\boldsymbol{n}}}{\boldsymbol{\epsilon}^{e\,Tr}} = \frac{\partial \boldsymbol{\partial}(\boldsymbol{e^e}/\left\|\boldsymbol{e^e}\right\|)}{\boldsymbol{\epsilon}^{e\,Tr}} = \frac{\partial \boldsymbol{\partial}(\boldsymbol{e^{e\,Tr}}/\left\|\boldsymbol{e^{e\,Tr}}\right\|)}{\boldsymbol{\epsilon}^{e\,Tr}} = \frac{1}{\left\|\boldsymbol{e}^{e\,Tr}\right\|}\left(\boldsymbol{I} - \frac{1}{3}\boldsymbol{\delta}\otimes\boldsymbol{\delta} - \hat{\boldsymbol{n}}\otimes\hat{\boldsymbol{n}}\right). \tag{3.62}$$

Substituting (3.62) in (3.61), and using the elements of the matrix $\boldsymbol{D}^e$ to enforce the chain rule, we have

$$\boldsymbol{a}^{ep} = \boldsymbol{\delta} \otimes \left(D^e_{11}\frac{\partial \epsilon^e_v}{\partial \boldsymbol{\epsilon}^{e\,Tr}} + D^e_{12}\frac{\partial \epsilon^e_s}{\partial \boldsymbol{\epsilon}^{e\,Tr}}\right) + \sqrt{\frac{2}{3}}\hat{\boldsymbol{n}} \otimes \left(D^e_{21}\frac{\partial \epsilon^e_v}{\partial \boldsymbol{\epsilon}^{e\,Tr}} + D^e_{22}\frac{\partial \epsilon^e_s}{\partial \boldsymbol{\epsilon}^{e\,Tr}}\right) + \frac{2Q}{3\epsilon^{e\,Tr}_s}\left(\boldsymbol{I} - \frac{1}{3}\boldsymbol{\delta}\otimes\boldsymbol{\delta} - \hat{\boldsymbol{n}}\otimes\hat{\boldsymbol{n}}\right). \tag{3.63}$$

The task is then reduced to determine the strain derivatives of the invariants ϵ^e_v and ϵ^e_s, which are obtained from the discretized flow rule, expressed in term of invariants

$$\frac{\partial \epsilon^e_v}{\partial \boldsymbol{\epsilon}^{e\,Tr}} = \frac{\partial}{\partial \boldsymbol{\epsilon}^{e\,Tr}}\left(\epsilon^{e\,Tr}_v - \Delta\gamma\frac{\partial \mathscr{F}}{\partial P}\right); \qquad \frac{\partial \epsilon^e_s}{\partial \boldsymbol{\epsilon}^{e\,Tr}} = \frac{\partial}{\partial \boldsymbol{\epsilon}^{e\,Tr}}\left(\epsilon^{e\,Tr}_s - \Delta\gamma\frac{\partial \mathscr{F}}{\partial Q}\right). \tag{3.64}$$

Eq. (3.64) can be written in a more efficient way introducing the 2×2 operator $\boldsymbol{D}^p$, with components D^p_{ij}, which maps the basis vectors $\boldsymbol{\delta}$ and $\sqrt{2/3}\hat{\boldsymbol{n}}$ onto the derivatives with respect to $\boldsymbol{\epsilon}^{e\,Tr}$ of the elastic strain invariants ϵ^e_v and ϵ^e_s

$$\frac{\partial \epsilon^e_v}{\partial \boldsymbol{\epsilon}^{e\,Tr}} = D^p_{11}\boldsymbol{\delta} + \sqrt{\frac{2}{3}D^p_{12}}\hat{\boldsymbol{n}}; \qquad \frac{\partial \epsilon^e_s}{\partial \boldsymbol{\epsilon}^{e\,Tr}} = D^p_{21}\boldsymbol{\delta} + \sqrt{\frac{2}{3}D^p_{22}}\hat{\boldsymbol{n}}. \tag{3.65}$$

Finally substituting (3.65) in (3.63) and defining

$$\boldsymbol{D}^{ep} = \boldsymbol{D}^e\boldsymbol{D}^p, \tag{3.66}$$

we obtain the desired consistent tangent operator

$$a^{ep}_{AB} = \left(D^{ep}_{11} - \frac{2Q}{9\epsilon^e_s{}^{Tr}_s}\right)\delta_A\delta_B + \sqrt{\frac{2}{3}}(D^{ep}_{12}\delta_A\hat{n}_B + D^{ep}_{21}\hat{n}_A\delta_B) + \frac{2Q}{3\epsilon^{e\,Tr}_s}(\delta_{AB} - \hat{n}_A\hat{n}_B) + \frac{2}{3}D^{ep}_{22}\hat{n}_A\hat{n}_B. \tag{3.67}$$

The coefficients of the operator $\boldsymbol{a}^{ep}$ depend on the operator $\boldsymbol{D}^p$. The reader should refer to (42) for close formulation.

Note that Eq. (3.84) is valid both for elastic and elasto-plastic loading. In fact, for elastic loading

$\boldsymbol{D}^p = \boldsymbol{I}$ and $\boldsymbol{D}^{ep} = \boldsymbol{D}^e$ and so Eq. (3.84) reduces to the tangential elasticity matrix (3.58). The correct computation of the algorithmic tangent moduli is crucial to obtain convergent solution of the large-scale non-linear analysis and to detect singularities in the domain.
The complete procedure to compute the update state of stress and the tangent operator is summarized in the following box.

1. Elastic deformation predictor: $\boldsymbol{b}^{e\,Tr} = \boldsymbol{f}_{n+1} \cdot \boldsymbol{b}^e_n \cdot \boldsymbol{f}^T_{n+1}$.
2. Spectral decomposition: $\boldsymbol{b}^{e\,Tr} = \sum_{A=1}^{3} (\lambda^{e\,Tr}_A)^2 \boldsymbol{n}^{Tr\,(A)} \otimes \boldsymbol{n}^{Tr\,(A)}$.
3. Principal elastic logarithmic strains: $\epsilon^{Tr}_A = \ln(\lambda^{e\,Tr}_A)$.
4. Deformation invariants $\epsilon^{e\,Tr}_v$ and $\epsilon^{e\,Tr}_s$ according to Eq. (3.42).
5. Elastic stress predictor P^{Tr} and Q^{Tr} according to Eq. (3.47).
6. Check if yielding: $\mathscr{F}(P^{Tr}, Q^{Tr}, P_{c,n}) \geq 0$?
   - No: elastic step. Set $(\epsilon^e_v, \epsilon^e_s) = (\epsilon^{e\,Tr}_v, \epsilon^{e\,Tr}_s)$, $P_c = P_{c,n}$ and $(P, Q) = (P^{Tr}, Q^{Tr})$. Compute elastic stress-strain matrix $\boldsymbol{a}^e$
   - Yes: plastic step. Solve Eq. (3.80), compute $\epsilon^e_v, \epsilon^e_s, \Delta\gamma$ and update P_c. Compute elastoplastic stress-strain matrix $\boldsymbol{a}^{ep}$
7. Principal elastic logarithmic strain ϵ^e_A and principal Kirchhoff tension β_A.
8. Updated left elastic Cauchy-Green tensor and Kirchhoff stress tensor:
   $\boldsymbol{b^e} = \sum_{A=1}^{3} (\exp(\epsilon^e_A))^2 \boldsymbol{n}^{Tr\,(A)} \otimes \boldsymbol{n}^{Tr\,(A)}$ and $\boldsymbol{\tau} = \sum_{A=1}^{3} \beta_A \boldsymbol{n}^{Tr\,(A)} \otimes \boldsymbol{n}^{Tr\,(A)}$

Numerical code

The crucial function that is responsible a) to compute the update state of stress and b) to compute the stress-strain matrix, is the function `tens`, which depends on the specific implemented material. In this section we present in detail the function `tensCC`, which implements the constitutive equations of the Cam Clay model presented so far.
The main function is reported in the following box.

```
1 function [tenspr,epse,Pc,aep,flag] = tensCC(Ge,defepr,Pcn)
2 %-------------------------------------------------------------
3 % tensCC:
4 %   Compute the Kirchhoff principal tension according to CC yield criterion.
5 %
6 % Syntax:
```

```
7  %   [tenspr,epse,Pc,aep,flag] = tensCC(Ge,defepr,Pcn)
8  %
9  % Input:
10 % Ge       : Material property.
11 % defepr   : Elastic principal deformation.
12 % Pcn      : Preconsolidation pressure at step n.
13 %
14 % Output:
15 % tenspr : Vector of Kirchhoff principal tension. [beta(1) beta(2) beta (3)]'
16 %   epse : Vector of elastic principal strain. [epse(1) epse(2) epse (3)]'
17 %   Pc   : Preconsolidation pressure at step n+1.
18 %  aep   : Algorithmic stress-strain matrix in pr direction (a_AB).
19 %  flag  : Flag for plasticity.
20 %
21 % Reference:
22 % Borja R.I., Tamagnini C., Cam-Clay plasticity, part III: Estension of the
23 % infinitesimal model to include finite strain, CMAME 155, (1998), 73-95.
24 %
25 % Date:
26 %   Version 1.0   25.10.13
27 %
28 % Created by: Nicolo' Spiezia
29 %-------------------------------------------------------
30
31 % Initialize vector
32
33 tenspr = zeros(3,1);
34 epse = zeros(3,1);
35
36 imax = 15;
37 toll = 10e-6;
38
39 % Set isotropic elasto-plastic parameter
40 mu0  = Ge(2);
41 alfa = Ge(3);
42 kappa = Ge(4);
43 lambda = Ge(5);
44 M = Ge(6);
45 P0 = Ge(7);
46 epsev0 = Ge(9);
47
48
49 % Compute volumetric trial strain
50 epsevTR = defepr(1,1)+defepr(2,1)+defepr(3,1);
51
52 % Compute deviatoric trial strain
53 epsedev(:,1) = defepr(:,1)-epsevTR/3;
54
55 epsesTR = sqrt(2/3)*norm(epsedev);
56
57 % Compute trial stress invariants
58 [Ptr,Qtr] = PQ( epsevTR, epsesTR, P0, alfa, kappa, epsev0, mu0);
59
60 % Check for plasticity
```

```
Ftr = (Qtr/M)^2+Ptr*(Ptr-Pcn);

if Ftr > toll % PLASTIC STEP
   flag = 1;

        % Solve NR system

            % Inizialize variables
            x = zeros(3,1);
            x(1,1) = epsevTR;    % epsev
            x(2,1) = epsesTR;    % epses
            x(3,1) = 0;          % dgamma

            Pc = Pcn;
            P = Ptr;
            Q = Qtr;

            for iter = 1:imax

                % evaluate residual
                r = [x(1,1) - epsevTR + x(3,1)*(2*P-Pc);
                     x(2,1) - epsesTR + x(3,1)*(2*Q/M^2);
                     (Q/M)^2 + P*(P-Pc)];


                if iter == 1
                r0 = norm(r);
                end

                NORMErec(iter,1) = norm(r)/norm(r0);

                % check for convergence
                if norm(r) < toll
                    break
                else

                    % evaluate tangent matrix for NR iteration
                    A = Atang(x(1,1),x(2,1),x(3,1),...
                                        P,Q,Pc,lambda,kappa,mu0,alfa,P0,epsev0,M);

                    % solve for displacement increment
                    dx = - (A\r);

                    x = x + dx;

                    % update

                    [P,Q]=PQ(x(1,1),x(2,1),P0,alfa,kappa,epsev0,mu0);

                    OMEGA = 1/(lambda-kappa);
                    Pc = Pcn*exp(-OMEGA*(epsevTR-x(1,1)));

                        if iter == imax
                        fprintf('\n No convergence RM \n')
```

```
115                             break
116                             end
117
118                     end
119                 end
120
121             %Update variable
122             epsev = x(1,1);
123             epses = x(2,1);
124             dgamma = x(3,1);
125
126             % Compute matrix Dep
127
128             Dep = DEPtens(epsev,epses,dgamma,P,Q,Pc,...
129                             lambda,kappa,mu0,alfa,P0,epsev0,M);
130
131
132     else % ELASTIC STEP
133         flag = 0;
134
135             %Update variable
136             epsev = epsevTR;
137             epses = epsesTR;
138
139             Pc = Pcn;
140             P = Ptr;
141             Q = Qtr;
142
143             % Compute matrix De
144
145             De = DEtens(epsev,epses,P,kappa,mu0,alfa,P0,epsev0);
146
147             Dep = De;
148
149     end
150
151     % Compute vector n
152
153     n(:,1) = epsedev(:,1)/norm(epsedev);
154
155     % Compute principal Kirchhoff tension
156
157     tenspr(:,1) = P*ones(3,1)+ sqrt(2/3)*Q*n(:,1);
158
159     % Compute principal elastic strain
160
161     epse(:,1) = (1/3)*epsev*ones(3,1)+ sqrt(3/2)*epses*n(:,1);
162
163     % Compute algorithmic stress-strain in principal direction
164
165     aep = (Dep(1,1)-2*Q/(9*epsesTR))*ones(3,1)*ones(3,1)'+...
166             sqrt(2/3)*Dep(1,2)*ones(3,1)*n(:,1)'+...
167             sqrt(2/3)*Dep(2,1)*n(:,1)*ones(3,1)'+...
168           ((2*Q)/(3*epsesTR))*(eye(3)-n(:,1)*n(:,1)')+...
```

```
169         (2/3)*Dep(2,2)*n(:,1)*n(:,1)';
170
171 end
```

The operator $\boldsymbol{A}$, necessary to solve the non-linear set of equations of the Return Mapping algorithm, is computed by the function `Atang`, which is reported in the following box.

```
1  function [A] = Atang( epsev,epses,dgamma,P,Q,Pc,lambda,kappa,mu0,alfa,P0,epsev0,M )
2  %-------------------------------------------------------
3  % ATANG Compute tangent for NR iteration for Cam Clay Return Mapping
4  %
5  % Reference:
6  % Borja R.I., Tamagnini C., Cam-Clay plasticity, part III: Estension of the
7  % infinitesimal model to include finite strain, CMAME 155, (1998), 73-95.
8  %
9  % Date: 25/10/2013
10 %   Version 1.0
11 %
12 % Created by: Nicolo' Spiezia
13 %-------------------------------------------------------
14
15 % Inizialize matrices
16 A = zeros(3);
17 [De, H, G] = deal(zeros(2));
18
19 % Compute parameter
20 OMEGA = -(epsev-epsev0)/kappa;
21 mue = mu0+(alfa/kappa)*(-P0*kappa*exp(OMEGA));
22 THETA = 1/(lambda-kappa);
23
24 % Compute matrix D
25
26 De(1,1) = -P/kappa;
27 De(2,2) = 3*mue;
28 De(1,2) = (3*P0*alfa*epses/kappa)*exp(OMEGA);
29 De(2,1) = (3*P0*alfa*epses/kappa)*exp(OMEGA);
30
31 % Compute matrix H
32
33 H(1,1) = 2;
34 H(2,2) = 2/(M^2);
35 H(1,2) = 0;
36 H(2,1) = 0;
37
38 % Compute matrix G
39
40 G = H*De;
41
42 % Compute matrix A
43
44 A(1,1) = 1+dgamma*(G(1,1)-THETA*Pc);
45 A(1,2) = dgamma*G(1,2);
```

```
A(1,3) = 2*P-Pc;

A(2,1) = dgamma*G(2,1);
A(2,2) = 1+dgamma*G(2,2);
A(2,3) = 2*Q/(M^2);

A(3,1) = De(1,1)*(2*P-Pc)+De(2,1)*(2*Q/(M^2))+THETA*Pc*(-P);
A(3,2) = De(1,2)*(2*P-Pc)+De(2,2)*(2*Q/(M^2));
A(3,3) = 0;

end
```

The stress-strain tensor $\boldsymbol{a}^e$ or $\boldsymbol{a}^{ep}$ is computed by the fucntion `tensCC` via the operator $\boldsymbol{D}_e$ and $\boldsymbol{D}_{ep}$, which are computed by the functions `DEtens DEPtens`, and are summarized in the following two boxes.

```
function DE = DEtens(epsev,epses,P,kappa,mu0,alfa,P0,epsev0)
%DEtens Compute the elastic tensor De

% Inizialize matrices
De = zeros(2);

% Compute parameter
OMEGA = -(epsev-epsev0)/kappa;
mue = mu0+(alfa/kappa)*(-P0*kappa*exp(OMEGA));

% Compute elastic tensor De (3.33a Part III)
DE(1,1) = -P/kappa;
DE(2,2)= 3*mue;
DE(1,2)= (3*P0*alfa*epses/kappa)*exp(OMEGA);
DE(2,1)= (3*P0*alfa*epses/kappa)*exp(OMEGA);

end
```

```
function Dep = DEPtens( epsev,epses,dgamma,P,Q,Pc,lambda,kappa,mu0,alfa,P0,epsev0,M )
%-------------------------------------------------------
% DEPtens: compute matrix Dep according to equatione 3.50
%
% Reference:
% Borja R.I., Tamagnini C., Cam-Clay plasticity, part III: Estension of the
% infinitesimal model to include finite strain, CMAME 155, (1998), 73-95.
%
% Date: 25/10/2013
%   Version 1.0
%
% Created by: Nicolo' Spiezia
%-------------------------------------------------------

% Inizialize matrices
```

```
16  [De,H,b,Dp] = deal(zeros(2));
17
18  % Compute parameter
19  OMEGA = -(epsev-epsev0)/kappa;
20  mue = mu0+(alfa/kappa)*(-P0*kappa*exp(OMEGA));
21  THETA = 1/(lambda-kappa);
22
23  % Compute matrix D
24
25  De(1,1) = -P/kappa;
26  De(2,2)= 3*mue;
27  De(1,2)= (3*P0*alfa*epses/kappa)*exp(OMEGA);
28  De(2,1)= (3*P0*alfa*epses/kappa)*exp(OMEGA);
29
30  % Compute matrix H
31
32  H(1,1) = 2;
33  H(2,2) = 2/(M^2);
34  H(1,2) = 0;
35  H(2,1) = 0;
36
37  % Compute matrix G
38
39  G = H*De;
40
41  % Compute matrix b
42
43  b(1,1) = 1+dgamma*(G(1,1)-THETA*Pc);
44  b(1,2) = dgamma*G(1,2);
45  b(2,1) = dgamma*G(2,1);
46  b(2,2) = 1+dgamma*G(2,2);
47
48  % Compute parameters
49
50  c1 = 1-dgamma*(-THETA*Pc)*(-1);
51  c2 = -dgamma*(-THETA*Pc)*0;
52
53  d1 = De(1,1)*(2*P-Pc)+De(2,1)*(2*Q/(M^2))+THETA*Pc*(-P);
54  d2 = De(1,2)*(2*P-Pc)+De(2,2)*(2*Q/(M^2));
55
56  e = d1*(b(2,2)*(2*P-Pc)-b(1,2)*(2*Q/(M^2)))+d2*(b(1,1)*(2*Q/(M^2))-b(2,1)*(2*P-Pc));
57
58  a1 = (d1*(b(2,2)*c1-b(1,2)*c2)+d2*(b(1,1)*c2-b(2,1)*c1)+det(b)*(-THETA*Pc)*(-P))/e;
59  a2 = sqrt(2/3)*(d2*b(1,1)-d1*b(1,2))/e;
60
61  % Compute matrix Dp
62
63  Dp(1,1)= b(2,2)*(c1-a1*(2*P-Pc))-b(1,2)*(c2-a1*(2*Q/(M^2)));
64  Dp(1,2)= b(1,2)*(-1+sqrt(3/2)*a2*(2*Q/(M^2)))-sqrt(3/2)*b(2,2)*a2*(2*P-Pc);
65  Dp(2,1)= b(1,1)*(c2-a1*(2*Q/(M^2)))-b(2,1)*(c1-a1*(2*P-Pc));
66  Dp(2,2)= b(1,1)*(1-sqrt(3/2)*a2*(2*Q/(M^2)))+sqrt(3/2)*b(2,1)*a2*(2*P-Pc);
67
68  Dp = Dp/det(b);
69
```

```
70  % Compute matrix Dep
71
72  Dep = De*Dp;
73
74  end
```

Numerical example

This section assesses the accuracy of the proposed integration algorithm. Since the finite deformation algorithm uses the same classical return mapping calculations of the infinitesimal theory, the accuracy analysis apply to both small and large strain formulations.
The values of material parameters used in the computation are the following: $\lambda = 0.018$, $\kappa = 0.13$, $M = 1.05$, $\mu_0 = 0$, $\alpha = 120$, $P_0 = -90KPa$ and $P_{c0} = -90KPa$. Hence, the initial condition corresponds to a normally consolidated soil with a preconsolidation pressure of $P_0 = P_{c0} = -90KPa$ on the isotropic axis.
Figg. 3-1 and 3-2 show the stress strain curves and stress path on the P-Q plane as functions of number of imposed strain increments. In particular, Fig. 3-1 shows the soil being deformed to total strains of $\epsilon_v = 0$ and $\epsilon_s = 0.05$ applied in proportional increment; Fig. 3-2 shows the soil being deformed to total strains of $\epsilon_v = -0.05$ and $\epsilon_s = 0.05$.

Note that in both case the solution is convergent, in the sense that the responses converge toward the solutions obtained using 100 steps.
This type of algorithm is exactly repeated at the Gauss point level, in order to solve classical Boundary value problem, as will be done in the next chapters of the thesis.

3.2.4 Continuous Cap model

Introduction

In this section we present an innovative constitutive model, developed to described the constitutive behavior of highly porous rock.
Before presenting in detail the formulation of the model, it is useful to briefly summarize the main features of dilation and compaction failure revealed by experimental studies on porous rocks.
In order to develop and evaluate possible constitutive models for high porosity rock it's necessary to understand the complex macro/microscopic behavior under different loading condition. A detailed discussion on the different failure mechanisms of porous rock is behind the scope of this work. Nevertheless it is fundamental, in order to better understand the following part of the work, briefly recall the main features of the mechanical response. In particular we consider two different loading programs, namely hydrostatic compression (uniform confining pressure) and axisymmetric compression (radial confining pressure applied to cylindrical specimens with an additional compressive axial

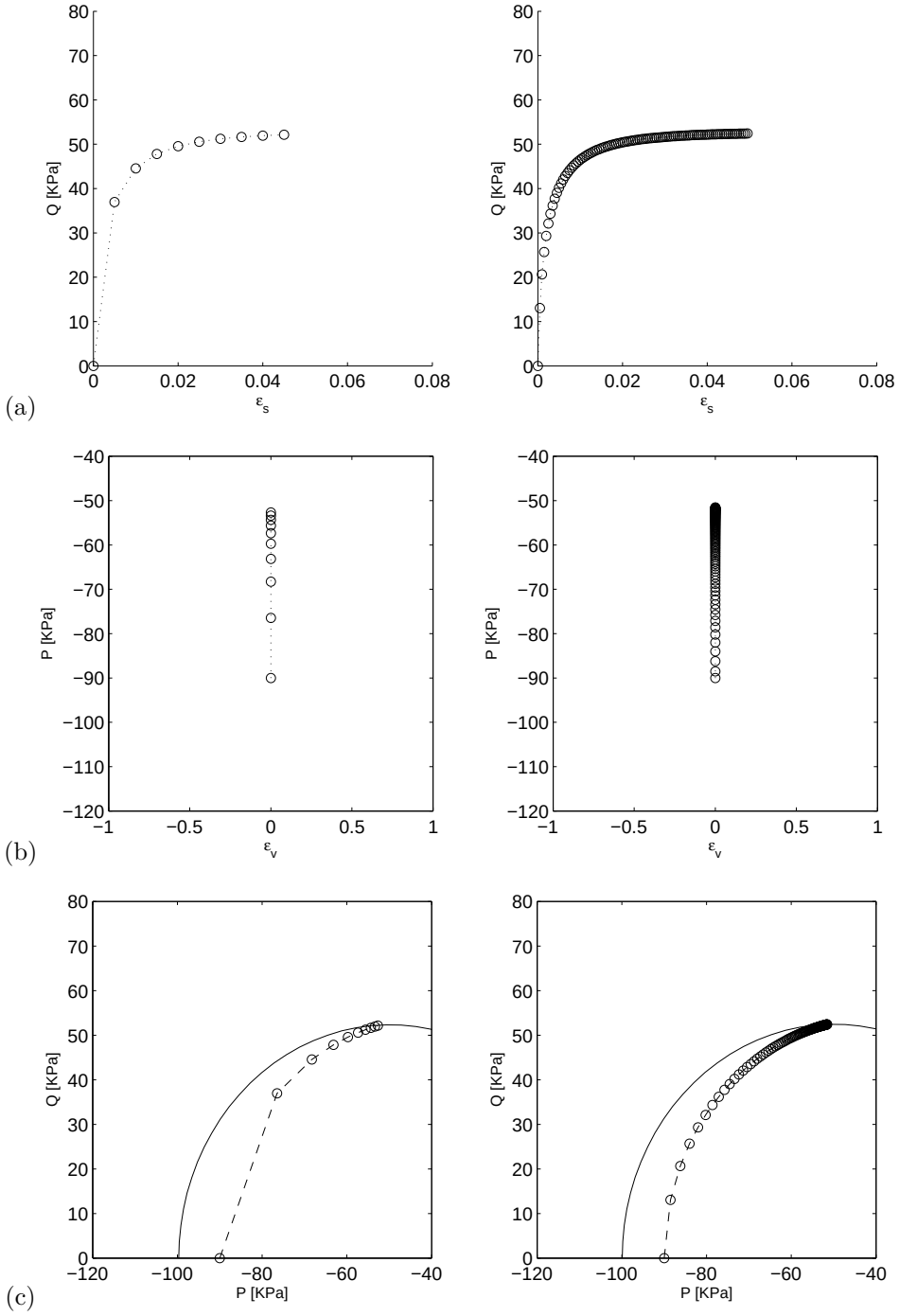

Figure 3-1: Convergence analysis with 10 increments (left) and 100 increments (right) imposing $\epsilon_v = 0$ and $\epsilon_s = 0.05$.

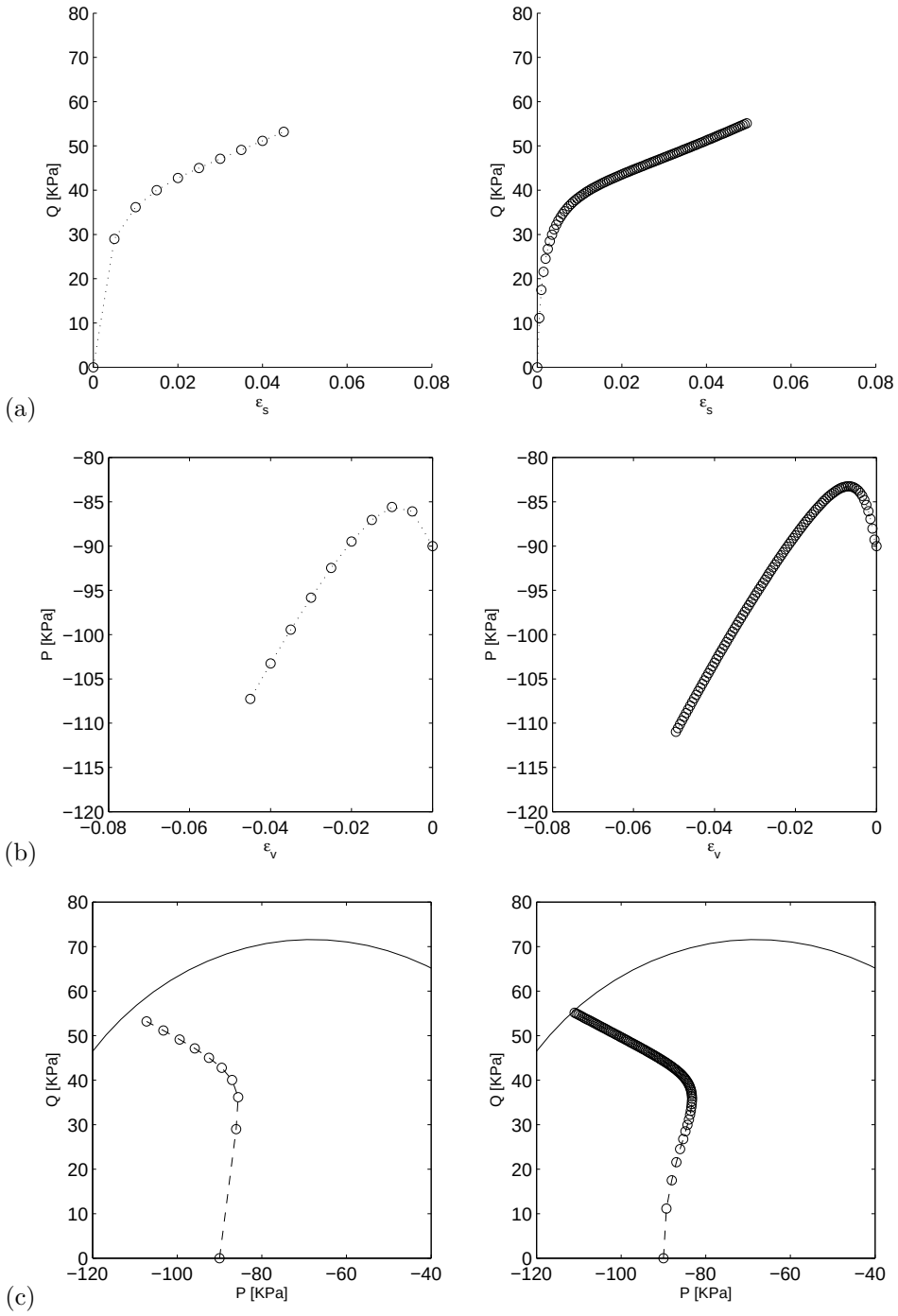

Figure 3-2: Convergence analysis with 10 increments (left) and 100 increments (right) imposing $\epsilon_v = -0.05$ and $\epsilon_s = 0.05$.

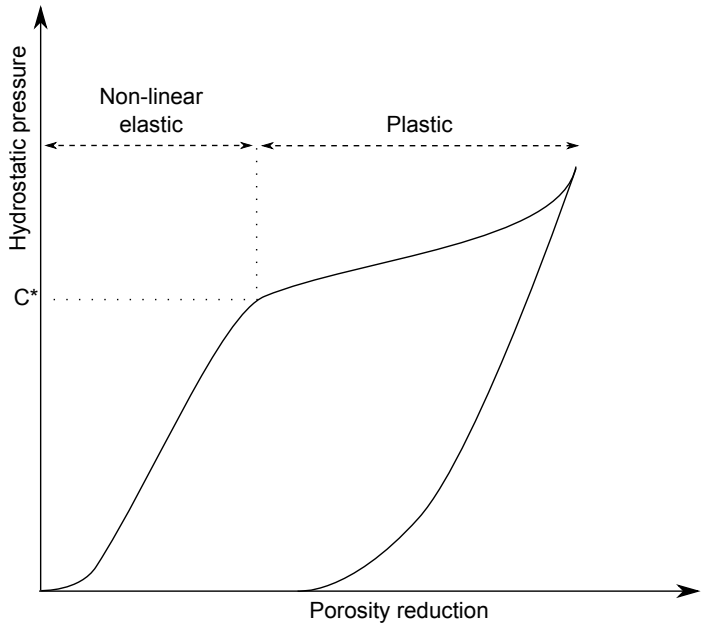

Figure 3-3: Hydrostatic pressure vs. volume strainvolume strain for high porosity rock.

load).

Under hydrostatic compression (53; 54; 55), the typical mechanical response for different sandstones of varying porosities is shown in fig. 3-3. Typically, the mechanical response of a porous sandstone is nonlinear, even in the elastic regime, specially for low pressure value. Initial compaction is associated with rearrangement of cement and loosely bonded grains, then it is associated with grain crushing, and the curve tends to be approximately linear. Note that, as the pore space is tightened by elastic deformation, the sample becomes progressively stiffer, as manifested by a decrease in compressibility. However, as the hydrostatic loading increases, the sample reaches a point where it suddenly becomes more compliant, showing a dramatic increase in compaction. After this point, corresponding to the grain crushing pressure, the rock experiences inelastic deformations, due to grain crashing and pore collapse. Finally, after a considerable amount of porosity has been crushed out, the rock begins to harden.

This inflection point occurs at a wide range of effective pressures, depending mainly on the porosity and average grain size (53). If a sample is loaded beyond this inflection point and then unloaded, the permanent compaction is significant, confirming the occurrence of inelastic deformation.

Under axisymmetric compression (56; 55) high porosity sandstones have two mainly different responses. When the confining pressure is relatively low, after volume compaction has been occurred, shear induced dilation is observed, and the specimen ultimately fail via shear localization. This behavior is common for most kind of geomaterials, and suggests the use of a shear yield surface, as Mohr-Coulomb or Drucker-Prager yield surface, or the one proposed by Rudnicki Rise (57). However, when the confining pressure is relatively high, the response is similar to the hydrostatic loading

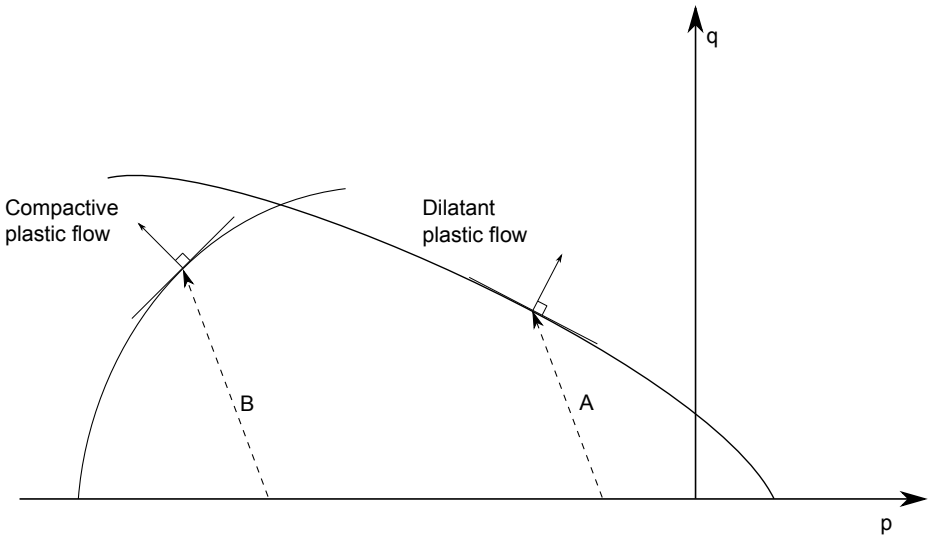

Figure 3-4: Two-yield surface model for high porosity rock. Loading path A (low confining pressure) intersects the shear yield surface, with negative slope. Loading path B (high confining pressure) intersects the cap yield surface, with positive slope. P: mean normal stress; Q: norm of second invariant of deviatoric stress.

previously described. The grain crushing begins at a lower mean stress, and a larger porosity reduction occurs for only a small increase in mean stress. This response is usually called *shear enhanced compaction* (56), and report a larger reduction in grain crushing pressure for smaller confining pressures. This behavior suggest the use of a cap yield surface, corresponding to compactive yield. Further, the defined cap may expand with porosity reduction.
In conclusion, loading path beginning at lower confining pressure leads to the shear yield surface, while loading path at higher confining pressure intersect the cap yield surface. These two different situations are shown schematically in Fig. 3-4.

The distinction between high and low confining pressure is far from trivial (2). Under axisymmetric compression at intermediate confining pressures, a transitional regime exist, where both yield surface (and consequently both damage mechanism) are active. The failure modes consist of compaction bands and/or shear bands. In this situation, the loading path intersects the yield surface in the vicinity of the region where the two yield surfaces would meet. Therefore it is proposed that the occurrence of two active damage mechanism, for loading in transitional regime, corresponds to activation of both the shear and cap surface.

Constitutive relations

As done for the Modified Cam-Clay model in the previous section, we describe the constitutive relations to take into account the mechanical behavior described so far. Again, a general elasto-plastic constitutive model is characterized bye the definition of the six following aspects.

1. *The free energy function*: most of the model developed for rocks assume linear elastic constitutive law, assuming bulk modulus and shear modulus constant.

   Experimental evidence, as reported briefly in previous section (2), show us that for rocks, as for most geomaterials, the response is non linear, even if elastic, especially for low level of the mean normal stress. The sample becomes stiffer as far as the hydrostatic pressure increase, suggesting a dependance of the bulk modulus from the applied pressure. The elastic shear modulus can be determined directly from the elastic bulk modulus through the assumption of a constant value of a Poisson's ratio, according to usual assumptions for clay (58), but this definition leads to a non-conservative nonlinear elasticity model in which energy may be extracted from unloading-reloading cycles (59). All these considerations suggest to use the same energy function as introduced for the Modified Cam Clay model in the previous section. This constitutive law well describes the elastic non linear behavior of rocks.

2. *The yield function*: as briefly summarized at the beginning of this section, depending on the confining pressure the rocks show two different plastic responses, mainly characterized by shear dilation or compaction. To describe this mechanical behavior two issues must be addressed: the shape of the initial yield surface and its evolution while accumulating plastic deformation. As far as the yield surface function(s), two possibilities are usually assumed (60): a single smooth yield surface or a multisurface, where two functions intersect in a vertex.

   As regard single surface model, they usually descend from the pioneering critical state model proposed by Schoefield and Wroth (61) for clay , employing an elliptical yield surface. Carroll (62) proposed a type of critical state plasticity model using a mobile parabolic yield surface. Grueschow and Rudnicki (63) proposed to describe compaction with the use of an elliptical yield surface, with varying axis. These models give good results as regard the compaction side, but usually they are coarse in reference to the dilatant side, due to the symmetry of the surface. Furthermore, non symmetric yield functions, as proposed for example for sand by Jefferies (64), require a more complex formulation, involving larger number of parameters arduous to be defined from laboratory test.

   On the other hand, the plastic surface can be described using two independent continuously differentiable yield functions, that intersects in a vertex. Usually these kind of models are based on the combination of a Mohr-Coulomb or Drucker-Prager yield surface in the zone of shear deformation and cap surfaces in the compaction zone. The most adopted was suggested by DiMaggio and Sandler (65), using an elliptical cap that intersect the shear-failure surface at the point of horizontal tangency to the ellipse. Since it's not required that the two functions intersect smoothly, the formulation is usually less complicated and fewer parameters are necessary.

   However, the weak point is now the lack of smooth transition between the two surfaces, and

therefore between the two plastic mechanism (66). The requirement that the cap surface intersect the shear surface at the point of horizontal tangency to the cap prevents pre-failure dilatant deformation, contradicting experimental observations. Furthermore, there is an indeterminacy of flow direction at the intersection point and the apex point produce an accumulation point in the solution of the stress-update algorithm.

To circumvent the shortcomings of the model described so far, we propose a yield surface which is characterized by two yield functions, but which intersect smoothly, resulting in a continuous surface. In doing so, we use a combined model based on a linear and an elliptical yield surface. The linear part of the yield surface $\mathscr{F}_1$ corresponds to shear failure zone and it is based on a Drucker-Prager formulation, which is a well-known and recognized model to describe shear deformation with dilatancy, supported by numerous experimental measurements for different kind of rocks

$$\mathscr{F}_1(P,Q) = Q - mP - c_0 = 0 \tag{3.68}$$

where m is the slope of the linear yield surface and c_0 is the intersection of the surface with the vertical axis, in a (P,Q) plot.

For the compaction failure zone, we suggest to use an elliptical yield surface $\mathscr{F}_2$, resembling the DiMaggio-Sandler failure envelope (65):

$$\mathscr{F}_2(P,Q,P_i) = B^2(P-P_i)^2 + A^2Q^2 - A^2B^2 = 0 \tag{3.69}$$

where A and B are respectively the minor and major semiaxis of the ellipse and P_i is the centroid. The intersection between the two surfaces is defined as the point in which $\mathscr{F}_1$ is tangent to $\mathscr{F}_2$, ensuring the two surfaces produce a unique surface without any angular point. The intersection point (P^*, Q^*) can be easily evaluated solving the equation

$$\frac{dQ(P^*)}{dP} = m \tag{3.70}$$

where

$$Q = \sqrt{B^2 - \frac{B^2}{A^2}(P-P_i)^2}. \tag{3.71}$$

The result of this equation reads

$$P^* = P_i \pm \frac{mA}{\sqrt{B^2/A^2 + m^2}}. \tag{3.72}$$

The intersection point lies always in the right part of the ellipse, then P^* must be greater then P_i and therefore only the solution with the sign "$-$" must be taken into account. Fig. 3-5 represents the two continuous yield surfaces, highlighting the principles parameters involved.

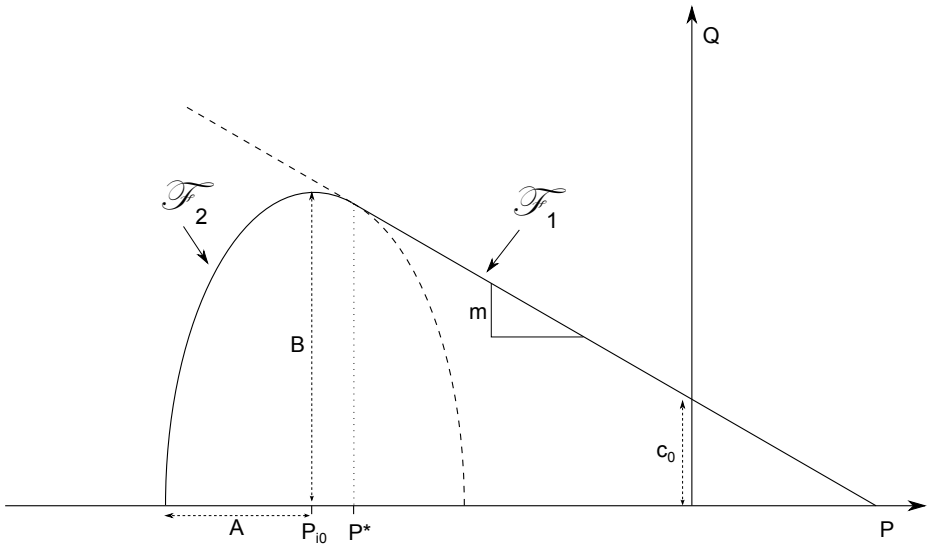

Figure 3-5: The two yield surfaces model. The elliptical yield surface is tangent to the linear surface in the point defined by (P^*, Q^*).

To the authors' knowledge, this formulation of the yield surface is new and improve the classical plastic cap model, ensuring a smooth surface.

3. *The hardening law*: once the initial yield surface has been defined, a central question to be answered is how the plastic surface evolve according to the accumulate plastic deformation. Experimental evidence shows that, after a significant amount of porosity has been crushed, the rock begins to harden. Once a considerable amount of porous has collapsed, the rock become almost incompressible, and the stress-strain curve in fig. 3-3 tends to assume an asymptotic vertical trend. Almost all the proposed model have two common features: (1) they assume the plastic yield behavior of the compactant rock is isotropic and (2) the strain hardening behavior is characterized by a yield function that depends solely on the plastic volumetric strain (3). Since plastic deformation of the solid grains can be considered negligible, the plastic volumetric strain can be assumed in first approximation as the plastic porosity change, and the expansion of the cap surface can be inferred mapping out contours in the stress space corresponding to specific value of porosity reduction.
   In this work, we propose that the elliptical surface can contract and expand according to the following criteria:

   (a) The width of the ellipse remain constant, i.e. $A = A_0$ where A_0 is the initial horizontal semi-axis of the ellipse. This approach is similar to what proposed by Carroll (62).

   (b) The elliptical surface can slide along the horizontal axis, remaining always tangent to the linear surface. This condition guarantees that the yield surface is always continuous. To

satisfy this condition, we impose that the vertical semi-axis varies according to

$$B = \sqrt{m^2 P_i^2 - A^2 m^2 + 2mc_0 P_i + c_0^2} \tag{3.73}$$

(c) The variation of P_i, i.e. the centroid of the ellipse, depends on the accumulated plastic volumetric strain according to

$$P_i = P_{i_0} \left(\frac{\epsilon^*}{\epsilon^* - \epsilon_v^p} \right)^r \tag{3.74}$$

where P_{i_0} is the initial value, ϵ^* is the volumetric deformation at ultimate compaction and r is the exponent that control the rate of volumetric hardening (67). This proposed hardening law is suggested by experimental evidence: as soon as the plastic volumetric deformation achieve a maximum value (corresponding to the collapse of the porous skeleton) the further plastic deformation can develop only in shear mode. This hyperbolic function reflects the presence of vertical tangent to curve in fig. 3-3.

Since the main emphasis in this work is made on the inelastic behavior of porous rocks during compaction, we assume that the linear surface remain fix throughout all the deformation process (perfect plasticity).

4. *The flow rule*: finally, we need to define how plastic strains evolve after the rock has yielded, i.e. define an appropriate plastic potential function. This issue is particular challenging to address, and there isn't a unique interpretation. The majority of authors assume the application of an associated flow rule, i.e. the yield surface is used as a potential surface. This, however, reduces the capabilities of the model, since the dilatancy coefficient is strictly related with the yield surface, which results in disagreement with experimental data. On the other hand, the use of a non associated flow rule gives more accurate description of the mechanism, but introduces new additional parameter in the formulation, and consequently requires additional measurements. In this work, we suggest to use for the linear side a potential function of the form

$$\bar{\mathscr{G}} = Q - \bar{m}P - \bar{c} = 0. \tag{3.75}$$

This non-associative law, assuming that $\bar{m} < m$, avoid the often excessive dilatancy predicted by the associative rule. The non-associative law is essentially obtained by adopting, as the flow potential, a Drucker–Prager yield function with the frictional angle replaced by a dilatancy angle.

For the cap side of the plastic surface we assume two flow rules, depending on the stress status. Let's introduce the point $(\tilde{P}, \tilde{Q})$ in which the plastic potential $\bar{\mathscr{G}}$ and the yield function $\mathscr{F}$ have

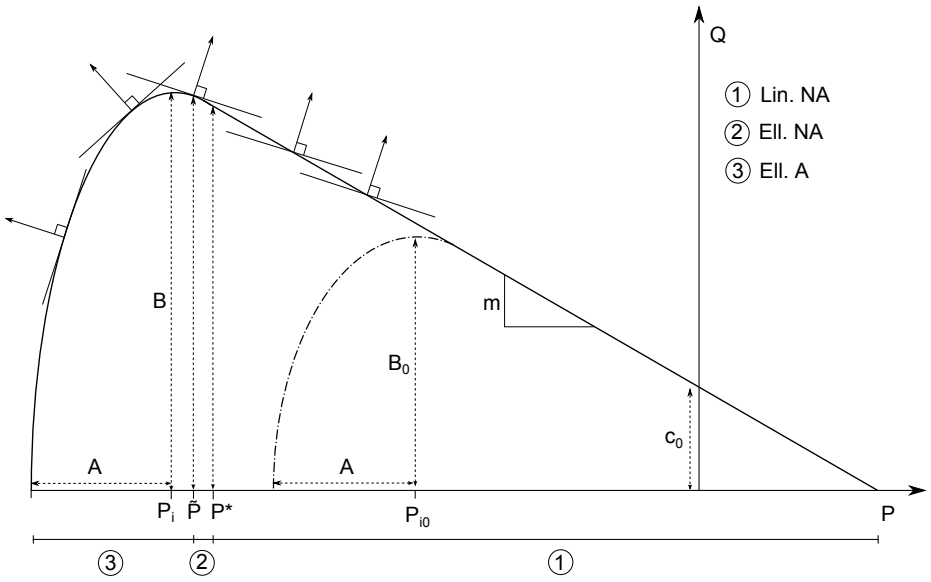

Figure 3-6: The two yield surfaces model

the same normal:

$$\frac{dQ(\tilde{P})}{dP} = \bar{m} \tag{3.76}$$

where Q has has been defined in (3.71). The result of this equation reads

$$\tilde{P} = P_i - \frac{\bar{m}A}{\sqrt{B^2/A^2 + \bar{m}^2}}. \tag{3.77}$$

Therefore, if $P < \tilde{P}$ we adopt an associative flow rule for the cap surface, otherwise, if $P > \tilde{P}$ we assume a non associative flow rule defined by the same plastic potential $\bar{\mathscr{G}}$.

This formulation ensures that along the complete yield surface there are no discontinuities with respect to flow vector, and therefore the transition from the dilatant to the compactive side is smooth, even in reference of the flow rule. Hence, with respect to the flow rule, we define three different regions of the plastic surface, depending on the yield function and the yield surface, as reported in fig. 3-6. The subdivision of the yield surface in these three different parts will be of central importance in the solution of the stress-update algorithm, as discussed in the next section.

5. *The K-K-T conditions*: the model has to fulfill the classical Karush-Kuhn-Tucker conditions as follows

$$\gamma \geq 0 \qquad \mathscr{F} \leq 0 \qquad \gamma\mathscr{F} = 0. \tag{3.78}$$

Description	Yield function $\mathscr{F}$	Plastic potential $\mathscr{G}$	Abbr.
Non-associative linear surface	$\mathscr{F}_1$	$\bar{\mathscr{G}}$	Lin. NA
Non-associative elliptical surface	$\mathscr{F}_2$	$\bar{\mathscr{G}}$	Ell. NA
Associative elliptical surface	$\mathscr{F}_2$	$\mathscr{F}_2$	Ell. A

Table 3.1: The three stress update algorithms

6. *The consistency conditions*: in case of plasticity, the following condition has to be satisfied

$$\gamma\dot{\mathscr{F}} = 0 \qquad \text{if} \qquad \mathscr{F} = 0. \tag{3.79}$$

Return Mapping algorithm and algorithmic tangent operator

Also for this set of equations it is possible to perform a fully implicit numerical integration, utilizing the same scheme performed in the strain invariant space (42), as done for the previous model. Again, it is assumed that the updated displacements are given, which implies that the elastic trial strain $\boldsymbol{\epsilon}^{e\,Tr}$ and the solution at time step t_n are known. The task is to compute the updated stress state $\boldsymbol{\beta}$ and the discrete plastic multiplier $\Delta\gamma$ for a given displacement increment. Consider the following local residual equations generated by the applied strain increment $\Delta\boldsymbol{\epsilon}$

$$\boldsymbol{r} = \boldsymbol{r}(\boldsymbol{x}) = \begin{Bmatrix} \epsilon_v^e - \epsilon_v^{e\,Tr} + \Delta\gamma\partial_P\mathscr{G} \\ \epsilon_s^e - \epsilon_s^{e\,Tr} + \Delta\gamma\partial_Q\mathscr{G} \\ \mathscr{F} \end{Bmatrix}; \qquad \boldsymbol{x} = \begin{Bmatrix} \epsilon_v^e \\ \epsilon_s^e \\ \Delta\gamma \end{Bmatrix}. \tag{3.80}$$

Note that now the function $\mathscr{G}$ appears in the set of equations instead of the th function $\mathscr{F}$. The aim is to dissipate the residual vector $\boldsymbol{r}$ by finding the solution vector $\boldsymbol{x}^*$ using a Newton's method, exactly as done before

$$\boldsymbol{x}^{k+1} = \boldsymbol{x}^k + \delta\boldsymbol{x}^k; \qquad -\boldsymbol{A}^k\delta\boldsymbol{x}^k = \boldsymbol{r}^k; \qquad \boldsymbol{A}^k = \frac{\partial\boldsymbol{r}^k}{\partial\boldsymbol{x}^k};\ k \leftarrow k+1, \tag{3.81}$$

where k plays the role of an iteration counter.
Depending on the loading path, different yield functions and plastic potential will be activated, in particular three different Return Mapping schemes need to be implemented, based on (3.80), and are summarized in the table 3.1.

A closed form expression for the consistent tangent operator $\boldsymbol{A}$ can be written for the three different set of nonlinear equations. The details can be found in appendix A. The question that need to be answered now is how to select the correct Return Mapping algorithm, above the three

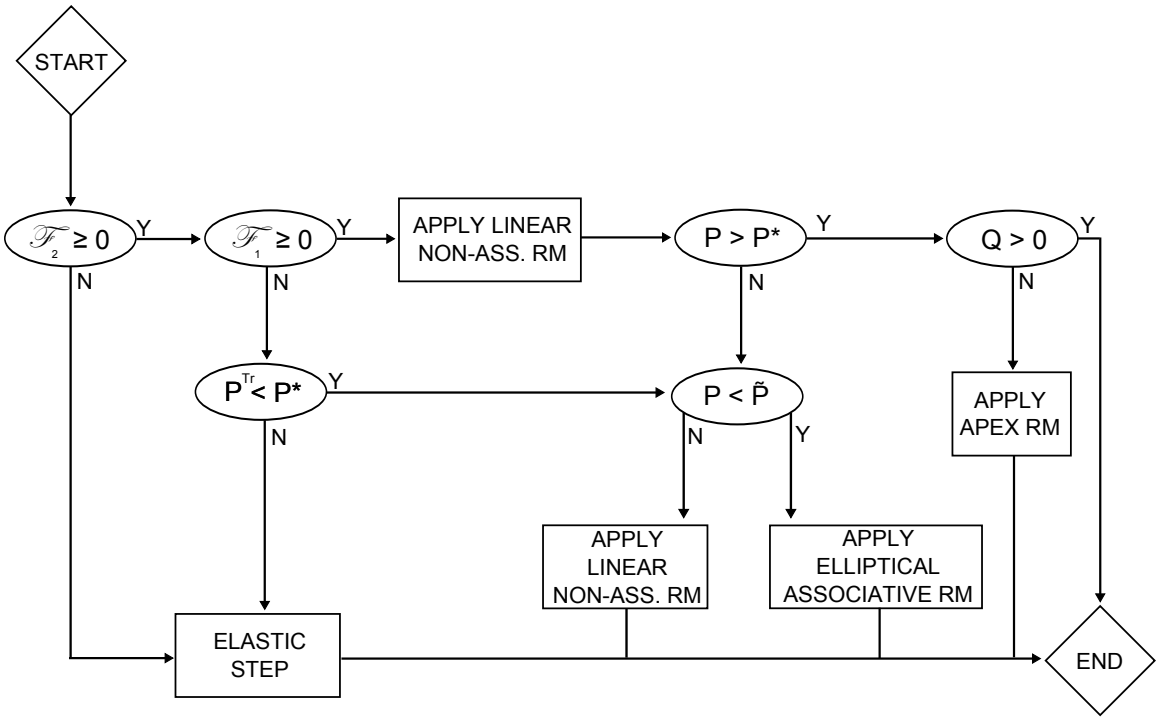

Figure 3-7: Algorithm for selection of the correct Return-Mapping algorithm.

presented, that fully satisfies the plastic consistency condition, for a given elastic trial state. In other words, it's necessary a procedure to identify which yield and potential functions are activated. The summary of a possible selection algorithm is shown in the flowchart of fig. 3-7.

If the elliptical surface is activated, then at every iteration the value of P_i need to be updated, according to (3.74). The current value of the volumetric plastic strain ϵ_v^e can be easily computed assuming the additive decomposition of the logarithmic strains

$$\epsilon_v = \epsilon_v^e + \epsilon_v^p = \epsilon_v^{e\,Tr} + \epsilon_{v,n}^p, \tag{3.82}$$

where $\epsilon_{v,n}^p$ is the plastic volumetric deformation at time step t_n.

As shown in fig. 3-6, the linear yield surface and the plastic potential functions create corners on the dilatant side of the hydrostatic axis. In this case, i.e. when the return mapping on the linear surface gives as result a negative value of Q, a standard procedure for apex formulation need to be implemented. The author can refer to (68) for further details.
Again, as done for the hyperelastic counterpart, we want to obtain the following 3×3 material tangent stiffness matrix necessary in (3.36), according to the procedure developed so far, in order to solve typical nonlinear boundary-value problems

$$\boldsymbol{a} = \frac{\partial \boldsymbol{\beta}}{\partial \boldsymbol{\epsilon}^{e\,Tr}} \tag{3.83}$$

.

Again, we can use the same structure derived for the Cam Caly model. Therefore, the task consists simply in computing the following consistent tangent operator

$$\boldsymbol{a}^{ep} = \left(D_{11}^{ep} - \frac{2Q}{9\epsilon_s^{e\,Tr}} \right) \boldsymbol{\delta} \otimes \boldsymbol{\delta} + \sqrt{\frac{2}{3}} D_{12}^{ep} (\boldsymbol{\delta} \otimes \hat{\boldsymbol{n}}) + \sqrt{\frac{2}{3}} D_{21}^{ep} (\hat{\boldsymbol{n}} \otimes \boldsymbol{\delta}) + \frac{2Q}{3\epsilon_s^{e\,Tr}} (\boldsymbol{I} - \hat{\boldsymbol{n}} \otimes \hat{\boldsymbol{n}}) + \frac{2}{3} D_{22}^{ep} \hat{\boldsymbol{n}} \otimes \hat{\boldsymbol{n}}, \quad (3.84)$$

where the coefficients of operator $\boldsymbol{a}^{ep}$ depends on the return mapping algorithm adopted, through the operator $\boldsymbol{D}^p$, i.e. on the form of the functions $\mathscr{F}$ and $\mathscr{G}$. For detailed results, the reader should refer to Appendix A for close formulation.
Note that eq. (3.84) is valid both for elastic and elasto-plastic loading. In fact, for elastic loading $\boldsymbol{D}^p = \boldsymbol{I}$ and $\boldsymbol{D}^{ep} = \boldsymbol{D}^e$ and so (3.84) reduces to the tangential elasticity matrix.

The complete procedure to compute the update state of stress and the tangent operator is summarized in the following box.

1. Elastic deformation predictor: $\boldsymbol{b}^{e\,Tr} = \boldsymbol{f}_{n+1} \cdot \boldsymbol{b}_n^e \cdot \boldsymbol{f}_{n+1}^t$.

2. Spectral decomposition: $\boldsymbol{b}^{e\,Tr} = \sum_{A=1}^{3} (\lambda_A^{e\,Tr})^2 \boldsymbol{n}^{Tr\,(A)} \otimes \boldsymbol{n}^{Tr\,(A)}$.

3. Principal elastic logarithmic strains: $\epsilon_A^{Tr} = \ln(\lambda_A^{e\,Tr})$.

4. Deformation invariants $\epsilon_v^{e\,Tr}$ and $\epsilon_s^{e\,Tr}$ according to eq. (3.42).

5. Elastic stress predictor P^{Tr} and Q^{Tr} according to eq. (3.47).

6. Check if yielding: $\mathscr{F}_2(P^{Tr}, Q^{Tr}, P_{i,n}) \geq 0$?
   No: elastic step, go to (9.). Yes: continue.

7. Check if yielding $\mathscr{F}_1(P^{Tr}, Q^{Tr}) \geq 0$?

   (a) Yes: Linear yield surface. Solve *Lin. NA*, compute $\epsilon_v^e, \epsilon_s^e, \Delta\gamma$ and set $P_i = P_{i,n}$.

   - Check correctness of algorithm: $P \geq P^*$?
     No: elliptical yield surface, go to (8.). Yes: continue.
   - Check cone apex: $Q \geq 0$?
     No: non valid algorithm, stop. Yes: correct, go to (10.).

   (b) No: check plastic point: $P^{Tr} \leq P^*$?
   No: elastic step, go to (9.). Yes: continue.

8. Elliptical yield surface.

   - For every iteration k check: $P \leq \tilde{P}$?
     No: Solve *Ell. NA*. Yes: Solve *Ell. A*.
   - Update P_i according to eq. (3.82) and eq. (3.74).
   - Compute ϵ_v^e, ϵ_s^e, $\Delta\gamma$
     . Compute elastoplastic stress-strain matrix $\boldsymbol{a}^{ep}$. Go to (10.).

9. Elastic step. Set $(\epsilon_v^e, \epsilon_s^e) = (\epsilon_v^{e\,Tr}, \epsilon_s^{e\,Tr})$, $P_i = P_{i,n}$ and $(P, Q) = (P^{Tr}, Q^{Tr})$. Compute elastic stress-strain matrix $\boldsymbol{a}^e$

10. Principal elastic logarithmic strain (ϵ_A^e) and principal Kirchhoff tension β_A.

11. Updated left elastic Cauchy-Green tensor and Kirchhoff stress tensor:
    $\boldsymbol{b^e} = \sum_{A=1}^{3} (\exp(\epsilon_A^e))^2 \boldsymbol{n}^{Tr\,(A)} \otimes \boldsymbol{n}^{Tr\,(A)}$ and $\boldsymbol{\tau} = \sum_{A=1}^{3} \beta_A \boldsymbol{n}^{Tr\,(A)} \otimes \boldsymbol{n}^{Tr\,(A)}$

Numerical code

In this section we present in detail the function `tensCCDP`, which implements the constitutive equations of the elastoplastic model presented so far.
The main function is reported in the following box.

```
function [tenspr,epse,epspv,aep,flag] = tensCCDP(Ge,defepr,epspvn)
%-------------------------------------------------------
% tensCCDP:
%   Compute the Kirchhoff principal tension according to Cap Continuos yield criterion.
%
% Syntax:
%   function [tenspr,P,Q,epse,epspv,aep,flag] = tensCCDP(Ge,defepr,epspvn,ip)
%
% Input:
% Ge      : Material property.
% defepr  : Elastic principal deformation.
% epspvn  : Platic volumetric strain at step n.
%
% Output:
% tenspr  : Vector of Kirchhoff principal tension. [beta(1) beta(2) beta (3)]'
% epse    : Vector of elastic principal strain. [epse(1) epse(2) epse (3)]'
% epspv   : Platic volumetric strain at step n+1.
% aep     : Algorithmic stress-strain matrix in pr direction (a_AB).
% flag    : Flag for plasticity.
%
% Date:
%   Version 1.0   25.10.13
%
% Created by: Nicolo' Spiezia
%-------------------------------------------------------

% Initialize vector
imax = 20;
toll = 10e-6;

tenspr = zeros(3,1);
epse = zeros(3,1);
NORMErec = zeros(imax,1);

% Set isotropic elasto-plastic parameter

mu0  = Ge(2);
alfa = Ge(3);
kappa = Ge(4);
m = Ge(5);
P0 = Ge(6);
Pi0 = Ge(7);
epsev0 = Ge(8);
A = Ge(9);
c0 = Ge(10);
```

```
46  pp = Ge(11);
47  epstar = Ge(12);
48  mbar = Ge(13);
49
50
51 % Compute volumetric trial strain
52  epsevTR = defepr(1,1)+defepr(2,1)+defepr(3,1);
53
54 % Compute deviatoric trial strain
55
56  epsedev(:,1) = defepr(:,1)-epsevTR/3;
57  epsesTR = sqrt(2/3)*norm(epsedev);
58
59 % Compute TRial stress
60
61  if epspvn<=0;
62  Pin = Pi0*(epstar/(epstar-epspvn))^pp;
63  else
64  Pin = Pi0;
65  end
66
67  [Ptr,Qtr] = PQ( epsevTR, epsesTR, P0, alfa, kappa, epsev0, mu0);
68
69  flag = 0;
70
71 % Compute trial yield surface
72
73          % CC yield surface
74          B2 = m^2*Pin^2-m^2*A^2+2*m*c0*Pin+c0^2;
75          F1tr = B2*(Ptr-Pin)^2+(A^2)*(Qtr^2)-(A^2)*B2;
76
77          % DP yield surface
78          F2tr = Qtr-m*Ptr-c0;
79
80          % Intersection CC/DP
81          a = Ge(9);
82          b = sqrt(m^2*Pin^2-m^2*A^2+2*m*c0*Pin+c0^2);
83          pstar = Pin-(m*a*b)/(sqrt((b^4/a^2)+m^2*b^2));
84
85   % Check for plasticity
86
87     if F1tr > toll
88
89          if F2tr > toll
90          flag = 1;
91          surf = 2;
92
93          Pi = Pin;
94
95          % !------------ Linear RM --------------!
96
97                          % Inizialize variables
98              x = zeros(3,1);
99              x(1,1) = epsevTR;    % epsev
```

```
100             x(2,1) = epsesTR;    % epses
101             x(3,1) = 0;          % dgamma
102
103
104             P = Ptr;
105             Q = Qtr;
106
107             for iter = 1:imax
108
109                 % evaluate residual
110
111                 F = Q-m*P-c0;
112
113                 dPG = -mbar;
114                 dQG = 1;
115
116                 r = [x(1) - epsevTR+x(3)*dPG
117                       x(2) - epsesTR+x(3)*dQG
118                             F                 ];
119
120                    if iter == 1
121                    r0 = norm(r);
122                    end
123
124                 NORMErec(iter) = norm(r)/norm(r0);
125
126                 % check for convergence
127                 if norm(r) < toll*r0
128
129                     break
130                 else
131
132                     % evaluate tangent matrix
133                 Atang = AtangDP( x(1,1),x(2,1),P,kappa,mu0,alfa,P0,epsev0,m,mbar);
134
135                     % solve for displacement increment
136                     dx = - (Atang\r);
137
138                     x = x + dx;
139
140                     % Update
141
142                     [P,Q]=PQ(x(1,1),x(2,1),P0,alfa,kappa,epsev0,mu0);
143
144                     epspv = epsevTR-x(1,1)+epspvn;
145
146
147
148                 end
149             end
150
151                 if iter == imax
152                 fprintf('No convergence of RM')
153                 end
```

```
154
155
156         %Update variable
157         epsev = x(1,1);
158         epses = x(2,1);
159         dgamma = x(3,1);
160
161         % Compute matrix Dep for linear non-associative
162
163        Dep = DEPtensDP( epsev,epses,P,kappa,mu0,alfa,P0,epsev0,m,mbar);
164         % !---------------------------------------------!
165
166                 % Check for correct surface
167                 B2 = m^2*Pin^2-m^2*A^2+2*m*c0*Pin+c0^2;
168                 F1 = B2*(P-Pin)^2+(A^2)*(Q^2)-(A^2)*B2;
169
170
171
172                 if F1 > toll && P < pstar
173                    surf = 1; % Goto elliptical surface
174                 end
175
176         else
177             if Ptr<pstar
178             flag = 1;
179             surf = 1;
180             end
181
182         end
183
184     end
185
186
187     if flag ==1 && surf == 1
188         % !-------------------- elliptical RM ----------------------!
189             flag = 2;
190
191             % Inizialize variables
192             x = zeros(3,1);
193             x(1,1) = epsevTR;    % epsev
194             x(2,1) = epsesTR;    % epses
195             x(3,1) = 0;          % dgamma
196
197             Pi = Pin;
198             P = Ptr;
199             Q = Qtr;
200
201             for iter = 1:imax
202
203                 b = sqrt(m^2*Pi^2-m^2*A^2+2*m*c0*Pi+c0^2);
204                 ptilde = Pi-(mbar*A*b)/(sqrt((b^4/A^2)+mbar^2*b^2));
205
206                 % evaluate residual
207                 B2 = m^2*Pi^2-m^2*A^2+2*m*c0*Pi+c0^2;
```

```
208
209                 F = B2*(P-Pi)^2+(A*Q)^2-B2*A^2;
210
211                 if P < ptilde  % Associative RM1
212                 RM = 1;
213
214                 dPF = 2*B2*(P-Pi);
215                 dQF = 2*(A^2)*Q;
216
217                 r = [x(1) - epsevTR+x(3)*dPF
218                      x(2) - epsesTR+x(3)*dQF
219                             F                 ];
220
221                    if iter == 1
222                    r0 = norm(r);
223                    end
224
225                 NORMErec(iter) = norm(r)/norm(r0);
226
227                 % check for convergence
228                 if norm(r) < toll*r0
229
230                     break
231                 else
232
233                     % evaluate tangent matrix
234                 Atang = AtangCC( x(1,1),x(2,1),x(3,1),P,Q,Pi,kappa,mu0,...
235                        alfa,P0,epsev0,pp,Pi0,epstar,A,B2,m,c0,epspvn,epsevTR);
236
237                     % solve for displacement increment
238                     dx = - (Atang\r);
239
240                     x = x + dx;
241                 end
242
243
244                 else   % Non Associative RM2
245                 RM = 2;
246
247                 dPG = -mbar;
248                 dQG = 1;
249
250                 r = [x(1) - epsevTR+x(3)*dPG
251                      x(2) - epsesTR+x(3)*dQG
252                             F                 ];
253
254                    if iter == 1
255                    r0 = norm(r);
256                    end
257
258                 NORMErec(iter) = norm(r)/norm(r0);
259
260                 % check for convergence
261                 if norm(r) < toll*r0
```

```
262
263                     break
264                 else
265
266                     % evaluate tangent matrix
267                 Atang = AtangDPCC( x(1,1),x(2,1),P,Q,Pi,kappa,mu0,...
268                 alfa,P0,epsev0,pp,Pi0,epstar,A,B2,m,mbar,c0,epspvn,epsevTR);
269
270                     % solve for displacement increment
271                     dx = - (Atang\r);
272
273                     x = x + dx;
274
275                 end
276                 end
277                 % Update
278
279                     [P,Q]=PQ(x(1,1),x(2,1),P0,alfa,kappa,epsev0,mu0);
280
281                     epspv = epsevTR-x(1,1)+epspvn;
282
283
284                     Pi = Pi0*(epstar/(epstar-epspv))^pp;
285
286             end
287
288             if iter == imax
289                 fprintf('No convergence of RM')
290             end
291
292
293         %Update variable
294         epsev = x(1,1);
295         epses = x(2,1);
296         dgamma = x(3,1);
297
298         % Compute matrix Dep
299         if RM == 1;
300         Dep = DEPtensCC( epsev,epses,dgamma,P,Q,Pi,kappa,mu0,alfa,...
301                         P0,epsev0,pp,Pi0,epstar,A,B2,m,c0,epspvn,epsevTR);
302         flag = 22;
303         else
304         Dep = DEPtensDPCC( epsev,epses,P,Q,Pi,kappa,mu0,alfa,...
305                         P0,epsev0,pp,Pi0,epstar,A,B2,m,mbar,c0,epspvn,epsevTR);
306         flag = 21;
307         end
308         % !---------------------------------------------------------!
309
310     end
311
312      if flag == 0 % ELASTIC STEP
313
314
315       %Update variable
```

```
316       epsev = epsevTR;
317       epses = epsesTR;
318
319       Pi= Pin;
320       P = Ptr;
321       Q = Qtr;
322       epspv = epspvn;
323
324       % Compute matrix De
325
326       De = DEtens(epsev,epses,P,kappa,mu0,alfa,P0,epsev0);
327
328       Dep = De;
329
330     end
331
332  % Compute vector n
333
334  n(:,1) = epsedev(:,1)/ norm(epsedev);
335
336  % Compute principal Kirchhoff tension
337
338  tenspr(:,1) = P*ones(3,1)+ sqrt(2/3)*Q*n(:,1);
339
340  % Compute principal elastic strain
341
342  epse(:,1) = (1/3)*epsev*ones(3,1)+ sqrt(3/2)*epses*n(:,1);
343
344  % Compute algorithmic stress-strain in principal direction
345
346
347  aep = (Dep(1,1)-2*Q/(9*epsesTR))*ones(3,1)*ones(3,1)'+...
348           sqrt(2/3)*Dep(1,2)*ones(3,1)*n(:,1)'+...
349           sqrt(2/3)*Dep(2,1)*n(:,1)*ones(3,1)'+...
350          ((2*Q)/(3*epsesTR))*(eye(3)-n(:,1)*n(:,1)')+...
351          (2/3)*Dep(2,2)*n(:,1)*n(:,1)';
352
353  end
354  end
```

Depending on the plastic mechanism, the operator $\boldsymbol{A}$, necessary to solve the non-linear set of equations of the Return Mapping algorithm, is computed by different functions `Atang`, which are reported in the following three boxes.

```
1  function Atang = AtangDP( epsev,epses,P,kappa,mu0,alfa,P0,epsev0,m,mbar)
2
3  % AtangDP Compute tangent for NR iteration for
4  % linear non associative Return Mapping
5
6  % Inizialize matrices
7  [De] = deal(zeros(2));
```

```
8
9  % Compute parameter
10 OMEGA = -(epsev-epsev0)/kappa;
11 mue = mu0+(alfa/kappa)*(-P0*kappa*exp(OMEGA));
12
13 Kp = 0;
14
15 % Compute derivative of Yield Function
16 dPF = -m;
17 dQF = 1;
18 dPiF = 0;
19
20 % Compute derivative of Plastic potential
21 dPG = -mbar;
22 dQG = 1;
23
24 % Compute matrix D
25
26 De(1,1) = -P/kappa;
27 De(2,2)= 3*mue;
28 De(1,2)= (3*P0*alfa*epses/kappa)*exp(OMEGA);
29 De(2,1)= (3*P0*alfa*epses/kappa)*exp(OMEGA);
30
31
32
33 % Compute matrix A
34
35 Atang = [                    1                    0                                   dPG
36                              0                    1                                   dQG
37           De(1,1)*dPF+De(2,1)*dQF+Kp*dPiF    De(1,2)*dPF+De(2,2)*dQF      0     ];
38
39 end
```

```
1  function Atang = AtangCC( epsev,epses,dgamma,P,Q,Pi,kappa,mu0,...
2                     alfa,P0,epsev0,pp,Pi0,epstar,A,B2,m,c0,epspvn,epsevTR)
3
4  % AtangCC Compute tangent for NR iteration for elliptical Return Mapping
5
6  % Inizialize matrices
7  [De] = deal(zeros(2));
8
9  % Compute parameter
10 OMEGA = -(epsev-epsev0)/kappa;
11 mue = mu0+(alfa/kappa)*(-P0*kappa*exp(OMEGA));
12
13 Kp = pp*Pi0*((epstar/(epstar-epsevTR+epsev-epspvn))^(pp-1))*...
14                    (-epstar/(epstar-epsevTR+epsev-epspvn)^2);
15
16 % Compute derivative of Yield Function
17 dPF = 2*B2*(P-Pi);
18 dQF = 2*(A^2)*Q;
19 dPiF = (2*Pi*m^2+2*m*c0)*((P-Pi)^2-A^2)+B2*2*(P-Pi)*(-1);
```

```
20
21  dPPF = 2*B2;
22  dQQF = 2*(A^2);
23  dPQF = 0;
24
25  dPPiF = 2*((2*Pi*m^2+2*m*c0)*(P-Pi)-B2);
26  dQPiF = 0;
27
28  % Compute matrix D
29
30  De(1,1) = -P/kappa;
31  De(2,2)= 3*mue;
32  De(1,2)= (3*P0*alfa*epses/kappa)*exp(OMEGA);
33  De(2,1)= (3*P0*alfa*epses/kappa)*exp(OMEGA);
34
35  % Compute matrix H
36
37  H = [ dPPF   dPQF
38        dPQF   dQQF];
39
40  % Compute matrix G
41
42  G = H*De;
43
44  % Compute matrix A
45
46  Atang = [    1+dgamma*(G(1,1)+Kp*dPPiF)          dgamma*G(1,2)          dPF
47                 dgamma*(G(2,1)+Kp*dQPiF)          1+dgamma*G(2,2)        dQF
48             De(1,1)*dPF+De(2,1)*dQF+Kp*dPiF   De(1,2)*dPF+De(2,2)*dQF     0    ];
49
50  end
```

```
1   function Atang = AtangDPCC( epsev,epses,P,Q,Pi,kappa,mu0,alfa,P0,...
2                       epsev0,pp,Pi0,epstar,A,B2,m,mbar,c0,epspvn,epsevTR)
3
4   % AtangDPCC Compute tangent for NR iteration
5   % for linear associative Return Mapping
6
7   % Inizialize matrices
8   [De] = deal(zeros(2));
9
10  % Compute parameter
11  OMEGA = -(epsev-epsev0)/kappa;
12  mue = mu0+(alfa/kappa)*(-P0*kappa*exp(OMEGA));
13
14  Kp = pp*Pi0*((epstar/(epstar-epsevTR+epsev-epspvn))^(pp-1))*...
15                      (-epstar/(epstar-epsevTR+epsev-epspvn)^2);
16
17  % Compute derivative of Yield Function
18  dPF = 2*B2*(P-Pi);
19  dQF = 2*(A^2)*Q;
20  dPiF = (2*Pi*m^2+2*m*c0)*((P-Pi)^2-A^2)+B2*2*(P-Pi)*(-1);
```

```
21
22
23 % Compute derivative of Plastic potential
24 dPG = -mbar;
25 dQG = 1;
26
27 % Compute matrix D
28
29 De(1,1) = -P/kappa;
30 De(2,2)= 3*mue;
31 De(1,2)= (3*P0*alfa*epses/kappa)*exp(OMEGA);
32 De(2,1)= (3*P0*alfa*epses/kappa)*exp(OMEGA);
33
34 % Compute matrix A
35
36 Atang = [    1                                  0                                  dPG
37              0                                  1                                  dQG
38           De(1,1)*dPF+De(2,1)*dQF+Kp*dPiF    De(1,2)*dPF+De(2,2)*dQF    0    ];
39
40 end
```

The stress-strain tensor $\boldsymbol{a}^e$ or $\boldsymbol{a}^{ep}$ is computed by the fucntion `tensCCDP` via the operator $\boldsymbol{D}_e$ and $\boldsymbol{D}_{ep}$, which are computed by the functions `DEtens` and `DEPtens`. Depending on the plastic mechanism, and therefore the Return Mapping scheme, three different operator $\boldsymbol{D}_{ep}$ are needed, which are reported in the following three boxes

```
1  function Dep = DEPtensCC(epsev,epses,dgamma,P,Q,Pi,kappa,mu0,...
2                  alfa,P0,epsev0,pp,Pi0,epstar,A,B2,m,c0,epspvn,epsevTR)
3 %-------------------------------------------------------
4 % DEPtens: compute matrix Dep for associative elliptical surface
5 %
6 % Date: 29/10/2013
7 %   Version 1.0
8 %
9 % Created by: Nicolo' Spiezia
10 %-------------------------------------------------------
11 % Inizialize matrices
12 [De,b,Dp] = deal(zeros(2));
13
14 % Compute parameter
15 OMEGA = -(epsev-epsev0)/kappa;
16 mue = mu0+(alfa/kappa)*(-P0*kappa*exp(OMEGA));
17
18 Kp = pp*Pi0*((epstar/(epstar-epsevTR+epsev-epspvn))^(pp-1))*...
19                  (-epstar/(epstar-epsevTR+epsev-epspvn)^2);
20
21 KpTR = pp*Pi0*((epstar/(epstar-epsevTR+epsev-epspvn))^(pp-1))*...
22                  (epstar/(epstar-epsevTR+epsev-epspvn)^2);
23
24 % Compute derivative of Yield Function
25 dPF = 2*(B2)*(P-Pi);
```

```
dQF = 2*(A^2)*Q;
dPiF = (2*m^2*Pi+2*m*c0)*((P-Pi)^2-A^2)+B2*2*(P-Pi)*(-1);

dPPF = 2*B2;
dQQF = 2*(A^2);
dPQF = 0;

dPPiF = 2*((2*m^2*Pi+2*m*c0)*(P-Pi)-B2);
dQPiF = 0;

% Compute matrix D

De(1,1) = -P/kappa;
De(2,2)= 3*mue;
De(1,2)= (3*P0*alfa*epses/kappa)*exp(OMEGA);
De(2,1)= (3*P0*alfa*epses/kappa)*exp(OMEGA);

% Compute matrix H

H = [ dPPF   dPQF
      dPQF   dQQF];

% Compute matrix G

G = H*De;

% Compute matrix b

b(1,1) = 1+dgamma*(G(1,1)+Kp*dPPiF);
b(1,2) = dgamma*G(1,2);
b(2,1) = dgamma*(G(2,1)+Kp*dQPiF);
b(2,2) = 1+dgamma*G(2,2);

% Compute parameters

c1 = 1-dgamma*KpTR*dPPiF;
c2 = -dgamma*KpTR*dQPiF;

d1 = De(1,1)*dPF+De(2,1)*dQF+Kp*dPiF;
d2 = De(1,2)*dPF+De(2,2)*dQF;

e = d1*(b(2,2)*dPF-b(1,2)*dQF)+d2*(b(1,1)*dQF-b(2,1)*dPF);

a1 = (d1*(b(2,2)*c1-b(1,2)*c2)+d2*(b(1,1)*c2-b(2,1)*c1)+det(b)*KpTR*dPiF)/e;
a2 = sqrt(2/3)*(d2*b(1,1)-d1*b(1,2))/e;

% Compute matrix Dp

Dp(1,1)= b(2,2)*(c1-a1*dPF)-b(1,2)*(c2-a1*dQF);
Dp(1,2)= b(1,2)*(-1+sqrt(3/2)*a2*dQF)-sqrt(3/2)*b(2,2)*a2*dPF;
Dp(2,1)= b(1,1)*(c2-a1*dQF)-b(2,1)*(c1-a1*dPF);
Dp(2,2)= b(1,1)*(1-sqrt(3/2)*a2*dQF)+sqrt(3/2)*b(2,1)*a2*dPF;

Dp = Dp/det(b);
```

```
80
81 % Compute matrix Dep
82
83 Dep = De*Dp;
84
85 end
```

```
1  function Dep = DEPtensDP( epsev,epses,P,kappa,mu0,alfa,P0,epsev0,m,mbar)
2  %-------------------------------------------------------
3  % DEPtensDP: compute matrix Dep for linear non-associative surface
4  %
5  % Date: 14/01/2014
6  %   Version 1.0
7  %
8  % Created by: Nicolo' Spiezia
9  %-------------------------------------------------------
10 % Inizialize matrices
11 [De,Dp] = deal(zeros(2));
12
13 % Compute parameter
14 OMEGA = -(epsev-epsev0)/kappa;
15 mue = mu0+(alfa/kappa)*(-P0*kappa*exp(OMEGA));
16
17 % Compute derivative of Yield Function
18 dPF = -m;
19 dQF = 1;
20
21 % Compute derivative of Plastic potential
22 dPG = -mbar;
23 dQG = 1;
24
25 % Compute matrix D
26
27 De(1,1) = -P/kappa;
28 De(2,2)= 3*mue;
29 De(1,2)= (3*P0*alfa*epses/kappa)*exp(OMEGA);
30 De(2,1)= (3*P0*alfa*epses/kappa)*exp(OMEGA);
31
32 % Compute parameters
33
34 d1 = De(1,1)*dPF+De(2,1)*dQF;
35 d2 = De(1,2)*dPF+De(2,2)*dQF;
36
37 e = d1*dPG+d2*dQG;
38
39 a1 = d1/e;
40 a2 = d2/e;
41
42 % Compute matrix Dp
43
44 Dp(1,1)= 1-a1*dPG;
45 Dp(1,2)= -a2*dPG;
```

```
Dp(2,1)= -a1*dQG;
Dp(2,2)= 1-a2*dQG;

% Compute matrix Dep

Dep = De*Dp;

end
```

```
function Dep = DEPtensDPCC( epsev,epses,P,Q,Pi,kappa,mu0,alfa,...
                  P0,epsev0,pp,Pi0,epstar,A,B2,m,mbar,c0,epspvn,epsevTR)
%-----------------------------------------------------------
% DEPtensDPCC: compute matrix Dep feo linear associative surface
%
% Date: 29/10/2013
%   Version 1.0
%
% Created by: Nicolo' Spiezia
%-----------------------------------------------------------
% Inizialize matrices
[De,Dp] = deal(zeros(2));

% Compute parameter
OMEGA = -(epsev-epsev0)/kappa;
mue = mu0+(alfa/kappa)*(-P0*kappa*exp(OMEGA));

Kp = pp*Pi0*((epstar/(epstar-epsevTR+epsev-epspvn))^(pp-1))*...
                  (-epstar/(epstar-epsevTR+epsev-epspvn)^2);

KpTR = pp*Pi0*((epstar/(epstar-epsevTR+epsev-epspvn))^(pp-1))*...
     (epstar/(epstar-epsevTR+epsev-epspvn)^2);

% Compute derivative of Yield Function
dPF = 2*(B2)*(P-Pi);
dQF = 2*(A^2)*Q;
dPiF = (2*m^2*Pi+2*m*c0)*((P-Pi)^2-A^2)+B2*2*(P-Pi)*(-1);

% Compute derivative of Plastic potential
dPG = -mbar;
dQG = 1;

% Compute matrix D

De(1,1) = -P/kappa;
De(2,2)= 3*mue;
De(1,2)= (3*P0*alfa*epses/kappa)*exp(OMEGA);
De(2,1)= (3*P0*alfa*epses/kappa)*exp(OMEGA);

% Compute parameters

d1 = De(1,1)*dPF+De(2,1)*dQF+Kp*dPiF;
d2 = De(1,2)*dPF+De(2,2)*dQF;
```

```
44
45  e = d1*dPG+d2*dQG;
46
47  a1 = (d1+KpTR*dPiF)/e;
48  a2 = d2/e;
49
50  % Compute matrix Dp
51
52  Dp(1,1)= 1-a1*dPG;
53  Dp(1,2)= -a2*dPG;
54  Dp(2,1)= -a1*dQG;
55  Dp(2,2)= 1-a2*dQG;
56
57  % Compute matrix Dep
58
59  Dep = De*Dp;
60
61  end
```

3.3 Constitutive law for the fluid phase

We now consider the fluid flow problem and discuss a constitutive law as we developed for the solid phase. Assuming laminar flow, we can adopt the generalized Darcy's law to obtain the following linear constitutive equation

$$\bar{\boldsymbol{v}} = -\boldsymbol{k} \cdot \text{grad}(\Pi), \tag{3.85}$$

where $\boldsymbol{k}$ is the second-order permeability tensor and Π is the fluid potential. The negative sign in Eq. (3.88) implies that the fluid always flows in the direction of decreasing potential. The permeability tensor $\boldsymbol{k}$ ma be assumed to be symmetric and positive-definite in the majority of cases.
For incompressible flow the potential Π may be decomposed into a pressure part Π^p and an elevation part Π^e. Let the elevation part of the potential be measured in the direction of the gravity acceleration vector $\boldsymbol{g}$; then the decomposition of Π takes the form

$$\Pi = \Pi^p + \Pi^e = \frac{p}{g\rho_f} + \Pi^e, \tag{3.86}$$

where g is the gravity acceleration constant. Taking the spatial gradient of Eq. (3.86) we obtain

$$\text{grad}(\Pi) = \frac{\text{grad}(p)}{g\rho_f} + \frac{\boldsymbol{g}}{g}. \tag{3.87}$$

Thus, substituting into Eq. (3.88) we obtain the constitutive relation for fluid flow

$$\bar{\boldsymbol{v}} = -\boldsymbol{k} \cdot \left(\frac{\text{grad}(p)}{g\rho_f} + \frac{\boldsymbol{g}}{g} \right). \tag{3.88}$$

The equation above will be inserted in the mass balance equation, to take into account the fluid diffusion process.

It is sometimes assumed that the permeability of the soil skeleton varies with the soil's porosity, or, equivalently, with the Jacobian J, i.e. $\boldsymbol{k} = \boldsymbol{k}(J)$. For example, it is possible to use the Kozeny-Carman equation (6) to express the evolution of the saturated permeability with deformation

$$\boldsymbol{k} = k(J)\mathbf{1}, \tag{3.89}$$

where $\mathbf{1}$ is the second-order identity tensor and $k(J)$ is of the form

$$k(J) = \frac{\rho_f g}{\mu} \frac{D^2}{180} \frac{(J - \phi_0^s)^3}{J(\phi_0^s)^2}, \tag{3.90}$$

where μ is the dynamic viscosity of the fluid, D is the effective diameter of the grains and ϕ_0^s is the initial volume fraction of the solid.

Chapter 4

Numerical implementation of the model

4.1 Introduction

The aim of this section of the work is describing how the overall set of equations derived so far can be solved with a numerical code in the framework of finite element model. Due to the assumption of geometric and material non linearities, the numerical solution of the differential equations is a challenging task, that requires complex procedures.
Before moving to the solution aspects, let us recall the equations derived so far for the solid-fluid mixture, pointing out in particular the hypothesis that we considered in the development of the model. The fundamental equations that need to be solved are the balance of mass and the balance of linear momentum as derived from Chapter 2, which read

$$\begin{cases} B\mathrm{div}(\boldsymbol{v}) + \mathrm{div}\left(-\boldsymbol{k}\cdot\left(\dfrac{\mathrm{grad}(p)}{g\rho_f} + \dfrac{\boldsymbol{g}}{g}\right)\right) = 0 \\ \mathrm{DIV}(\boldsymbol{P}) + \rho_0\boldsymbol{G} = \rho_0^s\boldsymbol{a} + \rho_0^f\boldsymbol{a}_f \end{cases} \tag{4.1}$$

where the Darcy's law has been inserted in the mass balance equation.
For the sake of completeness, let's recall the main assumptions underlying the above equations:

- two phases fully saturated continuum body;
- no mass exchange between the two phases;
- isothermal continuum body;
- laminar flow of the fluid phase.

The Eq. (4.1) can be further simplified under this additional assumptions

- incompressible solid and fluid phases, i.e. K_s,$K_f \longrightarrow \infty$;
- no inertial effects, i.e. $\boldsymbol{a} = \boldsymbol{a}_f = 0$.

Assuming the additional above assumptions, Eq. (4.1) simplifies as follow

$$\begin{cases} \mathrm{div}(\boldsymbol{v}) + \mathrm{div}\left(-\boldsymbol{k} \cdot (\dfrac{\mathrm{grad}(p)}{g\rho_f} + \dfrac{\boldsymbol{g}}{g})\right) = 0 \\ \mathrm{DIV}(\boldsymbol{P}) + \rho_0 \boldsymbol{G} = 0 \end{cases} \tag{4.2}$$

which constitutes the fundamental system of equations of the mechanics for the fully saturated porous media. Note that the first equation (balance of mass) is written in the deformed configuration, while the second equation (balance of linear momentum) is written in the undeformed configuration. The idea is to use the undeformed configuration whenever possible since the undeformed domain is fixed throughout the entire solution process. Therefore we will manipulate the first equation to obtain a more suitable form.
Then, we will derived the finite element form of the balance laws, in order to solve numerically the set of equations. Finally we will present the overall structure of the code which has been developed to solve the numerical model.

4.2 Variational equations and linearization

Following the standard procedures of variational principles, let's define the space of potentials as

$$\mathscr{C}_\theta = \left\{\Pi : \boldsymbol{\varphi}(\mathscr{B}) \to R^{n_{sd}} | \Pi \in H^1, \Pi = \Pi_\theta \text{ on } \partial\boldsymbol{\varphi}^\theta\right\} \tag{4.3}$$

and the corresponding space of variations as

$$\mathscr{V}_\theta = \left\{\psi : \boldsymbol{\varphi}(\mathscr{B}) \to R^{n_{sd}} | \psi \in H^1, \psi = 0 \text{ on } \partial\boldsymbol{\varphi}^\theta\right\}. \tag{4.4}$$

Further, let $H : \mathscr{C}_\theta \times \mathscr{V}_\theta \longrightarrow R$ be given by

$$H(\boldsymbol{\varphi}, \Pi, \psi) = \int_{\varphi(\mathscr{B})} \left[\psi \mathrm{div}(\boldsymbol{v}) - \mathrm{grad}\psi \cdot \left(-\boldsymbol{k} \cdot \left(\frac{\mathrm{grad}(p)}{g\rho_f} + \frac{\boldsymbol{g}}{g}\right)\right)\right] \mathrm{d}V - \int_{\partial\varphi(\mathscr{B})} \psi q \, \mathrm{d}A. \tag{4.5}$$

The balance of mass is given by the condition $H(\boldsymbol{\varphi}, \Pi, \psi) = 0$ which is equivalent to the first of Eq. (4.2).
Let's define the space of configuration as

$$\mathscr{C}_{\boldsymbol{\varphi}} = \left\{\boldsymbol{\varphi} : \mathscr{B} \to R^{n_{sd}} | \varphi_i \in H^1, \boldsymbol{\varphi} = \boldsymbol{\varphi}_d \text{ on } \partial\mathscr{B}^d\right\} \tag{4.6}$$

and the space of variations as

$$\mathscr{V}_{\boldsymbol{\varphi}} = \left\{ \boldsymbol{\eta} : \mathscr{B} \to R^{n_{sd}} | \eta_i \in H^1, \boldsymbol{\eta} = \mathbf{0} \text{ on } \partial\mathscr{B}^d \right\} \tag{4.7}$$

where H^1 is the usual Sobolev space of functions of degree one. Further, let $G : \mathscr{C}_{\boldsymbol{\varphi}} \times \mathscr{V}_{\boldsymbol{\varphi}} \longrightarrow R$ be given by

$$G(\boldsymbol{\varphi}, \Pi, \boldsymbol{\eta}) = \int_{\mathscr{B}} (\mathrm{GRAD}\boldsymbol{\eta} : \boldsymbol{P} - \rho_0 \boldsymbol{\eta} \cdot \boldsymbol{G}) \, \mathrm{d}V_0 - \int_{\partial\mathscr{B}^t} \boldsymbol{\eta} \cdot \boldsymbol{t} \, \mathrm{d}A_0. \tag{4.8}$$

The balance of linear momentum is given by the condition $G(\boldsymbol{\varphi}, \Pi, \boldsymbol{\eta}) = 0$, which is equivalent to the second of the Eq. (4.2) if $\boldsymbol{P}$ and $\boldsymbol{\eta}$ are assumed to be C^1.
The weak form of the boundary-value problem is therefore as follows. Find $\boldsymbol{\varphi} \in \mathscr{C}_{\boldsymbol{\varphi}}$ and $\Pi \in \mathscr{C}_\theta$ such that

$$H(\boldsymbol{\varphi}, \Pi, \psi) = G(\boldsymbol{\varphi}, \Pi, \boldsymbol{\eta}) = 0 \tag{4.9}$$

for all $\boldsymbol{\eta} \in \mathscr{V}_{\boldsymbol{\varphi}}$ and $\psi \in \mathscr{V}_\theta$.
The above conditions emanates directly from the strong form of the boundary-value problem. However, the functions H and G posses an awkward structure that is not directly amenable to standard matrix manipulations. The function $G(\boldsymbol{\varphi}, \Pi, \boldsymbol{\eta})$ can be rewritten in the following form, invoking the decomposition with the effective stress introduced in the Chapter 2

$$G(\boldsymbol{\varphi}, \Pi, \boldsymbol{\eta}) = \int_{\mathscr{B}} (\mathrm{GRAD}\boldsymbol{\eta} : \bar{\boldsymbol{\tau}} - \theta \mathrm{div}\, \boldsymbol{\eta} - \rho_0 \boldsymbol{\eta} \cdot \boldsymbol{G}) \, \mathrm{d}V_0 - \int_{\partial\mathscr{B}^t} \boldsymbol{\eta} \cdot \boldsymbol{t} \, \mathrm{d}A_0. \tag{4.10}$$

The balance of mass equation is written with respect to the current configurations, and therefore the integrals are computed in the current varying volume. Hereafter, the function $H(\boldsymbol{\varphi}, \Pi, \psi)$ needs to be reformulated in such a way that the integration is done with respect to the common undeformed reference configuration $\mathscr{B}$. The domain of integration can be reckoned quite easily from the undeformed configuration by introducing the Jacobian J. A standard result of continuum mechanic states that the time derivative of the Jacobian is $\dot{J} = J\mathrm{div}(\boldsymbol{v})$. In addition, let $\bar{\boldsymbol{V}} \cdot \boldsymbol{N} = -Q$ be the prescribed volumetric rate of flow per unit undeformed area across the boundary $\partial\mathscr{B}$. $\bar{\boldsymbol{V}} = J\boldsymbol{F}^{-1} \cdot \bar{\boldsymbol{v}}$ is the Piola trasform of the Darcy velocity $\bar{\boldsymbol{v}}$, and Q is positive when pointing inward relative to the undeformed surface $\partial\mathscr{B}$ with outward unit normal $\boldsymbol{N}$. Substituting into Eq. (4.5) results in the variational equation for balance of volume, now reckoned with respect to the undeformed configuration $\mathscr{B}$

$$H(\boldsymbol{\varphi}, \Pi, \psi) = \int_{\mathscr{B}} \left[\psi \dot{J} - \mathrm{grad}\psi \cdot J \left(-\boldsymbol{k} \cdot \left(\frac{\mathrm{grad}(p)}{g\rho_f} + \frac{\boldsymbol{G}}{g} \right) \right) \right] \mathrm{d}V_0 - \int_{\partial\mathscr{B}^h} \psi Q \, \mathrm{d}A_0. \tag{4.11}$$

Note that in the case of impermeable boundaries $q = Q = 0$, i.e no fluid is supplied to the system. To avoid possible source of confusion, we remind that $\boldsymbol{g} \equiv \boldsymbol{G}$.
With the above operations, the two variational equations that need to be solved are

$$\begin{cases} H = \displaystyle\int_{\mathscr{B}} \left[\psi \dot{J} - \mathrm{grad}\psi \cdot \left(-\boldsymbol{k} \cdot (\frac{\mathrm{grad}(\theta)}{g\rho_f} + J\frac{\boldsymbol{G}}{g}) \right) \right] \mathrm{d}V_0 - \int_{\partial\mathscr{B}^h} \psi Q \, \mathrm{d}A_0 = 0 \\ G = \displaystyle\int_{\mathscr{B}} (\mathrm{GRAD}\boldsymbol{\eta} : \bar{\boldsymbol{\tau}} - \theta \mathrm{div}\, \boldsymbol{\eta} - \rho_0 \boldsymbol{\eta} \cdot \boldsymbol{G}) \, \mathrm{d}V_0 - \int_{\partial\mathscr{B}^t} \boldsymbol{\eta} \cdot \boldsymbol{t} \, \mathrm{d}A_0 = 0 \end{cases} \tag{4.12}$$

Again, we point out that both the equations are written in the weak (integral) form and in reference to the undeformed initial configuration. We observe now that the first of equation of (4.12), namely the mass balance equation, contains a rate form, i.e. the variation in time of J, and therefore requires a temporal discretization. This can be done recovering the well-known backward differentiation scheme. This typology of algorithms has the peculiarity to be unconditionally stable, and therefore turns out to be the most appropriate procedure in this contest. The time discretization of H reads

$$H_{\Delta t} = \int_{\mathscr{B}} \psi \frac{J_{n+1} - J_n}{\Delta t} \mathrm{d}V_0 - \int_{\mathscr{B}} \left[\mathrm{grad}\psi \cdot \left(-\boldsymbol{k} \cdot \left(\frac{\mathrm{grad}(\theta)}{g\rho_f} + J\frac{\boldsymbol{G}}{g} \right) \right) \right]_{n+1} \mathrm{d}V_0 - \int_{\partial\mathscr{B}^h} \psi Q_{n+1} \mathrm{d}A_0 = 0. \tag{4.13}$$

The crucial point now for the solution of the numerical model is the linerization of Eq. (4.12). In fact, it's necessary to develop exact expressions for the first derivatives of the functions H and G to use in Newton-type iterations. More specifically, we want the linearization of the non-linear two-field linear momentum and mass conservation equations at some configurations $\boldsymbol{\varphi}^0$ and pressure θ^0, which corresponds to some infinitesimal variations $\delta\boldsymbol{u}$ and $\delta\theta$.
The first variation of Eq. (4.12) can be obtained following standard procedures, and the complete derivation will be omitted for the sake of brevity (17). The variation of $H_{\Delta t}$, with Δt fixed, gives

$$\begin{aligned} \delta H_{\Delta t} = & \int_{\mathscr{B}} \frac{\psi}{\Delta t} J \mathrm{div}\, \delta\boldsymbol{u} \mathrm{d}V_0 + \int_{\mathscr{B}} \mathrm{grad}\psi \cdot \frac{\boldsymbol{k}}{\rho_f g} \cdot \mathrm{grad}\, \delta\theta \, \mathrm{d}V_0 \\ & - 2 \int_{\mathscr{B}} \mathrm{grad}\, \psi \cdot \mathrm{symm} \left(\frac{\boldsymbol{k}}{\rho_f g} \cdot \mathrm{grad}^t \delta\boldsymbol{u} \right) \cdot \mathrm{grad}\, \theta \, \mathrm{d}V_0 \\ & - \int_{\mathscr{B}} \mathrm{grad}\psi \cdot [\mathrm{grad}\delta\boldsymbol{u} - (\mathrm{div}\delta\boldsymbol{u})\mathbf{1}] \cdot \boldsymbol{k} \cdot \frac{\boldsymbol{G}}{g} J \mathrm{d}V_0 - \int_{\partial\mathscr{B}} \psi \delta Q \, \mathrm{d}A_0, \end{aligned} \tag{4.14}$$

where δQ is the variation of the fluid flux Q, g is the gravity acceleration constant and $\boldsymbol{G}$ is the vector of gravity accelerations. In this derivation it's assumed that the spatial permeability tensor $\boldsymbol{k}$ is constant during the deformation process.

The variation of G gives

$$\delta G = \int_{\mathscr{B}} \text{grad}\, \boldsymbol{\eta} : (\boldsymbol{c} + \bar{\boldsymbol{\tau}} \oplus \mathbf{1}) : \text{grad}\, \delta\boldsymbol{u}\, \text{d}V_0 - \int_{\mathscr{B}} (\delta\theta \text{div}\, \boldsymbol{\eta} - \theta \text{grad}^t \boldsymbol{\eta} : \text{grad}\delta\boldsymbol{u}) \text{d}V_0 \\ - \int_{\mathscr{B}} \rho_f J \text{div}(\delta\boldsymbol{u})\boldsymbol{\eta} \cdot \boldsymbol{G} \text{d}V_0 - \int_{\partial\mathscr{B}} \boldsymbol{\eta} \cdot \delta\boldsymbol{t} \text{d}\, A_0, \quad (4.15)$$

where $\delta\boldsymbol{u}$, $\delta\theta$ and $\delta\boldsymbol{t}$ are the respective variations of the displacement vector, Kirchhoff pore fluid pressure and the traction vector. The first integral in Eq. (4.15) contains the initial stress term $(\bar{\boldsymbol{\tau}} \oplus \mathbf{1})_{ijkl} = \tau_{jl}\delta_{ik}$, with $(\mathbf{1})_{ij} = \delta_{ij}$ being the Kronecker delta, as well as the spatial tangent stiffness tensor $\boldsymbol{c}$; the third integral represents the variation of the (non-constant) reference mass density ρ_0 reflecting the amount of fluid with a constant mass density ρ_f that enters into or escapes from the soil matrix due to the variation of the Jacobian.
Since G and $H_{\Delta t}$ are both zero, their first variations δG and $\delta H_{\Delta t}$ also must vanish.

4.3 Finite element formulation

The aim of this section is to derive the spatial discretized equations starting from the differential equations developed in the former section. In doing so, we will use the finite element method following standard lines. The corner stone of the finite element method is to interpolate the displacement function with a so called-shape function, and compute the displacements in a finite number of points of the continuum body. In the framework of solid-fluid mixture, the idea is to introduce two possibly distinct spatial interpolation function matrices $\boldsymbol{N}^{\varphi}(\boldsymbol{x})$ and $\boldsymbol{N}^{\theta}(\boldsymbol{x})$ for approximating the solid phase motion $\boldsymbol{\varphi}$ ant the pore pressure field θ. Therefore, the primary variables that are computed on the nodes of the finite element mesh are the displacement of the solid skeleton and the pressure of the fluid phase.
Let the solid phase motion $\boldsymbol{\varphi}$ be approximated by the spatial displacement field $\boldsymbol{u}^h(\boldsymbol{x}) \in R^{n_{sd}}$. In matrix form

$$\boldsymbol{u}^h(\boldsymbol{x}) = \boldsymbol{N}^{\varphi}(\boldsymbol{x})\boldsymbol{d} + \boldsymbol{N}_g^{\varphi}(\boldsymbol{x})\boldsymbol{d}_g, \quad (4.16)$$

where $\boldsymbol{d} \in R^{NQ}$ is the unknown nodal solid displacement vector and $\boldsymbol{d}_g$ is the vector of prescribed nodal solid displacement. In analogous way, let the spatial Kirchhoff pore pressure field θ be approximated by the function $\theta^h(\boldsymbol{x}) \in R^1$. In matrix form we have

$$\theta^h(\boldsymbol{x}) = \boldsymbol{N}^{\theta}(\boldsymbol{x})\boldsymbol{\theta} + \boldsymbol{N}_r^{\theta}(\boldsymbol{x})\boldsymbol{\theta}_r, \quad (4.17)$$

where $\boldsymbol{\theta} \in R^{NP}$ is the unknown nodal Kirchhoff pore pressure vector and $\boldsymbol{\theta}_r$ is the vector of prescribed nodal Kirchhoff pore pressure. The weighting functions $\boldsymbol{\eta}$ and ψ may be approximated in a similar

fashion in terms of their nodal values $\tilde{\boldsymbol{\eta}}$ and $\tilde{\psi}$ as follows

$$\boldsymbol{\eta}^h(\boldsymbol{x}) = \boldsymbol{N}^{\varphi}(\boldsymbol{x})\tilde{\boldsymbol{\eta}}; \qquad\qquad \boldsymbol{\psi}^h(\boldsymbol{x}) = \boldsymbol{N}^{\theta}(\boldsymbol{x})\tilde{\boldsymbol{\psi}} \tag{4.18}$$

where $\tilde{\boldsymbol{\eta}} \in R^{NQ}$ and $\tilde{\boldsymbol{\psi}} \in R^{NP}$.

With these preliminaries, it is possible to discretize spatially the balance laws. The finite element equation for the balance of mass is

$$H^h_{\Delta t} = -\tilde{\boldsymbol{\psi}}^t \left[\frac{\boldsymbol{J}(\boldsymbol{d})}{\Delta t} + \boldsymbol{\Phi}(\boldsymbol{\theta}) + \boldsymbol{H}_{EXT} \right] = \boldsymbol{0}, \tag{4.19}$$

where

$$\boldsymbol{J}(\boldsymbol{d}) = -\int_{\mathscr{B}} \boldsymbol{N}^{\theta t}(J_{n+1} - J_n)\mathrm{d}V_0; \tag{4.20a}$$

$$\boldsymbol{\Phi}(\boldsymbol{\theta}) = \int_{\mathscr{B}} \boldsymbol{E}^t J_{n+1}\bar{\boldsymbol{v}}_{n+1}\mathrm{d}V_0; \tag{4.20b}$$

$$\boldsymbol{H}_{EXT} = \int_{\partial\mathscr{B}} \boldsymbol{N}^{\theta t} Q_{n+1}\mathrm{d}A_0. \tag{4.20c}$$

The matrix $\boldsymbol{E}$ is the gradient-pressure operator with the structure

$$\boldsymbol{E} = [\mathrm{grad}N^{\theta}_1, \mathrm{grad}N^{\theta}_2, ..., \mathrm{grad}N^{\theta}_{NP}]. \tag{4.21}$$

The finite element equation for the balance of linear momentum is

$$G^h = \tilde{\boldsymbol{\eta}}^t \left[\boldsymbol{N}^s(\boldsymbol{d}) + \boldsymbol{N}^w(\boldsymbol{\theta}) - \boldsymbol{F}_{EXT} \right] = \boldsymbol{0}, \tag{4.22}$$

where

$$\boldsymbol{N}^s(\boldsymbol{d}) = \int_{\mathscr{B}} \boldsymbol{B}^t \left\{ \bar{\boldsymbol{\tau}} \right\} \mathrm{d}V_0; \tag{4.23a}$$

$$\boldsymbol{N}^w(\boldsymbol{\theta}) = -\int_{\mathscr{B}} \boldsymbol{b}^t(\boldsymbol{N}^{\theta}\boldsymbol{\theta} + \boldsymbol{N}^{\theta}_r\boldsymbol{\theta}_r)\mathrm{d}V_0; \tag{4.23b}$$

$$\boldsymbol{F}_{EXT} = \int_{\mathscr{B}} \rho_0 \boldsymbol{N}^{\varphi t}\boldsymbol{G}\mathrm{d}V_0 + \int_{\partial\mathscr{B}} \boldsymbol{N}^{\varphi t}\boldsymbol{t}\mathrm{d}A_0. \tag{4.23c}$$

The term $\{\bar{\boldsymbol{\tau}}\}$ is a vector that contains the element of the effective stress tensor $\bar{\boldsymbol{\tau}}$. For example, if $n_{sd} = 2$, then $\{\bar{\boldsymbol{\tau}}\} = [\bar{\tau}_{11}, \bar{\tau}_{22}, \bar{\tau}_{12}]^t$. The matrix $\boldsymbol{B}$ is the usual spatial strain-displacement transformation matrix with structure

$$\boldsymbol{B} = [\boldsymbol{B}_1, \boldsymbol{B}_2, ..., \boldsymbol{B}_{NQ}]. \tag{4.24}$$

Finally, the matrix $\boldsymbol{b} = \{\boldsymbol{1}\}^t \boldsymbol{B}$, where for $n_{sd} = 2$, $\boldsymbol{b} = [1, 1, 0]^t$ and for $n_{sd} = 3$, $\boldsymbol{b} = [1, 1, 1, 0, 0, 0]^t$.

Since $\tilde{\boldsymbol{\psi}}$ and $\tilde{\boldsymbol{\eta}}$ are both arbitrary, the conditions stated in Eqq. (4.19) and (4.22) can be satisfied solving the following system of equations

$$\begin{cases} \boldsymbol{r}_{\varphi}(\boldsymbol{d},\boldsymbol{\theta}) = \boldsymbol{N}^{s}(\boldsymbol{d}) + \boldsymbol{N}^{w}(\boldsymbol{\theta}) - \boldsymbol{F}_{EXT} = \boldsymbol{0} \\ \boldsymbol{r}_{\theta}(\boldsymbol{d},\boldsymbol{\theta}) = \dfrac{\boldsymbol{J}(\boldsymbol{d})}{\Delta t} + \boldsymbol{\Phi}(\boldsymbol{\theta}) + \boldsymbol{H}_{EXT} = \boldsymbol{0} \end{cases} \tag{4.25}$$

In conclusion, the essence of the problem consists in determining the configurations defined by the nodal values $\boldsymbol{d}$ and $\boldsymbol{\theta}$ such that

$$\boldsymbol{r}(\boldsymbol{d},\boldsymbol{\theta}) = \boldsymbol{0}, \tag{4.26}$$

i.e. determining the solution of the non-linear system such that the balance of mass and linear momentum equations are fulfilled.
The Eq. (4.26) is highly non linear, due to the assumption of large deformations and inelastic material for the solid phase. The solution of the system can be obtained with a Newton-Raphson scheme. If $\boldsymbol{r}(\boldsymbol{d}^{k},\boldsymbol{\theta}^{k}) \neq \boldsymbol{0}$ for some trial configuration $(\boldsymbol{d}^{k},\boldsymbol{\theta}^{k})$, the solution of the equation may be obtained with iterations until the correct solution is found. The aim is to dissipate the vector $\boldsymbol{r}$ by finding the solution vector $\boldsymbol{x}^{*} = \{\boldsymbol{d},\boldsymbol{\theta}\}^{*t}$

$$\boldsymbol{x}^{k+1} = \boldsymbol{x}^{k} + \delta\boldsymbol{x}^{k}; \qquad -\boldsymbol{K}^{k}\delta\boldsymbol{x}^{k} = \boldsymbol{r}^{k}; \qquad \boldsymbol{K}^{k} = \frac{\partial \boldsymbol{r}^{k}}{\partial \boldsymbol{x}^{k}};\ k \longleftarrow k+1 \tag{4.27}$$

where k plays the role of an iteration counter. The consistent tangent operator $\boldsymbol{K}$, which plays a crucial role to get quadratic convergence of the scheme, can simply be assembled from the linearized equations, i.e. Eq. (4.14) and (4.15) written in matrix form.
Let's consider first the linearization of the mass balance equation (4.14) and, introducing the shape and weighting functions, we get

$$\delta H^{h}_{\Delta t} = -\frac{\tilde{\boldsymbol{\psi}}^{\boldsymbol{t}}}{\Delta t}[\boldsymbol{K}_{\theta\varphi}\delta\boldsymbol{d} + \boldsymbol{K}_{\theta\theta}\delta\boldsymbol{\theta}] \tag{4.28}$$

where

$$\boldsymbol{K}_{\theta\varphi} = -\int_{\mathscr{B}} J\boldsymbol{N}^{\theta t}\boldsymbol{b}\mathrm{d}V_0 + \Delta t\int_{\mathscr{B}}\left(\frac{1}{g\rho_f}\boldsymbol{E}^{t}\boldsymbol{A}\tilde{\boldsymbol{B}} - J\boldsymbol{E}^{t}\boldsymbol{W}\tilde{\boldsymbol{B}}\right)\mathrm{d}V_0; \tag{4.29a}$$

$$\boldsymbol{K}_{\theta\theta} = -\frac{\Delta t}{\rho_f g}\int_{\mathscr{B}}\boldsymbol{E}^{t}\boldsymbol{k}\boldsymbol{E}\mathrm{d}V_0; \tag{4.29b}$$

where $\delta\boldsymbol{d}$ and $\delta\boldsymbol{\theta}$ are the first variations of $\boldsymbol{d}$ and $\boldsymbol{\theta}$. The matrix $\tilde{\boldsymbol{B}} = [\boldsymbol{B}\ \ \boldsymbol{B}^{sk}]^{t}$, where $\boldsymbol{B}^{sk}$ is the skew component of $\tilde{\boldsymbol{B}}$ representing the rotational effect. The exact formulation of $\boldsymbol{A}$ and $\boldsymbol{W}$ can be

found in (1). Note that the second term of $\boldsymbol{K}_{\theta\varphi}$ is due to the assumption of finite strain, and this term vanishes in case of small strain.
Let's consider now the linearization of the linear momentum equation (4.15) and, introducing the shape and weighting functions, we get

$$\delta G^h_{\Delta t} = \tilde{\eta}^t[\boldsymbol{K}_{\varphi\varphi}\delta\boldsymbol{d} + \boldsymbol{K}_{\varphi\theta}\delta\boldsymbol{\theta}] \tag{4.30}$$

where

$$\boldsymbol{K}_{\varphi\varphi} = \int_{\mathscr{B}} (\boldsymbol{B}^t\boldsymbol{C}\boldsymbol{B} + \tilde{\boldsymbol{B}}^t\boldsymbol{T}\tilde{\boldsymbol{B}} + \tilde{\boldsymbol{B}}^t\boldsymbol{I}_\theta\tilde{\boldsymbol{B}} - \rho_f J\boldsymbol{N}^{\theta t}\boldsymbol{G}\boldsymbol{b})\mathrm{d}V_0; \tag{4.31a}$$

$$\boldsymbol{K}_{\varphi\theta} = -\int_{\mathscr{B}} \boldsymbol{b}^t\boldsymbol{N}^\theta \mathrm{d}V_0. \tag{4.31b}$$

The first two terms of Eq. (4.31a) can be combined together, in order to obtain a single term. In fact the equation can be manipulated as follow

$$\int_{\mathscr{B}} (\boldsymbol{B}^t\boldsymbol{C}\boldsymbol{B} + \tilde{\boldsymbol{B}}^t\boldsymbol{T}\tilde{\boldsymbol{B}})\mathrm{d}V_0 = \int_{\mathscr{B}} (\boldsymbol{G}^t\boldsymbol{a}\boldsymbol{G})\mathrm{d}V_0 \tag{4.32}$$

where $\boldsymbol{a} = \alpha_{ijkl} - \bar{\boldsymbol{\tau}}_{il}\mathbf{1}_{jk}$ and the operator $\boldsymbol{G}$ is the full (non-symmetric) strain gradient operator, which contains the derivatives of the shape functions. This last formulation has been adopted in the implementation of the code.
The complete consistent tangent operator is given by

$$\boldsymbol{K} = \begin{bmatrix} \boldsymbol{K}_{\varphi\varphi} & \boldsymbol{K}_{\varphi\theta} \\ \boldsymbol{K}_{\theta\varphi} & \boldsymbol{K}_{\theta\theta} \end{bmatrix}$$

In general, the matrix $\boldsymbol{K}$ is non-symmetric and indefinite. However, under certain circumstances the matrix can be symmetric. This happens if $\boldsymbol{K}_{\theta\theta} = \boldsymbol{K}_{\theta\theta}{}^t$ which is true if and only if the permeability tensor $\boldsymbol{k}$ is symmetric. Furthermore, for small strain analysis the Jacobian J is identically equal to unity, while the second integral in Eq. (4.29a) vanishes identically since it originally arises from geometric non-linearity. Thus, for this condition, $\boldsymbol{K}_{\theta\varphi} = \boldsymbol{K}_{\varphi\theta}{}^t$. Under the assumption of small strains, the last term in the Eq. (4.31a) also vanishes, since this term is simply the linearization of the constant Jacobian. Thus, under the assumption of small strains, $\boldsymbol{K}_{\varphi\varphi} = \boldsymbol{K}_{\varphi\varphi}{}^t$, provided that $\boldsymbol{C}$ is symmetric.

4.4 Comparison with the small strains formulation

In this section we want to point out the differences between the small strains formulation and the finite strains formulation derived so far for the fully saturated porous media. Assuming small strains theory, the equations-and therefore the numerical solution-simplifies significantly.
Under the simplified hypothesis of small strain, the velocity $\boldsymbol{v}$ can be expressed in term of displacement as $\boldsymbol{v} = \dot{\boldsymbol{u}}$ and the effective stress can be computed as $\bar{\boldsymbol{\sigma}} = \bar{\boldsymbol{\tau}} = \boldsymbol{c} : \operatorname{grad} \boldsymbol{u}$, where $\boldsymbol{u}(\boldsymbol{x}, t)$ is a vector field of infinitesimal solid displacements of $\mathscr{B}$ reckoned from a self-equilibrating condition of geostatic stresses and $\boldsymbol{c} = \boldsymbol{c}(\boldsymbol{x})$ is a given fourth-order, time-independent tensor field of elasticities, defined in $\mathscr{B}$, which possesses both the major and minor symmetries. Note that the term "grad $\boldsymbol{u}$" may be replaced with the infinitesimal strain tensor "$\boldsymbol{\epsilon}$", where $\boldsymbol{\epsilon} = \operatorname{symm}(\operatorname{grad}\boldsymbol{u})$, due the minor symmetry of $\boldsymbol{c}$ with respect to its third and fourth indices. Hence, the strong form of the mass and linear momentum balance equations can be simplified as

$$\begin{cases} \operatorname{div}(\dot{\boldsymbol{u}}) + \operatorname{div}\left(-\boldsymbol{k} \cdot \dfrac{\operatorname{grad}(p_e)}{g\rho_f}\right) = 0 \\ \operatorname{div}(\boldsymbol{c}\operatorname{grad}\boldsymbol{u} - p_e\mathbf{1}) = \mathbf{0} \end{cases} \tag{4.34}$$

where $p_e = \theta_e$ is the excess pore fluid pressure. Note that Eqq. (4.34) are identical to those developed for the Biot consolidation theory (5; 69). Consequently, the variational form of the balance of mass can be simplified as

$$H = \int_{\mathscr{B}} \left(\psi \operatorname{div}(\dot{\boldsymbol{u}}) + \operatorname{grad}\psi \cdot \frac{\boldsymbol{k}}{g\rho_f} \cdot \operatorname{grad} p_e\right) \mathrm{d}V_0 - \int_{\partial\mathscr{B}^t} \psi q \mathrm{d}A_0 \tag{4.35}$$

ad the variational form of the linear momentum can be simplified as

$$G = \int_{\mathscr{B}} (\operatorname{grad}\boldsymbol{\eta} : \boldsymbol{c} : \operatorname{grad}\boldsymbol{u} - p_e \operatorname{div}\boldsymbol{\eta}) \, \mathrm{d}V_0 - \int_{\partial\mathscr{B}^t} \boldsymbol{\eta} \cdot \boldsymbol{t} \mathrm{d}A_0 \tag{4.36}$$

Again, the aim of the problem consists now in finding the solution $(\boldsymbol{u}, \boldsymbol{p_e})$ for which $H = G = 0$. The system of equation is now linear and no iteration are required for the numerical solution.

4.5 Overview of the numerical code

The set of equations derived in the previous section has been implemented in a new finite element toolbox called GEOFEM 973 (*www.geofem973.it*), specifically developed to solve non linear elastoplastic coupled problems. The code is written using MATLAB®language, which is particularly tailored for vector and matrix calculations. Furthermore, this language permits to easily plot all the computed results once the solution is computed. In this section we will briefly describe the main feature of this code, assuming a 2D (plane strain) framework.

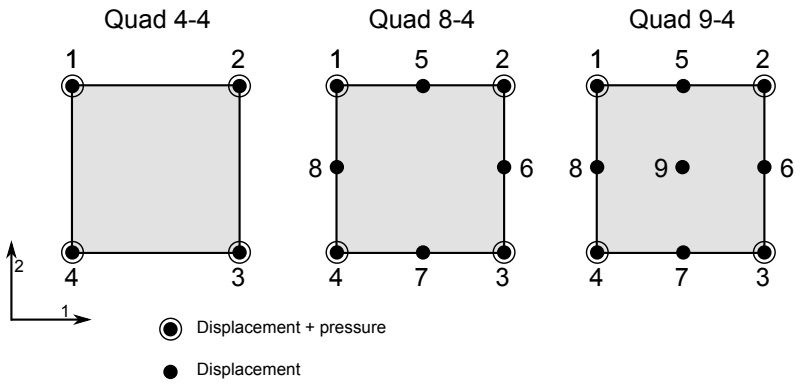

Figure 4-1: Element type and intrinsic node order for quadrilateral elements.

The code adopts three type of quadrilateral elements, namely `quad4-4`, `quad8-4`, `quad9-4`, where the first number indicates the nodes with associated displacements and the second number the node with associated pressure. The three elements are represented in Fig. 4-1.

The typology of the finite element is extremely important for coupled problem, where the mixed elements need to satisfy the LBB-condition for stability (70; 71; 72). It's important to point out that only the element `quad9-4` satisfies the LBB-condition, and therefore guarantees the stability of the solution. The other two elements don't guarantee the stability of the solution of the boundary value problem, as it will be demonstrated in the next section of the thesis.
The code reads the input data directly from the workspace of variables, which are usually created, for advanced geometries, with a pre-processor. The variables of the input file are recalled as follow:

- Nodes coordinate matrix

$$\mathtt{X} = \begin{bmatrix} x^1 & y^1 \\ x^2 & y^2 \\ \vdots & \vdots \\ x^n & y^n \end{bmatrix}$$

  with n total nodes.

- Topology matrix

$$\mathtt{T}(e,:) = \begin{bmatrix} node^1 & node^2 & \dots & node^{ne} & mat_e \end{bmatrix}$$

  for every element e with ne number of nodes and material property mat_e. The order of the nodes is as depicted in Fig. 4-1.

- Constraints matrix

$$\mathtt{C} = \begin{bmatrix} node^1 & 1/2/3 & c^1_{imp} \\ node^2 & 1/2/3 & c^2_{imp} \\ \vdots & \vdots & \vdots \\ node^{nc} & 1/2/3 & c^{nc}_{imp} \end{bmatrix}$$

  with nc total constrained nodes, $1 = u_x$, $2 = u_y$, $3 = p$ and c_{imp} is the prescribed value.

- Prescribed nodal force/flux

$$\mathtt{P} = \begin{bmatrix} node^1 & F^1_1 & F^1_2 & Q^1 \\ node^2 & F^2_1 & F^2_2 & Q^2 \\ \vdots & \vdots & \vdots & \\ node^{np} & F^{np}_1 & F^{np}_2 & Q^{np} \end{bmatrix}$$

  with np total nodal applied force/flux.

- Material parameters

$$\mathtt{G}(mat_e, :) = \begin{bmatrix} \rho_e & param_1 & \dots & param_n \end{bmatrix}$$

  for every material type mat_e with density ρ_e and n parameters.

- Solver parameters

  - `epsr` : tolerance for Newton Raphson iteration;
  - `imax` : maximum number of Newton Raphson iteration;
  - `incr` : coefficients for load increment;
  - `nip` : number of Gauss integration points;
  - `step` : step increments;

The main steps and expressions involved in the the driver of the program are shown in the following box.

DRIVER FILE FOR ELASTOPLASTIC COUPLED ANALYSIS AT FINITE STRAINS.

1. Define system parameters: $dof, dop, ndof, ndop, ne, nelem$;
2. Vectors and matrices initialization: $\boldsymbol{inc}, \boldsymbol{f}, \boldsymbol{solution}, \boldsymbol{RESrec}, \boldsymbol{Srec}, \boldsymbol{PLrec}, \boldsymbol{FLAGrec}$;
3. Identify (un)constrained DOF: $\boldsymbol{iu}, \boldsymbol{ic}$ [`DOFglobal`, `Const`];
4. Set nodal external forces/fluxes: $\boldsymbol{f}$ [`SetLoad`];

   `for t = 1:time`

   (a) Recall plastic variables at time step n: $\boldsymbol{PLn}$;

   `for i = 1:imax`

   i. Compute internal forces/fluxes: $\boldsymbol{g} = \boldsymbol{g}(\boldsymbol{inc}_{old}, \boldsymbol{Dinc})$ [`geQuad`];

   ii. Compute residual: $\boldsymbol{r} = \boldsymbol{g} - \boldsymbol{f}$;

   iii. Check for convergence

   If no convergence:

   - Compute tangent stiffness: $\boldsymbol{KK} = \boldsymbol{KK}(\boldsymbol{inc}_{old}, \boldsymbol{Dinc})$ [`KKeQuad`];
   - Compute increment: $\boldsymbol{dinc(iu)} = inv(\boldsymbol{KK}(\boldsymbol{iu}, \boldsymbol{iu}))(-\boldsymbol{r}(\boldsymbol{iu}))$;
   - Update solution: $\boldsymbol{Dinc} = \boldsymbol{Dinc} + \boldsymbol{dinc}$;

   `end`

   (b) Update solution vector: $\boldsymbol{inc}_{new} = \boldsymbol{inc}_{old} + \boldsymbol{Dinc}$;

   (c) Update elasto-plastic variables

   `end`

The code of the main processor is recalled in the following box.

```
%-------------------------------------------------------
% File:NLinDrive.m
%
% Driver for non linear analysis of (hyper-)elastoplastic
% u-P problem with Q8P4 elements.
%
% Input:
%
%   X    : Node coordinate array.
%   T    : Topology array.
%   G    : Material property array.
```

```
12 %   C     : Constraints.
13 %   P     : Prescribed nodal loads and flows.
14 %   step  : Time increment step.
15 %   nip   : Gauss point integration.
16 %   imax  : Maximum iteration number.
17 %   epsr  : Tollerance.
18 %
19 % Output:
20 %
21 %   solution: Nodal displacement and pressure array.
22 %   f     : Nodal force/fluxes array.
23 %   g     : Internal force/fluxes vector.
24 %   S     : System stress array.
25 %   PLrec: Plastic variables array.
26 %
27 % Note:
28 %   1)      Initial time step must be chosen in accordance
29 %           with the permeability.
30 %   2)      Backward differentiation formula implemented.
31 %
32 %  ------------------------------------------------------------------------  *
33 %    COPYRIGHT STATEMENT                                                     *
34 %                                                                            *
35 %    Copyright (C) 2014  Nicolo' Spiezia                                     *
36 %                                                                            *
37 %   This program is free software: you can redistribute it and/or modify     *
38 %   it under the terms of the GNU General Public License as published by     *
39 %   the Free Software Foundation, either version 3 of the License, or        *
40 %   (at your option) any later version.                                      *
41 %                                                                            *
42 %   This program is distributed in the hope that it will be useful,          *
43 %   but WITHOUT ANY WARRANTY; without even the implied warranty of           *
44 %   MERCHANTABILITY or FITNESS FOR A PARTICULAR PURPOSE.  See the            *
45 %   GNU General Public License for more details.                             *
46 %                                                                            *
47 %   You should have received a copy of the GNU General Public License        *
48 %   along with this program.  If not, see <http://www.gnu.org/licenses/>.    *
49 %                                                                            *
50 %   E-mail: nicolospiezia@gmail.com                                          *
51 %  ------------------------------------------------------------------------  *
52 % Add folder to Matlab search path
53 path(path,'..\FEMfiles');
54
55 ts = length(step);
56
57 % Define system parameters
58
59 dof = 2;    % Degree of freedom (displacement)
60 dop = 1;    % Degree of freedom (pressure)
61 dofp = dof+dop;
62
63 [DOF,nno,nnp] = DOFglobal(T,X);
64
65 ndof = nno*dof;   % Number dof (displacement)
```

```
66  ndop = nnp*dop;    % Number dop (pressure)
67  nd = ndof+ndop;    % Total number of DOF
68  ne = size(T,2)-1;
69  nelem = size(T,1);
70
71
72 % Initialization of vectors and matrices
73  [inc_new, inc_old,f] = deal(zeros(nd,1));
74  [solution] = deal(zeros(nd,ts));
75  [RESrec] = zeros(imax,ts);
76  [Srec] = zeros(4,nip^dof,nelem,ts);
77  [PLrec] = zeros(8,nip^dof,nelem,ts);
78  [FLAGrec] = zeros(nip^dof,nelem,ts);
79
80 % Inizialize PLrec
81  for i=1:size(T,1); % Over element
82      for j=1:nip^dof % Over GP
83      PLrec (1:4,j,i,1) = [1.00000001 1.00000002 0 1.00000003]';
84      PLrec (7,j,i,1) = G(T(i,ne+1),13); % Allocate Pc0
85      end
86  end
87
88 % Identify unconstrained/constrained dofs
89  [iu,ic] = Const(C,dof,dop,nd,DOF);
90
91 % Set nodal loads
92  f = SetLoad(f,P);
93
94
95    for t=1:ts
96
97    inc_old = solution(:,t);
98    Dinc = zeros(nd,1);
99
100   dt = step(t);    % Time increment
101
102   time=t
103
104
105   for iter=1:imax
106
107       itz = iter
108
109         % Recall plastic variable
110         PLn = PLrec (:,:,:,t);
111         % Compute internal forces and fluws
112         [g] = deal(zeros(nd,1));
113         [g,S,PL,FLAG,ALFA] = gQuad(g,T,X,G,inc_old,Dinc,nip,dt,DOF,PLn);
114
115         % residual
116         r = g - f;
117
118                 % check for convergence
119                 RESrec(iter,t) = norm(r(iu,1))/norm(f(iu,1));
```

```
120
121                     if norm(r(iu,1)) < epsr*norm(f(iu,1))
122                         break
123                     else
124
125                     % Compute increment
126                     dinc = zeros(nd,1);
127
128                     KK = zeros(nd,nd);
129                     KK = KKQuad(KK,T,X,G,nip,dt,DOF,inc_old,Dinc,S,ALFA);
130
131                     dinc(iu) = KK(iu,iu)\(-r(iu));
132
133                     Dinc = Dinc + dinc;
134
135                     end
136             end
137
138         if iter == imax
139         fprintf('\n No convergence in time step %d \n',t)
140         end
141
142         inc_new = inc_old+Dinc;
143
144         solution(:,t+1) = inc_new;
145         Srec(:,:,:,t+1) = S;
146
147         % record plastic variables
148         PLrec(:,:,:,t+1) = PL;
149         FLAGrec(:,:,t+1) = FLAG;
150
151     end
```

The functions `DOFglobal`, `Const`, `SetLoad` follow standard approach in in finite element analysis, and are not reported in this thesis.

The most interesting functions are those responsible for the computation of the internal forces/fluxes (`GQuad`) and for the tangential operator (`KKQuad`). This two functions compute the two quantities in each element, and then they assemble the contribution for the whole set of elements. In the remaining part of the section we will briefly describe these two functions, at the element level (marked by the letter `e`).

The function (`GeQuad`) computes the internal forces/fluxes at the element level according to Eq. (4.25), eliminating the external terms F and H. The source code of these two functions is given below.

```
1
2  % Number of nodes per element and dof's per node
3  ne  = size(Xe,1);
4  dof = 2;
```

```
5
6  Xep = Xe(1:4,1:2);
7  nep  = size(Xep,1);
8  dp = 1;
9
10 ue_new = ince_new(1:ne*dof);
11 ue_old = ince_old(1:ne*dof);
12 dinc = dince(1:ne*dof);
13
14 uep_old = ince_old(1:nep*dof);
15 uep_new = ince_new(1:nep*dof);
16 dincp = dince(1:nep*dof);
17
18 pe_old = ince_old(ne*dof+1:ne*dof+nep*dp);
19 pe_new = ince_new(ne*dof+1:ne*dof+nep*dp);
20
21 % Gauss points and weights.
22 [r w] = Gauss(nip);
23
24 % Initialize vectors.
25 [NSd NWt] = deal(zeros(ne*dof,1));
26 [Jd PHIt] = deal(zeros(nep*dp,1));
27 [Se, Te] = deal(zeros(4,nip^dof));
28 PLe = zeros(8,nip^dof);
29 ALFAe = zeros(16,nip^dof);
30 FLAGe = zeros(nip^dof,1);
31 warn = 0;
32
33 % Permeability values
34 kx = Ge(7);
35 ky = Ge(8);
36
37 % Gauss integration
38 ip = 0;
39 for i = 1:nip
40     for j = 1:nip
41             % Gauss point number
42             ip = ip + 1;
43
44             % Get element shape functions and Jacobian matrix
45             [Jt,B,~,~,~] = BQuad(Xe,r(i),r(j),ue_old+dinc);
46             [ ~, ~, dNp,Np, ~] = BQuad(Xep,r(i),r(j),uep_old+dincp);
47
48             % Get element deformation gradient and Left Cauchy-Green tensor
49             [F_old,~] = FbQuad(Xe,r(i),r(j),ue_old);
50             [F_new,b_new] = FbQuad(Xe,r(i),r(j),ue_old+dinc);
51
52             J_old = det(F_old);
53             J_new = det(F_new);
54
55             % Incremental deformation gradient
56             Ue_old = reshape(ue_old,size(Xe,2),size(Xe,1))';
57             X1e = (Xe + Ue_old);
58
```

```
59              [Fincr,~] = FbQuad(X1e,r(i),r(j),dinc);
60
61              % Check Jacobian
62              if J_new<0
63              warn = 1; % Warning for negative determinant of F
64              end
65
66              % 1-Linear momentum equation-A
67
68              % Recall variables at time step n
69
70              Be =  [PLne(1,ip)  PLne(3,ip)  0
71                     PLne(3,ip)  PLne(2,ip)  0
72                     0           0           PLne(4,ip)];
73
74              epspvn = PLne(5,ip);
75              epspsn = PLne(6,ip);
76              Pcn = PLne(7,ip);
77
78              % Compute Trial left Cauchy-Green
79              BeTr = Fincr*Be*Fincr';
80
81              % Compute principal elastic deformation and direction
82
83              [avett,aval] = eig(BeTr);
84
85              epseTr = [log(sqrt(aval(1,1)))
86                        log(sqrt(aval(2,2)))
87                        log(sqrt(aval(3,3)))];
88
89              dirpr = avett;
90
91              % Compute principal Kirchhoff tension
92
93              [tenspr,epse,Pc,aep,epspv,epsps,FLAGe(ip,1)] = tensCC(Ge,epseTr,Pcn,epspvn,epspsn);
94
95              % Compute left Cauchy Green tensor at n+1
96
97              stretpr(:,1) = exp(epse(:,1));
98
99              Be = zeros(3);
100
101             for ii=1:3
102
103               Be(1:3,1:3) = Be(1:3,1:3)+(stretpr(ii))^2*dirpr(:,ii)*dirpr(:,ii)';
104
105             end
106
107             % Compute Kirchhoff tension tensor
108
109             TTe = zeros(3);
110
111             for ii=1:3
112
```

```
113                 TTe(1:3,1:3) = TTe(1:3,1:3)+tenspr(ii)*dirpr(:,ii)*dirpr(:,ii)';
114
115               end
116
117               Te(:,ip) = [TTe(1,1) TTe(2,2) TTe(1,2) TTe(3,3) ]';
118
119               % Compute Cauchy tension
120               Se(:,ip) = Te(:,ip)/det(F_new);
121
122               % Evaluate internal force
123
124               NSd = NSd + w(i)*w(j)*B'*Se(1:3,ip)*det(Jt);
125
126
127               % Compute alfa tensor
128
129               stretTr(:,1) = exp(epseTr(:,1));
130               [ALFAe(:,ip) alfatens] = alfa(aep,tenspr,stretTr.^2,dirpr);
131
132
133               % Find minimum determinant of Eulerian acustic tensor
134
135                theta = 0:1:180;
136               determ = zeros(length(theta),1);
137                for nn=1:length(theta)
138                nvet = [cosd(theta(nn)); sind(theta(nn)); 0 ];
139
140                ae = AEEu(alfatens,TTe,nvet);
141
142                determ(nn)= det(ae);
143                end
144
145                BIF = [min(determ)];
146
147               % Allocate variables
148
149               PLe(:,ip)= [Be(1,1); Be(2,2); Be(1,2); Be(3,3); epspv; epsps; Pc; BIF];
150
151
152               % 1-Linear momentum equation-B
153
154               m(1:3,1)= [1,1,0]';
155
156               NWt = NWt + w(i)*w(j)*(B'*(m*Np*pe_new))*det(Jt);
157
158               % 2-Mass balance equation-A
159               Jd = Jd + w(i)*w(j)*(Np'*(J_new-J_old)/J_new)*det(Jt);
160
161               % 2-Mass balance equation-B
162               perm = [kx 0
163                       0  ky];
164
165               PHIt = PHIt + w(i)*w(j)*(dNp'*(perm*dNp*pe_new))*det(Jt);
166       end
```

```
167  end
168
169
170  gef = NSd-NWt;
171  gep = -Jd-dt*PHIt;
172
173  ge= [gef
174       gep];
175
176  end
```

The function (`KKeQuad`) computes the tangential operator at the element level according to Eq. (4.33). The function is reported in the following box.

```
1   ne  = size(Xe,1);
2   dof = 2;
3
4   Xep = Xe(1:4,1:dof);
5   nep  = size(Xep,1);
6   dp = 1;
7
8   ue_old=ince_old(1:ne*dof);
9   ue_new=ince_new(1:ne*dof);
10  dinc = dince(1:ne*dof);
11
12  uep_new=ince_new(1:nep*dof);
13  pe_new=ince_new(ne*dof+1:ne*dof+nep*dp);
14  dincp = dince(1:nep*dof);
15
16  % Material parameters
17
18  Ks = Ge(4);
19  n = Ge(5);
20  Kf = Ge(6);
21  kx = Ge(7);
22  ky = Ge(8);
23
24  KeFF = KeQuad(Xe,nip,ue_new,ue_old,uep_new,dinc,pe_new,Se,ALFAe);
25  KeFT = LeQuad(Xe,Ge,nip,Ks,ue_new,uep_new);
26  KeTF = LeTQuad(Xe,Ge,nip,Ks,ue_new,uep_new);
27  KeFF = HeQuad(Xe,Ge,nip,kx,ky,uep_new);
28
29  KKe=[  KeFF      KeFT
30         KeTF      dt*KeFF];
31  end
```

The functions which compute the four contributions to the tangent matrix are reported in the following boxes. Note that some terms, pertaining to some non linear contributions, haven't been implemented, in order to reduce the computational effort. In fact, these terms don't have a significant impact on the convergence of the Newton-Raphson scheme, and therefore they are not essential to

find the correct solution of the problem.

The term $\boldsymbol{K}_{\varphi\varphi}$ is computed by the following function.

```
function [Ke] = KeQuad(Xe,nip,ue_new,ue_old,uep,dinc,pe,Se,ALFAe)
%-------------------------------------------------------
%  KeQuad:
%   Creates the element stiffness matrix of an hyper-elastoplastic
%    4- or 8-node quadrilateral element in plane strain.
%
% Syntax:
%   [Ke] = KeQuad(Xe,nip,ue_new,ue_old,uep,dinc,pe,Se,ALFAe)
%
% Input:
%  Xe     : Element nodal coordinate array.
%  nip    : Number of Gauss points.
%  ue     : Element nodal displacements.
%  Se     : Element stress array at Gauss points.
% ALFAe   : Constitutive tangential operator.
%
% Output:
%  Kec    : Element stiffness matrix.
%
% Date:
%   Version 1.0   30.10.13
%
%   Created by Nicolo' Spiezia
%-------------------------------------------------------

% Number of nodes per element and dof's per node
ne  = size(Xe,1);
dof = size(Xe,2);

Xep = Xe(1:4,1:2);

% Gauss points and weights.
[r w] = Gauss(nip);

% Initialize matrices
[Ke] = deal(zeros(ne*dof));

% Gauss integration of stiffness matrix.
ip = 0;
for i = 1:nip
    for j = 1:nip

            ip = ip + 1;
            % Get element Jacobian matrix and strain interpolation matrix

            [Jt,~,~,~,G] = BQuad(Xe,r(i),r(j),ue_old+dinc);
            %[ ~, ~, ~,Np, ~] = BQuad(Xep,r(i),r(j),uep);
            [F,b] = FbQuad(Xe,r(i),r(j),ue_old+dinc);

```

```
            % Recall tensor sigma for 2D analysis
            [taumI,~]= prodton(Se(:,ip));

            % Recall consistent tangent algorithm

            alfa = (1/det(F))*reshape(ALFAe(:,ip),4,4);

            a = (alfa-taumI);

            Ke = Ke + w(i)*w(j)*(G'*a*G)*det(Jt);

    end
end

end
```

The term $\boldsymbol{K}_{\theta\theta}$ is computed by the following function.

```
function [He] = HeQuad(Xe,nip,kx,ky,uep_new)
%-------------------------------------------------------------
%  HeQuad:
%    Creates the element permeability matrix of
%     4- or 8-node quadrilateral element in plane strain.
%
% Syntax:
%    function [He] = HeQuad(Xe,nip,kx,ky,uep_new)
%
% Input:
%  Xe     : Element nodal coordinate array.
%  nip    : Number of Gauss points.
%  k      : Permeability matrix.
% uep_new: Updated displacement on the prssure nodes
%
% Output:
%  He    : Element permeability matrix.
%
% Date:
%    Version 1.0   30.10.13
%
%    Created by Nicolo' Spiezia
%-------------------------------------------------------------

% Extrapolate pressure node only
Xep = Xe(1:4,1:2);

% Number of nodes per element and dof's per node
ne  = size(Xep,1);

% Gauss points and weights.
[r w] = Gauss(nip);

perm=[kx 0
```

```
        0 ky];

% Initialize matrices
He=zeros(ne,ne);

% Gauss integration of stiffness matrix.

for i = 1:nip
    for j = 1:nip

            % Get element Jacobian matrix and strain interpolation matrix
            [Jt,~,dNp,~,~] = BQuad(Xep,r(i),r(j),uep_new);

            % Coupling element matrix
            He = He + w(i)*w(j)*(dNp'*(perm*dNp))*det(Jt);

    end
end
```

The term $\boldsymbol{K}_{\varphi\theta}$ is computed by the following function.

```
function [Le] = LeQuad(Xe,Ge,nip,Ks,ue_new,uep_new)
%-------------------------------------------------------
%  KeQuad:
%   Creates the element coupling matrix of a
%    4- or 8-node quadrilateral element in plane strain.
%
% Syntax:
%   function [Le] = LeQuad(Xe,Ge,nip,Ks,ue_new,uep_new))
%
% Input:
%  Xe    : Element nodal coordinate array.
%  Ge    : Element property vector.
%  nip   : Number of Gauss points.
%  ue    : Displacement vector.
%
% Output:
%  Le   : Element coupling matrix.
%
% Date:
%   Version 1.0   30.10.13
%
%   Created by Nicolo' Spiezia
%-------------------------------------------------------

% Extrapolate pressure node only

Xep = Xe(1:4,1:2);
nep  = size(Xep,1);

% Number of nodes per element and dof's per node
ne  = size(Xe,1);
```

```
dof = size(Xe,2);

% Gauss points and weights.
[r w] = Gauss(nip);

% Vector alfa

alfa(1,1)=1;
alfa(2,1)=1;
alfa(3,1)=0;


% Initialize matrices
Le=zeros(ne*dof,nep);

% Gauss integration of stiffness matrix.

for i = 1:nip
    for j = 1:nip

            % Get element Jacobian matrix and strain interpolation matrix
            [Jt,B, ~, ~, ~] = BQuad(Xe,r(i),r(j),ue_new);
            [ ~, ~, ~,Np, ~] = BQuad(Xep,r(i),r(j),uep_new);
            [F,b] = FbQuad(Xe,r(i),r(j),ue_new);

            J=det(F);

            % Coupling element matrix
            Le = Le + w(i)*w(j)*(B'*(alfa*Np ))*det(Jt);

    end
end
```

The term $\boldsymbol{K}_{\theta\varphi}$ is computed by the following function.

```
function [LeT] = LeTQuad(Xe,Ge,nip,Ks,ue_new,uep_new)
%---------------------------------------------------------
%  KeQuad:
%   Creates the element coupling matrix of a
%    4- or 8-node quadrilateral element in plane strain.
%
% Syntax:
%   [LeT] = LeTQuad(Xe,Ge,nip,Ks,ue_new,uep_new)
%
% Input:
%  Xe    : Element nodal coordinate array.
%  nip   : Number of Gauss points.
%  ue    : Updated displacement vector.
%
% Output:
%  Le    : Element coupling matrix.
%
```

```
% Date:
%    Version 1.0    30.10.13
%
%    Created by Nicolo' Spiezia
%-------------------------------------------------------

% Extrapolate pressure node only

Xep = Xe(1:4,1:2);
nep  = size(Xep,1);

% Number of nodes per element and dof's per node
ne  = size(Xe,1);
dof = size(Xe,2);

% Gauss points and weights.
[r w] = Gauss(nip);

% Alfa vector

alfa(1,1)=1;
alfa(2,1)=1;
alfa(3,1)=0;

% Initialize matrices
LeT=zeros(ne*dof,nep);

% Gauss integration of stiffness matrix.

for i = 1:nip
    for j = 1:nip

            % Get element Jacobian matrix and strain interpolation matrix
            [Jt,B, ~, ~, ~] = BQuad(Xe,r(i),r(j),ue_new);
            [ ~, ~, ~,Np, ~] = BQuad(Xep,r(i),r(j),uep_new);
            [F,b] = FbQuad(Xe,r(i),r(j),ue_new);

            J=det(F);

            % Coupling element matrix
            LeT = LeT + w(i)*w(j)*J*(B'*(alfa*Np))*det(Jt);

    end
end
```

The developed finite element code can be used to solve elastoplastic coupled model undergoing large deformations in plane strain analysis. The code has been applied to two problems pertaining geomechanical applications, namely consolidation processes under linear long foundation and wellbore drilling. The results will be presented in the next chapter of this thesis.

Chapter 5

Numerical analysis and results

5.1 Introduction

This chapter describes the results obtained from the numerical analysis performed with the finite element code presented in the previous chapter. Two examples, taken from real applications in the geomechanical field, have been investigated. The first example regards the consolidation process due to the application of a load on a surface, simulating for example the construction of a long strip foundation. Two situations are investigated, a one dimensional and a two dimensional plane strain process. This example, typical in the geotechnical literature, has been solved in particular to test the model and compare the results with other available cases.
The second example regards the drilling process of an horizontal wellbore in a porous rock formation. Predicting the evolution of displacements and pressure, the amount of accumulated plastic deformations and the propagation of localization band around a wellbore is a challenging task, that could have immense implication. In this chapter we show the results obtained from the coupled elastoplastic analysis, in order to give insight into the evaluation of the stability of the wellbore.
Obviously, these are just two examples and the code can be used to solve every kind of elastoplastic coupled problem undergoing large deformations.

5.2 Consolidation process under a uniformed distributed load on soft clay

This section presents the numerical results of the consolidation process of an elastoplastic saturated porous media, subjected to an applied load, in a one dimensional and two dimensional configuration.

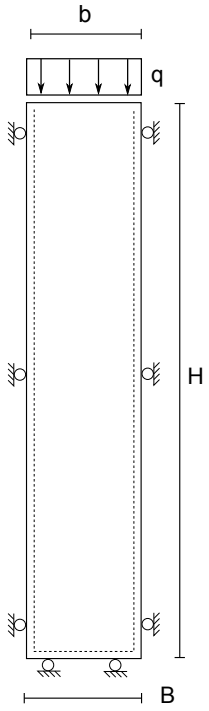

Figure 5-1: One dimensional consolidation: geometry and boundary conditions.

5.2.1 One dimensional consolidation

Description of the problem

The first example considers an initially stress-free hyperelastic porous skeleton subjected to a one dimensional consolidation process. The geometry and the boundary conditions of the problem are represented in Fig. 5-1.

The initial height of the column is $H = 5000mm$, $B = b = 1000mm$ and it is compressed with a vertical downward Cauchy load of $q = -90KPa$. The column assumes an impervious bottom base, that is fixed with respect to displacements, zero horizontal displacements on the vertical sides, and zero excess pore pressure on top.

The material is hyperelastic and it is described by the free energy function $\hat{\Psi}$ introduced in the Eq. (3.38) where $\epsilon_A^e = \ln(\lambda_A^e)$ are the elastic logarithmic principal stretches. The assumed values of the material parameters are $\lambda = 57.7KPa$ and $\mu = 38.5KPa$ (equivalent to Young's modulus of $E = 100KPa$ and Poisson's ratio of $\nu = 0.3$) (1). The vertical permeability is assumed to have a value of $k_x = k_y = 0.864mm/day$ and the column is fully saturated by water (unit weight $\rho_f g = 10KN/m^3$). Gravitational forces are not considered and the consolidation is assumed to be only due to the applied load. The column is discretized with 10 quadrilateral `Quad8-4` elements.

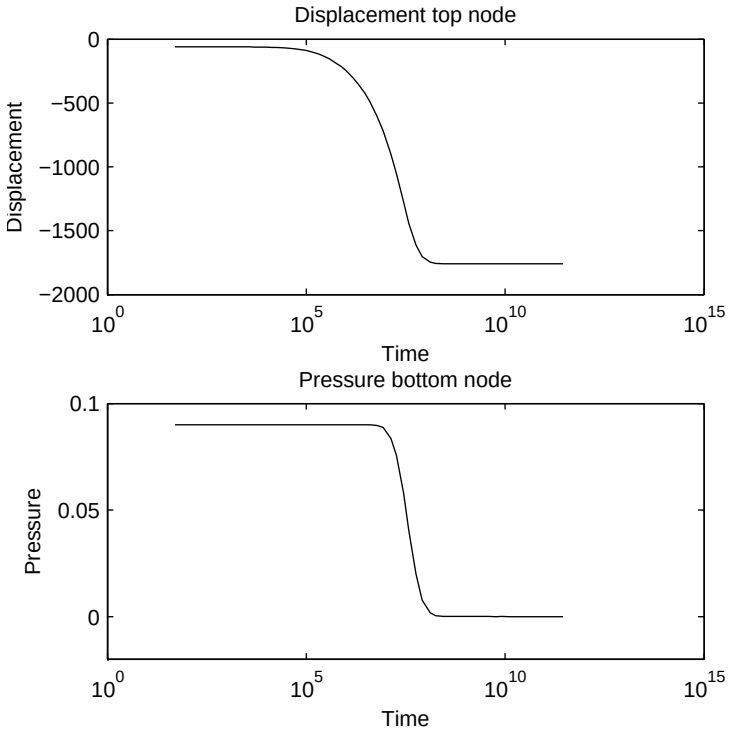

Figure 5-2: One dimensional consolidation: evolution with time $[s]$ of the displacement $[mm]$ of the top node and the pore pressure $[MPa]$ of the bottom node.

Numerical results and considerations

The consolidation process is summarized in Fig. (5-2), which plots the evolution with time of the displacement of the top node and the pressure of the bottom node. Only the overpressure is considered in this analysis, i.e. the hydrostatic pressure due to the self weight of the water is not taken into account.

The Figg. (5-3) and (5-4) plot the nodal Cauchy pore pressure and the vertical Cauchy effective stress at different time steps.

At the beginning of the consolidation process, as showed by the numerical results, the pore pressure counterbalances the applied external load. As far as the fluid permeates from the porous matrix, the solid skeleton counterbalances the external force, and therefore we observe the increase of the effective vertical stress. Since we assumed that the Biot coefficient $B = 1$, the sum of the pore pressure and the vertical effective stress must always be constant and equal to the applied external load. Note that both the pressure and the stress measures are computed with respect to the deformed configuration. It's therefore clear from this simple example that the equilibrium condition and the mass balance condition are imposed with respect of the updated configuration.
The Fig. (5-5) shows the isochrones at different time steps of the Cauchy pore pressure. The plot shows the diffusion process of the fluid through the column, until the steady state condition is

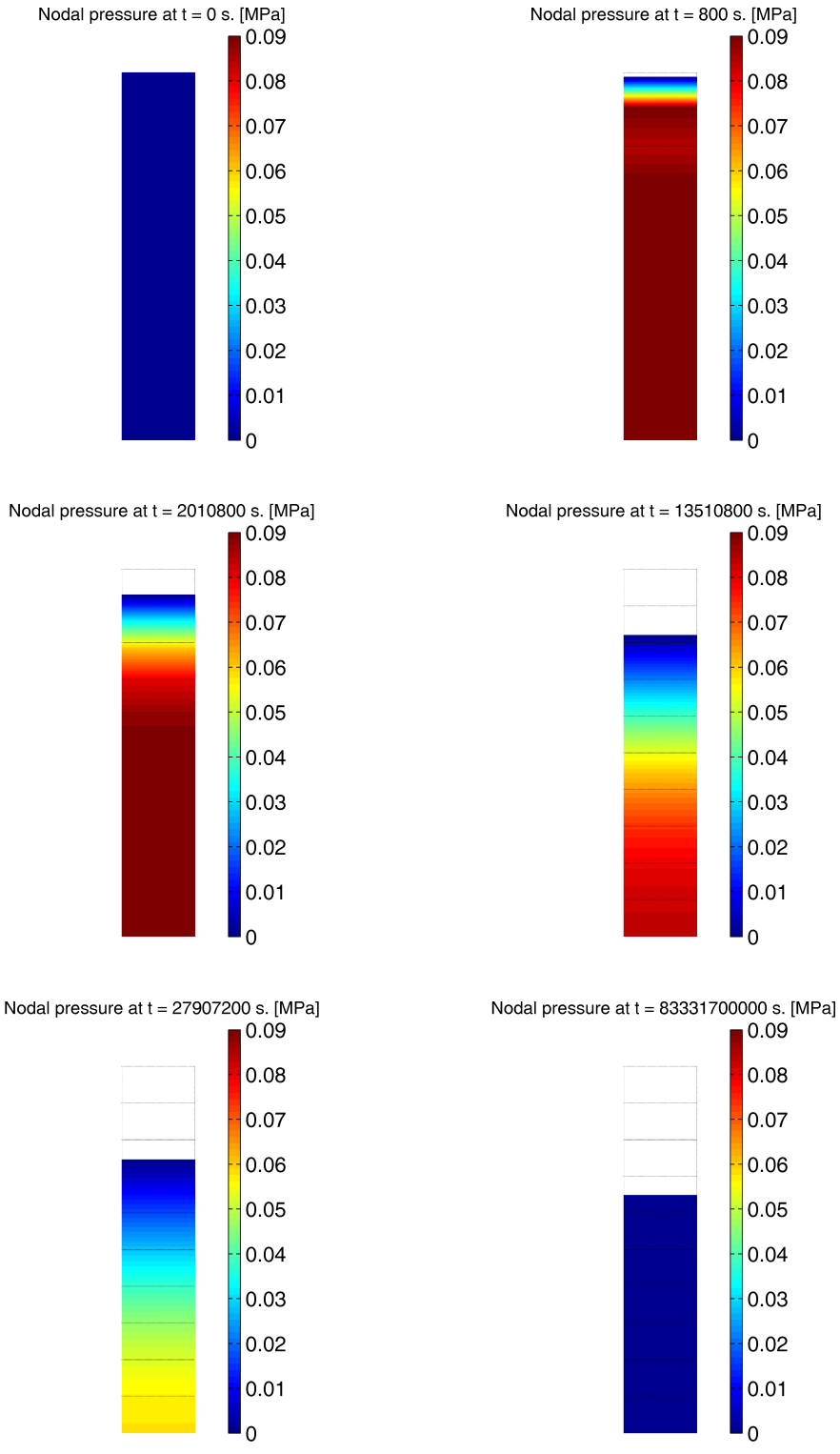

Figure 5-3: Nodal Cauchy pore pressure at different time steps.

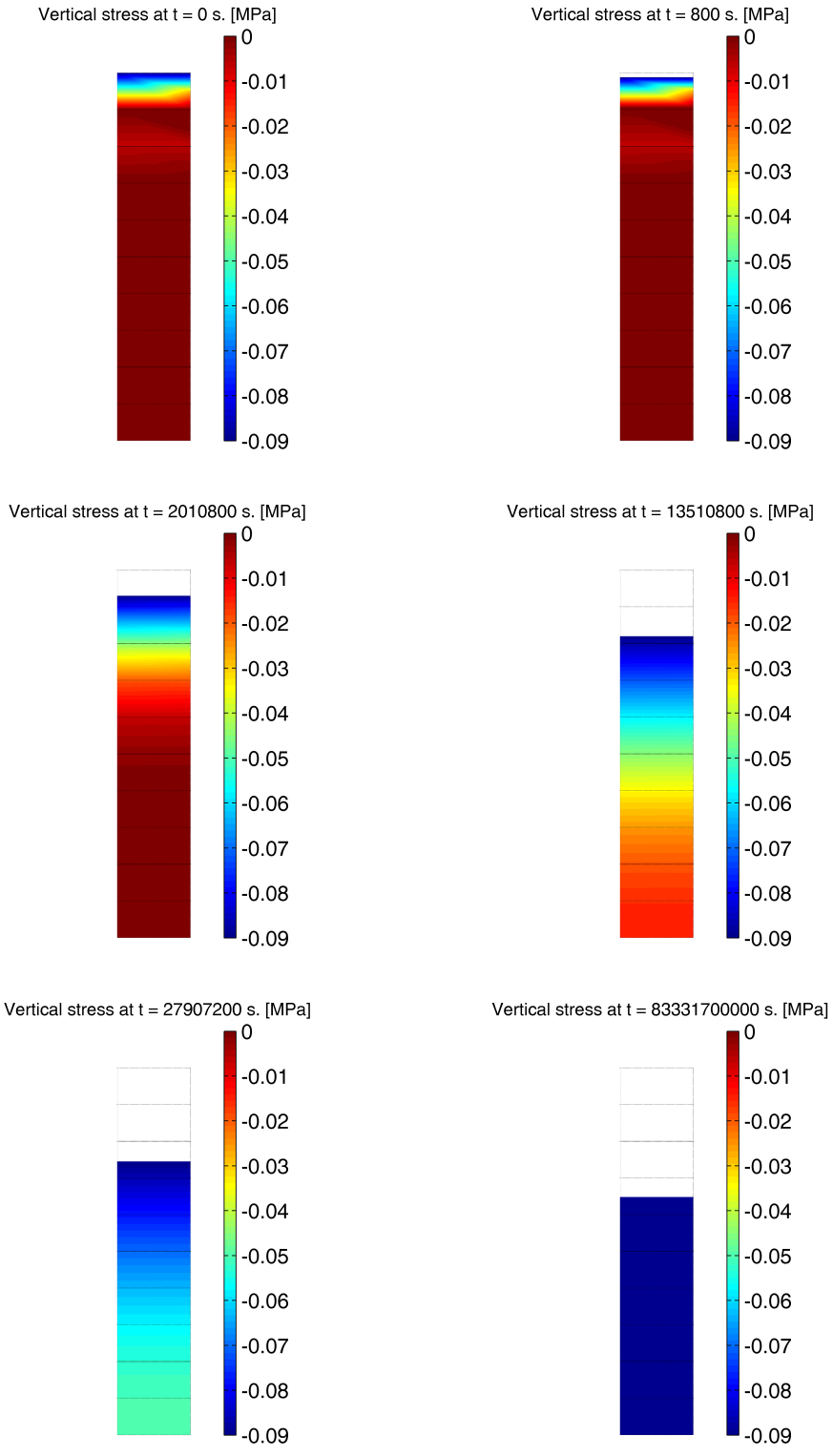

Figure 5-4: Cauchy effective vertical stress at different time steps.

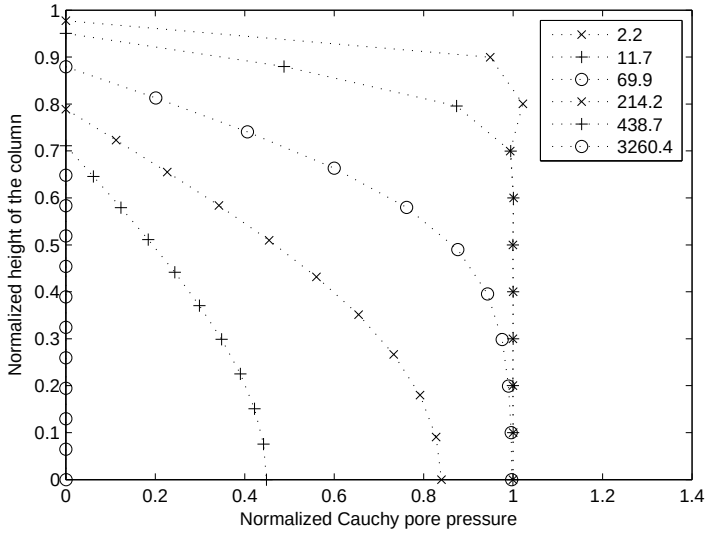

Figure 5-5: Isochrones of constant Cauchy pore pressure at different time [day].

reached with null overpressure in the column.

The Fig. (5-6) compares the results obtained by Borja et al. (1) for the same example, assuming also the small strain formulation (Terzaghi analytical solution). As can be observed, there is a significant difference between the two formulations. This is due to the fact that the considered material is pretty soft, and allows for significant displacement. Therefore, the small strain theory can't capture the correct final displacements. Furthermore, taking into account the updated configuration, the drainage length decreases as far as the consolidation proceeds, and hence the total time of consolidation is lower in the finite strain regime. Finally, note that the computed solution at finite strain is identical to the solution obtained by Borja et al., validating the implemented code.

Finally, Fig. (5-7) plots the convergence profile for different time step, showing the good performance of the implemented Newton-Raphson scheme.

5.2.2 Two dimensional plane strain consolidation

Description of the problem

We consider the problem of a strip flexible footing resting on a soft compressible clay. The problem is again solved using a two-dimensional domain, assuming plane strain analysis, and considering only one half of the geometry, taking advantage of the symmetry of the configuration.
The geometry and the boundary conditions of the problem are represented in Fig. 5-8.

The initial dimensions of the geometry are $B = 20000mm$ and $H = 5000mm$. It is applied instantly a strip load of intensity $q = -18KPa$ over a half-width of $b = 1000mm$, and after it is held constant. The domain assumes an impervious bottom base, that is fixed with respect to

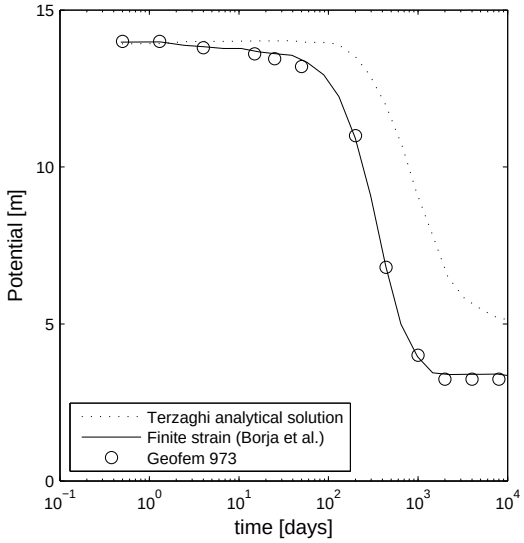

Figure 5-6: Comparison between the small strain and large strain formulation (1) for one dimensional elastic consolidation.

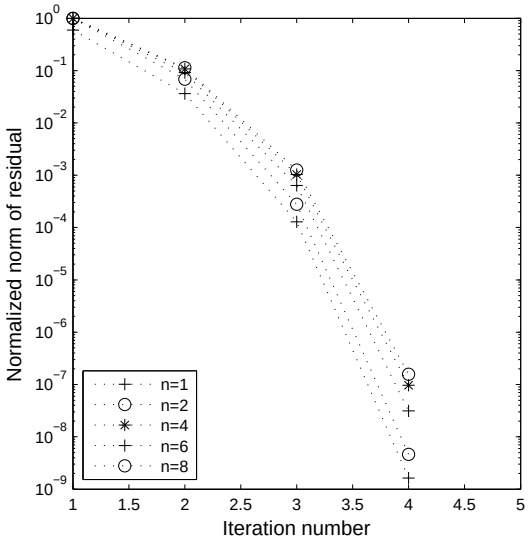

Figure 5-7: Normalized norm of force/fluxes residual vector versus iteration number.

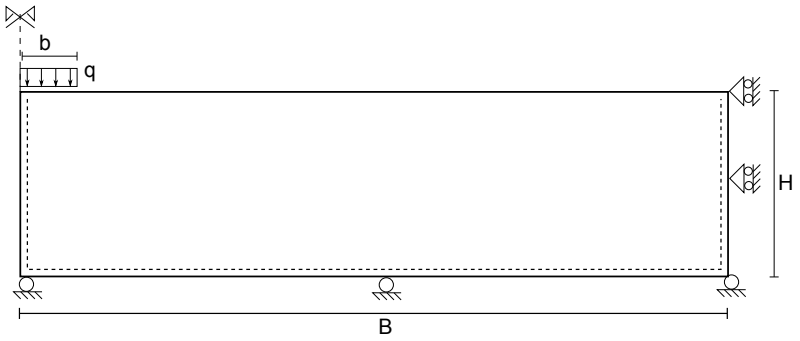

Figure 5-8: Two dimensional consolidation: geometry and boundary conditions.

displacements, zero horizontal displacements on the vertical sides, and zero excess pore pressure on the surface.

The material is modeled with the modified Cam-Clay described in Sec. 3.2.3. The assumed values of the material parameters are $\mu_0 = 200KPa$, $\alpha = 0$, $\kappa = 0.05$, $\lambda = 0.2$, $= 1$, $P_0 = -10Kpa$, $P_{c0} = -10KPa$ and $\epsilon^e_{v0} = -0.05$ (1). The density of the solid phase is $0.506ton/m^3$. The vertical permeability is assumed to have a value of $k_x = k_y = 0.864mm/day$ and the domain is fully saturated with water (unit weight $\rho_f g = 10KN/m^3$). The domain is discretized with quadrilateral `Quad8-4` elements. The initialization procedure entails running a preliminary analysis to generate the initial reference configuration produced by the gravity loads.

Numerical results and considerations

Fig. 5-9 plot the results of the initial configuration-when only the gravitational load is applied-in terms of nodal overpressure, equivalent Von Mises stress and preconsolidation pressure P_c. As can be observed, the fluid overpressure is uniformly equal to zero since the hydrostatic distribution is not taken into account. The equivalent Von Mises stress increases with depth, since it is due to the self weight of the solid skeleton. The preconsolidation pressure is equal to the initial value in top layers of the domain, while it increases in the bottom layers, defining the overconsolidation ratio of the domain. Therefore, the top layers are still in elastic regime and the bottom layers are in elastoplastic regime, at the beginning of the analysis. The vertical displacement, due to the application of the gravitational load of the top surface, is uniform and equal to $316.16mm$.

Fig. 5-10 represents the evolution with time of the nodal overpressure during the consolidation process. As can be observed, when the load is applied to the surface there is an immediate increase of the pressure just under the application point of the load. Then the diffusion process begins, dissipating the overpressure and reaching the final consolidated configuration. The displacement of the solid matrix evolves as far as the fluid diffuses through the porous matrix. The final displacement

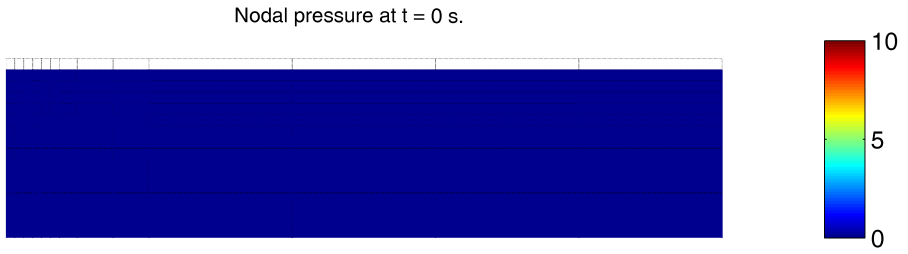

(a)

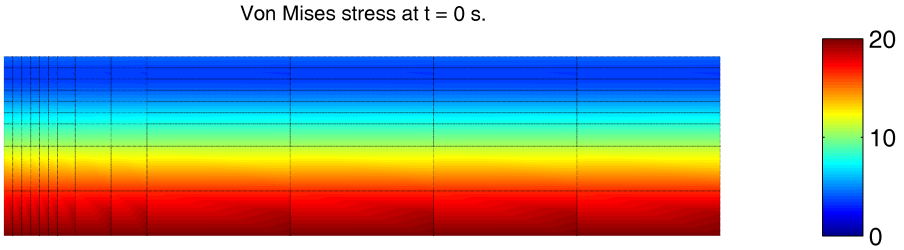

(b)

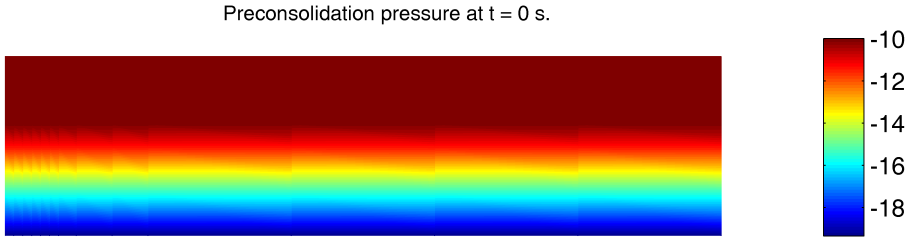

(c)

Figure 5-9: Initial configuration in terms of nodal pressure (a), equivalent Von Mises stress (b) and preconsolidation pressure (c)

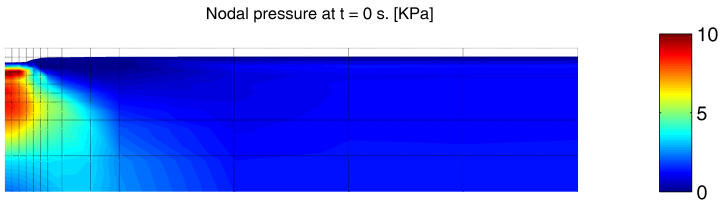

(a)

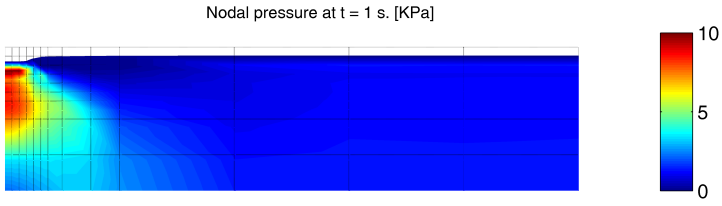

(b)

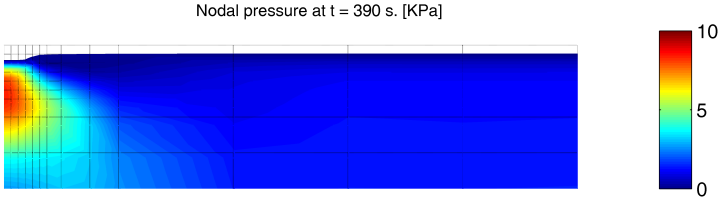

(c)

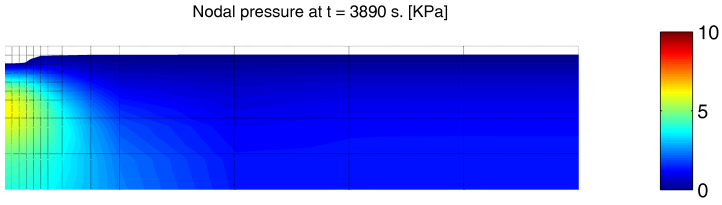

(d)

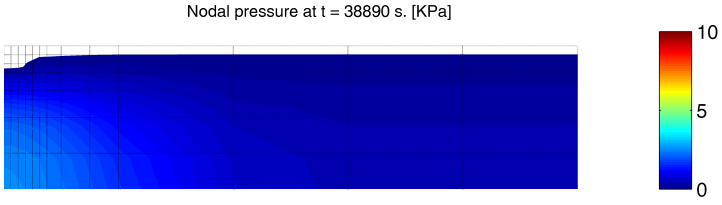

(e)

Figure 5-10: Nodal pore pressure distribution at different time steps.

of the top central node, due to the application of the gravitational load and the distributed load, is equal to $856.29mm$. This displacement is obtained when the load factor of the load is equal to 0.65, therefore the final displacement is computed for an applied load equal to $q = 0.65 \cdot 18 = 11.7KPa$. Behind this value the solution can't be computed, since the failure condition of the soil is found and the code can't converge to a meaningful solution.

Fig. 5-11 describes the evolution of the equivalent Von Mises stress with time. Initially the load is supported mainly by the ovepressure and later on, as far the diffusion process evolves, the load is carried by the solid matrix, with a consequent increase in the value of the effective stress.

Fig. 5-12 describes the evolution of the deviatoric plastic strain with time, focusing in the zone where the load is applied. At the beginning of the process the plastic deformations are relatively small, and they increase significantly at the end of the consolidation process. It is possible to observe the formation of a clear shear band, which constitutes the failure plane of the soil surface. In fact, after this point, the code can't find a stable solution of the problem, due to the loss of uniqueness.

5.3 Drilling process of an horizontal wellbore through a porous rock formation

5.3.1 Introduction

The second application which is investigated concerns the horizontal perforation of a horizontal wellbore in a porous fully saturated rock formation.

Wellbore instability in the oil and gas industry applications, in particular deep wellbore drilling, continues to be one of the major problems faced by scientists and engineers in that industry. The removal of the material, due to the drilling operation, alters strongly the in-situ stress concentration in the formation surrounding the hole, and can lead to localized stress-induced breakouts. Excessive breakouts can lead to problematic, and sometimes catastrophic, instabilities, resulting in well loss (73).

The problem of wellbore stability has become even more important in the last decades, due to the increasing number of horizontal and inclined wells, especially if the in-situ stress is significantly high. Drilling horizontal wells through producing strata can greatly improve reservoir drainage and hydrocarbon recovery. Moreover, under environmental restrictions, such as offshore platforms, inclined wells are drilled from a relatively small area towards all directions for a better exploitation. Drilling inclined and horizontal wells, though, is more difficult and more expensive, due to the more likely wellbore instabilities. To prevent instabilities during perforation, the wellbore is temporarily supported by the drilling mud pressure. If instability could occur, the value of the mud pressure need to be sufficiently high to prevent compressional failure, but also lower than a critical value which would

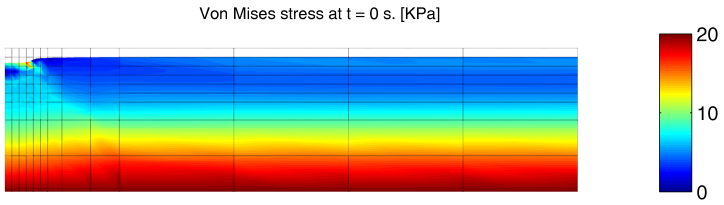

(a)

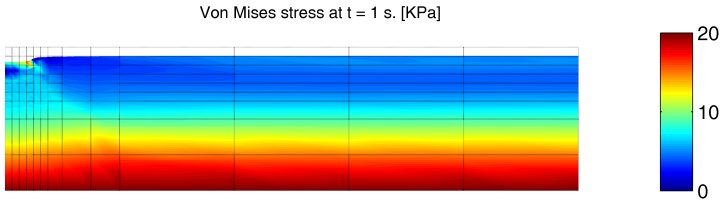

(b)

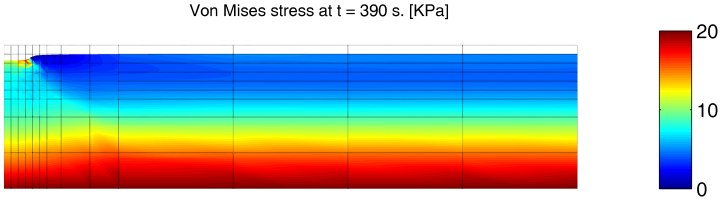

(c)

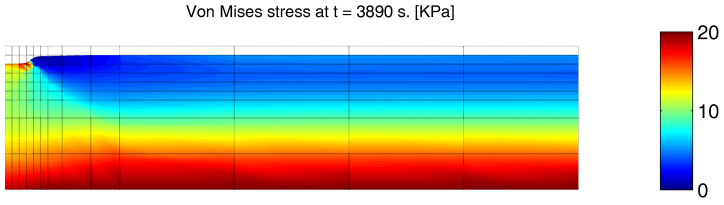

(d)

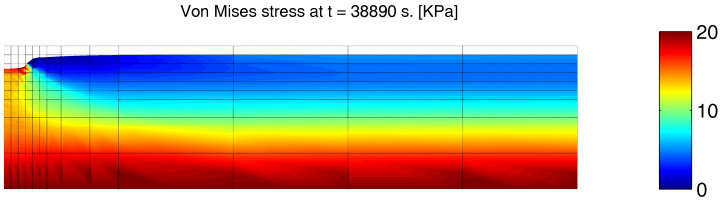

(e)

Figure 5-11: Equivalent Von Mises Cauchy stress distribution at different time steps.

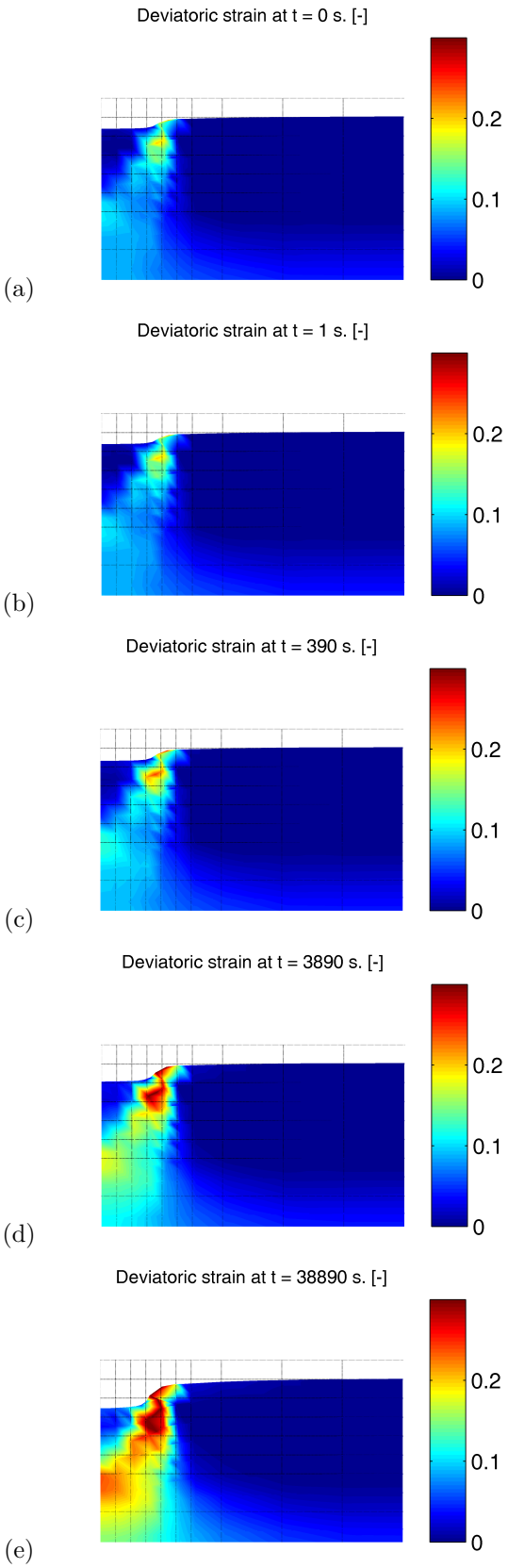

Figure 5-12: Deviatoric plastic deformation at different time steps.

cause tensile failure, and eventually consequent unintentional hydraulic fracturing. Nevertheless, even if the wellbore is sufficiently stable to avoid collapse, it's important to prevent sand production, since in horizontal well it may be more difficult to remove in horizontal well while drilling, resulting in a slower rate of penetration.

Traditionally the stability of a well is determined using models based on linear elasticity, and failure is assumed to occur when the stresses along the wall reach the failure or tensile strength of the rock. More realistic evaluation of the stability is predicted by elastoplastic models, which present the advantage of showing the extent of the damaged region, leading to a better indicator of instability. Clearly, this depend on the capability of the constitutive model to capture the different failure modes. Usually simple elastoplastic model such as Mohr-Coulomb or Drucker-Prager are used in the analysis, due to the lack of data available for the calibration of more sophisticated constitutive law. These models, characterized by a shear yield surface, can describe only the dilatant plastic mechanism preceding the failure, but are not able to describe the compactant plastic mechanism.

In the last two decades several experiments have been conducted on high porosity sandstones, to investigate in particular the compaction failure that can take place under certain stress conditions, in contrast with the more common dilatant failure (31; 32; 33).

Compactant failure typically occurs in porous rocks under relatively high confinement, with a failure mode conventionally described as homogeneous cataclastic flow, but can lead also to thin planar zones of pure compressional deformation, which are usually called 'compaction bands' (74; 75). Experimental studies on boreholes drilled in a cubical specimens of rock with different porosity, show that, if the porosity is high (22-25%), the failure is associated with the compactant mechanism, and in certain situation they developed a long and thin fracture, originated in the region of highest compressive stress concentrations (76; 77). These kind of mechanism failure, associated with a significant reduced of porosity, have as consequence a relevant reduction on permeability, thus adversely affecting the extraction or injection of fluids for energy production or storage. Additionally, the denser band material may affect the mechanical strength of the rock formation, causing damage of the wells, subsidence and trap sealing failure.

Since the compactant plastic mechanism can have an important role in the analysis of wellbore, an adequate constitutive elastoplastic model is necessary able to capture both the dilatant and compactant behavior, and the transition between this two failure criteria (2).

The simulations adopt the constitutive model developed in Sec. 3.2.4 for high porous rock. The model is calibrate against experimental data, showing the capability to reproduce laboratory test. In particular, the developed numerical model is applied to asses the stability of an horizontal wellbore, using experimental data available from a deep water reservoir offshore Brazil (4).

These simulations investigate the quasi-static transient phenomenon associated with the perforation, until the steady state condition is reached. The model describes the evolution of the stress

Description	Parameters
Hyperelastic response	k, P_0, $\epsilon^e_{v_0}$, μ_0, α
Plastic response (compactive side)	P_{i_0}, A, ϵ^*, r
Plastic response (dilatant side)	m, c_0, $\bar{m}$

Table 5.1: Parameters for the constitutive model

and pressure distribution, and moreover the propagation of the plastic zones around the borehole, elucidating the factors that either prevent or enhance the failure of the hole and the band initiation. The work demonstrates the capability of the finite deformations coupled approach to simulate the whole process.

5.3.2 Calibration of the constitutive model

This section discusses how the model can be calibrated against experimental data and at the same time shows the capability of the model to reproduce different laboratory test.
In the last two decades several experiments have been conducted on porous sandstones, with particular interest on the evaluation of the compaction mechanism and the transition from a dilatant to a compactant behavior (usually called brittle-ductile transition) (3; 55; 78; 79). The standard test consist on a triaxial experiment, in which the samples are ground to a cylindrical shape, jacketed with tubing, saturated with distilled water and deformed under fully drained conditions at a fixed pore pressure. In the various experiments, different axial and confining pressure are applied, monitoring the porosity change and the axial deformation.
In order to asses the capability and to calibrate the parameters of the presented constitutive model, we compare the numerical results with experimental data available from triaxial laboratory tests, conducted in different sandstones. Let us recall first the variables adopted, listed in table 5.1.

The parameters k, P_0 and $\epsilon^e_{v_0}$ determine the hydrostatic hyperelastic response, since they correlate the volumetric deformation ϵ^e_v with the pressure applied to the specimen according to Eq. $(3.47)_1$, assuming that ϵ^e_s is null. Therefore, they can be assessed considering the elastic part of the hydrostatic laboratory test on the rock. The reference pressure P_0 and the reference volumetric strain $\epsilon^e_{v_0}$ simply establish the position of the hyperelastic curve, so the value of one parameter depends on the value of the other. Note that, assuming $\epsilon^e_{v_0} = 0$, the initial bulk modulus is equal to P_0/k, which corresponds to the tangent in $\epsilon^e_v = 0$ of the hydrostatic curve in a (P, ϵ^e_v) diagram, then allowing better calibration of the parameter.
The parameters μ_0 and α control the deviatoric response, governing the deviatoric deformation with respect to the applied stress. In particular, the parameter α describes the pressure-dependence of the elastic shear modulus μ, but, since the effective mean normal stress did not vary significantly during testing, we assume that it is negligible, and we take a constant shear modulus. Once the

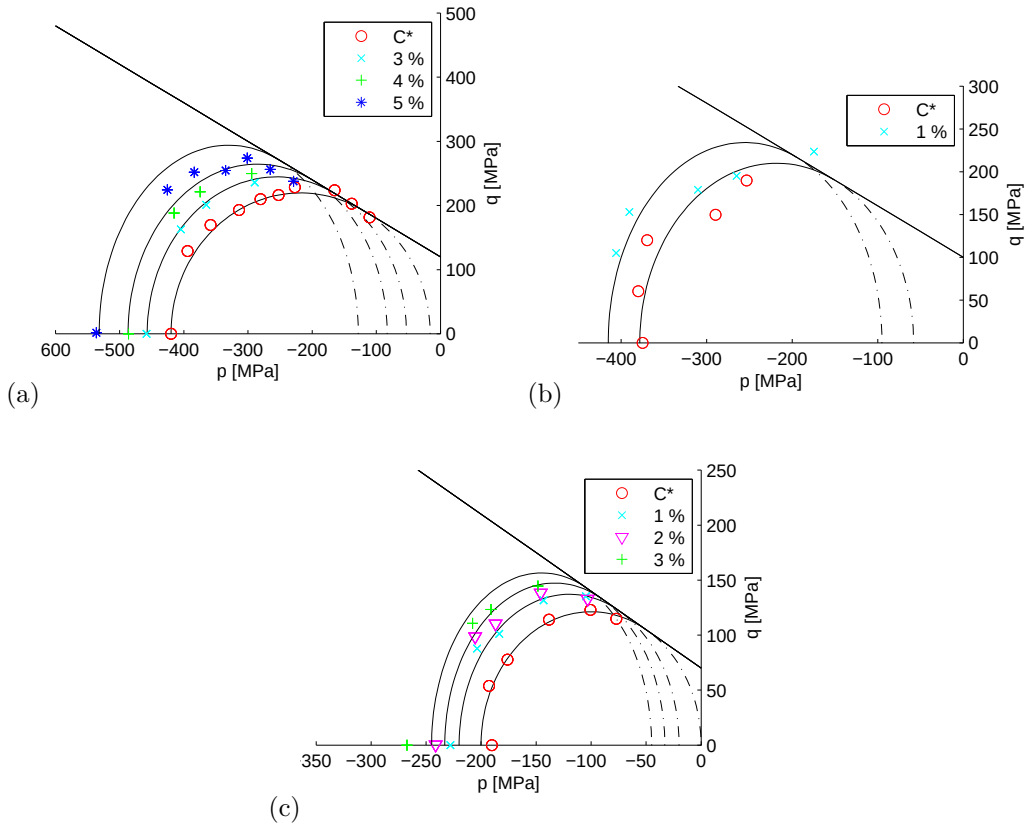

Figure 5-13: Evolution of the elliptical surface as function of the initial yield stress C^* and the plastic volumetric strain for (a) Bentheim, (b) Berea and (c) Adamswiller sandstones. Experimental data are taken from (2).

bulk modulus is known, the shear modulus can be estimated, assuming a reasonable Poisson's ratio. As far as the compactive plastic response, P_{i_0} and A, which describe the initial size of the elliptical yield surface, can be evaluated plotting the reduction of porosity after pore collapse starts for different loading path. Fig **??** represents experimental data on the initial yield stress (corresponding to pore collapse) and evolution of the yield stress as function of plastic volumetric strain for different sandstones. The data are interpolated by different ellipsis, with constant minor semiaxis A and variable major semiaxis B, giving preliminary information as regard the position of the initial ellipse and the linear yield function. Note that the pore collapse pressure, corresponding to the inflection point in the hydrostatic curve, is nothing but the sum of P_{i_0} and A. The parameters ϵ^* and r describe the hardening behavior of the compaction side, and the easiest way to calibrate is using the plastic part of the curve in the hydrostatic test.

Finally, m and c_0 determine the plastic dilatant behavior. Again, they can be assessed interpolating the experimental data of dilatant plastic deformation on a (p, q) diagram, for different loading path. Alternatively, if the cohesion c and the angle of internal friction ϕ are known, according to the Mohr-Coulomb friction law, m and c_0 can be estimated imposing that the linear yield surface

match the Mohr-Coulomb yield criterion. The parameter $\bar{m}$ controls the non associative flow rule for the dilatant side of the yield surface, and it is usually assumed to be lower than m, reflecting, that according to the experimental evidence, the dilatancy angle is lower than the frictional angle. The task is now to use the developed constitutive model to describe the hydrostatic compaction behavior of different rocks, using the return mapping algorithm presented in the previous section. The deformation process is governed by a scalar function $c(t) > 0$, $c(0) = 0$ which maps the point in the undeformed configuration $\boldsymbol{X}$ in the current configuration $\boldsymbol{x}$

$$x_A = (1 - c(t))X_A \qquad\qquad A = 1, 2, 3. \tag{5.1}$$

The deformation gradient $\boldsymbol{F}$ at time t_n can be evaluated as

$$\mathbf{F}_n = \frac{\partial \boldsymbol{x}_n}{\partial \boldsymbol{X}} = \begin{bmatrix} 1 - c_n & 0 & 0 \\ 0 & 1 - c_n & 0 \\ 0 & 0 & 1 - c_n \end{bmatrix}. \tag{5.2}$$

Hence, the relative deformation gradient $\boldsymbol{f}$ is

$$\boldsymbol{f} = \frac{\partial \boldsymbol{x}_{n+1}}{\partial \boldsymbol{x}_n} = \boldsymbol{F}_{n+1}\boldsymbol{F}_n^{-1}. \tag{5.3}$$

We view $c(t)$ as being applied in increments of Δc. Then (5.2) and (5.3) take the form

$$\boldsymbol{F}_{n+1} = \begin{bmatrix} 1 - (n+1)\Delta c & 0 & 0 \\ 0 & 1 - (n+1)\Delta c & 0 \\ 0 & 0 & 1 - (n+1)\Delta c \end{bmatrix}; \tag{5.4}$$

$$\boldsymbol{f} = \begin{bmatrix} \frac{1+(n+1)\Delta c}{1+n\Delta c} & 0 & 0 \\ 0 & \frac{1+(n+1)\Delta c}{1+n\Delta c} & 0 \\ 0 & 0 & \frac{1+(n+1)\Delta c}{1+n\Delta c} \end{bmatrix}. \tag{5.5}$$

where n indicates the number of the increment. The function $c(t)$ is increased, corresponding to a compression in the three principal directions, until the maximum value in compression is achieved, according to the experimental data. Then $c(t)$ decreases, and the complete loading and unloading path can be simulated.

For each increment n we define the deformation gradient $\boldsymbol{F}$ and then we compute the Jacobian $J = \det(\boldsymbol{F})$. Since we defined $\epsilon_A = \ln(\lambda_A)$ as the logarithmic principal stretch, we can write

$$\epsilon_v = \sum_{A=1}^{3} \epsilon_A = \sum_{A=1}^{3} \ln(\lambda_A) = \ln(\lambda_1\lambda_2\lambda_3) = \ln(J), \tag{5.6}$$

Parameter	**Sandstone**				
	Boise	Berea	Bentheim	St. Peter	Adamswiller
k (MPa)	0.015	0.015	0.010	0.030	0.015
P_0 (MPa)	-10	-12	-15	-10	-10
$\epsilon^e_{v_0}$	0	0	0	0	0
μ_0 (MPa)	500	500	500	500	500
α	0	0	0	0	0
P_{i_0} (MPa)	-40	-190	-210	-200	-100
A (MPa)	30	180	200	120	100
ϵ^*	-0.22	-0.1	-0.12	-0.18	-0.15
r	1.5	0.8	0.4	1.2	1.5
m	-1.0	-0.6	-0.6	-1.0	-0.7
c_0 (MPa)	100	100	120	145	70
$\bar{m}$	-0.7	-0.4	-0.4	-0.8	-0.6

Table 5.2: Parameters for the constitutive model

i.e. for every value of the the Jacobian we obtain the volumetric deformation. We define a procedure to determine the porosity reduction Δn, since the experimental data are usually expressed using this parameter. Assuming that V_0 and n_0 are respectively the initial volume and porosity ($V_0 = 1$ for the sake of simplicity), the deformed volume in the current configuration is nothing but $V = 1 - \Delta n$. Hence the the following relation holds

$$\epsilon_v = \ln(J) = \ln(V/V_0) = \ln(1 - \Delta n). \tag{5.7}$$

The numerical procedure consists in imposing the deformation, increasing linearly the function $c(t)$ with assigned increments, and compute the relative stress status, using as variables the principal logarithmic strains and the principal Kirchhoff tension, as explained in the previous section. In order to compare the results with experimental data is then necessary to convert the computed quantity with laboratory variables, i.e. the Cauchy tension $p = P/J$ and the changing in porosity Δn.
Fig. 5-14 represents the results obtained from the model compared with the experimental data for different hydrostatic compaction test of several sandstone. The value of the parameters adopted for the different rocks are listed in Table 5.2. With an appropriate calibration, the numerical results match really well the experimental data. In particular the model is efficient in capturing the nonlinear response of the elastic phase, the hydrostatic yield pressure (identified by the knee in the curve) and the hardening behavior during plastic compaction. Especially, this model turns to be particular accurate for those rocks in which the elastic or plastic response is highly nonlinear, giving better results than the traditional linear model. The constitutive model can describe efficiently also the unloading deformation process, for which an appropriate nonlinear elastic model is even more important to capture accurately the behavior. Further considerations can be done comparing the values among the different rocks, that may be helpful if the experimental data are not available. The parameters affected by the largest variation range are P_{i_0} and A, i.e. by the pore collapse pressure,

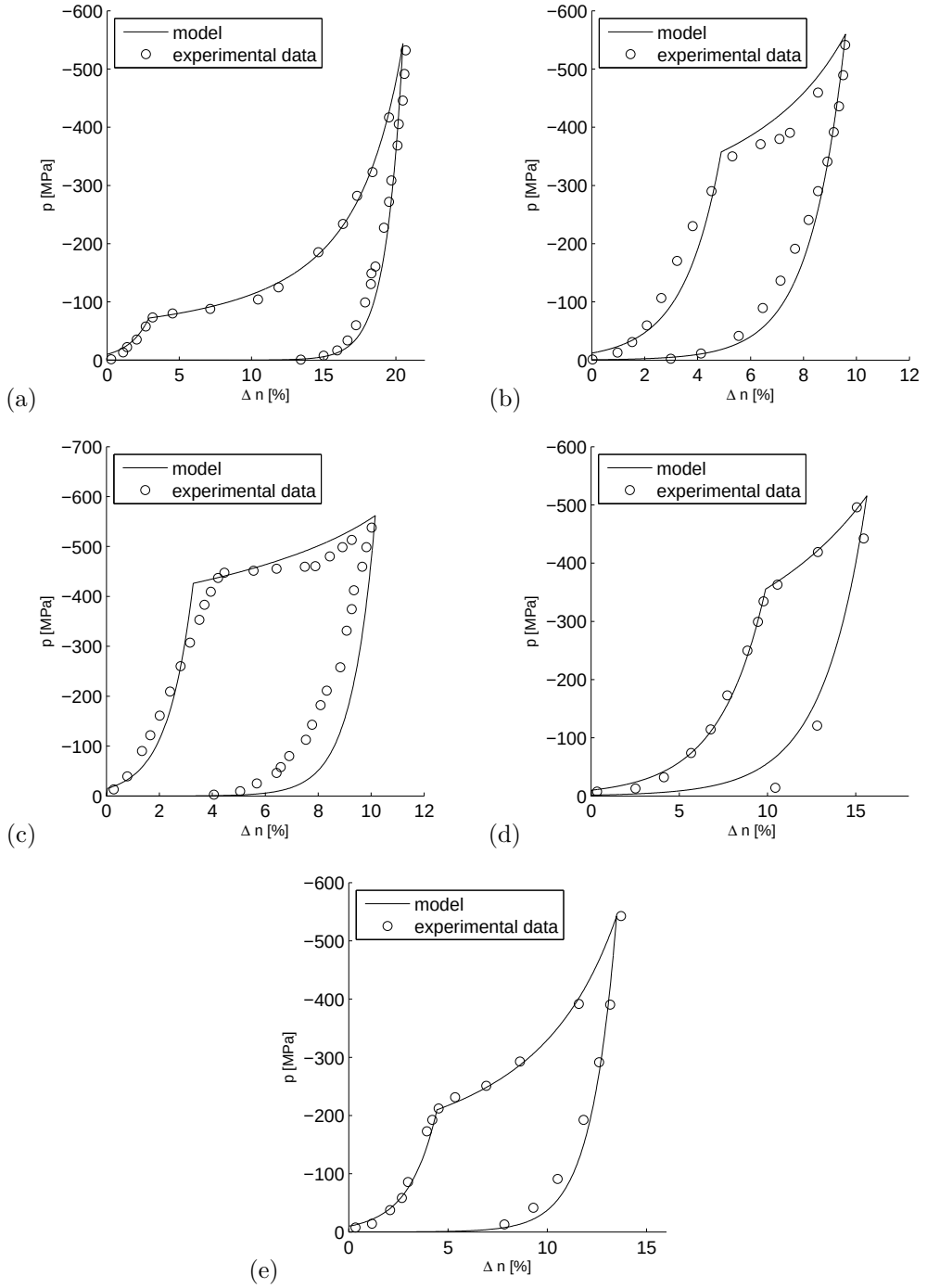

Figure 5-14: Comparison between experimental data and model simulation of a hydrostatic test for (a) Boise, (b) Berea, (c) Bentheim, (d) St. Peter and (e) Adamswiller sandstones. p is the Cauchy mean stress and Δn is the porosity reduction. Experimental data are taken from (2).

which vary significantly among the samples. Nevertheless, the value of the pore collapse pressure can be identified easily from a simple hydrostatic test. Therefore, the model can be used even if few laboratory data are available.

Let's now consider a triaxial compression experiment, where the porosity reduction is measured in function of the mean stress, for different values of confining pressure P_c. To reproduce numerically this laboratory test, we established a procedure in which the process is now driven by the stress. The value of P and $Q = 3(P - P_c)$ are increased by increment, with $P > P_c$ and P_c fixed, and for each increment the total volumetric strain ϵ_v is computed. This computed value is then converted in terms of porosity reduction, to make it comparable with common experimental data. For a given value of (P, Q), if the point that describes the stress status lies inside the elastic domain then the actual value of ϵ_v^e is computed according to Eq. (3.47). Since the stress point belongs to the elastic domain, ϵ_v^e corresponds to the total volumetric deformation ϵ_v. If the loading path intersects the yield surface in the linear side, then the surface cannot expand anymore and the limit load is identified, which is associated with a shear failure. Otherwise, if the loading path intersects the yield cap, the plastic surface expands, according to the hardening law. Thus for each load increment we updated the elliptical plastic surface imposing that $\mathscr{F}_2 = 0$, i.e. we determined the value of P_i such that the equation is fulfilled. Subsequently, we computed the volumetric plastic deformation ϵ_v^p relative to the stress status, which was summed to the elastic counterpart ϵ_v^e to obtain the total volumetric deformation ϵ_v. This procedure is summed up in the following box.

1. Initial stress state and hardening parameter: (P^{n+1}, Q^{n+1}) and P_i^n.
2. Check stress status: $\mathscr{F}_1(P^{n+1}, Q^{n+1})$ and $\mathscr{F}_2(P^{n+1}, Q^{n+1}, P_i^n) \geq 0$?
   - If No: elastic status.
     (a) Solve inversely (3.47) and compute ϵ_v^e and ϵ_s^e.
     (b) Update variables: $\epsilon_v = \epsilon_v^e$ and $P_i^{n+1} = P_i^n$.
   - If Yes: plastic status.
     – Check loading path: $P \geq P^*$?
     – If No: elliptical surface.
       (a) Solve inversely $\mathscr{F}_2(P^{n+1}, Q^{n+1}, P_i^{n+1}) = 0$ and compute P_i^{n+1}.
       (b) Solve inversely Eq. (3.74) and compute ϵ_v^p.
       (c) Update variables: $\epsilon_v = \epsilon_v^e + \epsilon_v^p$.
     – If Yes: linear surface. No expansion allowed.

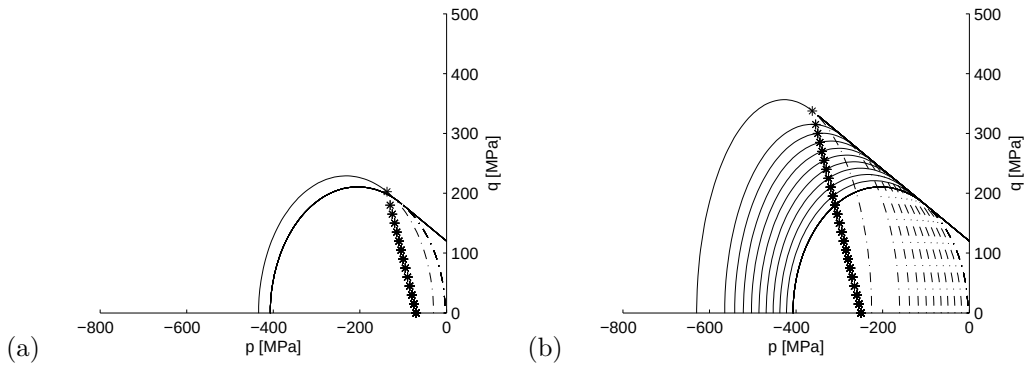

Figure 5-15: Expansion of the yield surface for different loading path, with confining pressure equal to (a) -70 MPa and (b) -250 MPa.

Two examples of loading path, starting from a different confining pressure, are shown in Fig. 5-15. For low value of confining pressure, the loading path intersects the dilatant yield surface, rather for high value it intersects the cap surface, determining a progressive expansion according to the hardening law for the compactant side. Note that for high confining pressure the plastic mechanism is compactant as far as the loading path intersect the cap surface, and finally it turns to be dilatant, according to the brittle-ductile transition theory.

In this case, we considered experimental results obtained from Berea, Bentheim and Darley Dale sandstones. Fig. 5-16 shows the results obtained, comparing the experimental data and the prediction obtained by the model. The model can capture well the plastic mechanisms, in particular with respect to the value of the stress yielding and the hardening behavior of the rock. Among the three porous rocks, the model fits better the experimental data for Berea and Bentheim. These two rocks are characterized by a sharp transition between elastic and elastoplatic behavior, with a dramatic decrease of porosity after the yielding pressure has been reached. The results are less accurate for Darley Dale sandstone, for which the transition from the elastic to the plastic response is smoother. Note that the hardening behavior becomes more nonlinear as far as the confining pressure increase, approaching the solution for hydrostatic compaction, according to the experimental data.

This procedure for calibration of the constitutive model discussed in this section will be adopted in the next part of the paper to evaluate the parameters for the rock formation where a horizontal wellbore has been drilled.

5.3.3 Description of the problem

The simulations are performed on horizontal wellbore drilled in Campos Basin field (4), a reservoir located 290 Km offshore Brazil cost. The water depth is about 1900-2400 m and the reservoir is located 5000 m underground, below a salt layer that may reach 2000 m. The formation is characterized by high porosity (20-30%) and low permeability (1-10 mD). An experimental investigation

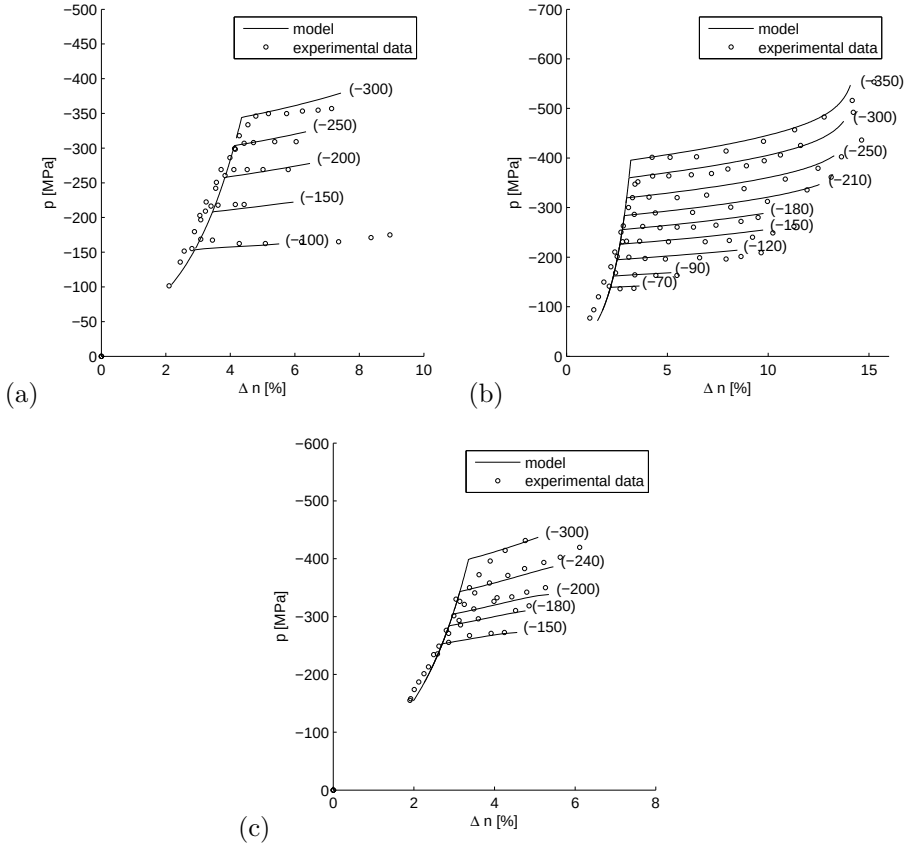

Figure 5-16: Mean stress versus volumetric strain for triaxial compression experiments on (a) Berea, (b) Bentheim and (c) Darley Dale sandstones. The confining pressures are indicated by numbers (in MPa) next to each curve. Experimental data are taken from (3).

Young's Modulus	Poisson ratio	Cohesion	Friction angle
E (MPa)	ν	c (MPa)	ϕ (°)
1200	0.15	8.5	42

Table 5.3: Available material parameters (4).

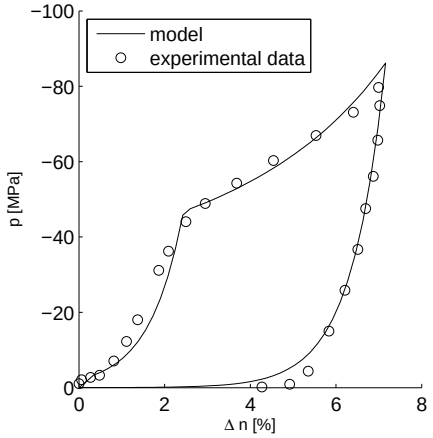

Figure 5-17: Hydrostatic compression test on Campos Basin field

was conducted to define the mechanical properties of the rock formation, testing samples with classical laboratory experiments. The parameters emerging from the investigations are reported in table 5.3. As discussed in the previous section, the availability of laboratory data permits a better calibration of the model. Fig. 5-17 reproduces the hydrostatic compression test conducted on a samples from the drilled rock formation. As done before, this experimental data has been used to calibrate the proposed constitutive model, in particular assessing k, P_0, $\epsilon^e_{v_0}$, P_{i_0}, A, ϵ^* and r. We considered a constant shear modulus μ_0 and its value was estimated from the bulk modulus, $\mu_0 = 3(1-2\nu)K^e/2(1+\nu)$, assuming $\nu = 0.15$. We evaluated the parameters to define the linear yield function, i.e. m and c_0, such that to approximate the Mohr-Coulomb yield surface. One of the most common approximations used is obtained by forcing both criteria to predict identical collapse loads under plane strain conditions. In this case (80) the constants m and c_0 read

$$m = -\sqrt{3}\frac{3\tan\phi}{\sqrt{9+12\tan^2\phi}}; \qquad c_0 = \sqrt{3}\frac{3}{\sqrt{9+12\tan^2\phi}}c, \tag{5.8}$$

where c is the cohesion of the rock and ϕ is the angle of internal friction. Since rocks are usually not particularly subjected to dilation, we assumed that the dilatancy angle is equal to 5°, and we extimated $\bar{m}$ again using the first of Eq. (5.8) Table 5.4 summarizes the parameters utilized for the constitutive model in the numerical simulations.

As far as the in-situ geostatic stresses in the reservoir production region, we assumed that the effective principal horizonatal stresses were equal in both principal directions, and read $\sigma_H = \sigma_h =$

Parameter	k	P_0 (MPa)	$\epsilon^e_{v_0}$	μ_0	α	P_{i_0} (MPa)
Value	0,01	-5	-0,01	600	0	-35

Parameter	A (MPa)	ϵ^*	r	m	c_0 (MPa)	$\bar{m}$
Value	10	-0,1	1,5	-1,08	10	-0.15

Table 5.4: Parameters data for high porosity rock of Campos Basin field.

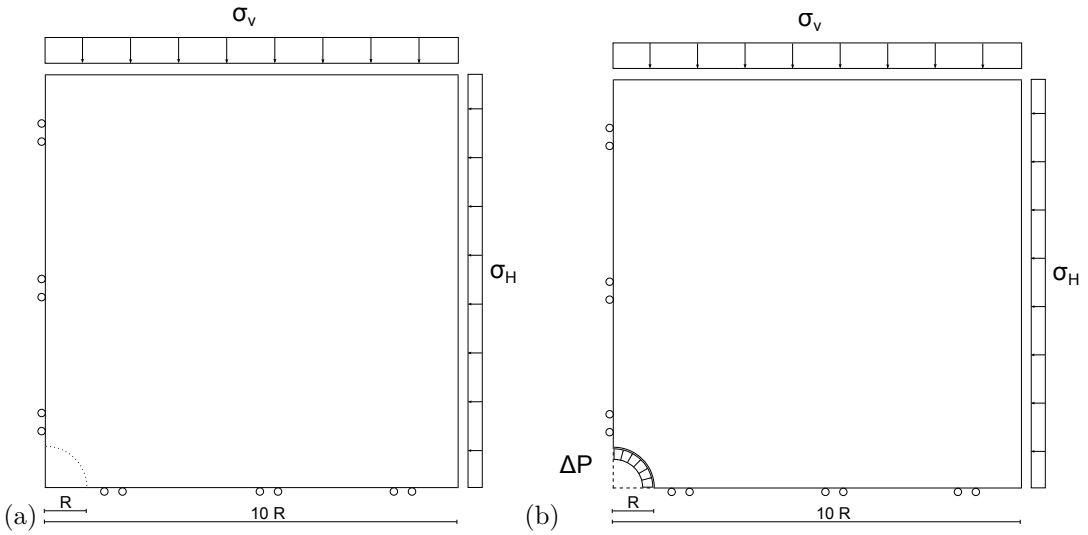

Figure 5-18: Plane strain domain of a quarter of the borehole. (a) In-situ configuration: only far field stress applied without the hole. (b) Drilling configuration: far field stress and mud pressure, with the hole.

9.0 MPa. The effective vertical stress was assumed to be $\sigma_V = 32.1$ MPa. The open-hole wellbore radius is $R = 4.25'' = 107.95$ mm. The wellbore axis is parallel to the direction of the principal horizontal far-field stress σ_h. Since the length of the well is much longer compared to the dimensions in the other directions, it is a reasonable assumption that deformations are constrained in the plane perpendicular to the axis. Hence, we assumed for this numerical analysis a plane strain condition. Then the principal stress acting on the plane of the borehole section are the vertical and the horizontal stress. The effects of the gravitational load are already accounted in the effective stress field, so the density of the material is ignored.

The dimension of the complete domain considered for the numerical simulation is ten times the radius of the bore. Since the problem is doubly symmetric, the discretized domain represents only one quarter of the complete geometry. The finite element geometry, with the boundary conditions, is represented in Fig. 5-18.

The analysis consists in two phases: first the vertical and horizontal stresses are applied to the complete domain, i.e. as the rock formation is still intact, in order to simulate the in-situ stress condition before the drilling process. Subsequently, the elements corresponding to the borehole are removed from the domain (decreasing progressively the stiffness), to simulate the process of drilling,

and the mud pressure is applied. Two type on analysis are performed: the first series of analysis considers only the mechanical problem, without considering the coupling effect between the solid and fluid phase. For this type of simulations the domain is discretized with standard quadrilateral 8-nodes element. The second series of analysis considers the coupled problem, taking into account the solid displacement/fluid diffusion process around the hole. This type of simulations use mixed `quad8-4` elements.

5.3.4 Numerical results and considerations

Solid analysis

In this section the simulations consider only the solid mechanical problem, without taking into account the coupled aspects between the solid and the fluid phases. Therefore all the measures of tension should be considered as effective.
In the first series of analysis we considered different values of the pressure $\Delta P = P_m - P_p$ applied on the internal wall of the cavity. P_m is the pressure of the mud used to support the wellbore and P_p is the pore pressure surrounding the hole. Except for special cases, the minimum mud pressure corresponds to the pore pressure in the rock formation so that the well does not flow while drilling. Hence, we assumed initially that $\Delta P = 0$ and then, incrementing the mud pressure, $\Delta P = 4$, $\Delta P = 8$, $\Delta P = 12$, $\Delta P = 16$ MPa. The aim of the analysis is to assess the stress configuration around the bore, the deformations, the plastic mechanism and the eventual formation of localization bands.
First of all, we computed the solution for $\Delta P = 0$ MPa using two different mesh refinement, in order to assess the optimal discretization of the domain and the eventual mesh sensitivity of the solution. The domain was discretized first with 448 8-nodes quadrilateral elements (the elements in the hole are not accounted), with 16 elements along the borehole. Then, the same domain was discretized with 1024 8-nodes elements, with now 32 elements along the wall. Fig. 5-19 shows the results in terms of plastic strain for the two refinements. As can be observed, the deformation around the hole in the coarser mesh is more diffused and the solution less accurate. Comparing the value of the plastic deformation at the Gauss Points of the first and last element along the wall, we observed relative differences up to 25 %. Hence, we adopted for all the analysis the finer mesh, which gave us better results in a still reasonable amount of computational time.
Fig. 5-20 represents the results obtained in terms of radial and circumferential stress and Fig. 5-21 in terms of volumetric and deviatoric plastic strain, for the different values of the mud pressure.

When the mud pressure is equal to the pore pressure surrounding the wellbore (a) $\Delta P = 0$ MPa we observe a wide plastic zone in correspondence of the area of maximum stress, i.e. along the

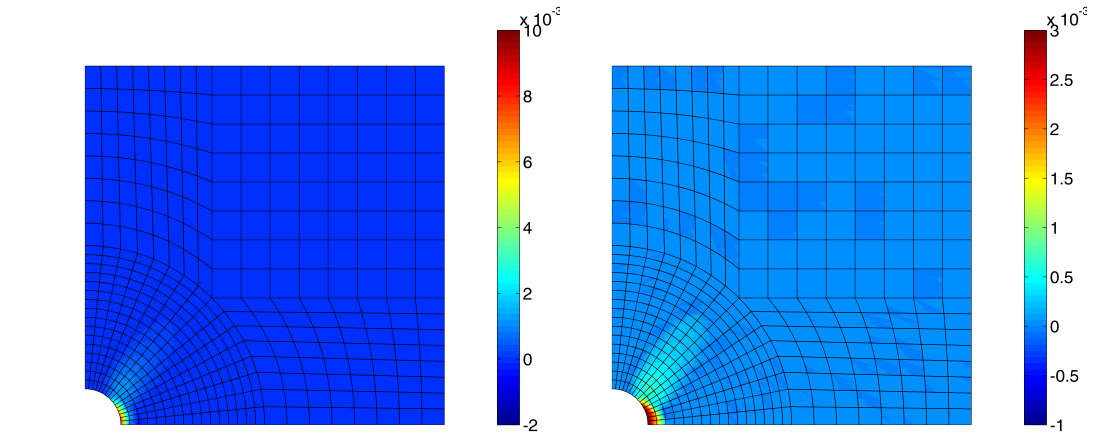

(a)

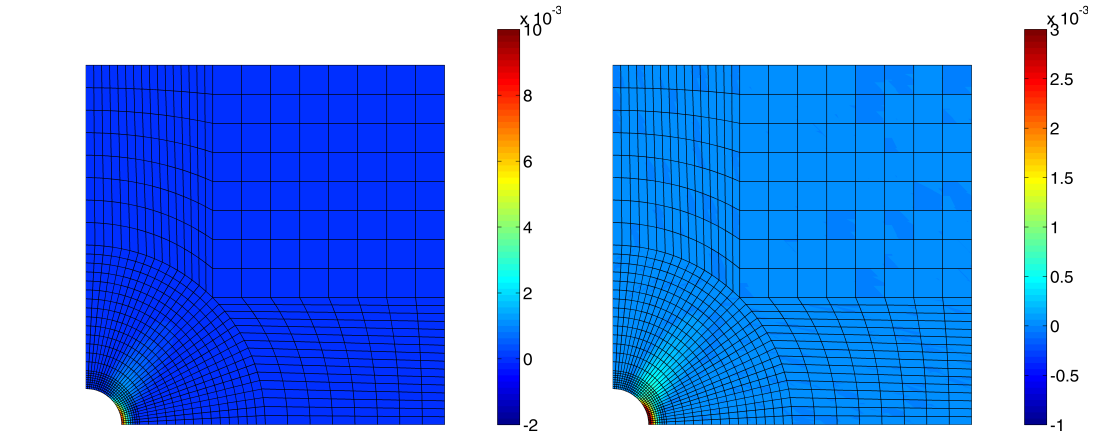

(b)

Figure 5-19: Volumetric (left) and deviatoric (right) plastic strain for different mesh refinement: (a) 448 8-nodes quadrilateral element, (b) 1024 8-nodes quadrilateral elements (elements in the hole not accounted).

bore wall in the direction of the minimum far field stress. In this area the plastic volumetric strain is positive, therefore the stress is such that the plastic mechanism is dilatant. When the pressure applied at the wall is increased, the maximum radial stress decreases, thanks to the contribution given by the mud pressure, and the plastic zone is reduced. When the effective pressure applied to the wall is $\Delta P = 4$ MPa (case (b)), the results show a narrower area where the material reached the dilatant plastic limit. For $\Delta P = 8$ MPa (case (c)) the dilatant plastic area is further reduced, but we observe that a new area characterized by negative plastic volumetric deformation begins. Hence, the stress field along the direction of minimum in-situ stress is such that the plastic mechanism is compactant. In addition, a new area of plastic deformation starts at the bore wall in the direction of the maximum far field stress, characterized by a dilatant behavior. For $\Delta P = 12$ MPa (case (d)) we observe two clearly distinct plastic zone. Along the direction of the minimum far field stress the rock formation reaches the compactant plastic limit. Along the direction of the maximum far field stress the dilatant

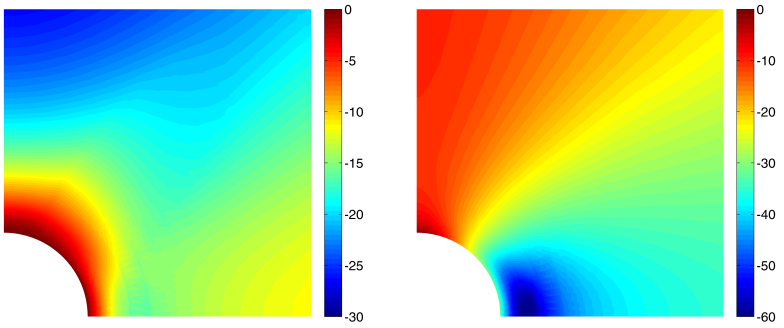
0
-5
-10
-15
-20
-25
-30
0
-10
-20
-30
-40
-50
-60

(a)

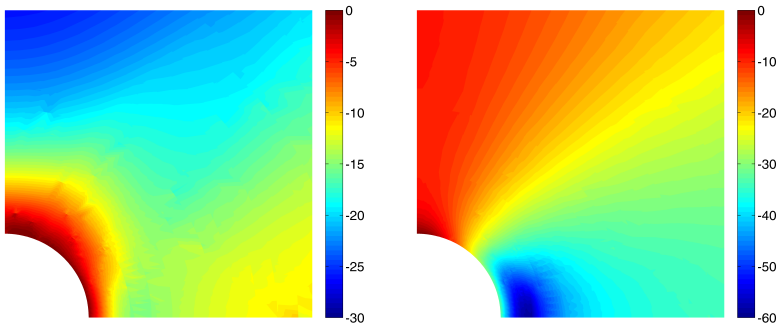
0
-5
-10
-15
-20
-25
-30
0
-10
-20
-30
-40
-50
-60

(b)

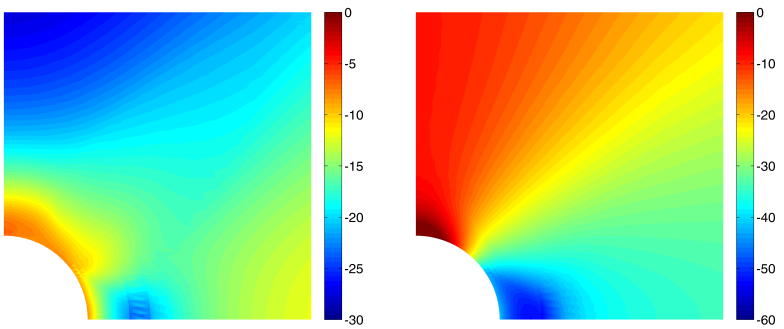
0
-5
-10
-15
-20
-25
-30
0
-10
-20
-30
-40
-50
-60

(c)

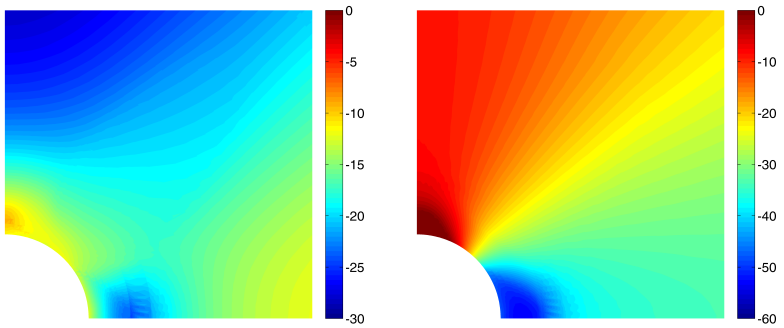
0
-5
-10
-15
-20
-25
-30
0
-10
-20
-30
-40
-50
-60

(d)

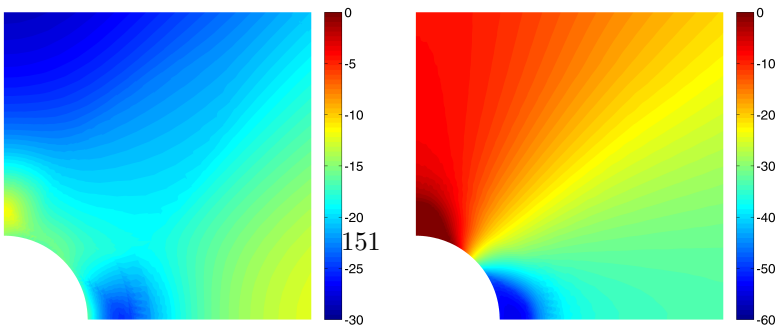
0
-5
-10
-15
-20
-25
-30
0
-10
-20
-30
-40
-50
-60

(e)

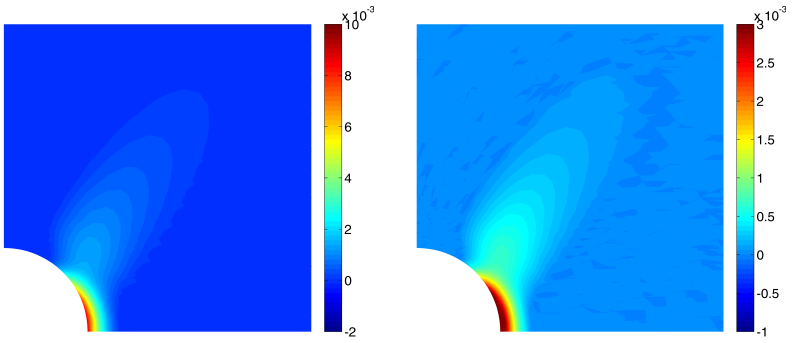
x 10^-3
10
8
6
4
2
0
-2
x 10^-3
3
2.5
2
1.5
1
0.5
0
-0.5
-1

(a)

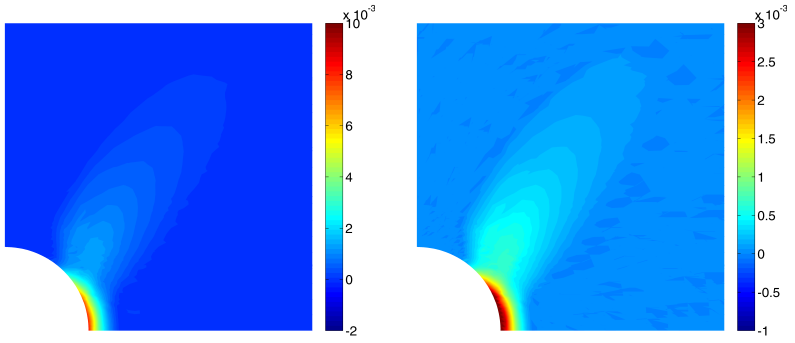
x 10^-3
10
8
6
4
2
0
-2
x 10^-3
3
2.5
2
1.5
1
0.5
0
-0.5
-1

(b)

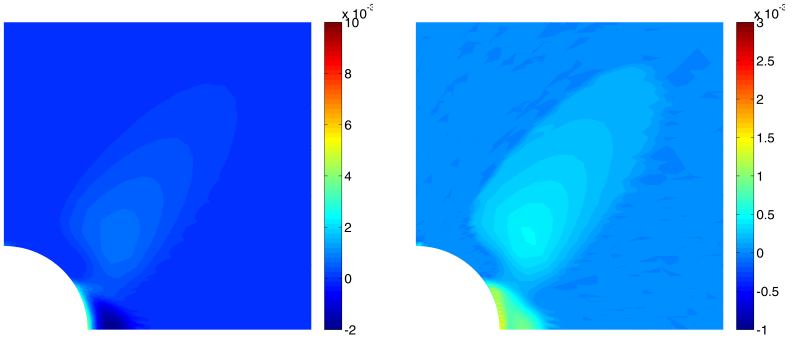
x 10^-3
10
8
6
4
2
0
-2
x 10^-3
3
2.5
2
1.5
1
0.5
0
-0.5
-1

(c)

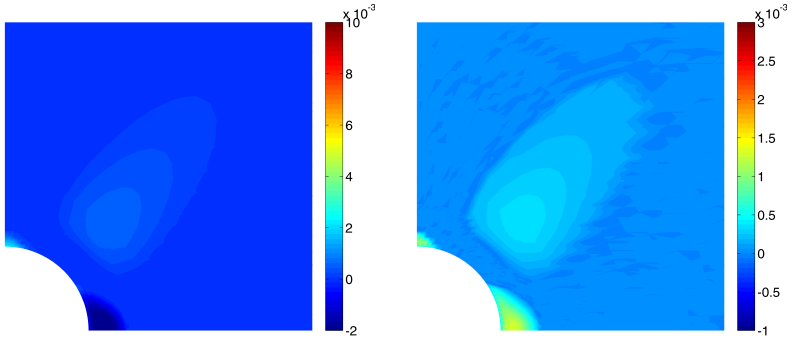
x 10^-3
10
8
6
4
2
0
-2
x 10^-3
3
2.5
2
1.5
1
0.5
0
-0.5
-1

(d)

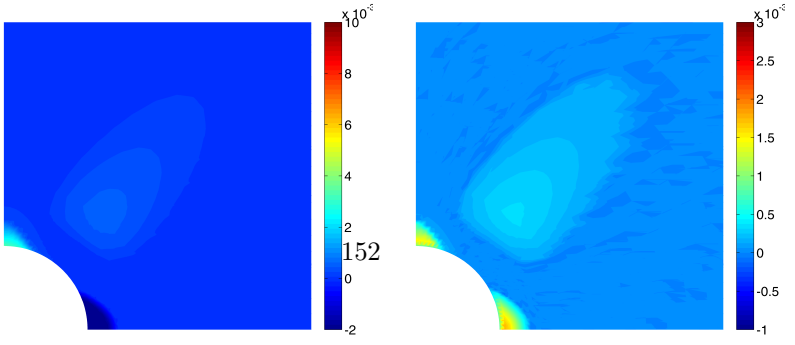
x 10^-3
10
8
6
4
2
0
-2
x 10^-3
3
2.5
2
1.5
1
0.5
0
-0.5
-1

(e)

plastic area further increased. For $\Delta P = 16$ MPa (case (e)) we observe a similar configuration, with the two distinct plastic zones. The numerical results show that an appropriate constitutive model is fundamental to capture correctly the elastoplastic status surrounding a horizontal well.
Note that the stress field around the hole is almost always negative, i.e. the rock formation is never subjected to a significant tensile stress that may cause a tensile fracture.
For this first set of configuration, where a constant in-situ stress and a varying mud pressure defined the stress status, we analyzed the localization function computed at every Gauss Point, to detect the eventual initiation of a shear or compactant band. The localization function F is calculated according to Eq. (**??**), computing the minimum value of the determinant of the Eulerian acoustic tensor defined in Eq. (**??**). Since the plane of the shear band is well defined, the search for the stationary point of F can be made by a sweep over half a unit circle. We defined localization when one or more Gauss points have detected the first negative incursion of the localization function. In this first series of analysis, the different stress configurations are not leading to any bifurcation point and no deformation band are observed.
Subsequently, we investigated how the variation of the in situ stress configuration influences the plasticity and the strain localization. Fig. 5-22 represents the most intriguing results in terms of deviatoric plastic strain on the left and in terms of localization function on the right. In this set of analysis we incremented the vertical in-situ stress and we maintained constant the horizontal stress and the mud pressure.

When the in-situ vertical stress is increased to the value of $\sigma_V = 39.0$ MPa (case (b)), we observe from the contour plot the initiation of a deformation band, arising from the bore wall. The band is associated with high deviatoric plastic deformation, therefore the formation of this band is associated with dilatant plastic mechanism. For an effective vertical stress equal to $\sigma_V = 42.0$ MPa (case (c)) the presence of the band is completely evident. Note that the simulations are valid only up to the bifurcation point and slightly beyond it, otherwise will exhibit mesh sensitivity, and finite element enhancement techniques are needed (81). We obtained similar results decreasing the value of the horizontal in-situ stress, maintaining constant the effective vertical stress. The numerical simulations suggest that, for the rock formation in analysis, a ratio between the vertical and horizontal stress of 4.3 is the threshold to develop strain localization.
In the first set of analysis we pointed out how the value of the mud pressure affects the plasticity around the wellbore. Therefore, we investigated how a variation of the mud pressure influences the band initiation. Fig. 5-23 shows the most relevant results obtained increasing the vertical effective stress with a constant mud pressure $\Delta P = 4$ MPa.

The initiation of the first localization band is detected when the vertical stress is increased to the value of $\sigma_V = 40.5$ MPa. The contour of the plastic deformations determines that what observed is a shear band. Comparing this result with the condition for band initiation when no overpressure

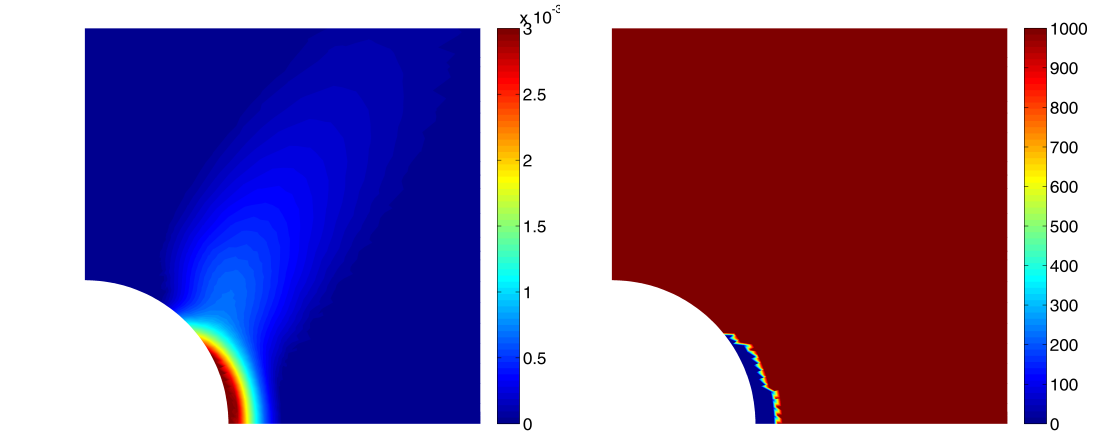

(a)

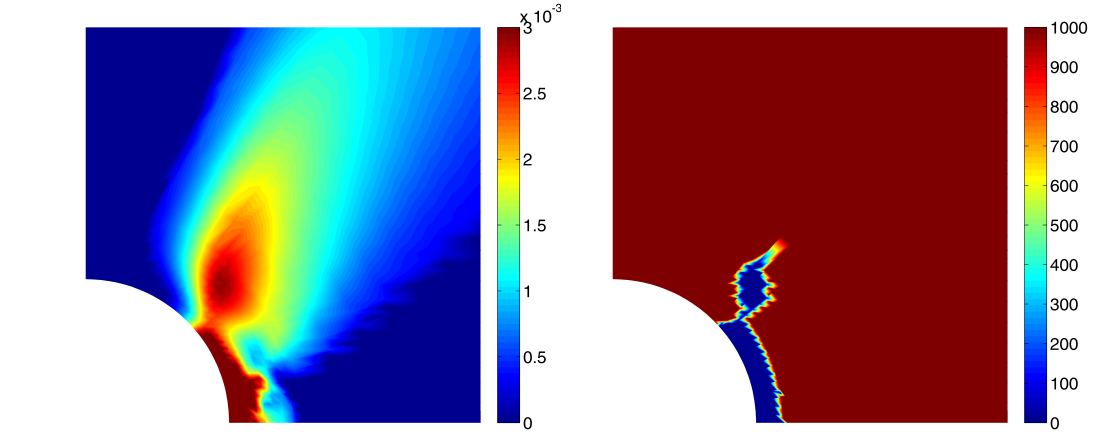

(b)

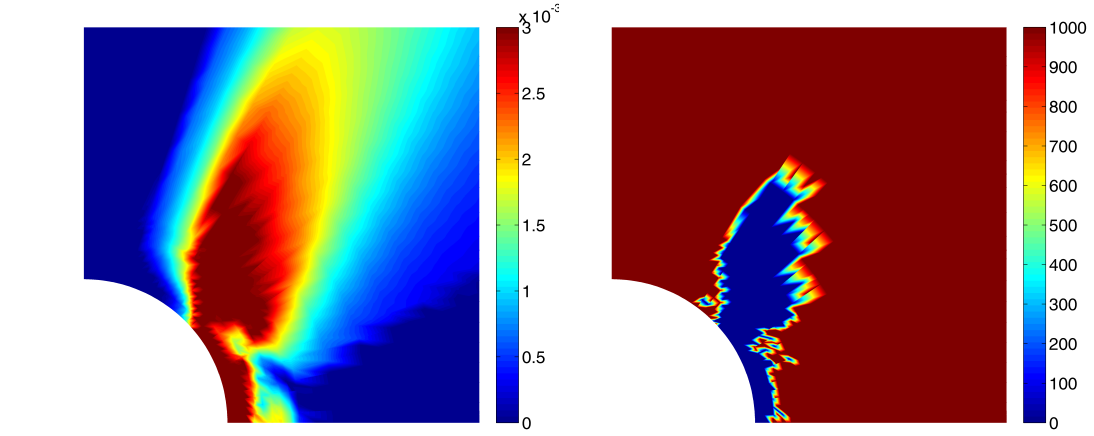

(c)

Figure 5-22: Plastic deviatoric deformation (left) and localization function (right) for different value of the vertical in-situ stress (a) $\sigma_V = 32.1$, (b) $\sigma_V = 39.0$, (c) $\sigma_V = 42.0$ MPa with balanced drilling ($\Delta P = 0$ MPa).

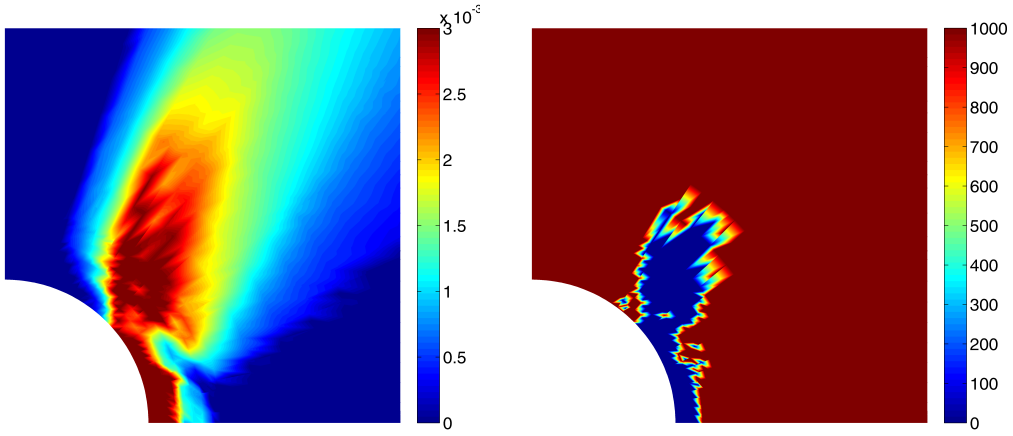

Figure 5-23: Plastic deviatoric deformation (left) and localization function (right) corresponding to the formation of band when $\sigma_V = 40.5$ with applied pressure $\Delta P = 4$ MPa.

is applied at the wall, we conclude that increasing the mud pressure slightly prevents the formation of band. However, it doesn't affect the plastic mechanism involved and the same failure pattern is observed.

So far we considered that the wellbore is perfectly circular, assuming a regular geometry in the finite element analysis. It is very unlikely that a wellbore has a perfect circular shape, in particular when drilled in a formation of high porosity rock. During drilling operations breakouts may occur, usually along the direction of the minimum far field stress, but these breakouts are tolerated as long as the stability of the well is not a concern. Then, we investigated how the presence of a breakout in correspondence of the direction of minimum in-situ stress can influence the plasticity and the formation of band around the hole. At this scope, we modified the discretized domain changing the geometry of the hole to reproduce the imperfection. Therefore, we performed another set of numerical simulations, to investigate the effect of an imperfection around the wall of the well. The vertical in-situ stress was incremented progressively, while the horizontal in-situ stress and the mud overpressure were maintained constant, respectively $\sigma_h = 9.0$ MPa and $\Delta P = 0$ MPa. The most interesting results are again related to the initiation of band of large deformation. Fig. 5-24 shows that, in the presence of an imperfection, the formation localizes at a significant lower value of the effective vertical stress.

When $\sigma_V = 22.5$ MPa (case (a)) the first bifurcation points appear, leading to a shear band of intense deformation. Increasing the vertical stress to the original value $\sigma_V = 32.1$ (case (b)) we observe that the band propagated even further. When the vertical stress is equal $\sigma_V = 39.2$ (case (c)) the band achieved a relevant extension and we interrupted the analysis. The band is associated with large deviatoric plastic strain. The origin of the band is in correspondence of the imperfection around the wall, and it propagates along the vertical direction. As demonstrated by the numerical

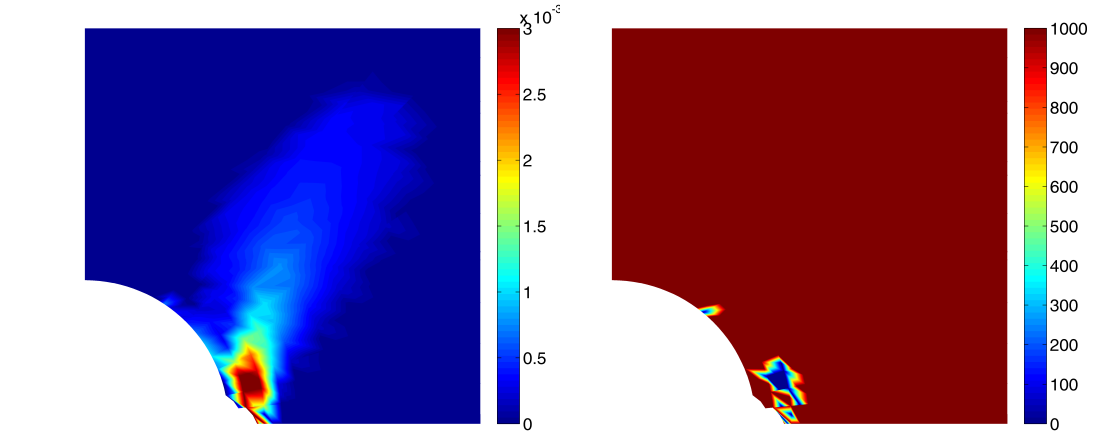

(a)

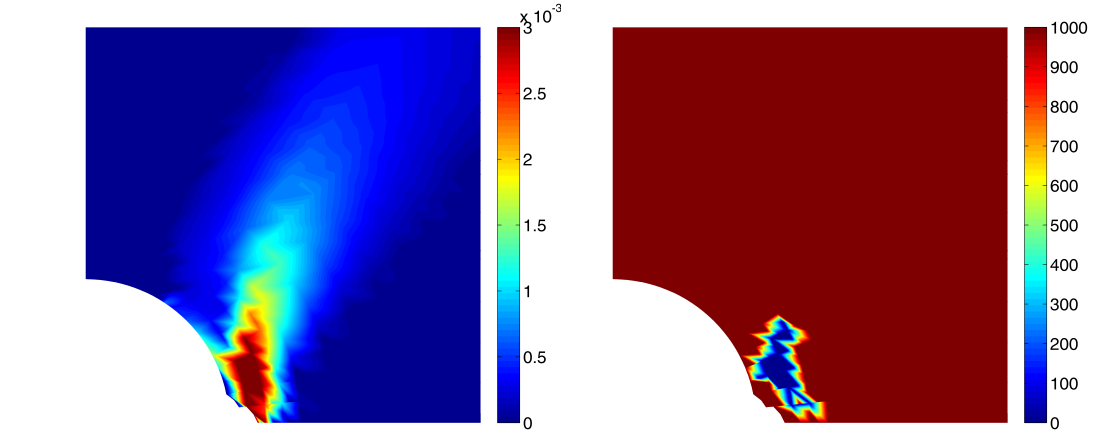

(b)

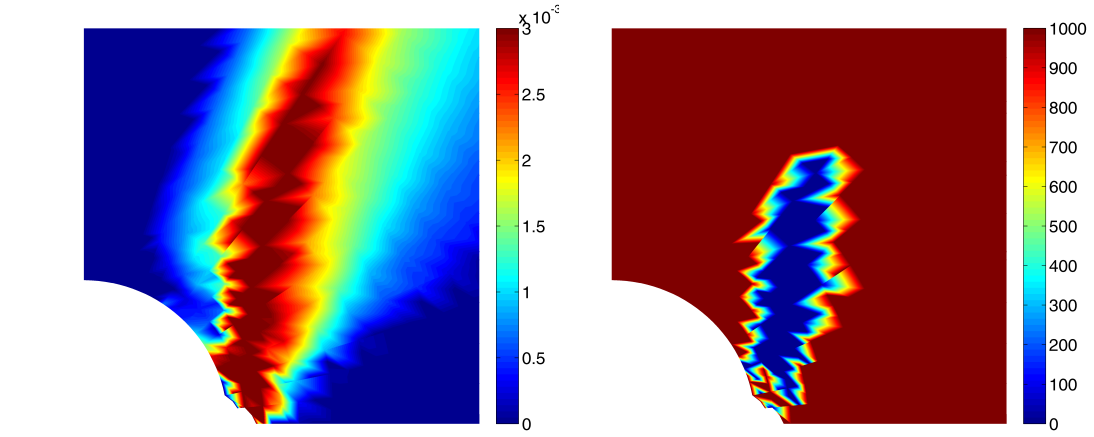

(c)

Figure 5-24: Plastic deviatoric deformation (left) and localization function (right) for different value of the vertical in-situ stress (a) $\sigma_V = 22.5$, (b) $\sigma_V = 32.1$, (c) $\sigma_V = 39.2$ (MPa) with balanced drilling ($\Delta P = 0$ MPa) assuming an imperfection around the wall.

simulation, the presence of imperfections can play an important role in the analysis of the plasticity and localization condition around a borehole, with relevant consequence in determining the stability of the well. The question that we would address now is how the mud pressure influences the condition for band localization, with an imperfection along the wall. Therefore, we applied a radial pressure at the domain with the imperfection, used in the previous analysis, and we increased incrementally the vertical effective stress. Fig. 5-25 shows the most relevant results for $\Delta P = 4$ MPa and $\Delta P = 8$ MPa applied to the borehole wall.

Comparing with the precedent result, we observe that the mud pressure influences significantly the band initiation. In fact, the effective vertical stress associated with band initiation is $\sigma_V = 29.6$ MPa for $\Delta P = 4$ MPa and $\sigma_V = 40.8$ MPa for $\Delta P = 8$ MPa, i.e. increasing the mud pressure helps in preventing band formation. Note that the shear band begins again in correspondence of the imperfection, but the direction is now less vertical, due to the difference stress condition.
The diagram in Fig. 5-26 summarizes the results obtained as concern the band initiation for all the simulations performed. The graph shows for every value of the mud pressure the corresponding value of the vertical stress that leads to a band initiation. When the hole is perfectly circular, increasing the mud pressure from the initial value $\Delta P = 0$ MPa slightly prevents the formation of a band. However, after the value has been increased up to $\Delta P = 4$ MPa, the beneficial effects are not observed anymore. When the hole is not perfectly circular, the mud pressure has a strong influence in the initiation of the bands. The results show a proportional correlation between the value of the pressure and the vertical stress necessary to initialize a deformation band.

Coupled analysis

The problem is now solved considering the coupling effects between the solid and the fluid phases, using the same geometry of the previous set of analysis. The fundamental difference of this method on analysis is that now the whole process can be simulated, taking into account not only the final steady state condition, but also the evolution of the process with time. In fact, this is inherently a process that evolves with time. Displacement boundary conditions are applied as in the previous analysis. In order to simulate the drilling process, the analysis is carried out in two stages. In the first stage, the full mesh is considered, the pressure is set equal to the pore fluid pressure of the reservoir in all the boundaries of the two external faces and the external loads simulating the in-situ stress are applied. In this fashion, the steady state condition of the intact reservoir is obtained, where the in-situ stresses are in equilibrium with the reservoir pore pressure. In the second stage the perforation of the wellbore is reproduced. The stiffness of the elements corresponding to the hole is progressively decreased, and at the same time the permeability is set to a very high value. At the same time, the value of the mud pressure is imposed to all the nodes along the wall. In this fashion, the complete diffusion problem is captured, until the steady state condition is reached. As

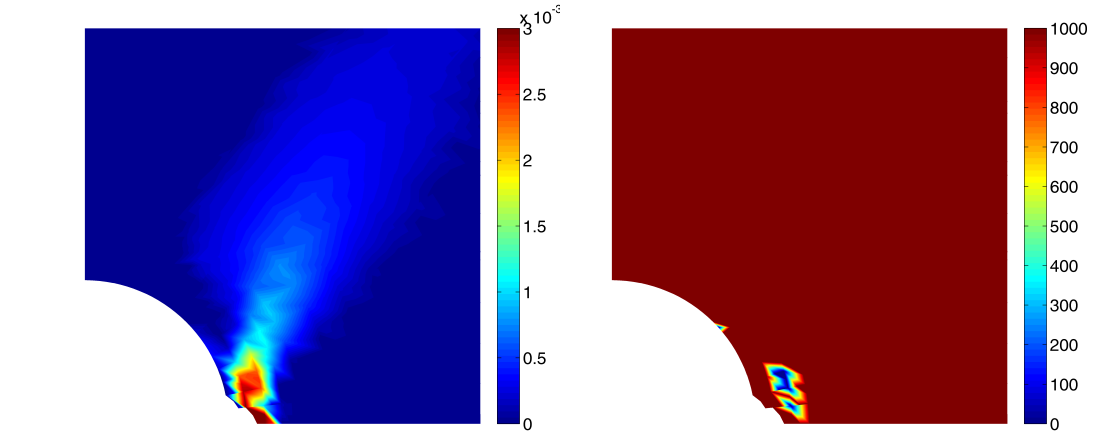

(a)

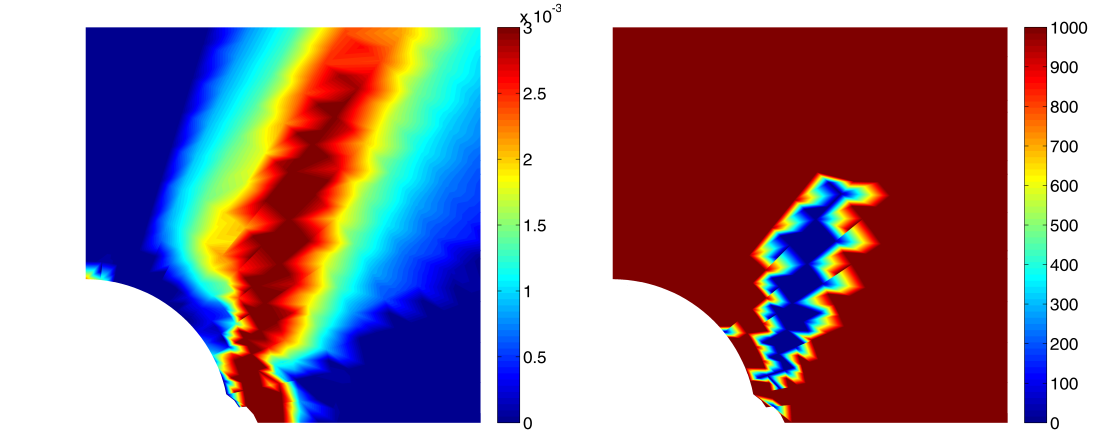

(b)

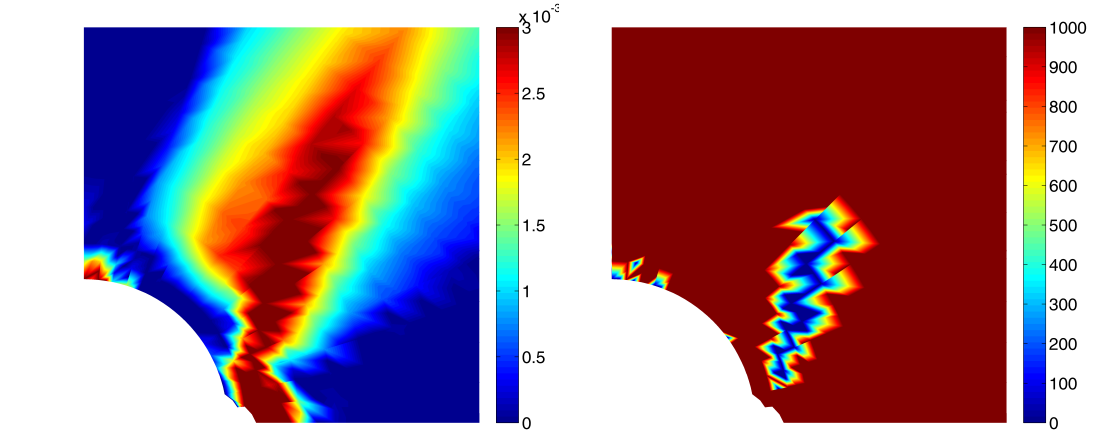

(c)

Figure 5-25: Plastic deviatoric deformation (left) and localization function (right) for different value of the vertical in-situ stress (a) $\sigma_V = 29.6$ (band initiation) and (b) $\sigma_V = 40.0$ with applied pressure $\Delta P = 4$ MPa, (c) $\sigma_V = 40.8$ (band initiation) with applied pressure $\Delta P = 8$ MPa assuming an imperfection around the wall.

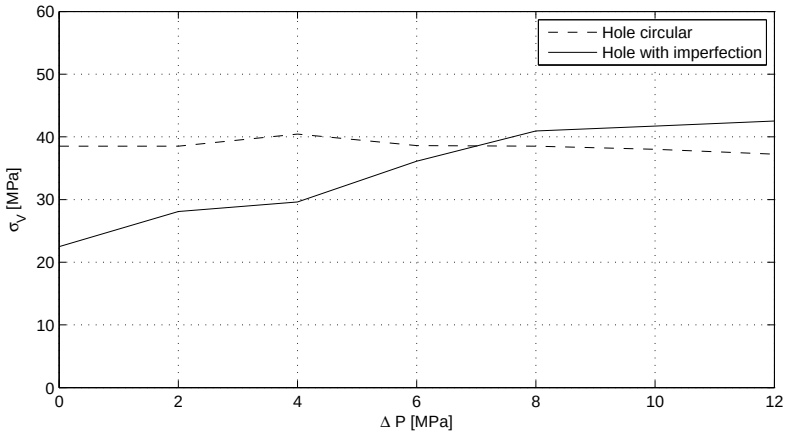

Figure 5-26: Vertical stress σ_V corresponding to band initiation for different value of the mud pressure ΔP.

far as the conductivity properties of the porous rock, the permeability of the rock is assumed to be $K = 10mD$ which corresponds to an approximate value of $\frac{\boldsymbol{k}}{\mu} = 1\frac{mm^4}{s^2}$. The initial porosity of the rock is assumed to be 30%. It is important to point out that in this type of analysis the applied external loads simulate the total in-situ stresses, while in the previous analysis the applied external loads simulate the effective in-situ stresses. As far as the constitutive law, the simulations adopt the same model as before, which is slightly simplified assuming a linear elastic law for the elastic regime. Fig. 5-27 shows the initial steady state condition, when the reservoir is intact and the in situ stress is in equilibrium with the pore fluid pressure, which is uniform and equal to $32MPa$. Note that, as aspected, the horizontal and vertical stresses, as can be observed from the subfigures (c) and (d) are equal to the effective stresses of the prevoius analysis. This first solution becomes the reference configuration of next analysis.

The first simulation investigates the case with balance drilling, i.e. when the mud pressure is equal to the fluid pore pressure. Fig. 5-28 shows the results in term of fluid pore pressure at different time steps, after the drilling process.

As can be observed, at the begining of the perforation there is an dramatic increase of pore preassure along the direction of minimum in situ stress, and a decrease of pressure along the direction of maximum stress. Depending on the permeability of the rock, th fluid diffuses, until the steady state condition is reached, which in this case consists again in a uniform distributed pressure of $32MPa$.
Fig. 5-29 shows the results in term of vertical displacements at different time steps, after the drilling process.

As can be observed, at the beginning of the preforation there are no significant displacements, and

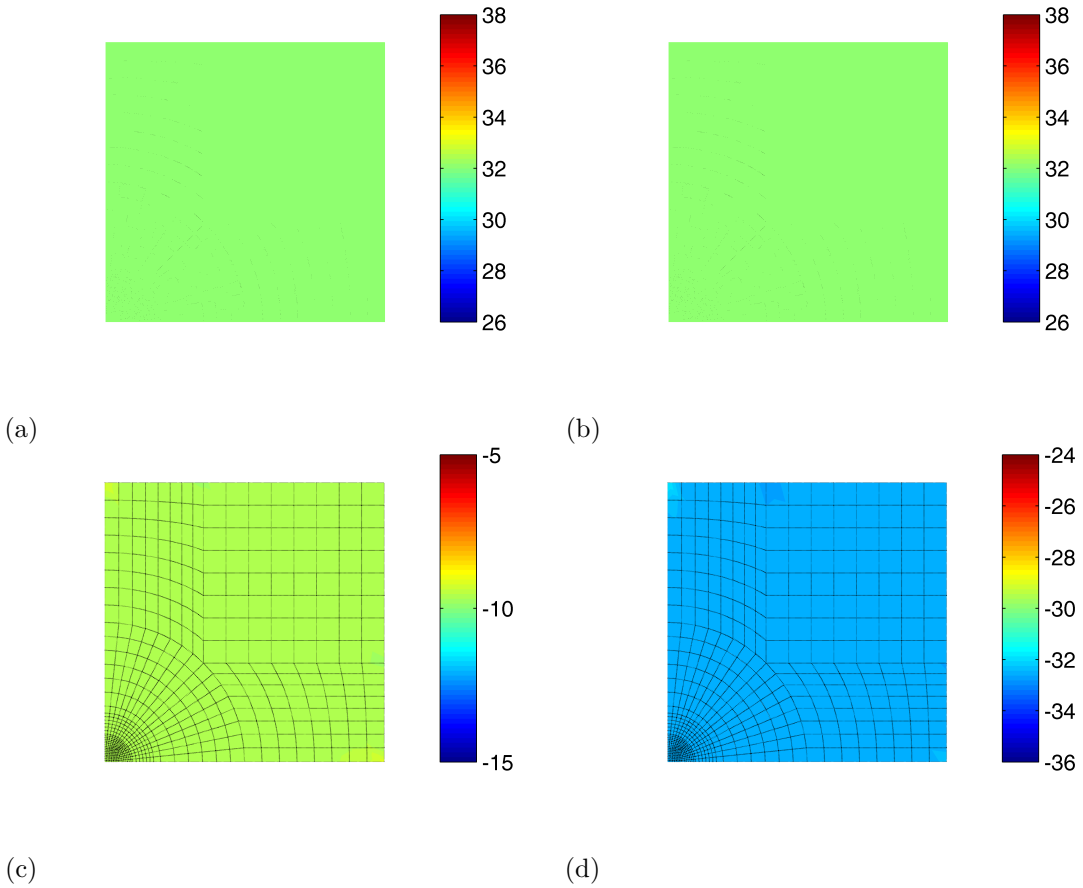

Figure 5-27: Initial steady state condition in term of (a) pore pressure [MPa], (b) vertical displacement [mm], (c) horizontal and (d) vertical stress [MPa].

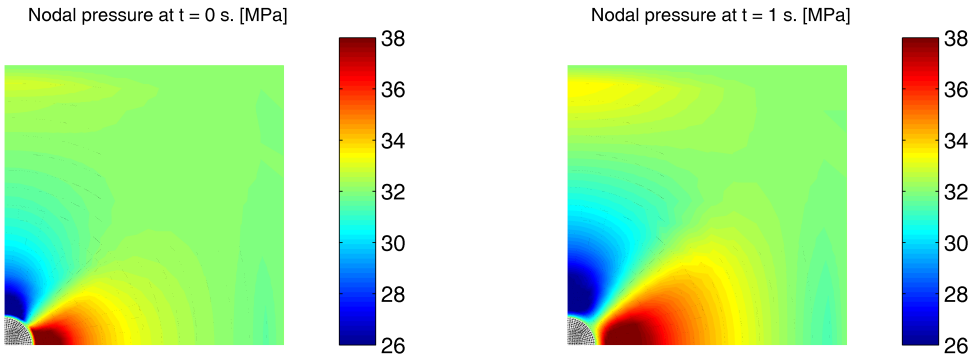

(a)

(b)

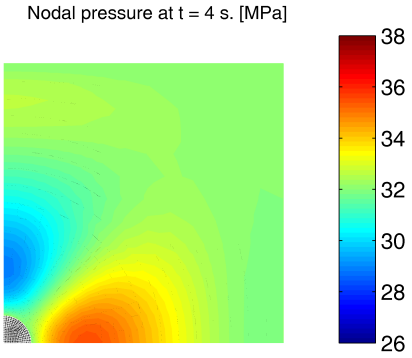

(c)

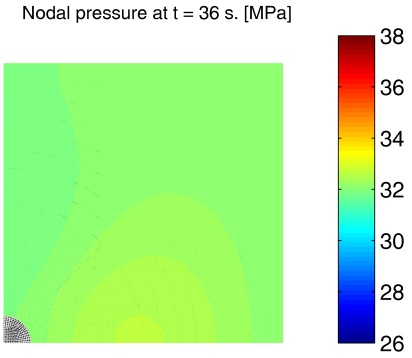

(d)

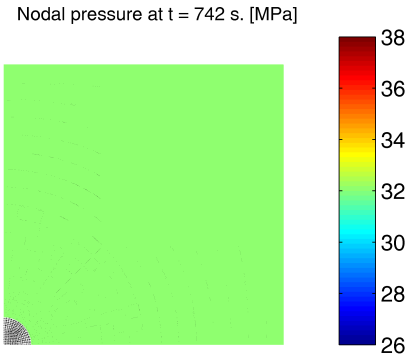

(e)

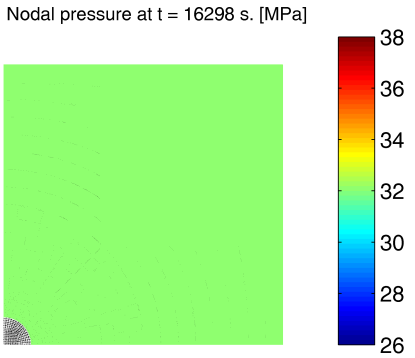

(f)

Figure 5-28: Evolution of the nodal pore pressure [MPa] at different time steps.

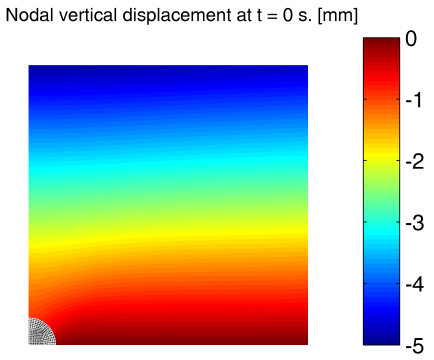

(a)

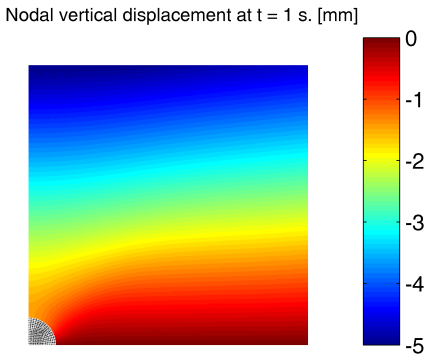

(b)

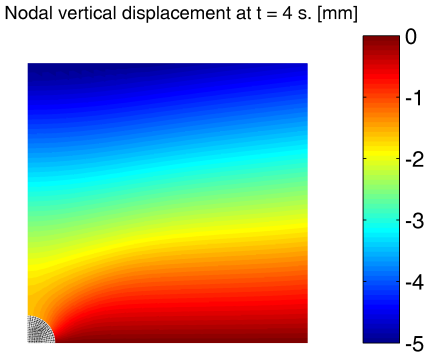

(c)

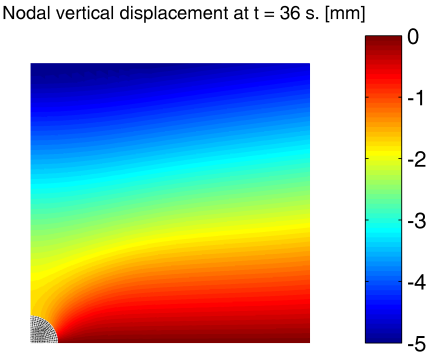

(d)

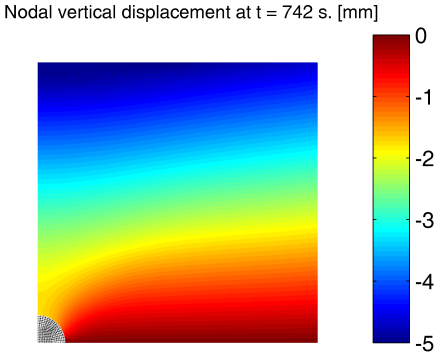

(e)

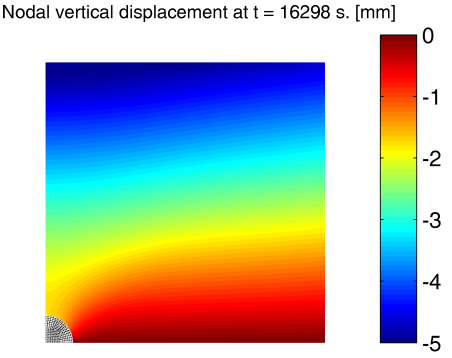

(f)

Figure 5-29: Evolution of the vertical displacements [mm] at different time steps.

they increase until the steady condition is reached, due to the diffusion process. The phenomenon can be considered as a consolidation process, where, instead of applying a load on the surface, it is removed part of the material supporting the allready applied external load, and the domain has to find a new equilibrated configuration.
Fig. 5-30 shows the results in term of deviatoric plastic strain at different time steps, after the drilling process.

As can be observed, there is an increase of the plastic region, and therefore of the failure zone, as far as the fluid diffuses around the wellbore. In fact, the extra total stress in the rock formation due to the removal of the rock is initially supported by the increased fluid pressure surrounding the hole, and subsequntly, by the rock, with behaves plasticcaly as far as the effective stress increase. After a sufficient interval of time, the steady state condition is reached, and the plastic zone assumed a fixed dimension.
As done before, the same simulation is done considering now an increased value of the mud pressure, equal to $\Delta P = 4MPa$. This corresponds to apply to the nodes along the wall of the wellbore a fluid pore pressure equal to $36MPa$. The initial reference condition for this simulation is the same as in the previous one. Fig. 5-31 shows the results in term of fluid pore pressure at different time steps, after the drilling process.

The evolution of the pore pressure is similar to the case when the the mud pressure is equal to zero, and the same trend can be observed. The fundamental difference consists in the fact that now, in the final steady state, the pore pressure in the reservoir is non longer uniform and equal to $32MPa$, but there is a homogeneous decrease of pressure, from the value of $36MPa$ along the wall of the wellbore to the value of $32MPa$ of the reservoir. Fig. 5-32 shows the results in term of vertical displacements at different time steps, after the drilling process.

Comparing the results obtained from this simulation with the previous results, there are no significant differences in term of vertical displacement when the mud pressure is increased of $4MPa$. The same trend is observed in both the analysis. Fig. 5-33 shows the results in term of deviatoric plastic strain at different time steps, after the drilling process.

As can be observed, increasing the mud pressure, as discussed also for the purely mechanical analysis, reduces the effective stress around the wellbore and therefore the plastic deformation of the rock. It is then possible quantify the contribution of the mud pressure in preventing the failure of the wellbore, as discussed in the previous section.
Figg. 5-34, 5-35, 5-36 show again the results in term of fluid pore pressure, vertical displacement and deviatoric plastic strain when the the value of the mud pressure arises to $\Delta P = 8MPa$. Same consideration can be extended also at this configuration, observing the contribution of the mud pressure in preventing the failure of the well.

ciao

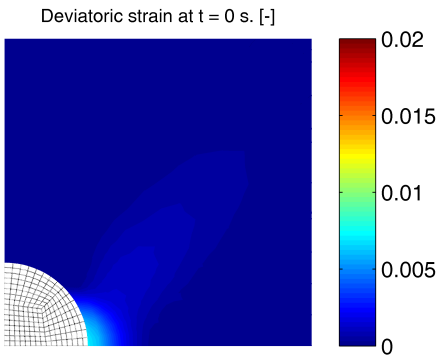

(a)

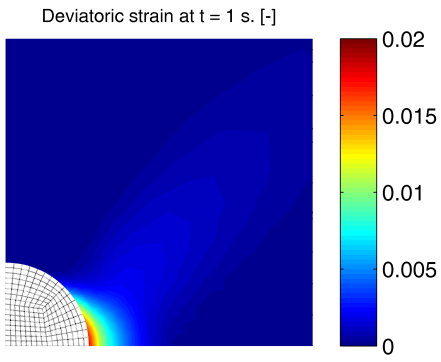

(b)

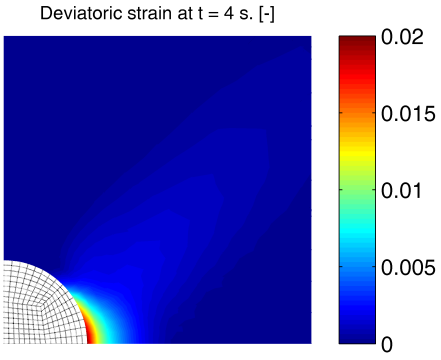

(c)

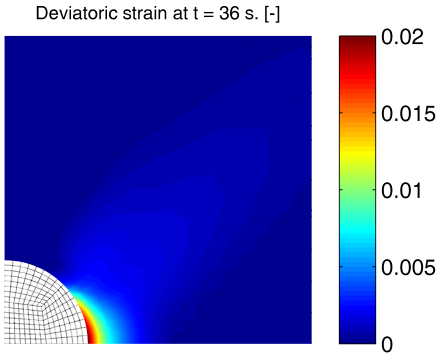

(d)

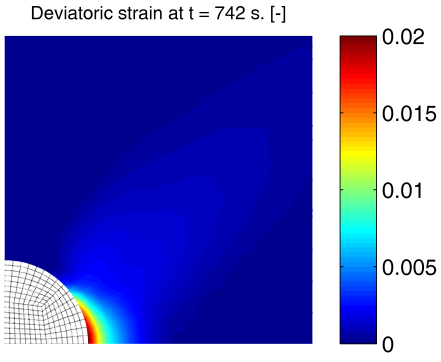

(e)

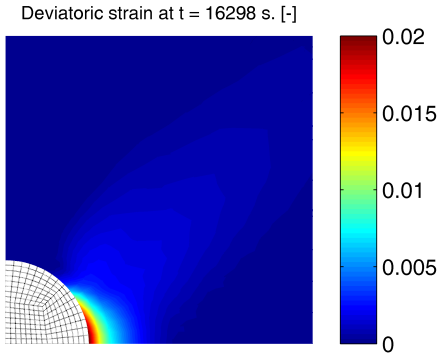

(f)

Figure 5-30: Evolution of the deviatoric plastic strain at different time steps.

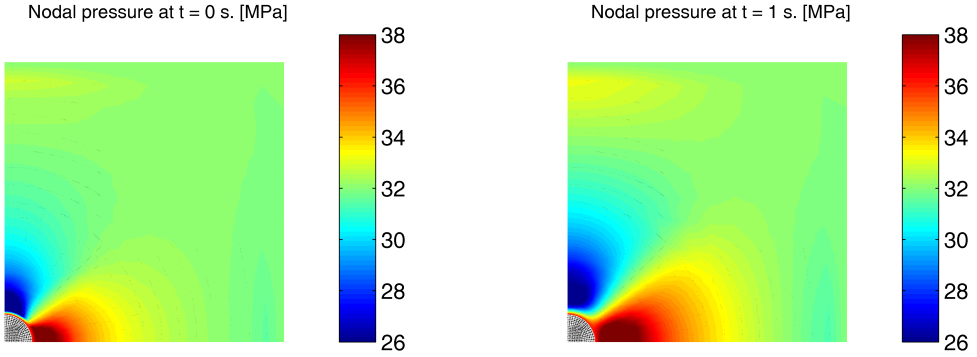

(a)

(b)

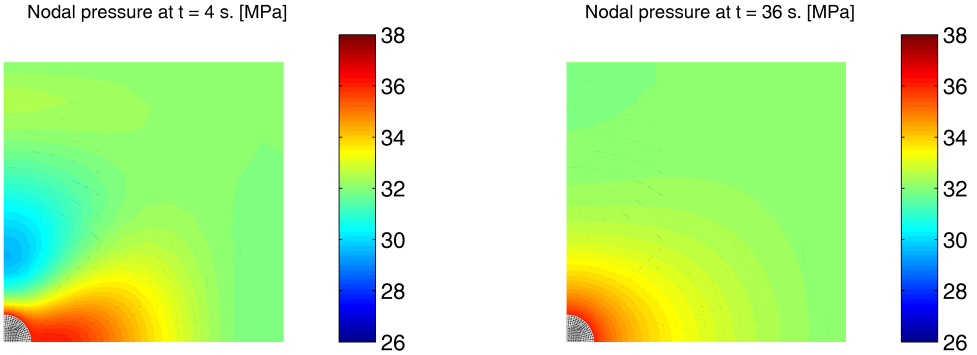

(c)

(d)

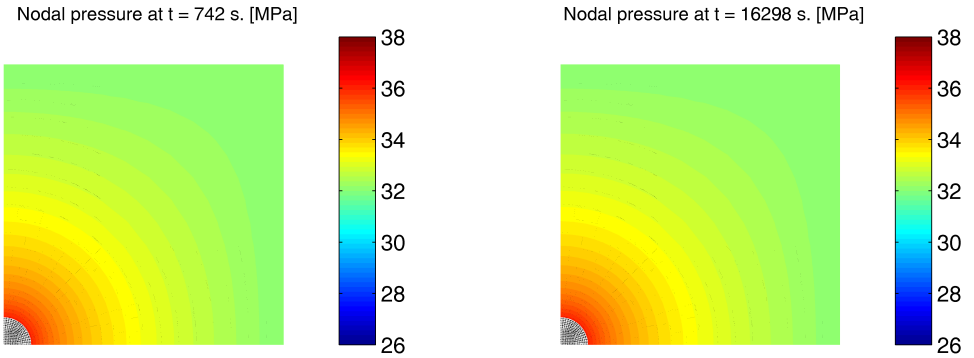

(e)

(f)

Figure 5-31: Evolution of the nodal pore pressure [MPa] at different time steps with applied mud pressure $\Delta P = 4MPa$.

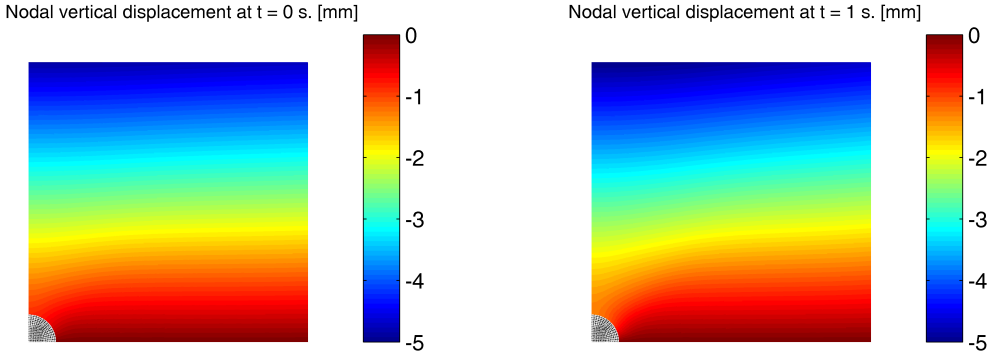

(a)

(b)

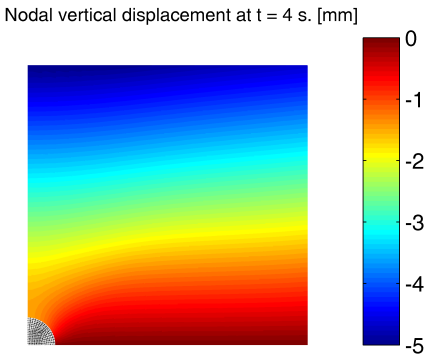

(c)

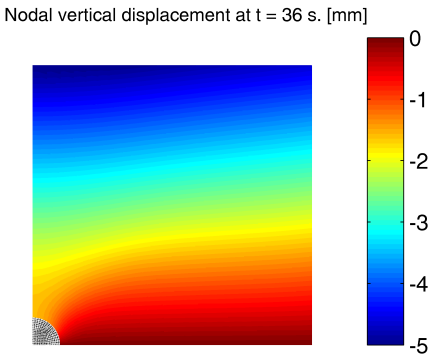

(d)

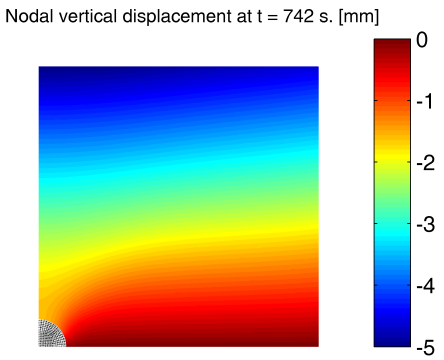

(e)

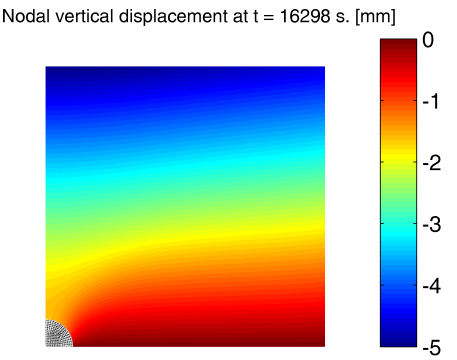

(f)

Figure 5-32: Evolution of the vertical displacements [mm] at different time steps with applied mud pressure $\Delta P = 4MPa$.

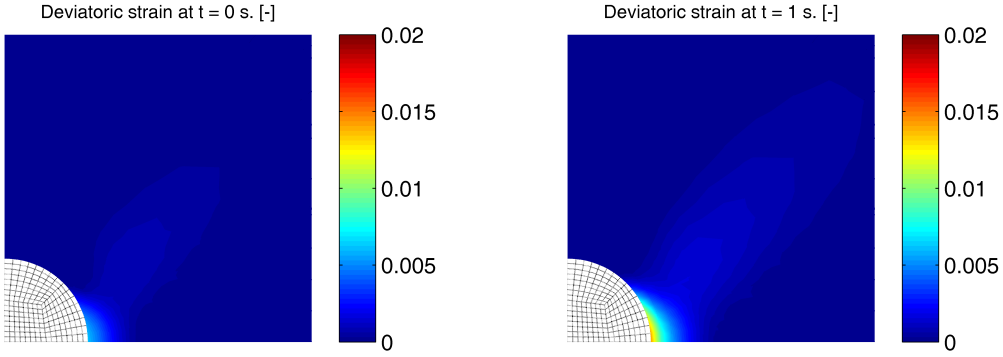

(a)

(b)

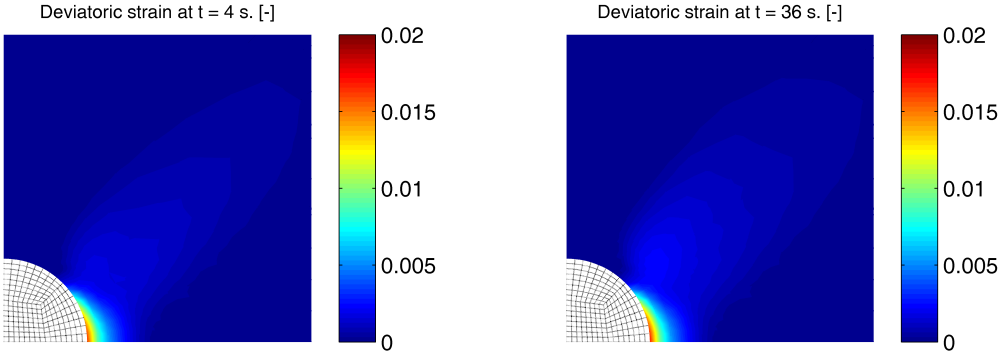

(c)

(d)

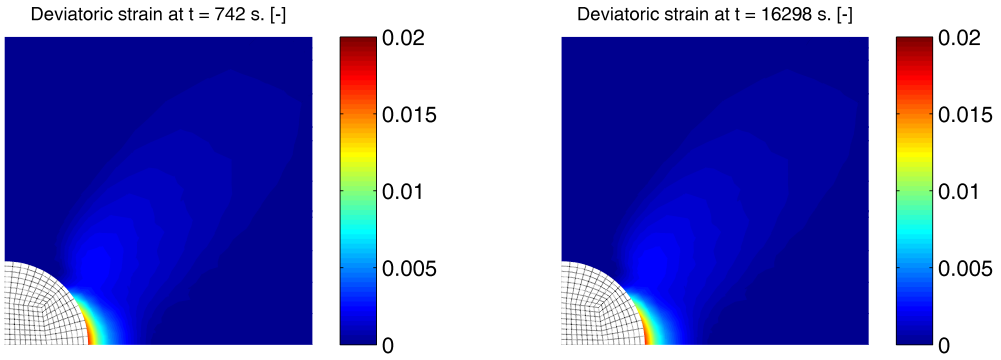

(e)

(f)

Figure 5-33: Evolution of the deviatoric plastic strain at different time steps with applied mud pressure $\Delta P = 4MPa$.

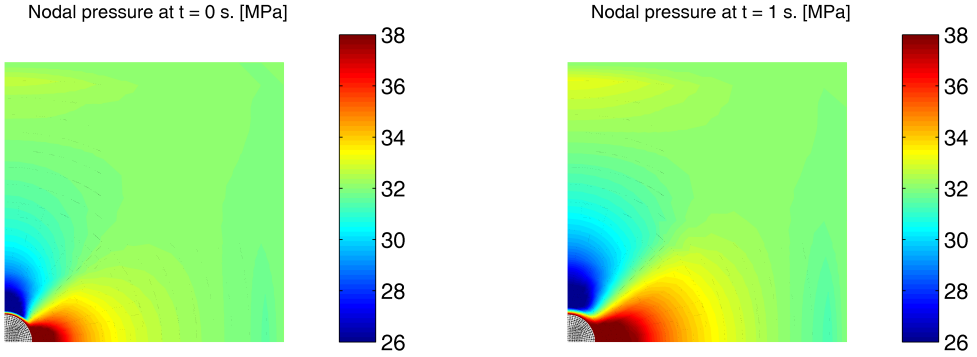

(a)

(b)

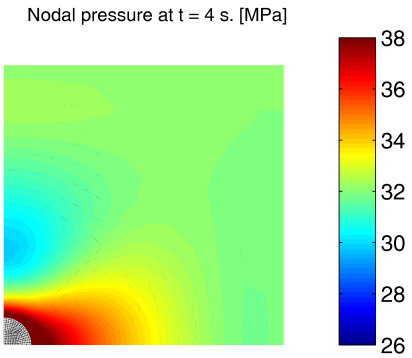

(c)

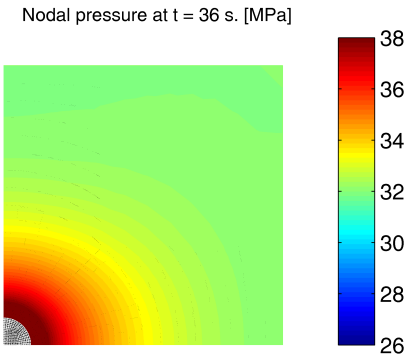

(d)

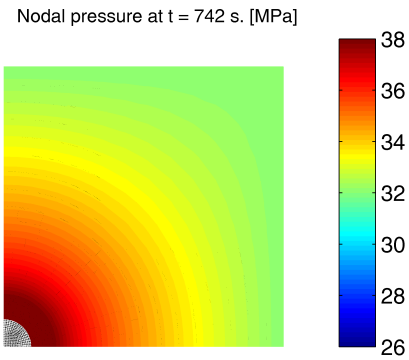

(e)

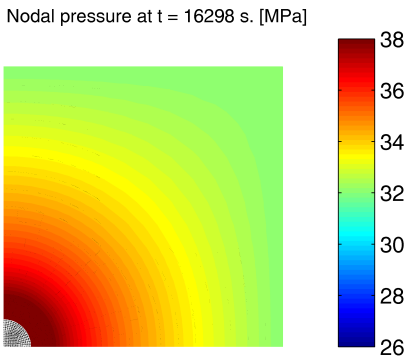

(f)

Figure 5-34: Evolution of the nodal pore pressure [MPa] at different time steps with applied mud pressure $\Delta P = 8MPa$.

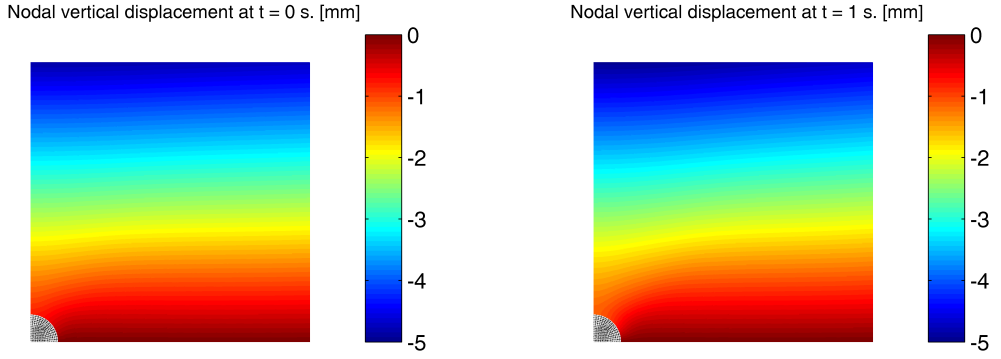

(a)

(b)

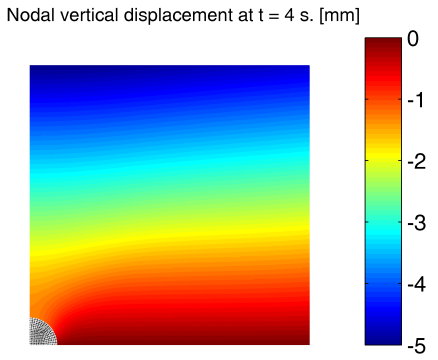

(c)

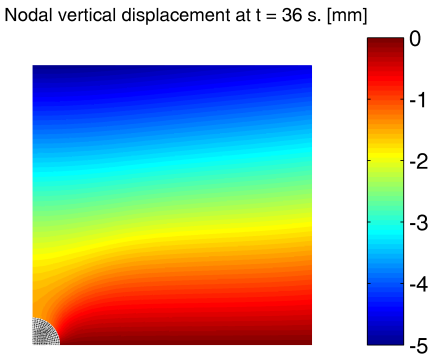

(d)

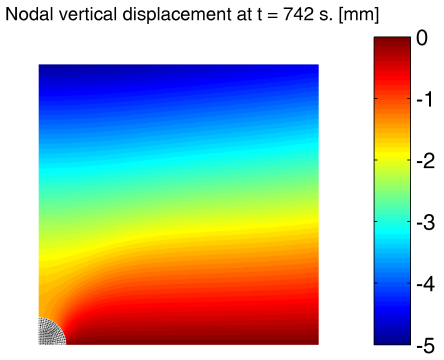

(e)

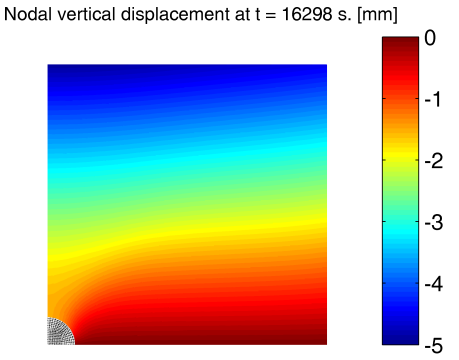

(f)

Figure 5-35: Evolution of the vertical displacements [mm] at different time steps with applied mud pressure $\Delta P = 8MPa$.

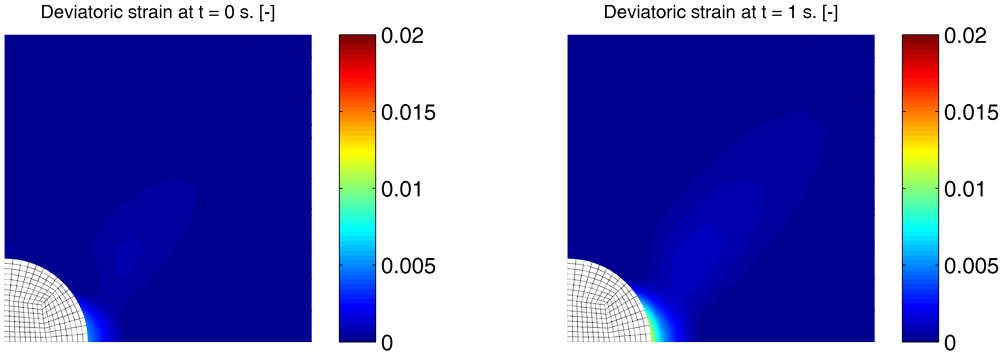

(a) (b)

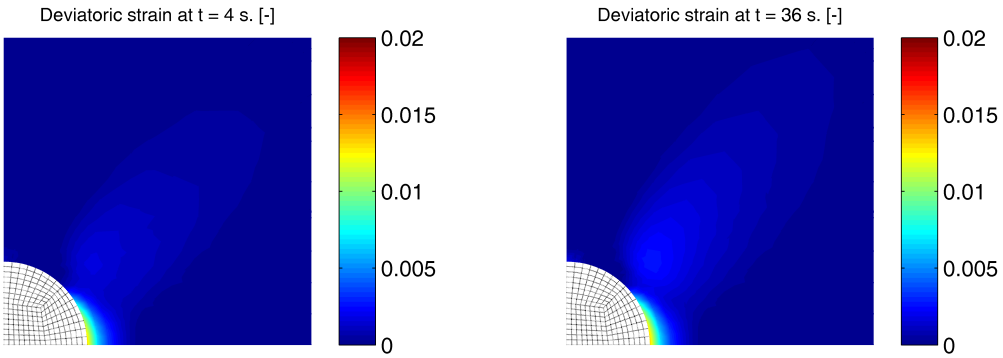

(c) (d)

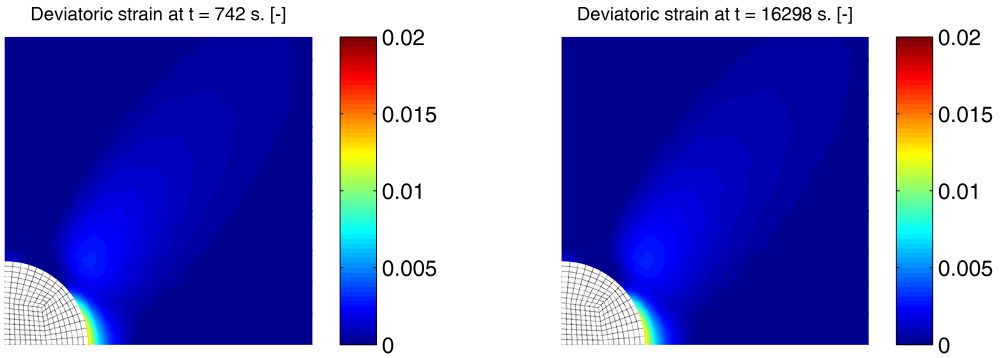

(e) (f)

Figure 5-36: Evolution of the deviatoric plastic strain at different time steps with applied mud pressure $\Delta P = 8MPa$.

Chapter 6

Conclusions and future developments

The present work furnishes a framework to deal with a coupled model for a multiphase material undergoing finite elastoplastic deformations. Three main aspects have been considered in this thesis: the theoretical formulation, based on the balance laws for the multiphase continuum body along with a thermodinamically consistent constitutive theory; the numerical solution, based on the implementation of the balance laws in a new finite element code, using mixed $\boldsymbol{u} - p$ elements; the application of the developed numerical code to evaluate, in particular, the elastoplastic deformations and band localization on a strip foundation on clay and around a horizontal wellbore drilled through a porous rock formation.

Numerical examples involving one-dimensional compression and two-dimensional plane strain loading on compressible clays demonstrate the usefulness of the finite deformation model. Specifically, a plane-strain example problem was run on clays to show that, unlike the commonly used hypoelastic-based finite strain models which are restricted to small elastic strains, the new formulation can also accommodate for the development of large elastic strains. In addition, the formulation used circumvents the rate issue in finite deformation analysis. A comparison of results of small strain and finite deformation analysis show that large deformation effects can significantly influence the predicted deformation and pore pressure responses of the soil. The second example, namely the perforation of a horizontal wellbore, demonstrated the capability of the coupled model to simulate the entire drilling process. Furthermore, the model can asses the large elastoplastic deformations and the propagation of the localization band along the hole. Finally, investigation of different configuration showed that the mud pressure and the presence of imperfections along the wall play an important role in the initiation of localized band, and therefore in the stability of the wellbore.

A lot of further future developments can be carried out starting from the work presented in this

thesis. The introduction into the numerical model of more phases, such as air, oil, gas etc, taking into account the unsaturated condition of the soil, or, more in general, of the porous material. The investigation of the role of the temperature in the elastoplastic constitutive equations, especially for high (e.g. geothermal energy) and low (e.g. frozen soil) temperature, or other state variables, such as for example the chemical concentration of a certain substance. As far as the numerical aspects, it may be of interest, and in certain circumstances necessary, explore stabilization techniques to handle the large changes in the shape of the elements, that can lead to the singularity of the element. In fact, it has been observed that the implemented numerical code fails to find a convergent solution if the shape of the element is extremely distorted, such that the computed deformation gradient is not positive anymore.

Finally, most of all the work can be expanded considering different applications-not only in the plane strain conditions-and used to solve others coupled elastoplastic problems.

Appendix A

Tangent operator for the Continuos Cap model

A.1 Derivation of the Jacobian matrix $\boldsymbol{A}$ in eq. (3.81)

The 3×3 Jacobian matrix $\boldsymbol{A}^k$ in eq. (3.81) for return mapping iteration is obtained by differentiating the component of $\boldsymbol{r}$ with respect to the variables $\boldsymbol{x}$ defined in eq. (3.80). For simplicity, the superscript (k) denoting the value at kth iteration is abbreviated in the following derivation. Depending on the return mapping algorithm, we will compute three different matrix, i.e. $\boldsymbol{A}^{NA}_{Lin}$, $\boldsymbol{A}^{NA}_{Ell}$, $\boldsymbol{A}^{A}_{Ell}$. Let us recall the Hessian matrix of ψ, $\boldsymbol{D}^e = \nabla\nabla\psi$ from eq. (3.57). For the linear non-associative return mapping, the matrix $\boldsymbol{A}^{NA}_{Lin}$ take the form

$$\boldsymbol{A}^{NA}_{Lin} = \begin{bmatrix} 1 & 0 & \partial_P \bar{\mathscr{G}} \\ 0 & 0 & \partial_Q \bar{\mathscr{G}} \\ D^e_{11}\partial_P \mathscr{F}_1 + D^e_{21}\partial_Q \mathscr{F}_1 & D^e_{12}\partial_P \mathscr{F}_1 + D^e_{22}\partial_Q \mathscr{F}_1 & 0 \end{bmatrix}, \tag{A.1}$$

where $\partial_P \bar{\mathscr{G}} = -\bar{m}$, $\partial_Q \bar{\mathscr{G}} = 1$, $\partial_P \mathscr{F}_1 = -m$ and $\partial_Q \mathscr{F}_1 = 1$. For the elliptical non-associative return mapping, the matrix $\boldsymbol{A}^{NA}_{Ell}$ take the form:

$$\boldsymbol{A}^{NA}_{Ell} = \begin{bmatrix} 1 & 0 & \partial_P \bar{\mathscr{G}} \\ 0 & 0 & \partial_Q \bar{\mathscr{G}} \\ D^e_{11}\partial_P \mathscr{F}_2 + D^e_{21}\partial_Q \mathscr{F}_2 + K_p \partial_{P_i} \mathscr{F}_2 & D^e_{12}\partial_P \mathscr{F}_2 + D^e_{22}\partial_Q \mathscr{F}_2 & 0 \end{bmatrix}, \tag{A.2}$$

where $\partial_P \mathscr{F}_2 = 2B^2(P - P_i)$, $\partial_Q \mathscr{F}_2 = 2A^2 Q$ and $\partial_{P_i} \mathscr{F}_2 = \frac{\partial B^2}{\partial P_i}((P - P_i)^2 - A^2) - 2b^2(P - P_i)$ with $\frac{\partial B^2}{\partial P_i} = 2m(mP_i + c_0)$. K_p is the plastic hardening modulus, and reads:

$$K_p = \partial_{\epsilon_v^e} P_i = \frac{-P_{i_0} r \epsilon^*}{\xi^2} \left(\frac{\epsilon^*}{\xi} \right)^{r-1} \tag{A.3}$$

with $\xi = (\epsilon^* - \epsilon_v^{e\,Tr} + \epsilon_v^e - \epsilon_{v,n}^p)$.

To compute the Jacobin matrix for the elliptical associative return mapping, let us introduce the Hessian matrix of $\mathscr{F}_2(P,Q)$ with P_i fixed:

$$\boldsymbol{H} = \nabla\nabla\mathscr{F}_2 = \begin{bmatrix} H_{11} & H_{12} \\ H_{21} & H_{22} \end{bmatrix} = \begin{bmatrix} \partial^2_{PP}\mathscr{F}_2 & \partial^2_{PQ}\mathscr{F}_2 \\ \partial^2_{QP}\mathscr{F}_2 & \partial^2_{QQ}\mathscr{F}_2 \end{bmatrix} = 2 \begin{bmatrix} B^2 & 0 \\ 0 & A^2 \end{bmatrix}, \tag{A.4}$$

and define the matrix $\boldsymbol{G} = \boldsymbol{H}\boldsymbol{D}^e$. For the elliptical associative return mapping, the matrix $\boldsymbol{A}^A_{Ell}$ take the form:

$$\boldsymbol{A}^A_{Ell} = \begin{bmatrix} 1 + \Delta\gamma(G_{11} + K_p \partial^2_{PP_i}\mathscr{F}_2) & \Delta\gamma G_{12} & \partial_P \mathscr{F}_2 \\ \Delta\gamma(G_{21} + K_p \partial^2_{QP_i}\mathscr{F}_2) & 1 + \Delta G_{22} & \partial_Q \mathscr{F}_2 \\ D^e_{11}\partial_P\mathscr{F}_2 + D^e_{21}\partial_Q\mathscr{F}_2 & D^e_{12}\partial_P\mathscr{F}_2 + D^e_{22}\partial_Q\mathscr{F}_2 + K_p\partial_{P_i}\mathscr{F}_2 & 0 \end{bmatrix}, \tag{A.5}$$

where $\partial^2_{PP_i}\mathscr{F}_2 = 2\left(\frac{\partial B^2}{\partial P_i}(P - P_i) - B^2\right)$ and $\partial^2_{QP_i}\mathscr{F}_2 = 0$.

A.2 Derivation of the consistent tangent operator $\boldsymbol{a}^{ep}$

In this section we derive the coefficients a^{ep}_{AB} for the consistent tangent operator for a return mapping in principal axes, defined as

$$a^{ep}_{AB} = \frac{\partial \beta_A}{\partial \epsilon_B^{e\,Tr}}, \qquad\qquad A, B = 1, 2, 3. \tag{A.6}$$

Again, the close form of $\boldsymbol{a}$ (where the superscript ep has been omitted for the sack of lightness) depends on the specific return mapping algorithm, therefore three different operators need to be derived. In order to reduce the derivatives to their lowest order, we expand (3.64). The expansion of $(3.64)_1$ reads:

$$b_{11}\frac{\partial \epsilon^e_v}{\partial \boldsymbol{\epsilon}^{e\,Tr}} + b_{12}\frac{\partial \epsilon^e_s}{\partial \boldsymbol{\epsilon}^{e\,Tr}} = c_1\boldsymbol{\delta} - \left(\frac{\partial \mathscr{G}}{\partial P}\right)\frac{\partial \Delta\gamma}{\partial \boldsymbol{\epsilon}^{e\,Tr}}, \tag{A.7}$$

while that for $(3.64)_2$ takes the form

$$b_{21}\frac{\partial \epsilon^e_v}{\partial \boldsymbol{\epsilon}^{e\,Tr}} + b_{22}\frac{\partial \epsilon^e_s}{\partial \boldsymbol{\epsilon}^{e\,Tr}} = c_2\boldsymbol{\delta} + \sqrt{\frac{2}{3}}\hat{\boldsymbol{n}} - \left(\frac{\partial \mathscr{G}}{\partial Q}\right)\frac{\partial \Delta\gamma}{\partial \boldsymbol{\epsilon}^{e\,Tr}}. \tag{A.8}$$

The coefficients b_{ij} and c_i will be computed in the remaining part of the section, leading to a

close form for the operator $\boldsymbol{D}^p$. The strain-gradient of $\Delta\gamma$ is obtained from the overall consistency condition

$$\frac{\partial \mathscr{F}}{\partial \boldsymbol{\epsilon}^{e\,Tr}} = \mathbf{0}. \tag{A.9}$$

Let us start from the linear non associative return mapping algorithm. In this case we have:

$$b_{11} = \partial_{\epsilon_v^e} r_1 = 1; \qquad b_{12} = \partial_{\epsilon_s^e} r_1 = 0; \tag{A.10}$$

$$b_{21} = \partial_{\epsilon_v^e} r_2 = 0; \qquad b_{22} = \partial_{\epsilon_s^e} r_2 = 1; \tag{A.11}$$

$$c_1 = 1; \qquad c_2 = 0; \tag{A.12}$$

Substituting in (A.7,A.8) we obtain:

$$\frac{\partial \epsilon_v^e}{\partial \boldsymbol{\epsilon}^{e\,Tr}} = \boldsymbol{\delta} - \frac{\partial \bar{\mathscr{G}}}{\partial P}\frac{\partial \Delta\gamma}{\partial \boldsymbol{\epsilon}^{e\,Tr}} \qquad \frac{\partial \epsilon_s^e}{\partial \boldsymbol{\epsilon}^{e\,Tr}} = \sqrt{\frac{2}{3}}\hat{\boldsymbol{n}} - \frac{\partial \bar{\mathscr{G}}}{\partial Q}\frac{\partial \Delta\gamma}{\partial \boldsymbol{\epsilon}^{e\,Tr}}. \tag{A.13}$$

In this case, eq. (A.9) reads

$$\frac{\partial \mathscr{F}_1(P,Q)}{\partial \boldsymbol{\epsilon}^{e\,Tr}} = \frac{\partial \mathscr{F}_1}{\partial P}\frac{\partial P}{\partial \boldsymbol{\epsilon}^{e\,Tr}} + \frac{\partial \mathscr{F}_1}{\partial Q}\frac{\partial Q}{\partial \boldsymbol{\epsilon}^{e\,Tr}} = \mathbf{0}, \tag{A.14}$$

which can be written as

$$\frac{\partial \mathscr{F}_1}{\partial \boldsymbol{\epsilon}^{e\,Tr}} = d_1\frac{\partial \epsilon_v^e}{\partial \boldsymbol{\epsilon}^{e\,Tr}} + d_2\frac{\partial \epsilon_s^e}{\partial \boldsymbol{\epsilon}^{e\,Tr}} = \mathbf{0}, \tag{A.15}$$

where

$$d_1 = D_{11}^e \partial_P \mathscr{F}_1 + D_{21}^e \partial_Q \mathscr{F}_1; \qquad d_2 = D_{12}^e \partial_P \mathscr{F}_1 + D_{22}^e \partial_Q \mathscr{F}_1. \tag{A.16}$$

Substituting (A.13) into (A.15) and solving for $\partial\Delta\gamma/\partial\boldsymbol{\epsilon}^{e\,Tr}$ we obtain

$$\frac{\partial \Delta\gamma}{\partial \boldsymbol{\epsilon}^{e\,Tr}} = a_1\boldsymbol{\delta} + a_2\sqrt{\frac{2}{3}}\hat{\boldsymbol{n}}, \tag{A.17}$$

where $a_1 = d_1/e$, $a_2 = d_2/e$ and $e = d_1\partial_P\bar{\mathscr{G}} + d_2\partial_Q\bar{\mathscr{G}}$. Finally, the last step involves backsubstitution. Inserting (A.17) into (A.13) and rearranging the terms we have:

$$\boldsymbol{D}^p_{LinNA} = \begin{bmatrix} 1 - a_1\partial_P\bar{\mathscr{G}} & -a_2\partial_P\bar{\mathscr{G}} \\ -a_1\partial_Q\bar{\mathscr{G}} & 1 - a_2\partial_Q\bar{\mathscr{G}} \end{bmatrix}. \tag{A.18}$$

For elliptical yield surface with non-associative flow rule, the procedure to compute $\boldsymbol{D}^p_{EllNA}$ is

very similar to what derived so far. In this case the expression (A.13) remains unchanged, while (A.9 reads

$$\frac{\partial \mathscr{F}_2(P,Q,P_i)}{\partial \boldsymbol{\epsilon}^{e\,Tr}} = \frac{\partial \mathscr{F}_2}{\partial P}\frac{\partial P}{\partial \boldsymbol{\epsilon}^{e\,Tr}} + \frac{\partial \mathscr{F}_2}{\partial Q}\frac{\partial Q}{\partial \boldsymbol{\epsilon}^{e\,Tr}} + \frac{\partial \mathscr{F}_2}{\partial P_i}\frac{\partial P_i}{\partial \boldsymbol{\epsilon}^{e\,Tr}} = \mathbf{0}, \tag{A.19}$$

which can be written as

$$\frac{\partial \mathscr{F}_2}{\partial \boldsymbol{\epsilon}^{e\,Tr}} = d_1\frac{\partial \epsilon_v^e}{\partial \boldsymbol{\epsilon}^{e\,Tr}} + d_2\frac{\partial \epsilon_s^e}{\partial \boldsymbol{\epsilon}^{e\,Tr}} + K^{(}Tr)_p\frac{\partial \mathscr{F}_2}{\partial P_i} = \mathbf{0}, \tag{A.20}$$

where

$$d_1 = D_{11}^e\partial_P\mathscr{F}_2 + D_{21}^e\partial_Q\mathscr{F}_2 + K_p\partial_P\mathscr{F}_2; \qquad d_2 = D_{12}^e\partial_P\mathscr{F}_2 + D_{22}^e\partial_Q\mathscr{F}_2. \tag{A.21}$$

end $K^T r_p = \partial_{\epsilon_v^{e\,Tr}} = -K_p$. Substituting (A.13) into (A.20) and solving for $\partial\Delta\gamma/\partial\boldsymbol{\epsilon}^{e\,Tr}$ we obtain the same expression in (A.17) where now $a_1 = (d_1 + K_p^{Tr}\partial_{P_i}\mathscr{F}_2)/e$, $a_2 = d_2/e$ and e as before derived. Again, inserting (A.17) into (A.13) and rearranging the terms we have:

$$\boldsymbol{D}_{EllNA}^p = \begin{bmatrix} 1 - a_1\partial_P\bar{\mathscr{G}} & -a_2\partial_P\bar{\mathscr{G}} \\ -a_1\partial_Q\bar{\mathscr{G}} & 1 - a_2\partial_Q\bar{\mathscr{G}} \end{bmatrix}. \tag{A.22}$$

Finally, let us compute the the opertator $\boldsymbol{D}_{EllA}^p$ for elliptical yield surface with associative flow rule. Also in this case, the derivation follows the same steps as already done for the other algorithms. In this case we have:

$$b_{11} = 1 + \Delta\gamma(G_{11} + K_p\partial^2_{PP_i}\mathscr{F}_2); \qquad b_{12} = \Delta\gamma G_{12}; \tag{A.23}$$

$$b_{21} = \Delta\gamma(G_{21} + K_p\partial^2_{QP_i}\mathscr{F}_2); \qquad b_{22} = 1 + \Delta\gamma G_{22}; \tag{A.24}$$

$$c_1 = 1 - \Delta\gamma(G_{11} + K_p^{Tr}\partial^2_{PP_i}\mathscr{F}_2); \qquad c_2 = -\Delta\gamma(G_{11} + K_p^{Tr}\partial^2_{QP_i}\mathscr{F}_2); \tag{A.25}$$

The strain-gradient of $\Delta\gamma$ is obtained from the overall consistency condition (A.20), which again can be written as (A.20) with d_1 and d_2 as in (A.16). Solving (A.20) for $\Delta\gamma/\partial\boldsymbol{\epsilon}^{\boldsymbol{e\,Tr}}$ we obtain the same expression as (A.17), where:

$$a_1 = \left[d_1(b_{22}c_1 - b_{12}c_2) + d_2(b_{11}c_2 - b_{21}c_1) + \tilde{b}K_p^{Tr}\partial_{P_i}\mathscr{F}_2\right]/e; \tag{A.26}$$

$$a_2 = \sqrt{2/3}(d_2b_{11} - d_1b_{12})/e; \tag{A.27}$$

$$e = d_1(b_{22}\partial_P\mathscr{F}_2 - b_{12}\partial_Q\mathscr{F}_2) + d_2(b_{11}\partial_Q\mathscr{F}_2 - b_{21}\partial_P\mathscr{F}_2); \tag{A.28}$$

with $\tilde{b} = b_{11}b_{22} - b_{21}b_{12}$. Inserting (A.17) into (A.13) and rearranging the terms, we obtain

$$\check{D}^p_{11} = b_{22}(c_1 - a_1\partial_P\mathscr{F}_2) - b_{12}(c_2 - a_1\partial_Q\mathscr{F}_2); \tag{A.29a}$$

$$\check{D}^p_{12} = b_{12}(-1 + \sqrt{3/2}a_2\partial_Q\mathscr{F}_2) - \sqrt{3/2}b_{22}a_2\partial_Q\mathscr{F}_2; \tag{A.29b}$$

$$\check{D}^p_{21} = b_{11}(c_2 - a_1\partial_Q\mathscr{F}_2) - b_{21}(c_1 - a_1\partial_P\mathscr{F}_2); \tag{A.29c}$$

$$\check{D}^p_{22} = b_{11}(1 - \sqrt{3/2}a_2\partial_Q\mathscr{F}_2) + \sqrt{3/2}b_{21}a_2\partial_P\mathscr{F}_2. \tag{A.29d}$$

In conclusion

$$\boldsymbol{D}^p_{EllA} = \check{\boldsymbol{D}}^p/\tilde{b}. \tag{A.30}$$

Bibliography

[1] Borja, R. I., Tamagnini, C., and Alarcón, E. (1998) Elastoplastic consolidation at finite strain part 2: finite element implementation and numerical examples. *Computer Methods in Applied Mechanics and Engineering*, **159**, 103–122.

[2] Wong, T.-f. and Baud, P. (2012) The brittle-ductile transition in porous rock: A review. *Journal of Structural Geology*, **44**, 25–53.

[3] Baud, P., Vajdova, V., and Wong, T.-f. (2006) Shear-enhanced compaction and strain localization: Inelastic deformation and constitutive modeling of four porous sandstones. *Journal of Geophysical Research*, **111**, B12401.

[4] Coelho, L. C., Soares, A. C., Ebecken, N. F. F., Alves, J. L. D., and Lau, L. (2005) The impact of constitutive modeling of porous rocks on 2-d wellbore stability analysis. *Journal of Petroleum Science and Engineering*, **46**, 81–100.

[5] Biot, M. A. (1941) General theory of three-dimensional consolidation. *Journal of applied physics*, **12**, 155–164.

[6] Bear, J. (2013) *Dynamics of fluids in porous media*. Courier Dover Publications.

[7] Boer, R. (2000) *Theory of porous media: highlights in historical development and current state*. Springer New York.

[8] Fung, Y. and Cowin, S. (1994) Biomechanics: Mechanical properties of living tissues. *Journal of Applied Mechanics*, **61**, 1007.

[9] Cowin, S. C. and Doty, S. B. (2007) *Tissue mechanics*. Springer.

[10] Coussy, O. (2004) *Poromechanics*. John Wiley & Sons.

[11] Jeremić, B., Cheng, Z., Taiebat, M., and Dafalias, Y. (2008) Numerical simulation of fully saturated porous materials. *International Journal for Numerical and Analytical Methods in Geomechanics*, **32**, 1635–1660.

[12] Lewis, R. W. and Schrefler, B. A. (1998) *The finite element method in the static and dynamic deformation and consolidation of porous media*. John Wiley.

[13] Zienkiewicz, O. C., Chan, A., Pastor, M., Schrefler, B., and Shiomi, T. (1999) *Computational geomechanics*. Wiley Chichester.

[14] Kojic, M., Filipovic, N., Vulovic, S., and Mijailovic, S. (1998) A finite element solution procedure for porous medium with fluid flow and electromechanical coupling. *Communications in numerical methods in engineering*, **14**, 381–392.

[15] Almeida, E. S. and Spilker, R. L. (1997) Mixed and penalty finite element models for the nonlinear behavior of biphasic soft tissues in finite deformation: part i alternate formulations. *Computer Methods In Biomechanics and Bio Medical Engineering*, **1**, 25–46.

[16] Almeida, E. S. and Spilker, R. L. (1998) Finite element formulations for hyperelastic transversely isotropic biphasic soft tissues. *Computer methods in applied mechanics and engineering*, **151**, 513–538.

[17] Borja, R. I. and Alarcón, E. (1995) A mathematical framework for finite strain elastoplastic consolidation part 1: Balance laws, variational formulation, and linearization. *Computer Methods in Applied Mechanics and Engineering*, **122**, 145–171.

[18] Borja, R. I. and Tamagnini, C. (1996) Critical state model at finite strains. vol. 1, pp. 148–151.

[19] Borja, R. (2002) Finite element simulation of strain localization with large deformation: Capturing strong discontinuity using a petrov-galerkin multiscale formulation. *Computer Methods in Applied Mechanics and Engineering*, **191**, 2949–2978.

[20] Borja, R. (2002) Bifurcation of elastoplastic solids to shear band mode at finite strain. *Computer Methods in Applied Mechanics and Engineering*, **191**, 5287–5314.

[21] Li, C., Borja, R., and Regueiro, R. (2004) Dynamics of porous media at finite strain. *Computer Methods in Applied Mechanics and Engineering*, **193**, 3837–3870.

[22] Uzuoka, R. and Borja, R. (2012) Dynamics of unsaturated poroelastic solids at finite strain. *International Journal for Numerical and Analytical Methods in Geomechanics*, **36**, 1535–1573.

[23] Song, X. and Borja, R. (2014) Mathematical framework for unsaturated flow in the finite deformation range. *International Journal for Numerical Methods in Engineering*, **97**, 658–682.

[24] Armero, F. (1999) Formulation and finite element implementation of a multiplicative model of coupled poro-plasticity at finite strains under fully saturated conditions. *Computer Methods in Applied Mechanics and Engineering*, **171**, 205–241.

[25] Armero, F. and Love, E. (2003) An arbitrary lagrangian-eulerian finite element method for finite strain plasticity. *International Journal for Numerical Methods in Engineering*, **57**, 471–508.

[26] Callari, C. and Armero, F. (2004) Analysis and numerical simulation of strong discontinuities in finite strain poroplasticity. *Computer Methods in Applied Mechanics and Engineering*, **193**, 2941–2986.

[27] Armero, F. and Linder, C. (2008) New finite elements with embedded strong discontinuities in the finite deformation range. *Computer Methods in Applied Mechanics and Engineering*, **197**, 3138–3170.

[28] Lee, E. H. (1969) Elastic-plastic deformation at finite strains. *Journal of Applied Mechanics*, **36**, 1–6.

[29] Hashiguchi, K. and Yamakawa, Y. (2012) *Introduction to finite strain theory for continuum elasto-plasticity*. John Wiley & Sons.

[30] Simo, J. (1992) Algorithms for static and dynamic multiplicative plasticity that preserve the classical return mapping schemes of the infinitesimal theory. *Computer Methods in Applied Mechanics and Engineering*, **99**, 61–112.

[31] Olsson, W. A. (1999) Theoretical and experimental investigation of compaction bands in porous rock. *J. Geophys. Res.*, **104**, 7219–7228.

[32] Baud, P., Klein, E., and Wong, T.-f. (2004) Compaction localization in porous sandstones: spatial evolution of damage and acoustic emission activity. *J. Struct. Geol.*, **26**, 603–624.

[33] Baud, P., Vinciguerra, S., David, S., Cavallo, A., Walker, A., and Reuschle, T. (2009) Compaction and failure in high porosity carbonates: mechanical data and microstructural observations. *Pure Appl. Geophys.*, **166**, 869–898.

[34] Holzapfel, G. A. (2000) *Nonlinear solid mechanics*, vol. 24. Wiley Chichester.

[35] Malvern, L. E. (1969) *Introduction to the Mechanics of a Continuous Medium*. No. Monograph.

[36] Marsden, J. E. and Hughes, T. J. (1994) *Mathematical foundations of elasticity*. Courier Dover Publications.

[37] Truesdell, C. and Noll, W. (2004) *The non-linear field theories of mechanics*. Springer.

[38] Ogden, R. W. (1997) *Non-linear elastic deformations*. Courier Dover Publications.

[39] Atkin, R. and Craine, R. (1976) Continuum theories of mixtures: basic theory and historical development. *The Quarterly Journal of Mechanics and Applied Mathematics*, **29**, 209–244.

[40] Bowen, R. M. (1982) Compressible porous media models by use of the theory of mixtures. *International Journal of Engineering Science*, **20**, 697–735.

[41] Bonet, J. (1997) *Nonlinear continuum mechanics for finite element analysis*. Cambridge university press.

[42] Borja, R. I. and Tamagnini, C. (1998) Cam-clay plasticity part iii: Extension of the infinitesimal model to include finite strains. *Comput. Methods. Appl. Mech. Engrg.*, **155**, 73–95.

[43] Borja, R. I. (2013) *Plasticity. Modeling and Computation*. Springer.

[44] Simof, J. and Hughes, T. (2008) Computational inelasticity.

[45] Lambe, T. W. and Whitman, R. V. (2008) *Soil mechanics SI version*. John Wiley & Sons.

[46] Lade, P. V. and Nelson, R. B. (1987) Modelling the elastic behaviour of granular materials. *Int. J. Num. Anal. Meth. Geomech.*, **11**, 521–542.

[47] Janbu, N. (1963) Soil compressibility as determined by odometer and triaxial tests. *Proc. European Conf. Soil Mech. Found Eng.*, **1**, 19–25.

[48] Duncan, J. M. and Chang, C. Y. (1970) Nonlinear analysis of stress and strain in soils. *J. Soil Mech. Found. Diu. A.S.C.E.*, **96**, 1629–1653.

[49] Houlsby, G. T. (1985) The use of a variable shear modulus in elastic-plastic for clays. *Comput. Geotech.*, **1**, 3–13.

[50] Callari, C., Auricchio, F., and Sacco, E. (1998) A finite-strain cam-clay model in the framework of multiplicative elasto-plasticity. *Int. J. Plasticity*, **14**, 1155–1187.

[51] Yamakawa, Y., Hashiguchi, K., and Ikeda, K. (2010) Implicit stress-update algorithm for isotropic cam-clay model based on the subloading surface concept at finite strains. *Int. J. Plasticity*, **26**, 634–658.

[52] Borja, R. I. and Andrade, J. E. (2006) Critical state plasticity. part vi: Meso-scale finite element simulation of strain locaization in discrete granular materials. *Comput. Methods Appl. Mech. Engrg.*, **195**, 5115–5140.

[53] Zhang, J., Wong, T.-f., and Davis, D. M. (1990) Michromechanics of pressure-induced grain crushing in porous rock. *Journal of Geophysical Research*, **95**, 341–52.

[54] David, C., Wong, T.-f., Zhu, W., and Zhang, J. (1994) Laboratory measurement of compaction-induced permeability change in porous rock: implications for the generation and maintenance of pore pressure excess in the crust. *Pure Appl. Geophys.*, **143**, 425–456.

[55] Wong, T.-f., David, C., and Zhu, W. (1997) The transition from brittle faulting to cataclastic flow in porous sandstones mechanical deformation. *Journal of Geophysical Research*, **102**, 3009–25.

[56] Wong, T.-f., Szeto, H., and Zhang, J. (1990) Effect of loading path and porosity on the failure mode of porous rocks. *Appl. Mech. Rev.*, **45**, 281–93.

[57] Rudnicki, J. W. and Rice, J. R. (1975) Condition for the localization of deformation in pressure-sensitive dilatant materials. *J. Mech. Phys. Solids.*, **23**, 371–94.

[58] Critical state model in computational geomechanics. *Engrg. Comput.*, **, pages =**.

[59] Zytynski, M., Rolph, M. K., Nova, R., and Wroth, C. P. (1978) On modeling the unloading-reloading behaviour of soils. *Int. J. Numer. Anal. Methods Geomech*, **2**, 87–93.

[60] Issen, K. A. (2002) The influence of constitutive models on localization conditions for porous rock. *Engineering Fracture Mechanics*, **69**, 1891–1906.

[61] Schofield, A. and Wroth, C. P. (1968) *Crticial State Soil Mechanics*. Mc-Graw-Hill.

[62] Carroll, M. M. (1971) A critical state plasticity theory for porous reservoir rock. *Recent Advances in Mechanics of Structured Continua*, **97**, 935–950.

[63] Grueschow, E. and Rudnicki, J. W. (2005) Elliptical yield cap constitutive modeling for high porosity sandstone. *International Journal of Solids and Structures*, **42**, 4574–4587.

[64] Jefferies, M. G. (1997) Nor-sand: a simple critical state model for sand. *Geotechnique,*, **47**, 255–272.

[65] Di Maggio, F. L. and Sandler, I. S. (1971) Material model for granular soils. *J. Eng. Mech. Div.*, **97**, 935–950.

[66] Fossum, A. F. and Fredrich, J. T. (2000) Cap plasticity models and compactive and dilatant pre-failure deformation. Tech. rep., Sandia National Labs., Albuquerque, NM (United States).

[67] Stefanov, Y. P., Chertov, M. A., Aidagulov, G. R., and Myasnikov, A. V. (2011) Dynamics of inelastic deformation of porous rock and formulation of localized compaction zones studied by numerical modeling. *Journal of the Mechanics and Physics of Solids*, **59**, 2323–2340.

[68] de Souza Neto, E. A., Peric, D., and Owen, D. R. J. (2009) *Computational Methods for Plasticity: Theory and Applications*. John Wiley and Sons.

[69] Biot, M. A. (1955) Theory of elasticity and consolidation for a porous anisotropic solid. *Journal of Applied Physics*, **26**, 182–185.

[70] Fortin, M. and Brezzi, F. (1991) *Mixed and hybrid finite element methods*. Springer.

[71] Sun, S. and Wheeler, M. F. (2005) Discontinuous galerkin methods for coupled flow and reactive transport problems. *Applied Numerical Mathematics*, **52**, 273–298.

[72] Malkus, D. S. and Hughes, T. J. (1978) Mixed finite element methods—reduced and selective integration techniques: a unification of concepts. *Computer Methods in Applied Mechanics and Engineering*, **15**, 63–81.

[73] Zoback, M. D. (2010) *Reservoir Geomechanics*. Cambridge University Press.

[74] Mollema, P. N. and Antonellini, M. A. (1996) Compaction bands: a structural analog for anti-mode i cracks in aeolian sandstone. *Tectonophysics*, **267**, 209–228.

[75] Issen, K. A. and Rudnicki, J. W. (2000) Condition for compaction bands in porous rock. *J. Geophys. Res.*, **105**, 21529–21536.

[76] Haimson, B. (2001) Fracture-like borehole breakouts in high-porosity sandstone: are they caused by compaction bands? *Physiscs and Chemistry of the Earth. Part A: Solid Earth and Geodesy*, **26**, 15–20.

[77] Haimson, B. and Kovachic, J. (2003) Borehole instability in high-porosity berea sandstone and factors affecting dimensions and shape of fracture-like breakouts. *Engineering Geology*, **69**, 219–231.

[78] Wong, T.-f., Baud, P., and Klein, E. (2001) Localized failure modes in a compactant porous rock. *Geophys. Res. Lett.*, **28**, 2521–2524.

[79] Vajdova, V. and Wong, T.-f. (2003) Incremental propagation of discrete compaction bands: acoustic emission and microstructural observation on circumferentially notched samples of bentheim sandstone. *Geophys. Res. Lett.*, **30**, 17–75.

[80] Chen, W.-F. and Mizuno, E. (1990) *Nonlinear Analysis in Soil Mechanics. Theory and Implementation*. Elsevier.

[81] Andrade, J. E. and Borja, R. I. (2006) Capturing strain localization in dense sands with random density. *Int. J. Numer. Meth. Engng.*, **67**, 1531–1564.